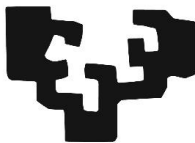


eman ta zabal zazu



Universidad  
del País Vasco

Euskal Herriko  
Unibertsitatea

*Magneto-optical ellipsometry and magnetometry  
of thin films and multilayers*

***Jon Ander Arregi Uribeetxebarria***

***PhD Thesis***

***Supervisor: Dr. Andreas Berger***

**2020**





***Jon Ander Arregi Uribeetxebarria***

***Supervisor: Dr. Andreas Berger***

***2020***



*Agurtzane, Iñigo  
ta gure gurasuei*

*Andoni, Joseba ta Tiagori*



# Laburpena

Magneto-optikak materialen hedatzen diren uhin elektromagnetikoen eremu magnetiko edo magnetizazio baten eraginpean jasandako fenomeno fisikoak ikertzen ditu. Lehen efektu magneto-optikoa 1845ean aurkitu zuen esperimentalki Faradayk, argia eremu magnetiko baten kokatutako beira batean zehar transmititzean, honek bere polarizazio egoera aldatzen zuela ikustean. Argiak izaera elektromagnetikoa duela frogatu nahian zebilen Faraday, eta saiakera haren ondoren bere kuadernoan “eremu magnetikoaren lerroak argizatzea, zein argia magnetizatzea” lortu zuela idatzi zuen. 30 urte inguru geroago, islapen geometriaren gertatzen den efektu baliokidea aurkitzen lehena izan zen Kerr, eta egun *Kerr efektu magneto-optikoa* (ingelesez, MOKE) izenez ezagutzen da fenomeno hau. Ordurako argiaren polarizazioari buruzko ideia aurreratuak existitzen baziren ere, 1908an argitaratu zuen Voigt-ek lehenbiziko aldiz MOKE efektutik eratorritako argiaren polarizazio aldaketak deskribatzeko trataera matematikoa, urte batzuk lehenago Maxwell-ek osatutako elektromagnetismoaren oinarri teorikoei jarraiki. Efektu magneto-optikoen jatorri mikroskopikoa azaltzeko, ordea, 1950eko hamarkadarararte itxaron behar izan zen. Mekanika kuantikoaren garapenak zein elektroiaren deskribapen erlatibistak lagunduta, MOKE efektua truke-energia magnetikoaren eta espin-orbita akoplamenduaren ondoriozkoa zela ulertu zen.

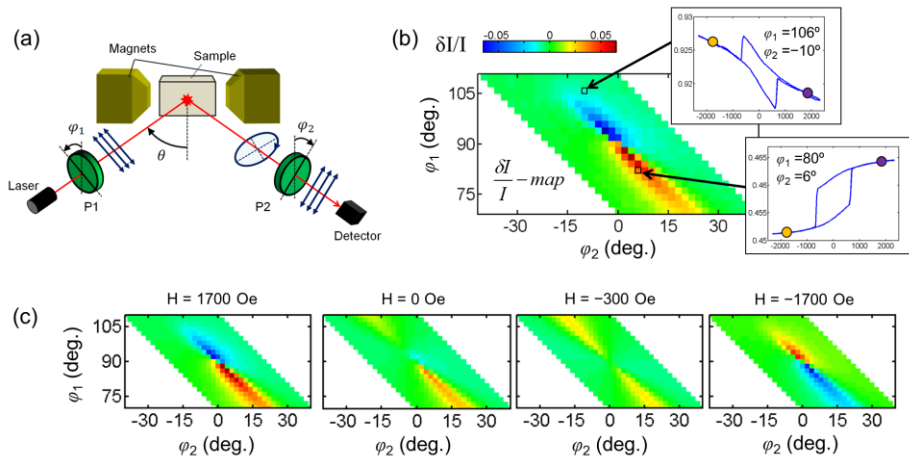
Lehen aurkikuntza esperimentaletik 150 urte baino gehiago pasatu diren arren, efektu magneto-optikoak oso sarri erabiltzen dira gaur egun material magnetikoen ikerkuntzan zein prozesu industrialetan. Argiaren polarizazio egoera zehaztasun handiz neurtzeko gaur egun existitzen den teknologia MOKE efektuan oinarritutako sentikortasun handiko karakterizazio magnetikoa ahalbidetzen du, materialen magnetizazioa nanoeskalan neurtzeko aukera emateraino (adibidez, atomo batzuetako lodiera duten geruza finen edo mikroeskalako elementuen histeresi ziklo magnetikoko neurtu daitezke). Horrez gain, laser-iturri pulsatuen laguntzarekin, naturan gertatzen diren prozesu magnetiko ultra-azkarrak (10-100 femtosegundoko denbora tartean) bereizteko gai den teknika bakarretakoa da. Hori dela eta, teknika magneto-optikoen garapena eta nanomagnetismoa zein espintronikari buruz ditugun ezagutza batera joan dira azken hamarkadetan.

Tesi honetan, efektu magneto-optikoan oinarria duen teknika esperimental bat landu da, elipsometria magneto-optiko orokortua (*generalized magneto-optical ellipsometry*, GME). Haren bidez, nanoeskalako geruza finen edo multigeruzen magnetizazio propietateak ahalik eta zehaztasun zein doitasun handienaz neurtu dira. GME teknikaren oinarria, zeina 1997an eman zuten ezagutzera Berger eta Puffall-ek, MOKE esperimentu batean lortu daitekeen informazio guztia osotasunean lortzean datza, horretarako laginetik islatutako argiaren polarizazio egoera konfigurazio desberdinetan neurtuz. MOKE saiakera arrunt batean balizko lagin baten histeresi zikloa neurtzea dagoeneko teknika esperimental arrunt bezala jo daitekeen arren, zera erakutsi nahi da: neurketak multzo egokitan eskuratu eta datuen analisi optimizatu eginez gero, zehaztasun eta bereizmen handiko informazio bilduma lortu daitekeela laginaren propietate optiko, magneto-optiko eta magnetikoen inguruan.

Tesiaren **1go Kapitulu**an nanomagnetismoak eta espintronikak garapen teknologikoan izan duen garrantzia azaltzen da lehenik. Ondoren, material magnetikoen oinarriko hainbat kontzeptu azaldu dira, hala-nola elkarrekintza magnetiko desberdinak, zein magnetizazioaren alderanzketa prozesua. Bestalde, efektu magneto-optikoen azalpen zabalago bat ere eman nahi izan da. **2. Kapitulu**an, doktoretza tesi hau osatzeko erabili diren teknika esperimentalak erakusten dira, oinarri zein prozedurei buruzko zehaztapenak emanez. Adibidez, laginen fabrikazioa eta beraien karakterizazio estrukturala, magnetikoa eta optikoa burutzeko pausuak deskribatu dira.

**3. Kapitulu**an, lan honen enborra izan den GME teknika aurkezten da. Muntaia esperimental, neurketa prozedura, eta analisi estrategia azaldu dira. GME teknikak muntaia esperimental erlatiboki sinplea duen arren (ikus L1 irudia), datu multzo handiak eskuratzea eskatu dezake sarritan. Hori dela eta, neurketa prozeduraren optimizazio bat burutu da esperimentuen eraginkortasuna hobetze aldera. Ondoren, kobaltozko geruza fin epitaxialetan egiaztatu da magnetometria burutzeko bere ahalmena. Hain zuzen ere, magnetizazio bektorearen hiru osagaiak kanpoko eremu magnetiko batek eragindako alderanzketa prozesuan zehar determinatu daitezkeela erakutsi da. Magnetizazio bektorea matematikoki bi angeluren bidez adieraziz,  $0.1^\circ$  eta  $0.01^\circ$  ordeneko doitasuna lortu da geruzaren planoan eta planotik kanpo duen orientazioaren angeluaren neurketan, hurrenez hurren. Magnetizazio bektorearen determinazio hain zehatza egiteko aukerak askotariko fenomeno magnetiko eta magneto-optikoak ulertzen laguntzeko bide ematen duela erakutsi da ondorengo kapituluetan. Izan ere, magnetizazio bektore osoaz gain, errefrakzio indizea eta akoplamendu magneto-optikoaren indarra ( $Q$  faktore konplexua) ere modu zehatzean lortzeko gaitasuna du GME teknikak, azken finean, tentsore dielektriko osoa aurkitzekoa. Azkenik, geruza magnetiko batek (kobaltoa) bere gainean anisotropia

optikoa duen beste geruza bat dueneko kasua ikertu da (kobalto oxidoa), efektu magneto-optikoa birrefringentziaren eraginez nola aldatzen diren aztertuz.



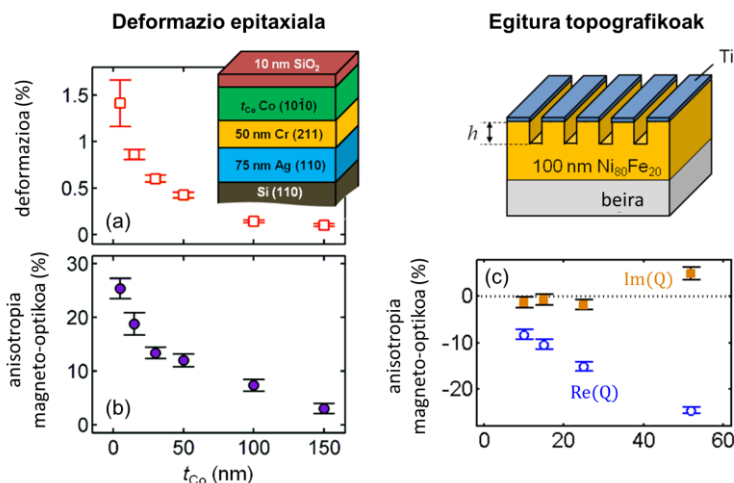
**L1 Irudia:** (a) GME teknikaren muntaia esperimental, tesi honetan eraikia eta optimizatua izan dena. Muntaia magneto-optikoa nagusiki laser batez, bi polarizatzaile linealez, fotodetektore batez eta elektroiman batez osatzen da. (b) Neurketa prozeduraren deskribapena. Histeresi ziklo magnetikoak neurtzen dira bi polarizatzaileen hainbat konfigurazio ezberdinetarako. Ereku magnetikoaren balioa alderantzean neurtzen diren fotoboltoiak eskuratzen dira, hortik  $\delta I/I$  intentsitate aldaketa erlatiboa polarizatzaileen orientazio desberdinetarako lotuz, eta kantitate honen mapa bidimentsionala (GME mapa) eraikiz. (c) GME maparen bilakaera, kanpoko eremu magnetikoa aldatu ahala. MOKE eragiten duten magnetizazio osagai bakoitzak simetria ezberdineko egiturak osatzen ditu GME mapan, haiek identifikatu eta bereiztea posible delarik.

Jarraian, material magnetikoetan gutxitan ikertu ohi den propietate bat aztertu da, anisotropia magneto-optikoa, alegia. Efektu magneto-optikoen anplitudea magnetizazioak materialean duen norabide kristalografikoaren menpekota dela pentsatzea arrazoizkoa bada ere, oso lan gutxik aztertu dute propietate hau sakonean. Adibidez, geruza magnetiko batean magnetizazioa bi norabide ezberdinetan saturatu eta gero, neurtutako MOKE efektuaren tamainan ezberdintasun txikiak aurkitu izan dira batzuetan. Orokorrean, ordea, anisotropiarik existitzen ez deneko kontsiderazioa egiten dute MOKE efektuaren inguruan argitaratzen diren lan gehienek.

Lan honetan, alde batetik kobaltozko geruza fin epitaxialak aztertu dira (**4. Kapitula**), zeintzuek egitura kristalografiko hexagonala duten eta beraz ardatz printzipal nagusi baten presentzia (egitura kubikoaren kasuan ez bezala). Ereku magnetiko baten bitartez magnetizazioa gradualki ardatz kristalografiko batetik bestera bideratu ahala, GME teknikaren bidez laginaren tentsore dielektriko osoa kuantifikatu da, ondoren informazio hau anisotropia magneto-optikoa era zehatzean determinatzeko erabiliz. Ikerketa sistematiko baten ondoren, honakoa ondorioztatu da: anisotropia

magnetiko-optikoa uste baino handiagoa izan daiteke geruza metaliko epitaxialetan, eta anisotropiaren anplitudeak deformazio epitaxialarekin korrelazio sendoa erakusten du (ikus L2 irudia). Ideia honi tiraka, kobaltozko geruzen deformazio epitaxialean eraginez anisotropia magneto-optikoa kontrolatzeko proposamena aurkeztu da. Era berean, MOKE neurketa baten bidezko magnetometria emaitzek akatsak izan ditzaketela ondorioztatu da kasu konkretu batzuetan, hots, baldin materialak anisotropia magneto-optikoa badu eta MOKE seinaleen interpretazioa gertaera hau arbuaiatuz egiten bada.

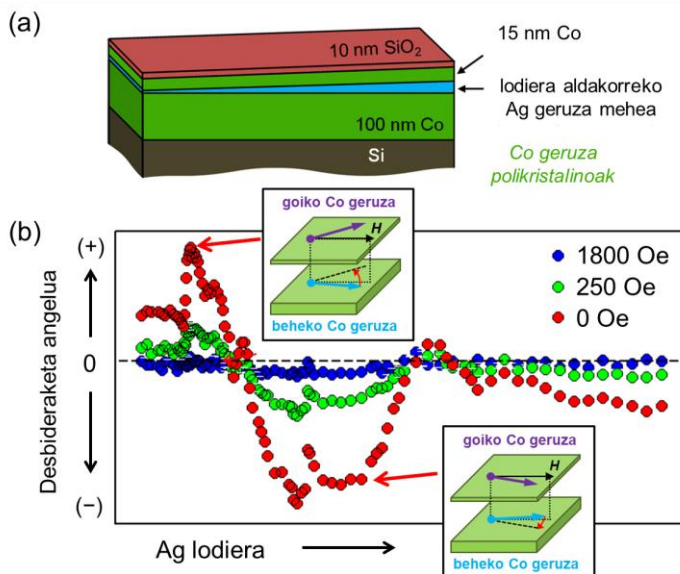
Litografikoki fabrikatutako gainazaleko egitura duten burdin-nikelezko geruza finen kasuan ere anisotropia magneto optikoa aztertu da (**5. Kapitulua**), anisotropia egitura topografikoaren sakonerarekin hazten dela aurkituz (ikus L2 irudia). Honez gain, lagin hauek laser argia ere difraktatzen dutenez, efektu magneto-optikoa difrakzioan aztertu da lehen eta bigarren difrakzio ordenean, seinalearen polarizazio azterketa eginez, eta polarizazioarekiko MOKE simetriak islapenaren kasuarekin alderatuz.



**L2 Irudia:** GME teknikaren bidezko anisotropia magneto-optikoaren neurketak lodiera ezberdineko kobaltozko geruza epitaxialetan (ezkerrean) eta litografia bidez sortutako gainazaleko egitura topografikoak dituzten nikel-burdinezko geruza finetan (eskuinean). Anisotropia magneto-optikoa eta deformazio epitaxialaren arteko korrelazio sendoa aurkitu da lehen kasuan. Bigarrenean, anisotropia magneto-optikoa egitura topografikoaren sakonerarekin batera hazten dela ikusi da.

Azkenik, **6. Kapitulua** Co/Ag/Co multigeruza sisteman aurkitutako ezohiko akoplamendu magnetiko baten ganean dihardu. Erdiko Ag geruzaren lodiera aldakorreko ziri-formako laginak fabrikatu dira, lodierak laginen propietate optiko, magneto-optiko eta magnetikoetan duen eragina ikertzeko. Lagin luzexkaren puntu desberdinetan GME neurketak eginez, kanpoko eremu magnetikoa zero deneko kasuan magnetizazioak Ag lodieraren menpeko desbideraketa bat erakusten duela aurkitu da.

Desbideraketa honek kiraltasun iraunkor bat erakusten du, zeinetan goiko eta beheko Co geruzetako magnetizazio bektoreen arteko bidea erlojuaren orratzen norabidekoa (edo aurkakoa) den beti, Ag lodiera jakin baterako (ikus L3 irudia). Fenomeno honen jatorria Co geruzen arteko akoplamendu magnetiko baten ondoriozkoa dela azaltzen da tesian, non haien arteko elkarrekintzak Co geruzen magnetizazioen arteko kiraltasun mota jakin bat ezartzen duen (Dzyaloshinskii-Moriya elkarrekintzaren bidez emana). Tesi honetan, eredu mikromagnetiko sinple baten bitartez elkarrekintzaren indarra Ag lodieraren menpe zenbatetsi ahal izan da (honen magnitude ordena  $0.1 \text{ mJ/m}^2$ -koa delarik), eta bere jatorri fisikoa erdiko Ag geruzan aurkitzen diren kobaltozko ezpurutasun ez magnetikoetan aurkitzen dela ondorioztatu.



**L3 Irudia:** (a) Co/Ag/Co multigeruza laginaren egitura, erdian ziri-formako Ag geruza duelarik (0.3-3 nm arteko lodiera aldakorrarekin). (b) GME neurketen bidez lortutako magnetizazio bektorearen angelua, Ag geruzaren lodiera ezberdinetarako. Kanpoko eremu magnetiko aski handi baterako ( $>1000 \text{ Oe}$ ), magnetizazio bektoreak ez du eremu magnetikoaren ardatzarekiko desbideraketarik erakusten (borobil urdinak). Kanpoko eremu magnetikoa txikiagotu ahala, Ag geruzaren lodieraren menpekota den desbideraketa erakusten du magnetizazioak, hau alde baterakoa edo besterakoa izanik Ag lodieraren arabera (borobil berde eta gorriak). Gainera, desbideraketak Ag lodierarekiko joera oszilakorra erakusten du, lodiera oso handia denean zerorantz joz ( $> 3 \text{ nm}$ ).

Tesiaren ondorioak **7. Kapitulu**an azaltzen dira. Labur esanda, GME teknika propietate optiko, magneto-optiko eta magnetikoak aztertzeko tresna sendoa eta zehatza dela erakutsi da. Gaitasun hauetatik abiatuta, geruza finetan zein multigeruza sistemetan fenomeno magneto-optiko eta magnetiko berriak aurkitu eta ikertu dira.



# Abstract

Over the last decades, the magneto-optical Kerr effect (MOKE) has gained widespread popularity as a characterization tool for the study of magnetism and magnetic materials. MOKE proved to be especially well suited to investigate magnetization effects at the nanoscale when it was first utilized in 1985 by Moog and Bader to measure magnetic hysteresis loops of Fe monolayer films. Nowadays it constitutes a widely employed form of magnetometry with the ability to obtain vector and depth- or layer-resolved magnetization information. Apart from enabling domain imaging when combined with light microscopy, it has also been successfully employed for the analysis of single nanostructures and periodic magnetic lattices, by making use of diffracted light signals. Furthermore, it constitutes one of the few viable methods, by which magnetization dynamics can be studied down to the femtosecond time scale, namely via ultrafast laser pulses, and it is crucially important in emerging fields with significant technological potential such as all-optical switching, spin transport at the nanoscale, and magnetoplasmonics.

This thesis investigates the implementation of a MOKE related technique, the *generalized magneto-optical ellipsometry* (GME), to a wide variety of magnetization reversal processes in magnetic thin film and multilayer systems. Due to its ability to distinguish true polarization effects from additional reflection effects such as birefringence, the GME technique allows to study the evolution and origin of the different polarization dependent modifications occurring from the combination of the optical, magneto-optical and magnetic properties of materials. The operation principle and optimization of the data acquisition scheme of GME are thoroughly explained in this thesis, leading to the demonstration of the three-dimensional vector magnetometry capability, based on symmetry arguments of the polarization dependent reflection matrix. This methodology allows performing magnetometry with an unprecedented precision in the determination of the magnetization angle.

Following the description of the magnetometry procedure, a detailed analysis of the dielectric tensor properties in magnetic films has been done via the GME technique, focused on a special MOKE property known as magneto-optical anisotropy.

This consists on the dissimilar coupling between magnetization and light for different magnetization orientations in the material as a result of structure or morphology. In particular, magneto-optical anisotropy is examined in epitaxial and patterned magnetic thin films. Due to the ability of GME to separate optical, magneto-optical and magnetic effects, the amplitude of this anisotropy has been reliably quantified in the systems under investigation. A clear correspondence between structural material properties and magneto-optical properties is established, and specifically, epitaxial strain and topographic depth are identified as possible sources. The effects of the presence of magneto-optical anisotropy on magnetometry are discussed, where a so-far unknown polarization effect for the transverse magnetization component is described. These findings are important for the present time, in which MOKE related techniques are acquiring a very relevant role in the experimental study of nanoscale magnetic and spintronic phenomena, with the correct interpretation of magneto-optical data being crucial for those experiments.

Last but not least, the GME methodology is applied to the study of multilayers of the type ferromagnet/noble-metal/ferromagnet, in which the noble-metal interlayer thickness is varied in the range from a few angstroms to a few nanometers. An anomalous interlayer magnetic exchange coupling is found between the two ferromagnetic layers in the Co/Ag/Co system, in which magnetization reversal occurs with an interlayer thickness-dependent predefined helicity. It is argued that the coupling originates from an impurity-mediated Dzyaloshinskii-Moriya interaction, which constitutes a novel manifestation of the interlayer exchange mechanisms found so far. A simple magnetic model allows quantifying the strength of the interaction.

# Table of contents

▪ <b>Laburpena</b> .....	i
▪ <b>Abstract</b> .....	vii

## 1. Introduction

1.1. Nanomagnetism and the development of magnetic data storage .....	1
1.2. Magnetization and overview of magnetic interactions.....	6
1.3. Hysteresis and magnetization reversal .....	17
1.4. Magneto-optical Kerr effect (MOKE) .....	27
1.5. Nanomagnetism and magneto-optics .....	38

## 2. Experimental techniques

2.1. Thin film and multilayer growth.....	41
2.2. Structural characterization via x-ray diffraction.....	52
2.3. Vibrating sample magnetometry .....	61
2.4. Spectroscopic ellipsometry .....	63

## 3. Generalized magneto-optical ellipsometry as a tool for vector magnetometry

3.1. Introduction: review of magneto-optical ellipsometry .....	67
3.2. Experimental setup and measurement procedure .....	70
3.3. GME dataset optimization .....	85
3.4. Three-dimensional vector magnetometry of magnetic thin films .....	89
3.5. Optical anisotropy effects in epitaxial Co/CoO bilayers.....	106
3.6. Measurement of non-uniform magnetization states .....	110
3.7. Conclusions.....	112

## 4. Strain-induced magneto-optical anisotropy in epitaxial hcp Co films

4.1. Introduction: early observations of magneto-optical anisotropy.....	115
4.2. Observation of magneto-optical anisotropy via GME .....	118
4.3. Study of Co films with varying thickness .....	126
4.4. Strain engineering of magneto-optics .....	135
4.5. Conclusions.....	144

<b>5. Magneto-optical ellipsometry of permalloy gratings in reflection and diffraction</b>	
5.1. Introduction: technological interest of artificially tailored materials and the concept of form birefringence .....	145
5.2. Sample description and measurement configuration .....	148
5.3. Optical and magneto-optical properties in reflection .....	152
5.4. Polarization analysis of magneto-optical effects in diffraction .....	160
5.5. Conclusions .....	166
<b>6. Oscillatory Dzyaloshinskii-Moriya type magnetic interlayer exchange coupling</b>	
6.1. Introduction: spin-polarized quantum size effects in magnetic ultrathin films and multilayers .....	167
6.2. Anomalous magnetization behavior in Co/Ag/Co multilayers .....	169
6.3. Conclusions .....	196
<b>7. Summary &amp; Outlook</b> .....	197
▪ <b>Appendix I</b>	
Polarization optics in stratified media .....	203
▪ <b>Appendix II</b>	
Derivation of the $\delta I/I$ expression for the GME technique .....	211
▪ <b>Appendix III</b>	
Magneto-optical anisotropy effects in systems with uniaxial symmetry .....	219
▪ <b>List of publications</b> .....	225
▪ <b>Acknowledgments</b> .....	227
▪ <b>References</b> .....	229

# Chapter 1

## Introduction

*The fundamental concepts of nanomagnetism and magneto-optics are introduced in this chapter. The historical importance of magnetic materials and nanomagnetism in the development of magnetic memories in general and the hard disk drive in particular is briefly explained as a motivation. Additional technological domains in which research in nanomagnetism is potentially relevant are also mentioned. Next, the fundamentals of magnetic interactions, magnetization reversal and magneto-optical effects are described, with special emphasis on phenomena occurring in nanomagnetic systems. Finally, the state-of-the-art and current relevance of magneto-optics in the fields of nanomagnetism and spintronics is highlighted. This sets a context for this thesis, in which the generalized magneto-optical ellipsometry (GME) technique is employed to investigate the fundamental optical, magneto-optical and magnetic properties of thin film and multilayer systems.*

### 1.1 Nanomagnetism and the development of magnetic data storage

Magnetic materials and magnetic phenomena have attracted humankind's interest since the ancient times, as people tried to elucidate the mechanisms behind the invisible forces exerted by bodies that could repel or attract other objects around. Nowadays a solid scientific understanding of magnetism is well established and (ferro)magnetic materials are widely utilized in a wide-variety of technological applications such as in motors, electrical generators, power transformers, sensors, loudspeakers, credit cards, etc. [1, 2].

Throughout the 20<sup>th</sup> century, ferromagnetic materials proved to be particularly useful to store non-volatile information due to their ability to remain 'permanently magnetized', allowing to save information even after the storing device is switched off. Magnetic memories were firstly introduced in the form of audio tapes, video cassette recorders, or floppy disks, where traditionally small magnetic particles of Fe<sub>2</sub>O<sub>3</sub> or ferrite materials were utilized [1]. The posterior invention of the hard disk drive (HDD), an electro-mechanical device with rapidly rotating platters coated with magnetic

## 1. Introduction

---

materials and storing digital bits of information, revolutionized the field of magnetic storage. This mainly happened due to its fast development in terms of areal density, information storage stability and production costs in the decades after its invention.

The first HDD was introduced by IBM in 1956 as a component of the RAMAC computer and had an areal density (number of information bits per disk area) of around 2000 bits/in<sup>2</sup> and a maximum capacity of 5 MB of data (see Fig. 1.1). The successive scientific and technological developments in the field of magnetism enormously increased the areal density (from  $\sim 0.1$  MB/in<sup>2</sup> in 1960, to  $\sim 10$  MB/in<sup>2</sup> in 1980, and  $\sim 25$  GB/in<sup>2</sup> in 2000 [1]). At the present time, modern HDD commercial devices are reaching areal densities of  $\sim 1$  TB/in<sup>2</sup> [2], such that modern and portable storage devices with capacities exceeding 1 TB can be bought for a price of about 100 euro (see Fig. 1.1). In addition, HDDs are designed to reliably retain information for several decades. The capacity, areal density, volume, pricing and average lifespan have been all improved by several orders of magnitude since the very first HDD model.

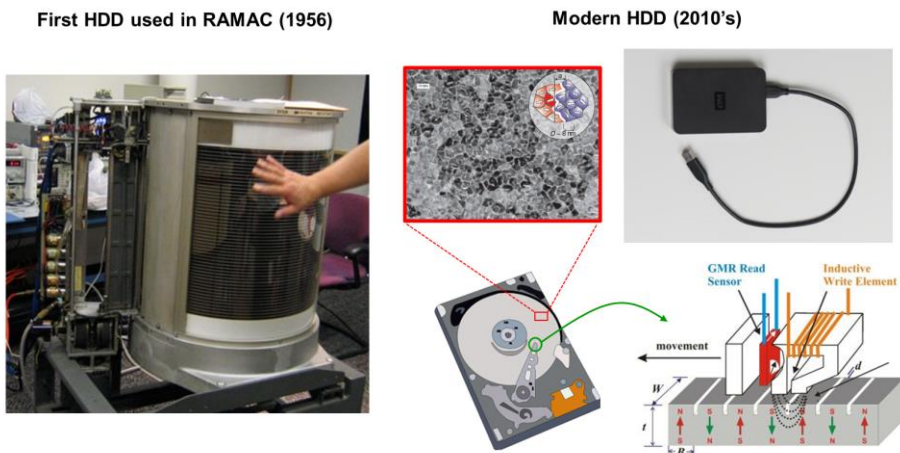


**Fig. 1.1:** (Left) Picture of a restored HDD device used in the IBM 350 RAMAC computer model from 1956, with a capacity of 5 MB. (Right) Representation of actual modern HDDs, with a capacity of a few TB. Schematics of the read-write head device and a transmission electron micrograph of a modern recording medium are shown. A write-read head placed in an actuator arm flies on top of the rotating disk and reads differently magnetized regions in the magnetic recording medium (e.g. granular CoCrPt or FePt films) via a magnetoresistive sensor, which are then interpreted as digital ('0' or '1') bits of information. A miniaturized electromagnet incorporated into the read-write head allows locally reversing the magnetic moment in small regions of the storage medium. The micrograph of the recording medium and the read-write head schematics are taken from Refs. [3] and [4], respectively. All other images are of public domain.

While these huge improvements were partially promoted by the drive to fulfill the needs of the industrial market, the scientific and technical progress in the field of magnetism played a key role in developing the platforms that would then enable creating a piece of technology that has deeply impacted our society and everyday lives. In particular, the parallel development of magnetic recording media and the information sensing mechanism in HDD devices (among other aspects) facilitated the spectacular progress in magnetic recording.

The foundations for these advances were initially set in the field of thin film magnetism, which already started more than 40 years ago [5]. However, a number of fundamental problems related to the challenging fabrication of high quality samples and sensitive enough magnetic experiments were only overcome in the late 1980's, when the field started to evolve more rapidly and numerous novel phenomena could be observed for the first time [5, 6]. The most remarkable phenomena were observed in magnetic multilayers, which are stacks of alternating magnetic and non-magnetic layers. Upon growing metallic multilayers with characteristic thicknesses that are comparable to the mean free path of electrons in metals ( $\sim 0.1-1$  nm) spin-dependent transport effects could be manifested [7], which then led to the discovery of the magnetic *interlayer exchange coupling* (IEC) [8] and *giant magnetoresistance* (GMR) [9, 10] effects (see Fig. 1.2).

IEC was discovered in 1986 upon observing that Fe layers separated by thin Cr layers tend to be magnetized in parallel or opposite orientations according to the spacer thickness [see Fig. 1.2(a)]. Soon afterwards (between 1988 and 1989) the GMR effect was independently reported by two groups who investigated magnetotransport effects in trilayer films composed of two identical ferromagnetic layers separated by a non-magnetic spacer. When the two magnetic layers are magnetized in the same direction, electrons with the opposite spin orientation with respect to that of the layers travel through the trilayer structure with low scattering probability [see bottom part of Fig. 1.2(b)], providing a resistance shortcut and a low resistance state overall. On the other hand, when the magnetic layers are oppositely magnetized, electrons with both spin orientations undergo a higher rate of collisions in one layer or the other, thus leading to an overall high resistance state [7].

The relative resistance variation between the two configurations was found to be much larger than other magnetoresistance effects, such as the anisotropic magnetoresistance (AMR), hence receiving the name of 'giant'. The sequence of these two discoveries is regarded as the first manifestation of the interaction of electron's charge and spin in solid-state devices, which caused the emergence of a new field in physics termed as spin electronics – or *spintronics*. Grünberg and Fert jointly received the Nobel Prize in Physics in 2007 for their discovery of the GMR effect.

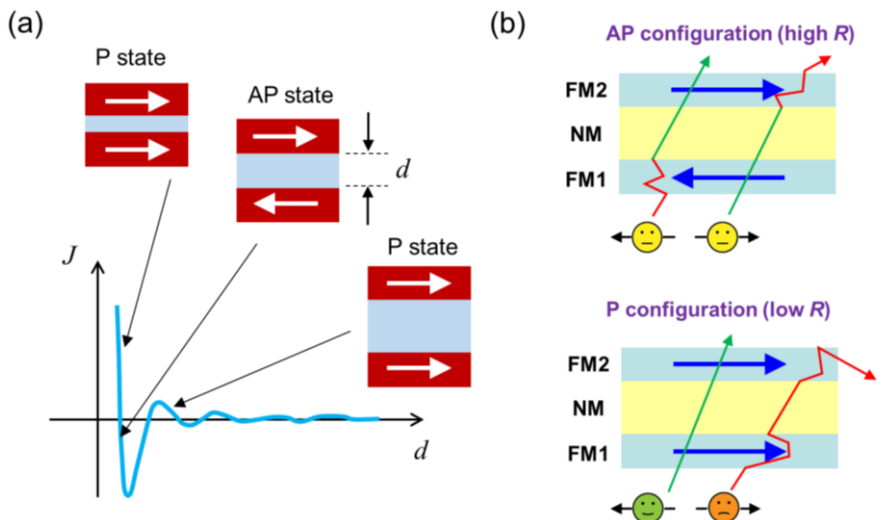


**Fig. 1.2:** The two landmark discoveries from the late 1980's in the field of thin film magnetism that led the way to the birth of spintronics: (a) interlayer exchange coupling (IEC) and (b) giant magnetoresistance (GMR). Panel (b) is adapted from Ref. [7].

The large size of the GMR effect led to its incorporation to the read head sensor of the HDD, replacing the less sensitive AMR readers [7], and thus helping to enormously improve the HDD performance figures. The GMR effect is regarded as an example in which a physical phenomenon was most rapidly implemented into a widespread technology in history ( $\sim 10$  years). Subsequent related findings of the *tunneling magnetoresistance* effect (TMR) and its massive magnetoresistance ratios [11, 12] have helped further progressing the capabilities of HDD devices. In the same way, important improvements in the design of magnetic recording media (such as the transition from longitudinal to perpendicular recording [3]) have equally contributed to the magnetic memory technology existing today.

The groundbreaking findings in the field of thin-film magnetism in the late 1980's paved the way to the large majority of current research areas in nanomagnetism and spintronics, where the interaction of magnetization dynamics and charged currents is investigated. Research in these areas is nowadays perceived to be of paramount importance to address a large number of technological challenges. The economies of developed countries dramatically depend on information related assets [13], yielding an ever increasing demand for computation and information storage resources. Magnetic storage continues being a key player here, with a remarkable 92% of all human generated digital data being stored in magnetic media (as of 2010 [13]). In the same way, it is necessary to foster more energy efficient and cleaner technologies.

The exploration of the limits of magnetic recording to smaller bit sizes and faster data rates leads to a number of fundamental physical problems or bottlenecks, limiting further growth of the associated HDD key figures. On one hand, thermal fluctuations have detrimental effects for the stability of magnetic bits upon reducing their size, compromising the long-term information retention (superparamagnetic limit [14]). On the other hand, the information write process via applied magnetic fields has a fundamental speed limitation according to the nature of the precessional switching mechanism [15]. These problems can be partially circumvented with special implementations of magnetic recording, such as in heat assisted magnetic recording (HAMR) [16], which is already delivering improved performance and capabilities.

Nowadays, alternative storage and novel computing platforms are intensely sought [17, 18], which strongly point to strategies based on field-free data writing processes that could be more energy efficient. For instance, the interaction of spin polarized currents with magnetized media is exploited within the spin-transfer torque effect [19, 20], which finds an important implementation in the realm of magnetoresistive random-access memories (STT-MRAM) [21]. On the other hand, the spin orbit torque (SOT) mechanism benefits from the large spin currents generated via the spin Hall effect (SHE) in non-magnetic materials with large spin orbit interaction. These spin currents can be efficiently used to manipulate the magnetization of adjacent nanomagnetic memory elements [22].

In addition, several research efforts focus on employing nanomagnetic spin configurations such as domain walls [23, 24] or skyrmions [25] as building blocks for memories or spin logic devices. Alternatively, magnonics aims to utilize dynamic oscillatory magnetization modes (spin waves) in order to build dissipation-less information and logic processing devices [26]. Advances in ultrafast magnetism have also shown manipulation of magnetization at femtosecond time scales by means of ultrashort laser pulses, which is about three orders of magnitude faster than the current data rates in existing magnetic recording technology ( $\sim 1-10$  ns) [27]. On the other hand, the emerging field of antiferromagnetic spintronics suggests employing antiferromagnets as information storage and logic platforms instead of ferromagnets [28], showing novel and smart ways to control magnetic order in these materials.

Finally, research in nanomagnetism and spintronics is also very active in other areas, such as in the design of novel permanent magnets and the development of new materials for energy applications [29]. In addition, innovative biomedical diagnostics and therapeutic treatments are nowadays based on nanomagnets [30-32], thus highlighting the high reach and versatility of these scientific fields.

## 1.2 Magnetization and overview of magnetic interactions

Upon application of a magnetic field  $\mathbf{H}$  onto a material, the response of the material to the field can be described with the quantity  $\mathbf{B}$ , termed as magnetic induction. The dependence between the two quantities ( $\mathbf{B} = \vec{\mu}\mathbf{H}$ , where  $\vec{\mu}$  is the magnetic permeability) is a specific property of the material and can consist from a simple and linear, to a complicated, history-dependent multivalued function upon considering the material's magnetic character and the surrounding medium [2]. In this thesis, we focus our interest on *magnetic solids*, which consist of materials possessing a large amount of magnetic moments [1]. Magnetic moments are the basic unit defining the strength of a magnet, and are often represented under the concept of magnetic dipoles (possessing magnetic north and south poles). The physical origin of magnetic moments is related to Ampèrian current loops in a material due to the motion of charges, as well as to the existence of spin and orbital angular momentum states of electrons [1].

The *magnetization*  $\mathbf{M}$  of a material is defined as the magnetic moment of the material per unit volume  $V$ , and hence reads as

$$\mathbf{M} = \frac{\sum_i \mathbf{m}_i}{V}, \quad (1.1)$$

where the sum over all magnetic moments  $\mathbf{m}_i$  in the material is taken. The magnetization is a material property and depends on the individual magnetic moments of the ions, atoms or molecules forming the material, as well as on how they mutually interact. Its unit in the Gaussian (or cgs) system is emu/cm<sup>3</sup>.

For a material possessing a magnetization  $\mathbf{M}$  (magnetized medium), the magnetic induction under an applied field  $\mathbf{H}$  can now be written as [2]

$$\mathbf{B} = \mathbf{H} + 4\pi\mathbf{M}. \quad (1.2)$$

A further relation can be introduced between magnetization and field as  $\mathbf{M} = \vec{\chi}\mathbf{H}$ , where the quantity  $\vec{\chi}$  is the magnetic susceptibility and it indicates how responsive is the material to an applied magnetic field. In the simple case in which  $\vec{\chi}$  is a scalar, a linear relation is hold between  $\mathbf{B}$  and  $\mathbf{H}$ , such that

$$\mathbf{B} = (1 + 4\pi\chi)\mathbf{H} \quad (1.3)$$

and hence recovering the permeability as  $\mu = 1 + 4\pi\chi$  (dimensionless quantity).

The magnetic response of any solid to an applied field can be defined regardless of this being very weak or very strong. The  $\mathbf{M}$  (or  $\mathbf{B}$ ) vs  $\mathbf{H}$  dependencies given via the magnetic susceptibility  $\chi$  are usually termed as magnetization curves (see also Section 1.3) and are indicative of the type of magnetic order possessed by a material. In the case of linear magnetic materials ( $\mathbf{M} = \chi\mathbf{H}$ ) the magnetization curve is a straight line. This is the case for diamagnetic and paramagnetic (as well as to a certain extent, for antiferromagnetic) materials, where very strong fields are required to induce rather modest changes in their magnetization [2]. Upon application of a nonzero field, diamagnetic materials develop a very small and negative susceptibility as a result of the electron orbital motion, such that a small opposing magnetization is induced against the applied field<sup>1</sup>. For this reason, diamagnets are repelled by magnetic fields [1].

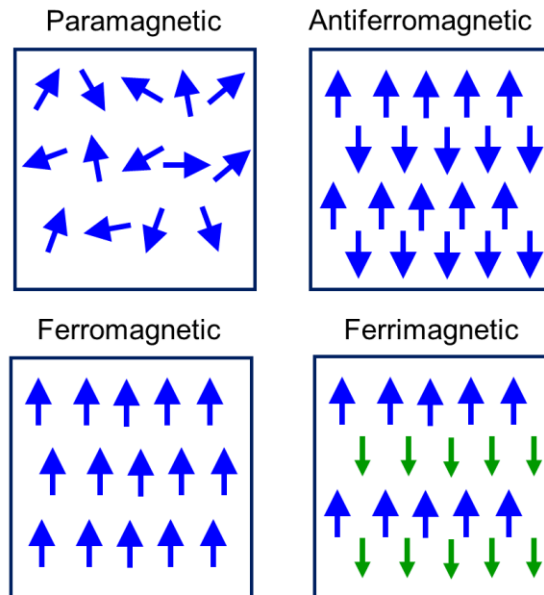


**Fig. 1.3:** Schematics of magnetic moment ordering in paramagnets, antiferromagnets, ferromagnets and ferrimagnets. Adapted from Ref. [2].

On the other hand, paramagnets possess permanent magnetic moments that are randomly oriented in space under the absence of an applied magnetic field, hence adding up to a zero net magnetization (see Fig. 1.3). An applied field induces a certain degree of alignment of misoriented moments along the field, causing a nonzero net magnetization. The susceptibility is positive in this case but again rather small (with  $\chi \sim 10^{-5}$  to  $10^{-3}$ ) [1]. In addition, antiferromagnets possess strongly interacting permanent

<sup>1</sup> In practice, all materials show a certain degree of diamagnetism [1].

magnetic moments that are generally oppositely oriented to their neighbors, such that the net magnetization is zero (see Fig. 1.3). Alignment of the magnetic moments can often be achieved at sufficiently large applied fields where the field dominates over other magnetic interactions (via spin canting, spin-flop or spin-flip phenomena) [1]. It is worth pointing that if heated above the Néel temperature  $T_N$  of the antiferromagnet, it undergoes a phase transition to a paramagnet.

For ferromagnetic and ferrimagnetic materials (see Fig. 1.3), the susceptibility is not linear anymore and the magnetization curves show a complex behavior termed as hysteresis (see Section 1.3). In addition, large magnetization values can be induced with relatively low applied field strengths, such that susceptibility values are large. Strongly interacting permanent magnetic moments tend to be aligned even in the absence of applied magnetic field, which leads to the appearance of the so-called *spontaneous magnetization* ( $M_S$ ). Ferromagnets also undergo a phase transition to the paramagnetic state upon warming the material above the Curie temperature ( $T_C$ ), where disorder overwhelms the interactions promoting internal alignment of magnetic moments, such that  $M_S$  goes to zero at  $T_C$ .

In ferrimagnetic materials, the situation is similar as for ferromagnets, but in this case two magnetic sublattices with opposing magnetic moment orientations exist. Ferrimagnetism can be regarded as a special case of antiferromagnetism, where the magnetizations of the two sublattices do not compensate each other and hence a nonzero net magnetization exists (see Fig. 1.3) [1]. Due to the different nature of magnetic interactions in each sublattice, ferrimagnets often show complicated temperature dependent behavior, exhibiting compensation points with vanishing magnetization<sup>2</sup>.

### *Energy contributions in ferromagnetic materials*

This thesis strongly focuses on investigating the magnetization behavior of **ferromagnetic materials**. For this reason, the magnetic interactions impacting the magnetization behavior ( $\mathbf{M}$  vs  $\mathbf{H}$ ) of these materials will be summarized below.

The most prominent interaction in ferromagnetic materials is the **exchange interaction**, which promotes the parallel alignment of neighboring microscopic magnetic moments or spins in the material. While its physical origin lies on electrostatic (Coulomb) interactions among electrons in the material, the key ingredient leading to

---

<sup>2</sup> Besides the different magnetic ordering types mentioned here, a wide variety of magnetic textures appear in nature as a result of the rich diversity of short- and long-range magnetic interactions. For an overview, see, for instance, Chapter 6 in Ref. [33].

its understanding consists on the quantum mechanical treatment of the electron and electron's spin [1].

Given that the behavior of ferromagnetic materials could not be explained solely in terms of magnetic dipole-dipole interactions, Weiss proposed the first modern theory for ferromagnets based on an internal molecular field mechanism in 1906. This assumed that ferromagnets are paramagnets with a very large internal magnetic field parallel to their magnetization, promoting a strong alignment of moments [2, 33]. However, the origin of ferromagnetism was not fully understood until a fully quantum mechanical many-body treatment was implemented. In 1928, Heisenberg showed that there is an energy term in the Hamiltonian of the electrostatic interaction that tends to orient the electron spins parallel (or antiparallel, for antiferromagnets) to each other. This term, known as the *exchange integral*, arises from the indistinguishability of electrons upon which they cannot share the same quantum state as stated by Pauli's exclusion principle, and it does not have a classical analog [1, 2, 33]. Explained in brief, the parallel alignment of spins in ferromagnets is favored by electrons with equal spin states occupying different atomic or molecular orbitals, hence avoiding spatial overlap and thus minimizing the energetically unfavorable Coulomb repulsion [2]. The Hamiltonian term corresponding to the Heisenberg exchange model is expressed as

$$E_{ex} = - \sum_{i,j} J_{ij} \mathbf{S}_i \cdot \mathbf{S}_j, \quad (1.4)$$

where the exchange integral  $J_{ij}$  promotes parallel or antiparallel alignment of spins  $i$  and  $j$  according to its sign<sup>3</sup>. A positive  $J_{ij}$  promotes parallel alignment of spins and thus ferromagnetism. In the case that  $J_{ij} < 0$ , antiferromagnetic ordering is promoted instead. The sign of the exchange integral can vary depending on the characteristics of the material as well as the conditions at which it is subjected (e.g. temperature).

Within the Weiss theory, the predicted molecular field values in order to explain ferromagnetism are usually exceeding  $\sim 1000$  kOe (or  $\sim 100$  T) [33]. Upon the introduction of the exchange interaction, one can see that the energy variations related with the electrostatic interaction are about three order of magnitude larger than those arising from magnetic dipole-dipole interactions (from which effective fields of  $\sim 1-10$  kOe are obtained), such that the exchange mechanism could also explain the correct order of magnitude of the interaction.

---

<sup>3</sup> Note that in some textbooks,  $J$  is sometimes replaced by an exchange constant with twice its value. Here, the sum in Eq. 1.4 can be written with  $2J$  if the sum is then only taken such that double spin counting is avoided [1].

In order to describe a vast majority of phenomena in nanomagnetism, it is more convenient to ignore the discrete nature of electrons, atoms and the lattice [1]. Under this approach, we consider classical spins that represent particular regions of the system, thus adopting a micromagnetic description. Additionally, one assumes that while ferromagnetic ordering is in place, nearest neighbor spins do not need to be completely aligned. By taking a further step towards a continuum approximation, one can define the magnetization as a function of the position in the system and scaled with respect to saturation magnetization, as  $\mathbf{m}(\mathbf{r}) = \mathbf{M}(\mathbf{r})/M_S$ . In this continuum limit, the exchange energy is expressed as the following integral over the system's space

$$E_{ex} = A \int [(\nabla m_x)^2 + (\nabla m_y)^2 + (\nabla m_z)^2] dV \quad (1.5)$$

where  $A$  is the exchange constant, a quantity proportional to the exchange integral energy for nearest neighbor moments in Eq. 1.4 [1]. The gradient operations in Eq. 1.5 indicate that non-uniform states of magnetization cause an increase of energy related to the exchange interaction in the system. Therefore, exchange tends to promote uniform states of magnetization. On the other hand, exchange energy is invariant with respect to rotation or inversion of  $\mathbf{m}(\mathbf{r})$ .

Another interaction to take into account upon considering the symmetry and structure of ferromagnetic crystalline materials is the **magnetocrystalline anisotropy energy**. It describes the phenomenon in which preferential magnetization orientations exist in materials, such that it is easier or harder to orient or saturate (i.e. fully align) the magnetization along certain crystallographic directions. These directions are termed as the *easy axes* and *hard axes* of the material, respectively [1]. This anisotropic energy contribution originates from the fact that the symmetries of the crystal lattice affect the electronic orbitals in such a way that the spin-orbit interaction enhances the spins to be aligned along certain directions within the crystal [34]. Magnetocrystalline anisotropy (MCA) is an important source of the more general phenomenon of *magnetic anisotropy*, which also considers additional sources for the existence of preferential orientations of magnetization.

A number of materials show only one preferential axis for magnetic moments (uniaxial anisotropy) while others show more than one (e.g. biaxial or triaxial anisotropy). For example, body-centered cubic (bcc) Fe contains 6 easy axes of magnetization, which are oriented along the  $\langle 100 \rangle$  directions (cube edges). The hard axis is oriented along the cube diagonal  $\langle 111 \rangle$  [2]. Opposite to this, hexagonal close-packed (hcp) Co shows a unique preferential magnetization along  $\langle 0001 \rangle$  ( $c$  axis).

The magnetization orientation dependence of the MCA energy density<sup>4</sup> for a uniaxial material can be expressed as [34]

$$\epsilon_K = K_1 \sin^2 \theta + K_2 \sin^4 \theta + K_3 \sin^6 \theta + \dots \quad (1.6)$$

where the anisotropy constants  $K_i$  represent the energy per unit volume upon orienting the magnetization of the system away from the uniaxial axis (e.g. the  $c$  axis in hcp Co) by an angle  $\theta$ . In general, the  $K_i$  constants keep decreasing the higher is the order considered in the series in Eq. 1.6, so that usually the first term (or the first two at the most) account very well for the description of MCA effects (for example,  $K_1 = 5 \cdot 10^6$  erg/cm<sup>3</sup> and  $K_2 = 1.5 \cdot 10^6$  erg/cm<sup>3</sup> for hcp Co) [1, 34].

Fig. 1.4 exhibits polar plots illustrating the magnetization orientation dependence of  $\epsilon_K$  for films with in-plane uniaxial [Fig. 1.4(a)] and biaxial [Fig. 1.4(b)] anisotropy. The dependence on the in-plane magnetization orientation  $\theta$  reads as  $\epsilon_{K,u} = K_u \sin^2 \theta$  and  $\epsilon_{K,bi} = K_{bi} \sin^2 \theta \cos^2 \theta$ , respectively. If  $K_u, K_{bi} > 0$ , energy is minimized for  $\theta = 0, 180^\circ$  in the uniaxial case and  $\theta = 0^\circ, 90^\circ, 180^\circ, 270^\circ$  in the biaxial case, thus constituting the easy axes (EA) of the systems. On the other hand, the hard axes (HA) are oriented along  $\theta = 90^\circ, 270^\circ$  and  $\theta = 45^\circ, 135^\circ, 225^\circ, 315^\circ$  respectively.

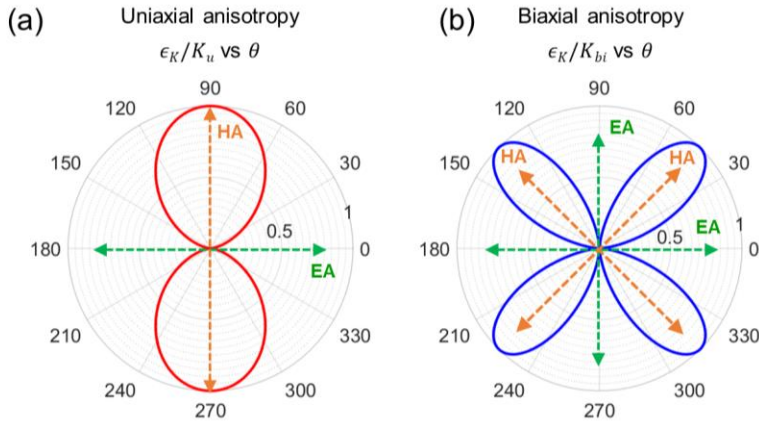


**Fig. 1.4:** Polar MCA energy plots in the plane of thin films with in-plane (a) uniaxial and (b) biaxial anisotropy. This is the case, for example, for Co(10 $\bar{1}$ 0) and Fe(001) oriented thin films, respectively. The easy (EA) and hard axes (HA) are indicated with arrows.

<sup>4</sup> Here, the volume integrated energy is usually expressed by the quantity  $E$ , whereas the energy density (energy per unit volume) is indicated by  $\epsilon$ .

In addition, the **Zeeman energy** represents the interaction of a ferromagnetic body with an externally applied magnetic field  $\mathbf{H}_a$ , which reads as [1]

$$E_M = \int \epsilon_Z dV = - \int \mathbf{M} \cdot \mathbf{H}_a dV, \quad (1.7)$$

where the negative sign indicates that the energy is minimized upon alignment of the magnetization with the applied field.

The next relevant energy term to consider in nanomagnetism is related to the **magnetostatic energy contributions**, which is originated from the long range dipolar interactions between the magnetic moments within a body and the magnetic field generated by the body itself. This interaction is closely related to the concept of **demagnetizing field**, by which a magnetic body tends to form non-uniform states of magnetization (thus demagnetizing itself) in order to save the energy associated with dipolar fields [1]. In order to explain this, one has to consider that whenever the magnetization  $\mathbf{M}$  inside a ferromagnetic body meets the surface, it has to abruptly stop at the boundary causing a divergence of  $\mathbf{M}$ . Thus following Maxwell's law,  $\nabla \cdot \mathbf{B} = 0$ , and Eq. 1.2, one can conclude that there is an opposite sign divergence of  $\mathbf{H}$

$$\nabla \cdot \mathbf{H} = -4\pi \nabla \cdot \mathbf{M} \quad (1.8)$$

which can be explained as if magnetic charges would have been placed on the surface of the ferromagnet, such that these charges act as  $\mathbf{H}$ -field sources at the boundary. This field opposes the magnetization direction inside the ferromagnetic body and tends to demagnetize it, hence being named as demagnetizing field  $\mathbf{H}_d$  [2]. This is a field created by the ferromagnet itself, and its vector has to be summed to the presence additional external fields [35].

The relation between  $\mathbf{H}_d$  and  $\mathbf{M}$  can be a very complex function of the position vector for a magnet of arbitrary shape, and is given by the demagnetization tensor  $\vec{\mathbf{N}}$

$$\mathbf{H}_d = -\vec{\mathbf{N}} \mathbf{M}, \quad (1.9)$$

a quantity that depends on the shape of the ferromagnetic body [1, 35]. For the case of an ellipsoidal magnet, the tensor  $N_{ij}$  can be diagonalized into demagnetizing factors fulfilling  $N_x + N_y + N_z = 4\pi$ . Special cases of an ellipsoidal magnet include a sphere

( $N_x = N_y = N_z = 4\pi/3$ ), a long cylinder parallel to the  $z$ -axis ( $N_x = N_y = 2\pi$ ,  $N_z = 0$ ), or a thin film in the  $xy$ -plane ( $N_x = N_y = 0$ ,  $N_z = 4\pi$ ) [1].

Fig. 1.5 illustrates the particular case of a thin film. When the magnetization is oriented in the film plane, essentially no magnetic charges are created at the horizontal ends of the film, as these are very far away from each other (if compared to the much thinner extent of the film thickness). Hereby, there is no demagnetizing field [Fig. 1.5(a)]. When the magnetization is instead oriented in the out of plane direction, magnetic charges are created at the interfacial regions where  $\mathbf{M}$  ends abruptly, hence generating a demagnetizing field  $\mathbf{H}_d$  opposed to  $\mathbf{M}$  [Fig. 1.5(b)]. The second scenario is energetically less favorable if compared to the first one, and thus in-plane magnetization configurations are usually more common in magnetic thin films, unless other interactions prevail over the magnetostatic energy (e.g. an externally applied magnetic field).

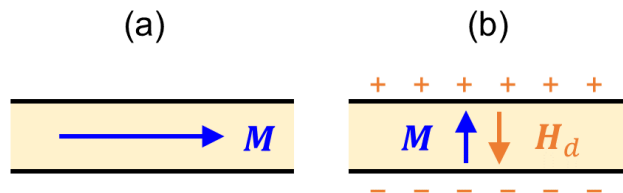


**Fig. 1.5:** Cross section sketches of a thin film when (a) in-plane and (b) out-of-plane magnetized. The demagnetizing field is negligible in (a), while divergence of  $\mathbf{M}$  at the interfaces in (b) causes magnetic charges at the surface and an opposing demagnetization field  $\mathbf{H}_d$ . Adapted from [1].

The magnetostatic energy contribution is quantified by considering the interaction energy of a magnetic dipole in the ferromagnet with the field generated by the rest of the dipoles within the same body. This is summarized as [1, 35]

$$E_M = -\frac{1}{2} \int_{V_{in}} \mathbf{M} \mathbf{H}_d dV \quad (1.10)$$

where the integration is over the volume of the ferromagnet ( $V_{in}$ ). The expression in Eq. 1.10 is reminiscent of the Zeeman energy term in Eq. 1.7, where the applied field is substituted by the demagnetizing field and a factor 1/2 is multiplied. Moreover, considering an ellipsoidal magnet and plugging Eq. 1.9 in Eq. 1.10, we obtain an expression for the magnetostatic energy density of the form [35]

$$\varepsilon_M = \frac{1}{2} (N_x M_x^2 + N_y M_y^2 + N_z M_z^2), \quad (1.11)$$

which looks like an anisotropy energy term (provided that the magnetization components are represented by their direction cosines, for example). In fact, the expression in Eq. 1.11 can be regarded as the energy density term for *shape anisotropy*, by virtue of which a ferromagnetic system can develop a magnetic anisotropy due to its shape. The fact that an in-plane magnetization orientation is preferential from a magnetostatic point of view was already commented above (see Fig 1.5). In particular, the effect of shape anisotropy is manifested in thin films by the energy term [1]

$$\varepsilon_M = 2\pi M_S^2 \cos^2 \theta, \quad (1.12)$$

where  $\theta$  is the angle between the film normal and  $\mathbf{M}$ . A Zeeman energy contribution comparable to the magnetostatic term in Eq. 1.12 is necessary to pull the magnetization of a thin film to the out-of-plane direction (in the absence of other interactions).

The shape anisotropy term is not only important for thin films but also for nanomagnetic elements (e.g. nanostructures or nanoparticles) with high aspect ratio and uniform magnetization states. In fact, magnetic anisotropy energy densities comparable to those obtained from MCA ( $\sim 10^6$  erg/cm<sup>3</sup>) can be present even in polycrystalline nanomagnets [2].

In the case of thin film magnetism, it is also important to briefly mention that factors such as magnetoelastic effects (coupling between magnetic properties and strain or stress) can generate **stress-induced** modifications of **magnetic anisotropy** [33], an effect that needs to be considered in nanometer-thick films where there exists a considerable stress as a result of the film-substrate mismatch, for example [36]. On the other hand, **surface** or **interface magnetic anisotropy** contributions exist in the ultrathin film limit, which originate from the reduced symmetry and lower coordination number of atoms at the surface [1]. This interaction modifies the overall balance of magnetic anisotropy and can promote the perpendicular alignment of magnetization in ultrathin or multilayer systems, which is a relevant asset for technological applications.

In addition, the **antisymmetric exchange** interaction, which is nowadays widely known as the **Dzyaloshinskii-Moriya (DM)** interaction, is of particular interest in systems with low symmetry, such as under spatial inversion symmetry breaking [1, 33]. The DM interaction originates from the spin-orbit interaction as a relativistic higher order term of the Hamiltonian, which acquires the form

$$\mathbf{H}_{DM} = -\mathbf{D}_{12} \cdot \mathbf{S}_1 \times \mathbf{S}_2 \quad (1.13)$$

and thus promotes the orthogonal alignment of spins  $\mathbf{S}_1$  and  $\mathbf{S}_2$ . Here, it is important to observe that the cross product operation implies that, opposite to the Heisenberg exchange, the system's energy does not remain invariant upon spin permutation but in fact reverses sign (it is antisymmetric). This means that the interaction promotes a chiral arrangement of spins depending on the sign of the  $\mathbf{D}$  vector in Eq. 1.13 [see Fig. 1.6(a)].

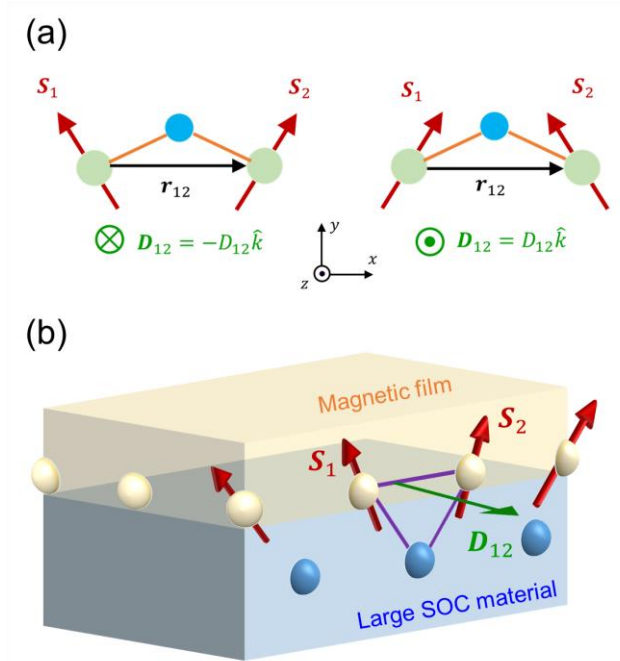


**Fig. 1.6:** (a) Spin canting under the presence of a Dzyaloshinskii-Moriya interaction with  $\mathbf{D}_{ij}$  vectors of opposite sign, causing an inverse chirality of the canting. (b) Schematic of the interfacial Dzyaloshinskii-Moriya interaction mechanism, originated from the spatial inversion symmetry breaking at the interface and the mediation of a high spin-orbit material atom adjacent to the magnetic film (adapted from Ref. [25]).

The interaction was initially studied in antiferromagnets such as  $\alpha$ - $\text{Fe}_2\text{O}_3$  where the presence of a small DM energy term ( $|D/J| \sim 10^{-2}$ ) causes spin canting of about  $1^\circ$ , leading to the occurrence of weak ferromagnetism [33, 37, 38]. The DM interaction was also found to be responsible to induce magnetic anisotropy of spin glass systems [39].

In the last decade, the DM interaction has experienced an enormous revival due to the discovery of skyrmions, vortex-like nanomagnetic configurations with a predefined chirality which originate from this interaction. Skyrmions exhibit interesting properties such as topological protection, which make them stable against external perturbations. While predicted earlier on, the first experimental observation of these

novel spin textures was reported in 2009 in materials with non-centrosymmetric lattices, such as MnSi [40].

A very large attention was quickly put on ultrathin magnetic film systems, as interfacial spins mediated by large spin-orbit coupling atoms in an adjacent metallic layer can also interact via the DM mechanism, a phenomenon termed as **interfacial DM interaction** [see Fig. 1.6(b)]. This interaction can cause considerable canting of the otherwise preferentially parallel spins within a ferromagnetic layer, as the magnitude of the DM interaction can be about  $\sim 10\text{-}20\%$  of the exchange interaction [41]. Following the findings in bulk materials, skyrmions in ultrathin magnetic films were soon afterwards observed via spin polarized scanning tunneling microscopy at cryogenic temperatures [42]. Subsequently, room-temperature novel chiral domain walls [43, 44] and nanoscale skyrmions [45, 46] were finally observed in multilayers systems in which magnetic ultrathin films are sandwiched between different materials in order to finely tune and enhance DM interactions. Nowadays, skyrmions and chiral spin textures constitute the central topic of extensive research efforts. Their stability and efficient interaction with currents [25] make them interesting for their incorporation into information storage or spin logic devices.

Finally, we also consider magnetic interactions between two magnetic films separated by a non-magnetic spacer, a phenomenon termed as **magnetic interlayer exchange coupling** (IEC) [see also Fig. 1.2(b)]. The effect was firstly reported by Grünberg and coworkers in 1986 [8] in the Fe/Cr/Fe system. The IEC coupling found here was bilinear in nature, causing parallel or antiparallel alignment of the magnetization vectors in the coupled layers, and following a Heisenberg type energy term  $\epsilon_{IEC} = -J_1(\mathbf{M}_1 \cdot \mathbf{M}_2)$ . Detailed successive experiments showed that the sign and strength of the coupling factor  $J_1$  is interlayer thickness dependent in an oscillatory fashion [47, 48], a fact that was theoretically explained in the frame of the Ruderman-Kittel-Kasuya-Yosida (RKKY) interaction [49]. Thus by tuning the interlayer thickness in the range from a few angstroms to a few nanometers, the coupling can be either ferromagnetic, antiferromagnetic or zero. A second type of coupling was observed soon thereafter in Fe/Cr/Fe systems as well, which promoted a perpendicular magnetization configuration of the Fe layers [50]. The observation of this non-collinear coupling, termed as **biquadratic**, was extended to additional multilayer systems [51] and the IEC energy was generalized by adding a term  $-J_2(\mathbf{M}_1 \cdot \mathbf{M}_2)^2$  (with  $J_2 < 0$ ).

The observation of IEC was a fundamental step towards the discovery of the GMR effect and it is frequently exploited in multilayer systems as tool to finely tune magnetic interactions.

### ***Total magnetic energy minimization and micromagnetics***

In summary, the total free energy of a magnetic system is finally obtained as the sum of all aforementioned energy contributions, such that the total energy density would read as

$$\varepsilon_{TOT} = \varepsilon_{ex} + \varepsilon_K + \varepsilon_M + \varepsilon_Z + \varepsilon_{DM} + \dots \quad (1.14)$$

a situation in which distinct energy contributions compete against each other. Finding the stable (and metastable) solutions of the above energy equation is generally not a simple task, and a very rich variety of magnetic textures and configurations emerge from the combination of the listed energy contributions. In addition, the non-linear character of the magnetostatic interaction adds a very high complexity to the problem, such that analytical solutions do not generally exist [1, 35].

In this thesis, we use relatively simple macrospin magnetic models which are however able to capture the essential physics of the systems that are under experimental study. This is enough, for instance, to quantify the relevant energy contributions of magnetic anisotropy or other interactions present in our systems. In order to simulate more complex spin textures with highly non-uniform magnetization states (e.g. vortices, internal structure of domain walls), approaches based on micromagnetic simulation software platforms are usually employed [52]. However, this aspect is beyond the goals of the present thesis.

## **1.3 Hysteresis and magnetization reversal**

The  $M(H)$  magnetization curves in the case of ferri- and ferromagnetic materials show a nonlinear, irreversible response of the magnetization to an applied field [33]. These curves, named as *hysteresis loops*, are typically obtained by applying a cyclic field  $H$  onto the ferromagnet and recording the magnetization projection  $M$  along the field axis. The shape of a typical hysteresis loop for a ferromagnet is shown in Fig. 1.7, where the magnetization component  $M$  along the field axis vs the field amplitude  $H$  is represented. Firstly, the magnetization saturates above a sufficiently high (positive or negative) magnetic field (see Fig. 1.7), upon which  $M$  is equal (or almost equal<sup>5</sup>) to the spontaneous magnetization  $M_S$ . Secondly, if we let the system evolve from a magnetic saturation at sufficiently large applied fields towards zero field, the magnetization does

---

<sup>5</sup> Along certain orientations of magnetic materials with considerable magnetic anisotropy, full saturation can only be reached asymptotically. Above certain threshold, a further increase in field only causes a very minor increase in magnetization.

not generally reduce to zero but shows a remanent magnetization  $M_r$  (see Fig. 1.7). This delay in the response of the magnetization to the field is called hysteresis [2, 34] and has important technological implications. If the field is further reduced towards negative values,  $M$  is inverted and acquires negative values at a special field value known as the coercive field  $H_c$  (see Fig. 1.7). Depending on the value of the coercivity, magnetic materials are often classified as soft (low  $H_c$ ) or hard (high  $H_c$ ), with the two types of magnets having complementary technological applications [33]. Upon further reducing the applied field towards more negative values, magnetization reaches the negative saturation state  $-M_S$  (see Fig. 1.7). The increasing field branch from negative to positive saturation follows an equivalent pathway as for the decreasing field branch, with inverted  $M$  and  $H$  values, and thus completing the full hysteresis loop<sup>6</sup>. Another special field point in the hysteresis loop is that related to the maximum slope of the  $M(H)$  function [34], which is termed as the switching field  $H_s$  (see Fig. 1.7), and is usually related to the stage during magnetization reversal at which irreversible magnetization processes occur<sup>7</sup>.

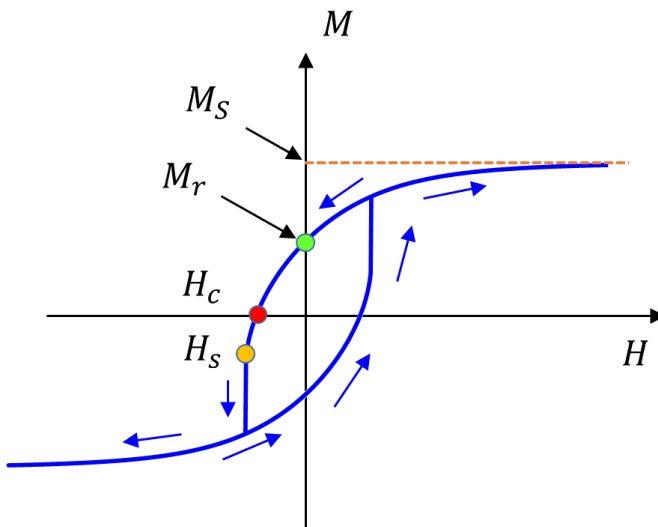


**Fig. 1.7:** Arbitrary  $M(H)$  hysteresis loop (blue curve) of a ferromagnetic material. The blue arrows indicate the evolution of  $M$  upon field cycling (decreasing and increasing field branches). A few characteristic quantities of the hysteresis loop are indicated: the saturation magnetization  $M_S$ , the remanent magnetization  $M_r$ , the coercive field  $H_c$ , and the switching field  $H_s$ .

<sup>6</sup> Except in some extraordinary cases, the symmetry  $M(H) = -M(-H)$ , indicative of time-reversal symmetry, is fulfilled in ferromagnetic hysteresis.

<sup>7</sup> Sometimes,  $H_s$  and  $H_c$  are equivalent.

### *Magnetization reversal mechanisms*

The shape and attributes (e.g.  $M_S$ ,  $H_C$ ) of the hysteresis loop in a ferromagnet strongly depend on the interplay of the magnetic interactions described in Section 1.2. Magnetization reversal processes are generally composed by complex rearrangements of microscopic magnetic moments that involve a very large number of degrees of freedom. However, a large set of magnetization processes and the hysteresis phenomenon itself can already be understood by means of simpler pictures upon treating the magnetization of the ferromagnetic system as a macrospin or, alternatively, as ensembles of macrospins [34]. Consequently, assuming this simplified macrospin behavior is often sufficient to explain the vast majority of phenomena in various magnetic materials. These principal fundamental reversal mechanisms are briefly presented below.

#### *(i) Coherent rotation*

Within the coherent rotation picture, the system is represented by assuming a single magnetization vector that accounts for the magnetic state of the whole system (uniform magnetization description). There are no relevant spatial dependent variations (non-uniform states) of magnetization and thus  $\mathbf{M}$  continuously rotates upon the action of an external applied field  $\mathbf{H}$ , with its change being uniform in space [34]. The coherent rotation process is associated to a continuous change of the local energy minimum for a single macrospin upon changing the applied field value. This process manifests in the smooth curved regions in the  $M(H)$  loops.

#### *(ii) Magnetization switching*

On the other hand, magnetization switching is related to processes in which a macrospin undergoes a field-induced transition from a local energy minimum (metastable magnetization state) to another local or global minimum in the energy landscape. Upon neglecting thermally induced stochastic reversal processes, the field has to provide the sufficient energy such that the barrier between the two (meta)stable states is suppressed and the macrospin vector can reorient in order to minimize its free energy [34]. These events are typically manifested as sharp changes and jumps in the  $M(H)$  curves and are associated to irreversible magnetization processes. Opposite to coherent rotation, inversion of the field cycling direction after a magnetization switching event will drive the system through a different path, leading to hysteretic effects and energy dissipation [34]. In magnetic thin films, switching events can be related to the abrupt nucleation of oppositely oriented magnetization regions followed by a fast, avalanche-like expansion of the inverted magnetization state (often termed as macroscopic Barkhausen jump [34]).

*(iii) Domain formation*

It is evident that non-uniform states of magnetization also need to be taken into account to correctly describe the magnetization reversal behavior of most ferromagnets. Trying to answer to the question of why certain ferromagnets have no net magnetization at zero field, but can in turn be saturated with relatively modest fields, Weiss suggested that ferromagnets may divide their body into magnetic domains [34]. Within each domain the magnetization is equal to the saturation magnetization, but different domains show a distinct orientation of the local magnetization, such that the macroscopic magnetization can add up to zero. This therefore explained why large magnetization values could be recovered under applying rather small fields, which re-orient domains without a too high cost in energy.

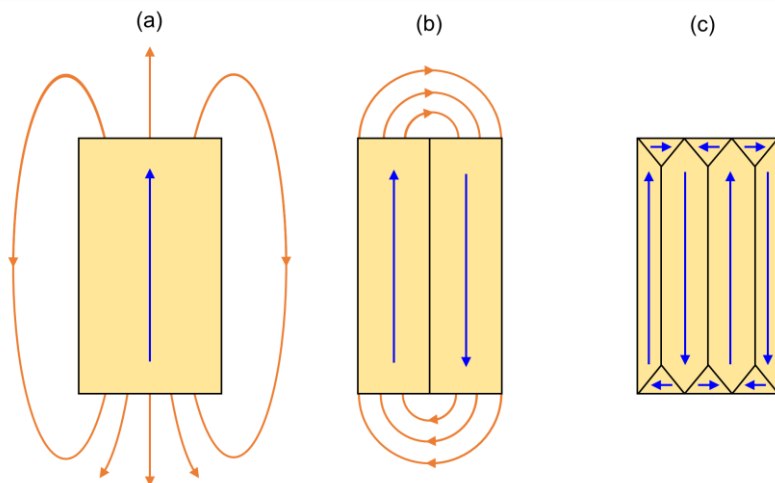


**Fig. 1.8:** (a) Uniformly magnetized sample. (b) The same sample divided into two domains. (c) The same sample showing a multidomain state with a flux closure configuration, in order to minimize the dipolar stray fields in space. The stray fields are indicated by the orange lines exiting the magnet.

The typically narrow transition regions between domains are known as magnetic domain walls, where magnetic moments gradually rotate as they go from one domain to another in order to form the boundary in a continuous fashion. Forming them costs an extra energy as parallel alignment of magnetic moments and thus exchange interaction is not satisfied therein. Nevertheless, domains and domain walls frequently exist in ferromagnets, as a result of the competition between all magnetic interactions. While energy is gained in the form of domain wall formation, a larger amount of energy corresponding to the magnetostatic interactions can often be saved by minimizing the amount of stray field energy or dipolar interactions.

The situation is illustrated in Fig. 1.8. A uniformly magnetized bar magnet as the one in Fig. 1.8(a) minimizes the exchange interaction, but on the other hand it has a large dipolar energy state due to the considerable amount of stray field exiting the magnet and adding up in the form of magnetostatic self-energy. The magnetostatic energy can be lowered if the magnet splits into differently oriented domains [Fig.1.8(b)], diminishing the amount of stray field. Moreover, ferromagnets frequently exhibit multidomain flux closure states such as the one illustrated in Fig. 1.8(c), where the stray field is essentially eliminated. Despite the energy cost introduced by the large presence of magnetic domain walls, the balance between the different energy contributions may still favor the formation of such multidomain states.

In relatively large ferromagnets, the low energy state at zero applied field is often the demagnetized (multidomain) state. However, as the sample size is reduced, the associated surface energies (e.g. cost of domain wall formation) can become excessively large as compared to volume energies (e.g. magnetostatic energies). Below a critical size ( $\sim 100$  nm) [1], the domain wall energy may not be compensated anymore by magnetostatic energy savings, such that uniform magnetization is promoted. This is often applicable to nanomagnets such as thin films, nanoparticles and nanostructures. As the existence of domains is suppressed in such systems, coherent rotation and switching processes alone can often adequately describe their magnetization reversal behavior. A simple model of these characteristics is explained below.

### *The Stoner-Wohlfarth model of ferromagnetism*

The Stoner-Wohlfarth (SW) model of ferromagnetic hysteresis was introduced in 1948 to describe the magnetization properties of single-domain grains and their assemblies [53, 54]. The model considers a grain with uniaxial magnetic anisotropy (which can be originated from MCA and/or shape anisotropy, among others) subjected to an external field or arbitrary orientation. Exchange energy is not explicitly included within the model (or is regarded as a constant offset), as it does not possess any angular dependence under the assumption of uniform magnetization.

A schematic of the considered grain is shown in Fig. 1.9(a). The magnetic anisotropy axis of the grain is indicated by the red arrow (along the  $x$ -axis). The applied field  $\mathbf{H}$  is oriented at an angle  $\beta$  away from the anisotropy axis ( $\hat{u}$  orientation). The magnetization  $\mathbf{M}$  will adopt an orientation  $\theta$  from the anisotropy axis upon fulfilling the balance between the restoring force exerted by the magnetic anisotropy energy and the Zeeman energy originated by the external applied field. Under the absence of additional interactions, the magnetization vector is confined in the plane defined by the anisotropy axis and the applied field vector [ $xy$ -plane, see Fig 1.9(a)].

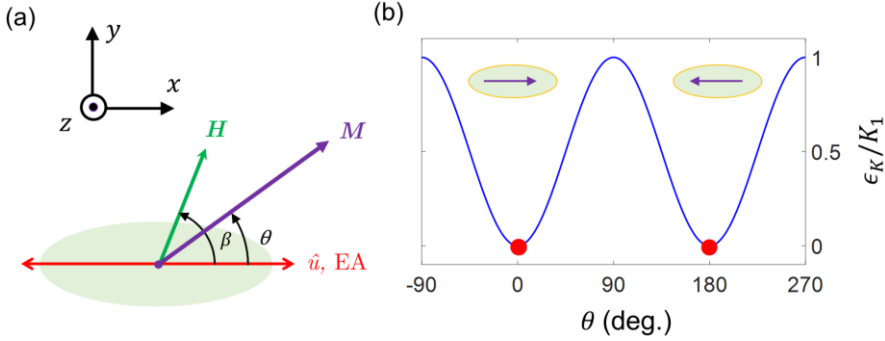


**Fig. 1.9:** (a) Schematic of the SW model. (b) Magnetization orientation dependent energy landscape under zero applied magnetic field. The system is bi-stable at zero field.

Under zero applied field, the energy density reads just as  $\epsilon_K = K_1 \sin^2 \theta$ , such that two stable states with equal energy exist,  $\theta = 0^\circ$  and  $180^\circ$ , corresponding to the easy axes (EA) of magnetization [see Fig. 1.9(b)]. The total energy for the SW grain under an applied field reads as [53, 54]

$$\epsilon = \epsilon_K + \epsilon_Z = K_1 \sin^2 \theta - HM_S \cos(\theta - \beta), \quad (1.15)$$

where the competition between magnetic anisotropy and Zeeman energy is evident, as the first tries to orient magnetization along the EA whereas the second promotes the alignment of magnetization with the field axis ( $\theta = \beta$ ). Eq. 1.15 can be simplified upon dividing the energy density by  $2K_1$

$$\frac{\epsilon}{2K_1} = \frac{1}{2} \sin^2 \theta - h \cos(\theta - \alpha) \quad (1.16)$$

where  $h = H/H_K$  is the reduced field and the quantity  $H_K = 2K_1/M_S$  is defined as the anisotropy field (the field required to overcome a  $2K_1$  energy barrier).

It is assumed that in equilibrium, the magnetization points in a direction  $\theta^*$  such that the energy is minimized. Fig. 1.10 shows the field dependence of the magnetization components that are parallel and perpendicular ( $m_{\parallel}$  and  $m_{\perp}$ ) to the applied field axis, for different applied field angle configurations ( $\beta = 0^\circ, 30^\circ, 60^\circ$  and  $90^\circ$ ). It can be seen that the easy axis hysteresis consists of a square  $M(H)$  curve, where the bi-stability is conserved during the entire reversal process. Reversal occurs by means of a big jump in the magnetization component parallel to the field. On the other hand,

the hard axis loop consists of a linear, anhysteretic curve that saturates at the  $h = \pm 1$  field points. For field orientations in between, reversal proceeds initially by a smooth curvature of the  $M(H)$  functions, followed by a magnetization jump (see Fig. 1.10).

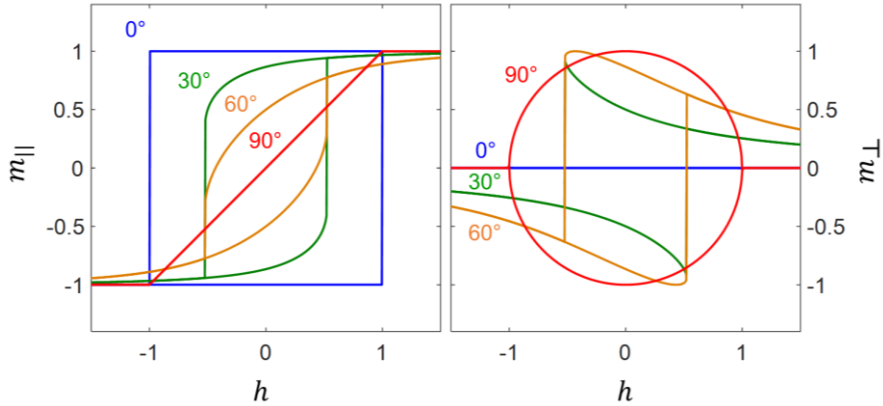


**Fig. 1.10:** Magnetic hysteresis loops of the magnetization components that are parallel and perpendicular to the applied field, computed for a single-grain SW particle.

In order to understand the reversal mechanisms at play within the SW model, Fig. 1.11 shows the magnetization orientation dependent energy landscapes during the increasing field branch of three reversal configurations, with  $\beta = 0^\circ$ ,  $60^\circ$  and  $90^\circ$ .

For  $\beta = 0^\circ$  (easy axis), we see that the magnetization orientation remains static at  $\theta = 180^\circ$  as the field is cycled from negative towards positive values. Magnetization reversal occurs when the local minimum at which the system is initially placed becomes a saddle point and the barrier separating this metastable state and the stable state at  $\theta = 0^\circ$  (global minimum) reduces to zero, upon which the magnetization ‘jumps’ to the new state via a switching mechanism (see Fig. 1.11).

For  $\beta = 60^\circ$ , the field contribution to the energy landscape is now aligned in a different way with the double potential well arising from the uniaxial anisotropy energy term. The effect of augmenting the field from negative towards positive values is firstly perceived as a  $\theta$ -shift of the energy minimum state where the system lies, thus causing the SW macrospin to continuously rotate towards the new energy minimum position. Upon reaching the switching point, reversal continues via switching as in the easy axis case and then follows by further coherent rotation upon increasing the field (Fig. 1.11).

Finally, the anhysteretic reversal process in the hard axis case ( $\beta = 90^\circ$ ) occurs only via the continuous shift of the energy minimum, such that no switching occurs and the only reversal mechanism consists of coherent magnetization rotation (see Fig. 1.11).

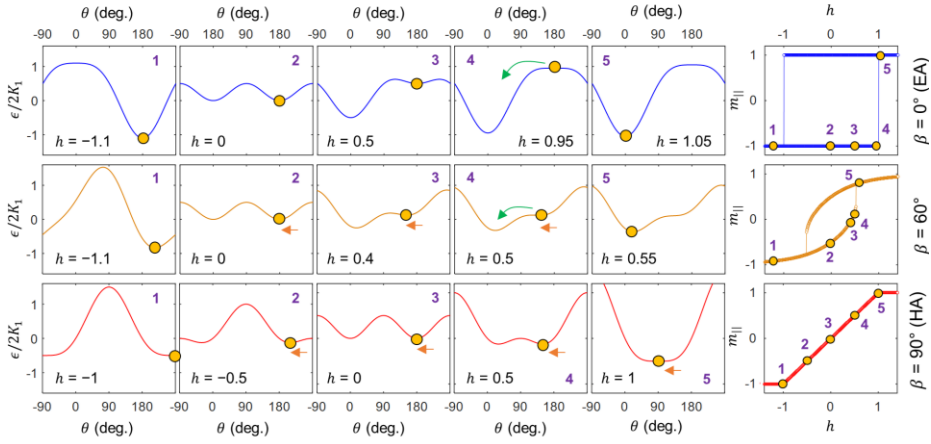


**Fig. 1.11:** Representation of magnetization orientation dependent energy landscapes during reversal for the SW model, for the cases in which  $\beta = 0^\circ$  (upper panel),  $60^\circ$  (central plane) and  $90^\circ$  (lower panel). A series of energy landscapes for different applied field values during reversal and the stable/metastable magnetization states are shown. The corresponding  $M(H)$  curves are displayed on the right hand side, indicating the magnetization states corresponding to the energy landscapes to the left (see numbers in the inset and numbered dots in the magnetization curves).

### *Self-consistent method for solving the Stoner-Wohlfarth model*

In order to solve the  $\theta = \theta(h, \beta)$  function describing the magnetization reversal process within the SW model, one can proceed by searching the value of  $\theta$  for which the energy is minimized for each  $(h, \beta)$  configuration. However, one has also to take into account that the global minimum does not indicate at all times the correct  $\theta = \theta(h, \beta)$  behavior or history, given that the system may be ‘locked’ in a local minimum (metastable state) before the field provides sufficient energy for the macrospin to overcome the energy barrier between the local and global minima.

An alternative way to compute magnetization curves consists on the effective field method. This is based on the assumption that the free energy of the system can be written as the scalar product of magnetization and a given effective field

$$\epsilon = -\vec{M} \cdot \vec{H}^{eff} \tag{1.17}$$

such that energy is minimized for the condition  $\vec{M} \parallel \vec{H}^{eff}$ . Upon computing the correct effective field, the magnetization orientation can be required to be parallel to it. For magnetization processes in the  $xy$  plane, the effective field is equal to

$$\vec{H}^{eff} = -\frac{1}{M_S} \left( \frac{\partial \epsilon}{\partial m_x} \hat{i} + \frac{\partial \epsilon}{\partial m_y} \hat{j} \right). \quad (1.18)$$

It is sometimes useful to write the anisotropy energy as a function of the magnetization angle cosine

$$\epsilon_K = K_1 \sin^2 \theta \approx -K_1 \cos^2 \theta = -K_1 m_x^2 \quad (1.19)$$

where  $\epsilon_K$  is only shifted by a constant energy term. The effective fields are obtained as

$$\begin{aligned} (H^{eff})_x &= -\frac{1}{M_S} \left( \frac{\partial \epsilon}{\partial m_x} \right) = H_K (m_x + h \cos \beta) \\ (H^{eff})_y &= -\frac{1}{M_S} \left( \frac{\partial \epsilon}{\partial m_y} \right) = H_K h \sin \alpha \end{aligned} \quad (1.20)$$

where  $\epsilon = \epsilon_K + \epsilon_Z$ . One can now impose that the magnetization vector is equal to the normalized effective field vector, such that

$$(m_x, m_y) = \frac{1}{\sqrt{(m_x + h \cos \beta)^2 + h^2 \sin^2 \beta}} (m_x + h \cos \beta, h \sin \beta) \quad (1.21)$$

leading to a self-consistent equation that is solved iteratively under the consideration of certain initial conditions.

### ***Stoner-Wohlfarth model with a second order magnetic anisotropy energy term***

Very often, the energy term  $\epsilon_K = K_1 \sin^2 \theta$  does not give realistic loop shapes when the field is applied along the hard axis of a ferromagnet. A better agreement with

experiments can be obtained by including a second order magnetic anisotropy energy term<sup>8</sup>

$$\epsilon_K = K_1 \sin^2 \theta + K_2 \sin^4 \theta. \quad (1.22)$$

Figure 1.12 shows exemplary hard axis hysteresis loops upon considering different values of the first- and second-order magnetic anisotropy energy densities (with  $K_1, K_2 > 0$ ). It is evident that upon introducing a nonzero  $K_2$  term in Eq. 1.22, the linear central part of the hard axis loop changes to a *S*-shaped  $M(H)$  curve, with its curvature being augmented the larger is  $K_2$  compared to  $K_1$  (see Fig. 1.12). Chang and Fredkin [55] explored the magnetization reversal behavior of a uniaxial macrospin for different  $(K_1, K_2)$  parameter values. They identified up to 8 regions in the  $(K_1, K_2)$  phase space leading to different reversal behavior, characterized by distinct easy axis directions and reversal nucleation field values. The strength of  $K_1$  and  $K_2$  contributions is also relevant for magnetic recording media, where the effect of the  $K_2/K_1$  ratio on the thermal effects and stability of thin-film media is investigated [56].

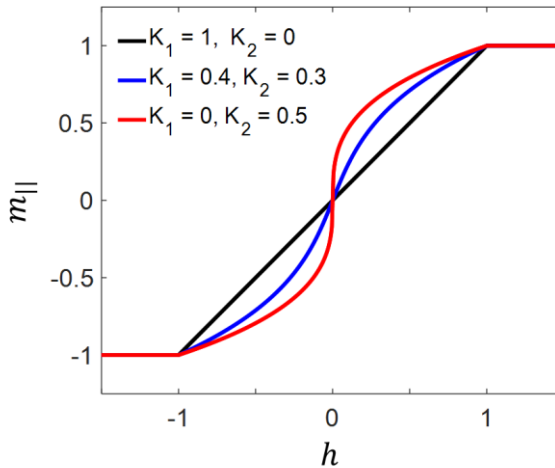


**Fig. 1.12:** Hard axis ( $\beta = 90^\circ$ ) hysteresis loops for different  $K_1, K_2$  values. The first- and second-order magnetic anisotropy energy densities are given in arbitrary units, such that saturation occurs at  $H = H_K = \frac{2K_1}{M_S} + \frac{4K_2}{M_S}$ .

<sup>8</sup> Here, if the anisotropy energy is again written as a function of cosines, the transformation involves more than a simple constant offset. New anisotropy energy density coefficients need to be defined. In order to convert the anisotropy energy to the expression  $\epsilon_K = -k_1 \cos^2 \theta - k_2 \cos^4 \theta$ , we have that  $k_1 = K_1 + 2K_2$  and  $k_2 = -K_2$ .

## 1.4 Magneto-optical Kerr effect (MOKE)

Magneto-optical effects are related to the influence of magnetic fields or the presence of a spontaneous magnetization on the propagation of light in matter. The light-matter interaction strongly depends on the electronic state of the considered medium (and hence on its magnetic state), with the associated phenomena derived from this interplay being classified as magneto-optical effects [57]. A brief summary of the polarization effects of light reflected (or transmitted) from magnetized media is provided here.

The first magneto-optical effect was discovered in 1845 by Faraday, who found that the linear polarization of light transmitted through a glass rod is rotated upon the application of a magnetic field along the propagation direction of light [57-60]. This finding, nowadays named as *Faraday effect*, constituted the first experimental confirmation of the electromagnetic nature of light and had a large influence in the subsequent development of the electromagnetic theory. The corresponding effect in reflection was discovered by Kerr around 30 years later upon investigating light reflection from the surface of a polished electromagnet pole made of iron, a phenomenon that was termed as the *magneto-optical Kerr effect (MOKE)* [57-60]. He reported his findings in two research articles from 1877 and 1878, in which he described polarization effects for magnetization orientations perpendicular to the iron surface (polar Kerr effect [61]) and contained in the plane of incidence of light (longitudinal Kerr effect [62]), respectively. About 20 years later, Zeeman discovered a third MOKE geometry [57] in which the magnetization was contained in the sample surface but perpendicular to the plane of incidence (transverse Kerr effect).

Fig. 1.13 shows a schematic of the Faraday and Kerr effects. Upon assuming a linearly polarized incident light beam that is transmitted or reflected from a medium (for the Faraday or Kerr effects, respectively), the resulting polarization state of light consists, in the most general case, of an elliptically polarized beam. The new polarization state is commonly represented<sup>9</sup> by a rotation of the polarization axis  $\theta$  and an acquired ellipticity  $\varepsilon$  (see Fig. 1.13). As experiments have shown that (for ferromagnetic materials) these quantities are proportional to the sample magnetization, it is interesting to determine  $\theta$  and  $\varepsilon$  in an experimental setting, as they give a way to track the sample's magnetization. These aspects will be discussed in detail below.

The first theoretical explanation of the Faraday and Kerr magneto-optical effects was proposed in 1884 by Lorentz in terms of the different response of harmonically bound classical electron oscillators to the electric field of left and right

---

<sup>9</sup> Within this thesis, we generally assume reflection from planar interfaces and thus the analysis of MOKE is always done by neglecting depolarization effects.

circularly polarized light [60, 63], which was also along the lines of earlier explanations suggested by Thomson based on the Lorentz force [59]. The result of this treatment can be understood as a difference in the refractive index of the medium for left and right circularly polarized light, which is why the Faraday and Kerr effects are often regarded as a *magnetic circular birefringence* effect.

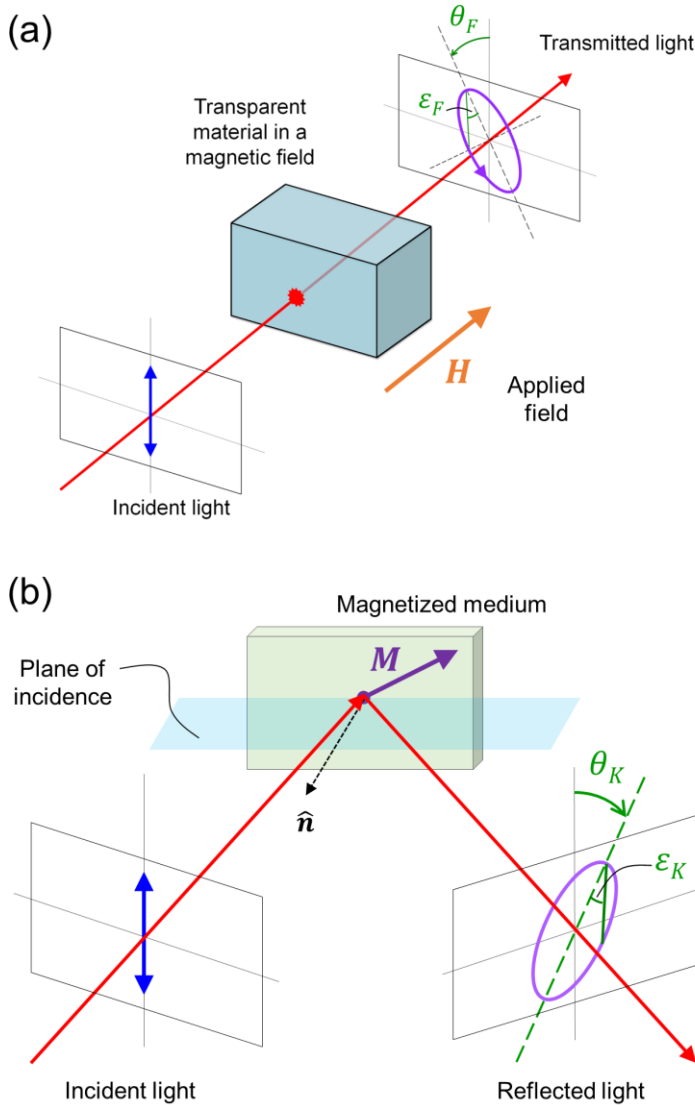


**Fig. 1.13:** Schematic representation of the magneto-optical (a) Faraday effect in transmission and (b) Kerr effect in reflection.  $\theta_F$  and  $\epsilon_F$ : Faraday rotation and ellipticity.  $\theta_K$  and  $\epsilon_K$ : Kerr rotation and ellipticity.

Apart from the Faraday and Kerr effects, further magneto-optical effects were experimentally found in the next couple of decades, such as the *Voigt effect* (associated with a *linear birefringence* of magnetic origin) or the *Cotton-Moutton effect* (which rather originates from the electric and magnetic anisotropy of paramagnetic liquids, although the two terms are often interchanged) [57, 60].

However, these early attempts to build a theory of magneto-optical effects could not explain the very large size of the effects measured in ferromagnetic materials<sup>10</sup>. It was seen in the following decades that the microscopic quantum description of the problem was essential to circumvent this. Voigt estimated that effective fields of the order of  $10^6$ - $10^7$  Oe should exist in ferromagnets in order to explain the size of the effect, in an analogy to the Weiss field that was proposed at the time to explain ferromagnetic order [59]. However, Heisenberg's introduction of the exchange interaction was still insufficient to accurately explain magneto-optical effects. Subsequent efforts brought an improvement by considering the interaction of the electron's spin with its orbital motion, i.e. the spin-orbit interaction. Hulme considered an interaction term of the form  $\sim(\nabla V \times \mathbf{p}) \cdot \mathbf{s}$ , originating from the electron's spin  $\mathbf{s}$  interacting with the effective magnetic field the electron 'feels' as it moves through the electric field  $-\nabla V$  with momentum  $\mathbf{p}$ , where  $V = -e\Phi(\mathbf{r})$  is the electric field of the electron in the crystal [59]. This effect is particularly strong for ferromagnetic materials due to the imbalance of spin-up and spin-down populations. Upon calculating the refractive indices for the left and right circular light, however, the correction seemed to be insufficient [64].

The complete theoretical description of magneto-optical effects for ferromagnets and the correct prediction of its size came upon considering the change of the electronic wave-functions as a consequence of the spin-orbit interaction, firstly shown by Kittel via an order of magnitude argument [65] and eventually described in a fully quantum mechanical derivation using perturbation theory by Argyres [66]. These works highlighted both the quantum mechanical as well as the relativistic origin of the effect originating from both exchange spin-orbit interactions. Nowadays, magneto-optical effects are treated within *ab initio* approaches such as density functional theory.

In summary, the description of magneto-optical effects can be realized either by a macroscopic electromagnetic theory, or in the context of a microscopic quantum mechanical treatment. A brief account on both approaches is included below.

---

<sup>10</sup> All considerations in this thesis are limited to magneto-optical effects in the visible light range (often termed as *conventional* magneto-optical effects [60]). It is worth to point out that analogous effects exist for shorter wavelengths, such as in the x-ray region.

*Electromagnetic description of magneto-optical effects*

A macroscopic approach based on electromagnetic fields in continuous media can readily treat a vast majority of experimental settings. The necessary ingredients are based on one hand on Maxwell's equations [67]

$$\begin{aligned}
 \nabla \cdot \mathbf{D} &= 4\pi\rho \\
 \nabla \cdot \mathbf{B} &= 0 \\
 \nabla \times \mathbf{E} &= -\frac{1}{c} \frac{\partial \mathbf{B}}{\partial t} \\
 \nabla \times \mathbf{H} &= \frac{4\pi}{c} \mathbf{J} + \frac{1}{c} \frac{\partial \mathbf{D}}{\partial t},
 \end{aligned}
 \tag{1.23}$$

where  $\rho$  and  $\mathbf{J}$  refer to free charges and currents, and  $c$  is the speed of light in vacuum. On the other hand, we also consider the material's constitutive equations, with  $\mathbf{D} = \vec{\epsilon}\mathbf{E}$ ,  $\mathbf{B} = \vec{\mu}\mathbf{H}$ , and  $\mathbf{j} = \vec{\sigma}\mathbf{E}$ , where  $\vec{\epsilon}$ ,  $\vec{\mu}$  and  $\vec{\sigma}$  are the permittivity, permeability and conductivity tensors (where we assumed a linear medium).  $\mathbf{E}$  and  $\mathbf{H}$  are the electric and magnetic vectors, respectively. While the permittivity or dielectric tensor  $\vec{\epsilon}$  is strongly frequency dependent, the  $\vec{\mu} = \mathbf{1}$  assumption is justified in the visible and near-infrared range, as the atomic magnetic moments cannot follow the fast variation of the magnetic field vector  $\mathbf{H}$  (400-600 THz in the visible range) [68]. By eliminating  $\mathbf{H}$  From Eqs. 1.23, the wave equation for the electric field  $\mathbf{E}$  is obtained

$$-\nabla^2 \mathbf{E} + \nabla(\nabla \cdot \mathbf{E}) + \frac{4\pi}{c^2} \vec{\sigma} \frac{\partial \mathbf{E}}{\partial t} + \frac{1}{c^2} \vec{\epsilon} \frac{\partial^2 \mathbf{E}}{\partial t^2} = 0,
 \tag{1.24}$$

where an electrically neutral medium has been considered ( $\rho = 0$ ). Upon considering solutions with the form of a plane wave,  $\mathbf{E} \sim \mathbf{E}_0 e^{i(\mathbf{k}\mathbf{r} - \omega t)}$ , Eq. 1.24 can be summarized as

$$-(\mathbf{k}:\mathbf{k})\mathbf{E} + (\mathbf{k} \cdot \mathbf{E})\mathbf{k} + \frac{\omega^2}{c^2} \vec{\epsilon} \mathbf{E} = 0,
 \tag{1.25}$$

where the permittivity tensor has been substituted  $\vec{\epsilon} \rightarrow \vec{\epsilon} + \frac{4\pi i}{\omega} \vec{\sigma}$  by an effective permittivity tensor (the dielectric tensor) comprising the true permittivity and the conductivity [57, 60]. The  $\mathbf{k}:\mathbf{k}$  term in Eq. 1.25 represents a dyadic product, a tensor with elements  $k_i k_j$  (where the  $k_i$  quantities are complex). Upon introducing a complex,

vectorial refractive index quantity  $\tilde{N}_i = k_i/k_0 = ck_i/\omega$ , Eq. 1.25 can be written as  $\tilde{N}^2 \mathbf{E} - (\tilde{\mathbf{N}} \cdot \mathbf{E}) \tilde{\mathbf{N}} - \vec{\epsilon} \mathbf{E} = 0$ , or alternatively, as

$$[\tilde{N}^2 \mathbf{I} - (\tilde{\mathbf{N}} : \tilde{\mathbf{N}}) - \vec{\epsilon}] \mathbf{E} = 0 \quad (1.26)$$

which is commonly known as the *Fresnel equation* [57, 60]. Here,  $\mathbf{I}$  is the identity matrix and  $\tilde{\mathbf{N}} : \tilde{\mathbf{N}}$  is again a dyadic product. For finding a nontrivial solution to the above equation, one must require that the determinant of the electric field coefficient vanishes, thus leading to an eigenvalue and eigenvector problem. Eq. 1.26 also indicates the dependence of the light propagation characteristics on the dielectric tensor  $\vec{\epsilon}$ , which in turn defines all frequency (or wavelength) dependent optical properties of the material, including magneto-optical effects. Thus, the symmetry of  $\vec{\epsilon}$  is of great importance for determining the outcome of the Fresnel equation.

On the following, we consider light reflection and refraction at the boundary of a magneto-optically active, semi-infinite medium with its ambient (e.g. air or vacuum). Magneto-optical effects for a ferromagnetic material are manifested in the dielectric permittivity tensor as a dependence of the optical properties on the magnetization direction [60], because the magnitude of magnetization can always be seen (at least locally) as the saturation magnetization. If one assumes that magneto-optical contributions to the dielectric tensor are small, this can be expanded as

$$\epsilon_{ij} = \epsilon_{ij}^{(0)} + K_{ijk} m_k + G_{ijkl} m_k m_l \dots \quad (1.27)$$

where the first term represents the magnetization independent dielectric tensor, and the second and third terms refer to magneto-optical effects that are linear and quadratic in magnetization (Einstein's summation convention is assumed) [60]. In order to describe MOKE, which is related to linear effects in magnetization, we will neglect quadratic and higher order terms. The resulting dielectric tensor is required to obey the Onsager reciprocity relation  $\epsilon_{ij}(\mathbf{M}) = \epsilon_{ji}(-\mathbf{M})$  and the symmetry considerations that are inherent to the structure<sup>11</sup> of the considered medium or material. Eventually, the dielectric tensor for a cubic material including MOKE reads as [59]

$$\vec{\epsilon} = (\epsilon_{ij}) = N^2 \begin{pmatrix} 1 & iQm_z & -iQm_y \\ -iQm_z & 1 & iQm_x \\ iQm_y & -iQm_x & 1 \end{pmatrix} \quad (1.28)$$

---

<sup>11</sup> For more details, see Appendix III.

where  $N = n + i\kappa$  is the refractive index and the quantity  $Q = Q_r + iQ_i$  is the magneto-optical coupling factor, a frequency-dependent material parameter defining the strength of linear MOKE effects. The dielectric tensor in Eq. 1.28 is composed of a diagonal part representing a scalar dielectric permittivity, with  $\varepsilon_{xx} = \varepsilon_{yy} = \varepsilon_{zz} = N^2$ , and an antisymmetric off-diagonal tensor proportional to the magneto-optical coupling factor. Here, we have defined<sup>12</sup> it as  $Q = -i\varepsilon_{xy}/\varepsilon_{xx}$ , for  $m_z = 1$ . The absolute values of  $Q$  are usually of the order of  $10^{-4}$  to  $10^{-2}$  [60].

Upon introducing the dielectric tensor  $\vec{\varepsilon}$  in Eq. 1.28 into the Fresnel equation (Eq. 1.26), the solutions to the eigenvalue and eigenvector problem can be sought for the problem of light being reflected and refracted at an air/magnetic medium interface. The solutions are not trivial for oblique incidence: the wave components within the interface plane are given by Snell's law, but a fourth order equation is usually obtained for the remaining component. The associated eigenvalues and eigenvectors (allowed propagation modes) can be linked with two forward-propagating and two backward-propagating modes, if looked along the direction perpendicular to the interface [60].

For simple geometries, the propagation modes can be computed without too much difficulties. As an illustrative example, we consider the case with light at normal incidence along the  $z$  direction ( $N_x = N_y = 0$ ) onto a medium that has a magnetization perpendicular to the interface ( $m_z = 1$ ). The only non-zero elements of the diagonal part of the dielectric tensor are  $\varepsilon_{xy} = -\varepsilon_{yx} = iN^2Q$ , such that the condition for the Fresnel equation to have a nontrivial solution reads as

$$\begin{vmatrix} \tilde{N}^2 - \varepsilon_{xx} & -\varepsilon_{xy} & 0 \\ \varepsilon_{xy} & \tilde{N}^2 - \varepsilon_{xx} & 0 \\ 0 & 0 & -\varepsilon_{xx} \end{vmatrix} = 0 \quad (1.29)$$

which can be worked out as  $(\tilde{N}^2 - \varepsilon_{xx})^2 + \varepsilon_{xy}^2 = 0$  and thus has the two results

$$\tilde{N}_{\pm}^2 = \varepsilon_{xx} \pm i\varepsilon_{xy} = N^2(1 \mp Q) \quad (1.30)$$

for the case in which  $\tilde{N}$  is positive (forward propagation along the  $z$  direction). Taking the square root and assuming small  $Q$  values,  $\tilde{N}_{\pm} = N\sqrt{1 \mp Q} \approx N(1 \mp Q/2)$ . One can also demonstrate that the eigenvectors fulfill  $E_y = \pm iE_x$ , which correspond to left and right circularly polarized light waves [59, 60].

---

<sup>12</sup> For an account of the sign convention schemes, see Appendix I.

If one now considers linearly polarized light as the superposition of left and right circularly polarized beams, the Faraday and Kerr effects can be seen as originating from the difference in refractive index for these two light components with opposite helicity (Eq. 1.30) [58]. The real part of the refractive index difference produces a phase retardation effect leading to a polarization rotation, whereas the imaginary part causes a dichroism (different absorption) for left and right circular light, hence leading to an ellipticity of the transmitted or reflected beam (see Fig. 1.13).

Since a large amount of interesting magnetic materials (and in fact, all magnetic materials studied in this thesis) are metallic, it is more convenient to measure the reflected light. Thus, our discussion will now be limited to the Kerr effect, or MOKE. In an experimental setting, the dielectric tensor can only be indirectly determined. The experimentally accessible parameters in MOKE are related to effective polarization changes of light (rotation and/or ellipticity). These are commonly represented using the  $s$ - and  $p$ -polarization basis, which define linear polarization states that are perpendicular and within the plane of incidence of the reflection experiment under oblique incidence (see Fig. 1.14), and often represented via the Jones matrix formalism.

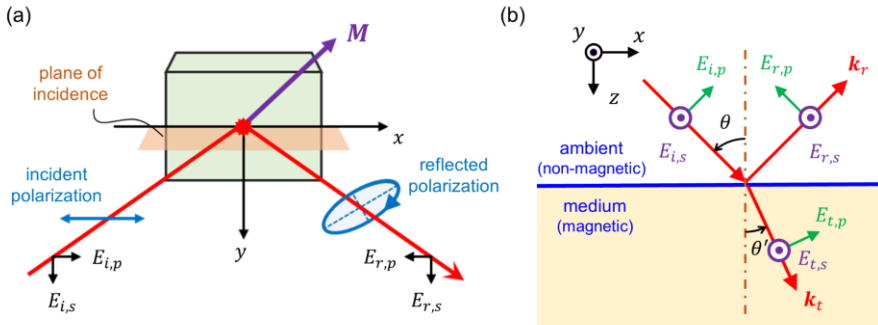


**Fig. 1.14:** Schematics of a MOKE experiment (a) from an oblique view and (b) from a side view, indicating the basis for the  $s$ - and  $p$ -polarization states in conjunction with the reference frame.

The description of polarization changes in reflection upon MOKE is realized by solving Maxwell's equations for the dielectric tensor form in Eq. 1.28 and imposing the continuity relationships for the corresponding components of the field vectors at the boundary between the ambient and MOKE active medium. From here, the reflection and transmission coefficients (complex ratio of the reflected and transmitted electric field components with respect to the incident ones) and their specific dependence on the magnetization components of the considered medium can be obtained for the special

cases of  $s$ - and  $p$ -polarized light. These are known as the Fresnel reflection coefficients (or Fresnel formulae), which are complex quantities that read as [69-71]

$$\begin{aligned}
 r_{ss} &= \left( \frac{E_{r,s}}{E_{i,s}} \right) = \frac{\cos \theta - N \cos \theta'}{\cos \theta + N \cos \theta'} \\
 r_{sp} &= \left( \frac{E_{r,s}}{E_{i,p}} \right) = -\frac{iNQ \cos \theta (\cos \theta' m_z + \sin \theta' m_x)}{\cos \theta' (N \cos \theta + \cos \theta') (\cos \theta + N \cos \theta')} \\
 r_{ps} &= \left( \frac{E_{r,p}}{E_{i,s}} \right) = -\frac{iNQ \cos \theta (\cos \theta' m_z - \sin \theta' m_x)}{\cos \theta' (N \cos \theta + \cos \theta') (\cos \theta + N \cos \theta')} \\
 r_{pp} &= \left( \frac{E_{r,p}}{E_{i,p}} \right) = \frac{N \cos \theta - \cos \theta'}{N \cos \theta + \cos \theta'} + \frac{2iNQ \cos \theta \sin \theta'}{N \cos \theta + \cos \theta'} m_y.
 \end{aligned}
 \tag{1.31}$$

Here,  $N$  is the refractive index of the magneto-optically active medium (the refractive index of the ambient is assumed to be equal to one), whereas  $\theta$  and  $\theta'$  are the incident and refracted light beam angles, related by Snell's law,  $\sin \theta = N \sin \theta'$ . The Fresnel coefficients are considered to linear order in magnetization<sup>13</sup>, which is a good assumption provided that  $Q$  is small. It can be appreciated that the particular magnetization dependence of the dielectric tensor in Eq. 1.28 is translated to a specific dependence of the Fresnel coefficients on the magnetization vectors. This can be usually summarized within the Fresnel reflection matrix

$$R = \begin{pmatrix} r_{ss} & r_{sp} \\ r_{ps} & r_{pp} \end{pmatrix} = \begin{pmatrix} r_s & Am_x + Bm_z \\ -Am_x + Bm_z & r_p + Cm_y \end{pmatrix}
 \tag{1.32}$$

where we have defined the magnetization independent complex reflectivity terms  $r_s$  and  $r_p$ , as well as the complex coefficients  $A$ ,  $B$ ,  $C$ , which summarize the above expressions. In MOKE, the absolute value of  $A$ ,  $B$ ,  $C$  is small compared to  $r_s$ ,  $r_p$ . From Eq. 1.32, the specific magnetization component on the polarization changes upon reflection can be seen more clearly. In brief, we see that the  $m_x$  and  $m_z$  components cause an intermixing of the  $s$ - and  $p$ -polarization states (similar to birefringence), while the  $m_y$  magnetization component only produces a change in the  $r_{pp}$  reflectivity term. The specificity of each magnetization component with respect to the Fresnel reflectivities in which they have an impact motivates a classification scheme in terms of three different

---

<sup>13</sup> For the Fresnel coefficients including quadratic terms in  $Q$ , see Ref. [69].

Kerr geometries: the longitudinal, transverse and polar Kerr effects (see Fig. 1.15 and the brief mention in the beginning of Section 1.4).

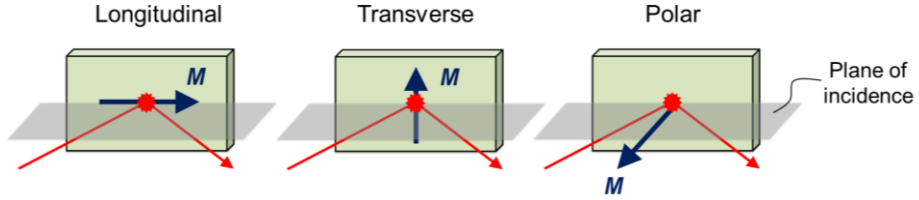


**Fig. 1.15:** Schematic representation of the three MOKE geometries upon different magnetization configurations with respect to the sample surface and the plane of incidence: longitudinal, transverse and polar.

The *longitudinal* Kerr effect is defined when the magnetization lies along the intersection of the sample plane and the plane of incidence ( $\propto m_x$ ); the *transverse* Kerr effect occurs upon the magnetization being in the sample plane but perpendicular to the plane of incidence ( $\propto m_y$ ); finally, the *polar* Kerr effect is described for configurations in which the magnetization is perpendicular to the sample plane ( $\propto m_z$ ). As can be concluded from Eqs. 1.31 and 1.32, the three effects contribute linearly to the Fresnel reflectivities, and thus they can be conveniently summed, as well as the effect of the individual magnetization components properly separated, under the presence of an arbitrary magnetization orientation. This property is of essential relevance in MOKE, as it enables performing vector magnetometry upon characterizing the polarization effects manifested by the Fresnel reflectivities. In the same way, the Kerr rotation  $\theta_K$  and ellipticity  $\varepsilon_K$  values in a MOKE experiment can be easily related to the Fresnel reflectivities in Eqs. 1.31, which show to be proportional to certain magnetization components. These properties (among others, such as the current technology which can straightforwardly provide highly sensitive polarization dependent measurements) make MOKE of paramount importance for the study of nanoscale magnetic materials.

In the case in which more complex sample structures such as multilayers or stratified media are considered, the semi-infinite medium approach followed above is not valid and more sophisticated computations need to be performed. Nowadays, the problem of considering MOKE in arbitrary media composed of magnetic and non-magnetic layers is treated within the *Transfer Matrix Method* formalism [72-75] (see Appendix I). However, approximations in the thin film regime (for cases in which the thickness is considerably smaller than the wavelength of light) provide compact formulae for MOKE [58, 59, 71].

***Microscopic origin of the magneto-optical Kerr effect***

A brief account of the microscopic origin of MOKE is described in what follows. In order to do so, one has to consider the light-matter interaction upon reflection as a photon absorption (and the subsequent photon emission) process, via an *electric dipole transition* between electronic states [60, 76, 77]. The contribution of conduction electrons is important in the infrared region, whereas for the more energetic visible and ultraviolet regions interband transitions dominate (for ferromagnetic transition metals,  $d \rightarrow p$  transitions in particular) [63].

Hereby, MOKE can be treated from the point of view of microscopic electronic structure via its relation to the conductivity tensor. The conductivity tensor can be calculated in terms of electronic transitions via the Kubo formalism. In particular, the imaginary part of the off-diagonal  $\sigma_{xy}$  conductivity reads as [76]

$$\text{Re}(\sigma_{xy}) = \frac{\pi e^2}{4\hbar\omega m^2 \Omega} \sum_{i,j} f(E_i)[1 - f(E_f)][|\langle i|p_-|f\rangle|^2 - |\langle i|p_+|f\rangle|^2] \delta(E_f - E_i - \hbar\omega) \quad (1.33)$$

where  $\omega$  is the light frequency,  $e$  and  $m$  are the electron's charge and mass, and  $\Omega$  is the atomic volume. In addition,  $f(E)$  is the Fermi-Dirac distribution function,  $\delta(E)$  is the Dirac function, and  $p_{\pm} = p_x \pm ip_y$  are the linear momentum operators acting in the electric dipole transition for left and right circularly polarized light. Furthermore,  $E_i$  ( $E_f$ ) and  $|i\rangle$  ( $|k\rangle$ ) indicate the energy and wave-function of the initial (final) state, respectively. The sum is taken over all possible initial and final states in  $k$ -space. In addition, the real and imaginary parts of the conductivity tensor are linked by the Kramers-Krönig relations [76].

Eq. 1.33 indicates a number of selection and conservation rules for the electric dipole transition to occur (i.e. for the expression in Eq. 1.33 not to vanish) [77]. First, the factor  $\delta(E_f - E_i - \hbar\omega)$  expresses energy conservation, the energy difference between the final and initial state must match the photon energy. Next, the spin direction of the electron is conserved in an electric dipole transition. An additional selection rule implies that the initial and final states must differ in their orbital quantum number by  $\Delta l = \pm 1$ , given that the angular momentum of the photon is equal to  $\hbar$  (such that transitions between  $s \leftrightarrow p$  or  $p \leftrightarrow d$  orbitals are only allowed). Finally, the variation of the orbital momentum projection (magnetic quantum number) must fulfill  $\Delta m_l = -1$  and  $\Delta m_l = 1$  for left and right circularly polarized light, respectively.

This scenario is schematized in Fig. 1.16, following the previous work by Bruno [76] and Hamrle [77], where the case in which a medium with magnetization perpendicular to its surface and light at normal incidence is considered for a

ferromagnetic transition metal. The quantized energy levels of the electronic  $p$ - and  $d$ -levels are represented by the states  $|l, m_l\rangle$ , while spin-up and down states are separately considered. On one hand, the exchange splitting separates the  $d$ -levels having spin up or down (exchange is neglected for  $p$ -levels), with spin-up states having a lower energy if we consider a magnetization-up state. On the other hand, the spin-orbit coupling breaks the degeneracy of  $p$  and  $d$  states with a different  $m_l$  (see Fig. 1.16).

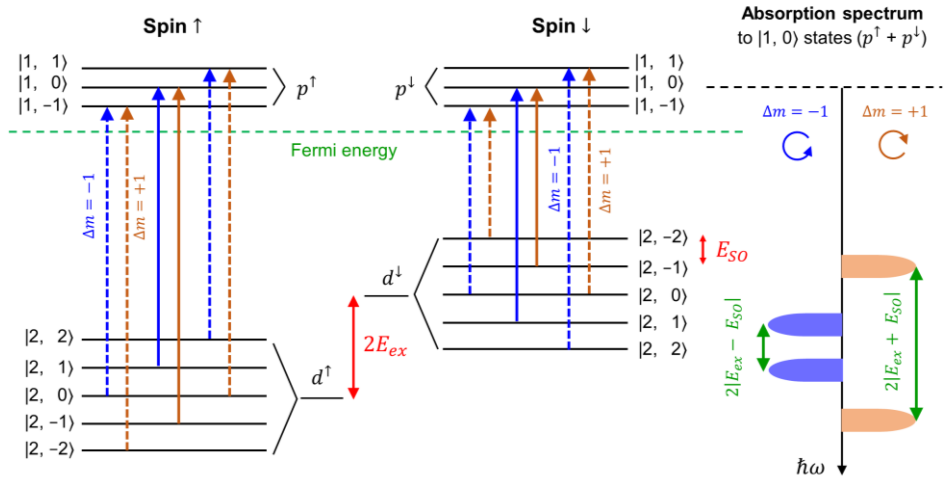


**Fig. 1.16:** Electronic states and electric dipole transitions (arrows) induced by left and right circularly polarized light. The sketch on the right hand side indicates the absorption spectra for opposite circular polarizations.

The arrows between states indicate the allowed  $d \rightarrow p$  transitions that obey the spin and angular momentum selection rules. Blue and orange arrows indicate transitions induced by left ( $\Delta m_l = -1$ ) and right ( $\Delta m_l = 1$ ) circular light. From the different length of the arrows, it can be seen that not all transition have the same energy difference. In particular, transitions that are induced by left and right circularly polarized photons occur at light frequencies that depend on the characteristic allowed transitions. This leads to different absorption spectra for left and circularly polarized light (see right hand side in Fig. 1.16), or in other words, a dichroism for circularly polarized light with different helicities – the *magneto-optical Kerr effect* (MOKE). It is already possible to see from this simplified picture that MOKE vanishes if either the exchange splitting or spin-orbit interaction vanish [76, 77].

## 1.5 Nanomagnetism and magneto-optics

The fields of nanomagnetism and magneto-optics have gone hand in hand in the last decades as a result of the powerful capabilities of magneto-optical characterization methods to investigate magnetic materials at the nanoscale. MOKE also had a relevant role in the operation of commercial magnetic memory devices, as in magneto-optical recording, where the information readout in the drive was performed via magneto-optical effects [78]. While commercial magneto-optical drives were popularized to some extent since their development in the 1980's, the use of this technology was eventually discontinued. Nowadays, MOKE still has an important role to perform quality control of commercial magnetic recording media in HDDs.

In the domain of nanomagnetism research, MOKE was first used in 1985 by Moog and Bader to measure hysteresis loops in ultrathin Fe films with monolayer sensitivity [79] and was subsequently applied to the investigation of other various phenomena in thin film magnetism. Some examples include the critical behavior of monolayer films [80] short-period oscillations of the IEC in multilayer systems [81] or the spin reorientation transition [82]. Nowadays, MOKE constitutes a widely employed form of magnetometry with the ability to obtain vector [83-85] and depth- or layer-resolved magnetization information [86, 87]. Magneto-optics is widely employed for the imaging of magnetic domains when combined with light microscopy [88, 89], and despite being limited in resolution by the diffraction limit, it enables the visualization of sub-micron spin textures such as skyrmion bubbles [90]. It was also shown that high signal-to-noise ratio hysteresis loops can be measured from single nanostructures with sizes in the range of  $\sim 100$  nm and below, either using wide-field microscopy [91] or focused laser approaches [92]. In addition, the analysis of diffracted MOKE signals from periodic lattices of magnetic nanostructures can retrieve information about non-uniform magnetization states at the nanoscale [93].

Magneto-optics also plays a key role in the field of ultrafast magnetism [27], which aims controlling the magnetization in nanomagnetic systems at subpicosecond timescales. Ultrafast magnetism was first established upon the discovery of the *ultrafast demagnetization* phenomenon in 1996 by Beaurepaire, Bigot and co-workers [94]. Using a pump-probe time-resolved measurement setting [see Fig. 1.17(a)], they observed that the MOKE signal of a thin Ni film considerably decreases within the first few-hundreds of femtoseconds after the system is excited with an ultrashort laser pulse ( $\sim 100$  fs) [see Fig. 1.17(b)]. This was a relatively unexpected finding, as it was widely accepted at the time that magnetization cannot be controlled in such fast time scales.

A further significant step came with the observation of *all-optical switching* (AOS), in which single ultrashort laser pulses of circularly polarized light were seen to

reverse the magnetization state of ferrimagnetic rare-earth/transition metal alloys with perpendicular anisotropy, such as GdFeCo [95]. The observation of this field-free route of magnetization control caused a very large interest in the research community, due to the relevant technological implications to create a new generation of faster and more energy efficient magnetic memories.

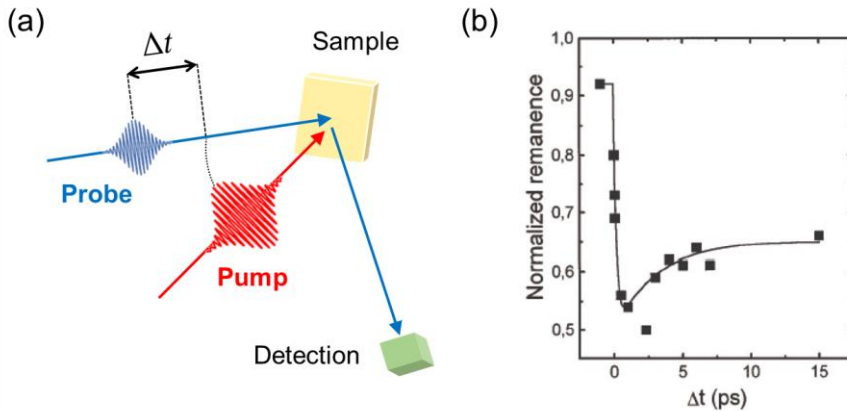


**Fig. 1.17:** (a) Schematic of the pump-probe magneto-optical Kerr effect measurement geometry, which allows time-resolved investigations of the magnetization dynamics in magnetic materials with a time resolution in the femtosecond time scale ( $\sim 100$  fs and below). (b) Seminal experiments by Beaurepaire and co-workers reporting on the laser-induced ultrafast demagnetization of a thin Ni film in sub-picosecond times scales (figure taken from [94]).

It was later seen that the AOS phenomenon in ferrimagnets is not a helicity dependent phenomenon (in which light pulses with different circular polarization can deterministically switch magnetization), but occurring by the only effect of the laser pulse heating. The realization of AOS has been extended in the recent years to ferromagnetic multilayers and alloys without rare-earth elements, and even to granular ferromagnets such as standard magnetic recording media [96, 97]. However, it seems like AOS in pure ferromagnets cannot be triggered by single laser pulses, although this problem can be circumvented by designing multilayer structures with exchange coupled ferri- and ferromagnetic layers [98]. The understanding on the role of the different mechanisms leading to AOS (e.g. pulse heating, the role of angular momentum of light, superdiffusive spin currents) is still intensely debated, with MOKE having a central role in the corresponding experimental research efforts, together with emerging pump-probe techniques performed at free electron laser facilities.

In addition, magneto-optical effects are recently very present within research on *antiferromagnetic materials*, despite these presenting a zero (or nearly zero) net

magnetization. For example, some antiferromagnets with antisymmetric exchange interactions often lead to spin canting states that cause the breaking of the sublattice moment compensation, hence presenting considerable MOKE signals [99]. Even compensated antiferromagnets can be studied using second-order magneto-optical effects such as the Voigt effect, in which the polarization analysis of transmitted or reflected light can discern 90°-oriented states of the spin axis in these materials. This feature has been recently used to track the laser-induced ultrafast collapse of antiferromagnetic ordering [100, 101], or even for the visualization of antiferromagnetic domains in NiO using wide-field optical microscopy [102].

MOKE has also been essential for the understanding of spin-dependent transport phenomena at the nanoscale. For instance, it enabled the first experimental observation of the spin Hall effect in semiconductors [103]. Magneto-optical detection of the same effect in metals has only been shown very recently [104]. As a consequence of these developments, MOKE-related methods are also acquiring a major importance in the field of spintronics.

Finally, it is also worth mentioning the appearance of emerging research topics in magneto-optics. For instance, the field of *magnetoplasmonics* explores the combination of magneto-optical and plasmonic functionalities in hybrid or nanoscale confined magnetic systems [105-107]. On one hand, the presence of plasmonic resonances can be used to produce a several-fold enhancement of MOKE signals. On the other hand, plasmonic features such as the resonant frequency can be tuned via applied magnetic fields due magnetization dependent, magneto-optically induced modifications of the optical properties. These special properties are explored in order to investigate fundamental properties of light-matter interactions, as well as to develop new platforms with improved performance in chemical and biological sensing.

In this thesis, the magneto-optical ellipsometry procedure is explored as a way to obtain the maximum possible information from a MOKE experiment. The extensive and precise information obtained using this experimental approach could be successfully applied to research in the domains mentioned in this section, where detection of small signals and the separation of different signal origins (i.e. optical, magneto-optical or magnetic) can be challenging but important to achieve.

# Chapter 2

## Experimental techniques

*This chapter serves as a brief overview of the main experimental techniques that have been utilized throughout this thesis for sample fabrication, as well as for structural, magnetic and optical characterization. As the magneto-optical experimental setups that have been employed in this thesis constitute a central theme, their description has been kept for the forthcoming chapter.*

### 2.1 Thin film and multilayer growth

The fast technological advances during the second half of 20<sup>th</sup> century, with the advent of modern high and ultra-high vacuum systems as well as the development of thin film deposition techniques, allow nowadays processing a substrate of choice such that a very small amount of material can be added on top in the form of a thin film [108]. Properties such as thickness, uniformity and roughness can be appropriately controlled, with the achievable thicknesses ranging from hundreds of microns down to a-few-angstrom, i.e. sub-monolayer quantities.

Widely employed thin film deposition methods include thermal or electron-beam evaporation, sputtering, molecular beam epitaxy or pulsed laser deposition, which are classified as physical vapor deposition (PVD) processes. PVD processes are characterized by the conversion of the material of interest from the solid state to a vapor phase, its transport to a substrate and the subsequent transformation back to the condensed phase in a thin film [108]. In contrast to chemical vapor deposition (CVD) processes, PVD does not involve chemical reactions on or at the proximity of the substrate to form coatings.

A vast majority of thin film deposition processes are carried out in previously pumped high or ultra-high vacuum chambers. This has mainly two objectives: (i) on one hand, avoiding or minimizing undesired contents in the fabricated films such as

contaminating agents; (ii) on the other hand, high vacuum is provided as a way to minimize the collisions of the deposits while they are transported from their source to the substrate, such that their mean free path is augmented by orders of magnitude [109]. Depending on the particular characteristics of the PVD process, thin film deposition is then done while the chamber is maintained in high or ultra-high vacuum (e.g. thermal or electron beam evaporation) or under the presence of gases (e.g. sputtering) [108].

Thin film deposition techniques constitute the backbone of the manufacturing process of several material platforms with technological relevance, such as thin film solar panels, hard disk drives or a wide variety of metallized coatings [108, 109].

In this thesis, I have utilized the sputtering technique, which is a widely employed tool in material science and nanotechnology, for the purpose of fabricating thin film and multilayer systems of very high and reproducible quality [110]. Apart from its use being extended in the semiconductor industry, it is probably the most utilized deposition technique for the fabrication of magnetic thin film and multilayer systems, given its stable operation, versatility, cost-effectiveness, the relative simplicity to combine different material species in one deposition process or to perform subsequent depositions, as well as for its atomic level thickness control.

### *Sputter deposition*

All thin film and multilayer systems studied in this thesis have been grown by sputter deposition, a PVD technique consisting on eroding a target of the material to be deposited, so that the free atoms are placed on a surface (or substrate) forming a film [110, 111]. This is accomplished by first creating a gaseous, self-contained plasma inside a previously pumped main chamber, for which argon (Ar) is employed in our case. The Ar atoms are ionized upon charging the source material electrically by a direct current (DC sputtering), such that the  $\text{Ar}^+$  ions from the plasma are accelerated into the source material, a negatively charged cathode, which is eroded via energy transfer by the ions. The resulting collision leads to the ejection of neutral atoms from the target, which travel in the chamber and follow a more or less straight trajectory depending on the gas pressure in the chamber. At low Ar pressures, the ejected atoms may fly toward an obstacle (substrate or chamber wall), impacting energetically with it. For relatively higher Ar pressures, the eroded atoms undergo a series of collisions with the Ar atoms in the chamber, moving diffusively and resembling random-walk-like trajectories [108, 109]. If a substrate is placed in their path, such as a Si wafer, this will become coated by a certain thickness of the sputtered material, depending on the amount of material that is being eroded per unit time from the target, the target-to-substrate distance, the mean free path of the eroded atoms in the Ar gas environment, and the elapsed time of

the sputtering process (see Fig. 2.1). The speed at which the material is deposited on the substrate is named as *sputter rate* or *thickness deposition rate*.

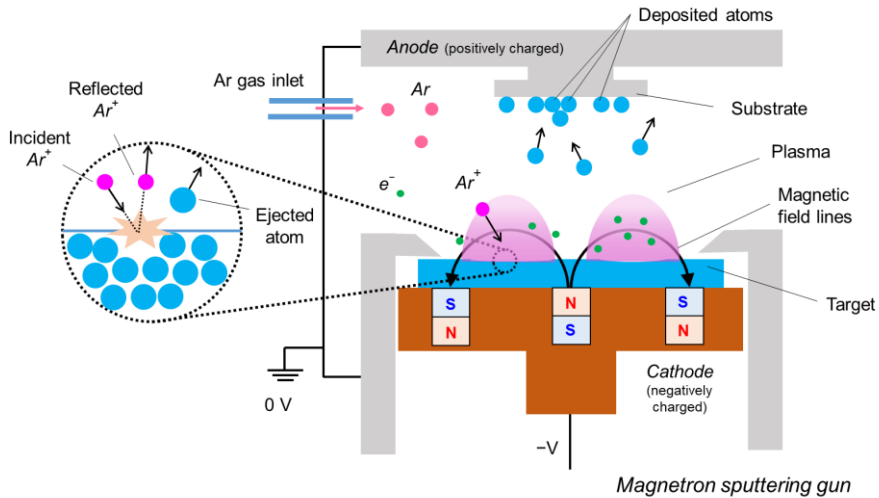


**Fig. 2.1:** Schematic and operation principle of magnetron sputtering.

The advantage of the utilization of a plasma lies on the fact that a continuous flow of  $\text{Ar}^+$  ions is self-sustained, thus avoiding the need to provide more ions externally. In the same way, the ion flux and its geometry can often be efficiently controlled in an easy way, by tuning parameters such as the Ar gas flow into the chamber, the Ar pressure in the chamber or the sputtering power and/or voltage [110].

However, placing the target on top of a bare cathode often causes low deposition rates as a result of the relatively low Ar atom ionization rate. The bombardment of the substrate by an excessive amount of free electrons can also create overheating or damage to the sample. In order to boost deposition rates as well as to avoid the complications derived from substrate heating/bombardment, strong magnet arrays are placed beneath the source target within the *magnetron sputtering* technique [110, 111]. The strong magnetic fields generated by the magnet arrays trap the free electrons directly above the target (see Fig. 2.1), as electrons follow helical paths along the magnetic field lines. The substrate bombardment that originated from the impact of these free electrons with the positively charged substrate environment is also suppressed in such a way, while at the same time increasing the ionization rate of neutral argon atoms by several orders of magnitude. This increase of the ion availability enhances Ar ion collision with the target and therefore the deposition rate is remarkably greater than in the previous configuration. Due to the geometry of the magnetic field lines generated by the permanent magnet array beneath the target material, this exhibits a “racetrack”

erosion as depletion of material occurs more frequently at the regions where the density of magnetic field lines is high. Different magnet array configurations are utilized in order to achieve the best efficiency and compatibility for different target materials (e.g. when utilizing source targets of ferromagnetic or diamagnetic and paramagnetic materials) [112].

In order to obtain a high chemical purity of the deposited films, it is crucial to have ultra-high vacuum (UHV) conditions in the chamber prior to the sputtering process. The relatively slow thin-film growth (usually  $< 1 \text{ \AA/s}$ ) can cause the intermixing of impurities coming from the environment with the actual film being grown, such that the chamber base pressure value has a clear impact on the quality of the deposited films. In our case, the vacuum level (base pressure) in the main chamber was  $5 \cdot 10^{-8}$  Torr or better prior to all deposition processes.

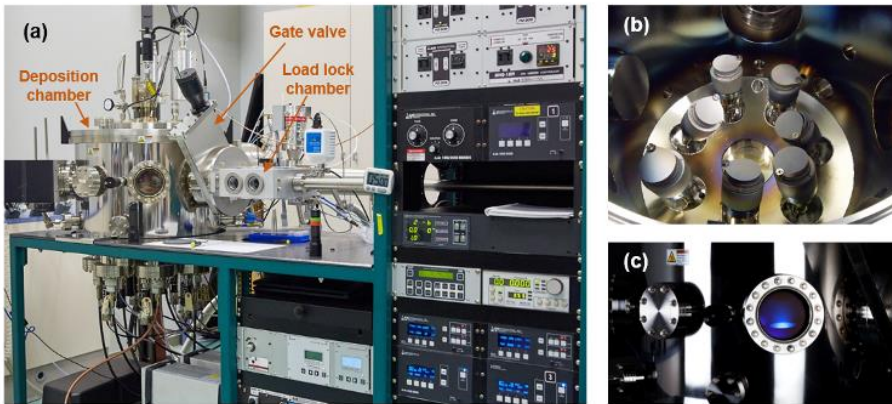


**Fig. 2.2:** (a) Picture of the sputter deposition tool at CIC nanoGUNE, where the main chamber, the load lock chamber as well as the gate valve placed between them are indicated. (b) View of the inside part of the main deposition chamber, where 7 magnetron sputtering guns are present. Notice the different tilt of them, which is interchangeable at any moment even if the chamber is under high vacuum conditions. (c) Detail of the plasma glow, as seen from a viewport, during the sputtering deposition process.

Our UHV sputter deposition system at CIC nanoGUNE is an *ATC series UHV* system by *AJA International Inc.* that has two vacuum chambers equipped with turbo-molecular pumps [see Fig. 2.2(a)]. The smaller one is a load lock chamber used to introduce substrates to the main chamber without having to break the much better vacuum in it. The substrate holder is transferred between the chambers by a manually controlled mechanical arm. The whole sputtering process occurs in the main chamber, where the base pressure prior to deposition is ensured to be of the order of  $10^{-8}$  Torr.

These excellent vacuum conditions are achieved by means of a high volume turbo molecular pump with a pumping speed capability of 1200 liters/second. A smaller turbomolecular pump is used for the load lock chamber, reaching rapidly (< 10 min) a low enough pressure value of the order of  $10^{-7}$  Torr. In such a way, the valve opening between the chambers for the mechanical transfer of the substrate (or the actual deposited samples back to the load lock) practically does not affect the vacuum conditions in the main chamber.

The source material targets are placed on guns, which are the tools that act as sputtering sources [see Fig. 2.2(b)]. The guns provide the correct grounded shielding and different magnet array configurations behind the target, depending on whether this is a ferromagnetic material or not, such that the overall plasma shape [see Fig. 2.2(c)] is not changed from gun to gun. Each gun can be connected to a power supply and a water-cooled line for the purpose of avoiding overheating. A power supply feeds the plasma state while this is losing energy into the surroundings. One can trigger this dynamic condition by introducing the sputtering gas into the main chamber and allowing it to reach a specific pressure. In our case, the high-purity Ar gas is introduced in the chamber at a flow of 20 standard cubic centimeters per minute (sccm), while a mechanically movable gate valve placed between the main chamber and the turbomolecular pump controls the Ar pressure by varying the relative opening position of this valve and thus increasing or decreasing the pumping efficiency. The Ar pressures at which sputtering processes are stable are usually in the  $10^{-4}$  -  $10^{-2}$  Torr range, while usual sputtering pressures employed for the work shown in this thesis were of the order of  $\sim 10^{-3}$  Torr.

The main chamber of our system is equipped with seven identical sputter guns, which permits growing a sequence of layers made of up to seven different materials without breaking the vacuum. The guns can be tilted in order to arrange multiple sputtering sources to a common focal point in a configuration known as confocal sputtering. As the system is equipped with two radio frequency (RF) and four direct current (DC) power supplies, co-deposition of up to six different materials for alloy fabrication is possible. The DC power supplies are used in the case of conducting metals, while the RF is commonly used for sputtering insulating materials. The RF source biases the insulating source target in an alternate fashion, thus this being positively (anode) and negatively (cathode) charged across oscillations, which are fast enough ( $\sim$  MHz range) to avoid charging effects in the target, which would impede the sputtering process. By introducing a bias to the oscillatory voltage, a non-zero voltage is effectively applied on average to the insulating target material, enabling plasma generation and the subsequent erosion of the target by  $\text{Ar}^+$  ions, hence facilitating the sputtering process.

An additional RF power supply is connected to the substrate holder for RF bias processes. This process can be done before deposition for substrate pre-cleaning purposes, as the bias creates plasma near the substrate itself. The bombardment of the  $\text{Ar}^+$  ions can be used to etch the substrate surface prior to deposition as well as for achieving low surface roughness and high uniformities when depositing insulating materials [113], among other applications. In addition, two lamps are placed on top of the substrate holder which facilitate heating up the substrate to temperatures as high as  $850^\circ\text{C}$  prior to, during or after growth. The heating option can be used, for example, to perform post-growth annealing processes that improve the crystallographic quality of deposited epitaxial films or multilayers, as well as to improve chemical ordering in alloy materials. Finally, the substrate holder can be rotated during deposition for an improved thickness uniformity of the sample. The tests realized on the system showed deposited thickness uniformities better than  $\pm 5\%$  for 20-nm-thick Ni films grown onto 4-inch diameter wafers [112].

### ***Thickness calibration by the quartz crystal monitor***

The deposition rate can be measured *in situ* in the AJA system by means of a quartz crystal microbalance (QCM) *SIGMA SQM-160*. The QCM is an electronic device tracking the frequency response of a quartz crystal as it is placed at the substrate position during deposition, such that deposition rate during can be monitored in situ with a precision of the order of  $\sim 0.01 \text{ \AA/s}$ . The operation principle of the QCM device is based on the measurement of mass variation per unit area for the material being attached to the device during deposition. This is accomplished by monitoring the change in frequency of a quartz crystal resonator, which is a piezoelectric material. The resonance frequency of the crystal is disturbed by the addition of a small mass during film deposition, such that the frequency shift can be related to the amount of material being deposited on the QCM device. This is done by taking into consideration the density as well as some other characteristics of the material, such as the compressibility factor (also known as the Z-factor). The deposition rate for a wide variety of elements and compounds can be calibrated with this tool. An accurate knowledge of the deposition rate enables us to control the deposited thickness with a very high precision, which is of fundamental importance when growing thin films and multilayers. Fig. 2.3(a) displays a deposition rate calibration performed during a Co deposition by the QCM device in a time interval of 5 minutes. The DC sputtering power was adjusted to 100 W, while the Ar gas pressure was set to 3 mTorr. The base pressure in the main chamber prior to the deposition process was  $3 \cdot 10^{-8}$  Torr.

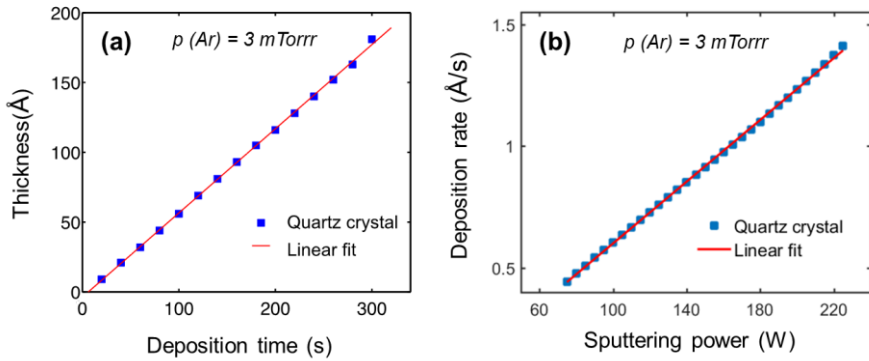


**Fig. 2.3:** (a) Deposited Co thickness at 100 W power and 3 mTorr Ar pressure conditions against the elapsed deposition time as measured by the quartz crystal monitor during 5 minutes of sputtering. The solid line represents a fit of the data to a straight line. (b) Sputtering power dependence of the deposition rate for Co at the same power and Ar pressure conditions. The solid line represents a fit of the data to a straight line.

The highly linear dependence of the deposited Co thickness vs the deposition time in Fig. 2.3(a) gives a convincing evidence of the stable operation condition and constant deposition rate during the entire deposition interval. A least squares fit of the data to a straight line reveals a deposition rate of  $0.60 \pm 0.02$  Å/s. It is worth noting that the straight line does not precisely go through the origin [see Fig. 2.3(a)]. This discrepancy may be originated by a slight delay of the deposition onset due to the finite amount of time for the shutter in the gun to open (which may take about 1-2 seconds).

The sputter power dependence of the deposition rate of Co at 3 mTorr is also indicated in Fig. 2.3(b), as measured via the QCM. This dependency is very close to being linear in the power range indicated here<sup>14</sup>. An increase of about  $0.06$  Å/s per W is extracted from the fit of the data to a straight line. Thus, the choice of sputtering power permits setting us the deposition rate we are interested once a calibration, as the one shown in Fig. 2.3, is done. While the utilization of the QCM is a useful and quick method to quantify deposition rates and predict film thicknesses, it is desirable to complement these measurements with calibrations obtained via x-ray reflectivity by actually measuring the real thickness of deposited films (see Section 2.2).

<sup>14</sup> The linear dependence between deposition rate and sputtering power does not necessarily remain at low sputtering power values ( $< 15$  W). The plasma state and the self-sustained production of Ar ionization might not be completely stable under these conditions (evidenced, for instance, by the observation of plasma blinking or varying color), leading to fluctuations of the deposition rate.

### *Epitaxial growth*

Deposited thin films exhibit in the most general case a polycrystalline or amorphous character, such that the film is composed by neighboring grains of different crystallographic orientation. The orientation distribution of such misoriented grains may show overall randomness or a certain preferential alignment with respect to the film geometry. In the latter case, it is said that the grown film is textured or displays a preferential crystallographic texture. In certain cases, thin film deposition may lead to a given preferential texture of the grown material because of the dissimilar relative surface energy of the different facets of a crystalline material. However, there is also a more controllable way to induce a desired crystallographic texture upon thin film deposition, which is epitaxial growth [108]. This consist on matching the crystal structure of the deposited material to that of the substrate at the interface, for which both crystalline lattices need to be compatible, in terms of the crystallographic symmetry and lattice dimensions. Thus epitaxy implies, in general, the use of single-crystal substrates. Other factors to take into consideration for epitaxy to occur are the absence of solid-state reactions or intermixing, for instance, at the film/substrate interface.

In case that the film of the material of interest and the substrate show incompatible lattice structures or dimensions, one can also devise an epitaxial growth sequence in which intermediate layers are employed between the substrate and the final film with the desired texture. This is the strategy that was followed in order to grow epitaxial hcp Co films by epitaxial growth onto single-crystal Si substrates, by utilizing sequential epitaxial growth of textured Ag and Cr films on the Si substrate<sup>15</sup>.

It is also extremely important to have clean and smooth surfaces starting from the very substrate. Thus it is strictly necessary to clean the substrates with agents such as acetone and isopropyl alcohol (IPA or propan-2-ol). In the case of epitaxial growth on oxidized wafers such as in the case of Si, the surface has to be also chemically treated in order to remove the oxide. This is done, for instance, by chemical etching via acids (e.g., hydrofluoric acid or HF for Si). In addition, it is also relevant working in clean chambers where ultra-high vacuum conditions are available prior to deposition, in order to avoid undesired coatings or presence of contaminants that would destroy the epitaxy or create instabilities during growth.

---

<sup>15</sup> While the epitaxial growth of hcp Co films was devised and optimized by previous work within the Nanomagnetism group at CIC nanoGUNE [112], all samples measured within this thesis were grown or fabricated by the author of the thesis, occasionally in collaboration with other group members.

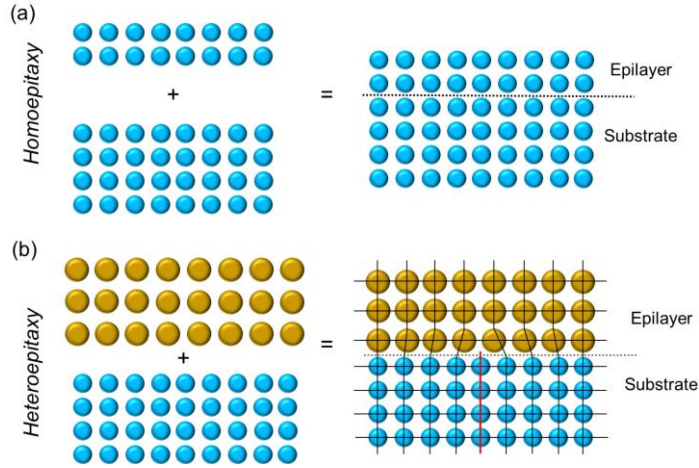


**Fig. 2.4:** Schematic of epitaxial growth for (a) a homoepitaxial epilayer and (b) a heteroepitaxial epilayer. In the second case, the mismatch between the two different lattices makes forces the epilayer to adapt the lattice geometry of the substrate by adopting its interatomic in-plane distances. As growth progresses stacking faults and misfit dislocation generally occur [see red line in (b)], which relieve the stress at which the epilayer is subjected.

Fig. 2.4 exhibits a schematic of two types of epitaxial growth sequences, namely *homoepitaxy* and *heteroepitaxy*. The former refers to the growth of the same kind of material species as the crystalline substrate, which consists on the best possible condition for epitaxy to occur. In the case of heteroepitaxy the *epilayer* (the layer being grown onto the substrate of a different material), will grow with a given preferential crystallographic texture if the crystal lattice compatibility with the substrate is fulfilled. Epitaxy is possible even when the substrate and film lattices show certain dissimilarities in terms of lattice dimensions (i.e. inter-atomic distances). In such case, it is said that a mismatch between the two exists, defined as [108]

$$\eta = 100 \times \frac{a_{film} - a_{subs}}{a_{subs}}, \quad (2.1)$$

with  $a_{film}$  and  $a_{subs}$  being the matching inter-atomic in-plane distances of the film and the substrate, respectively. Upon the existence of a film-substrate mismatch, it is observed that the epilayer atoms adopt the in-plane inter-atomic distances of the substrate in the early growth stages, resulting in a strained state of the material. However, as growth continues, and due to the fact that the elastic energy of the deformed film scales with its thickness, it results energetically more favorable at a certain point to introduce stacking faults and misfit dislocations, in which relieving the stress supported

by the epilayer is energetically more favorable than the cost introduced by dislocations. This strain relaxation process allows the film to partially or totally recover its most stable lattice configuration (see Fig. 2.4). Furthermore, it is also possible to control the complete lattice structure of films grown via epitaxy, leading to metastable structural phases of materials that do not exist in the bulk, such as bcc Co [114].

### ***Co-deposition of alloy films from different sputter targets***

In order to deposit an alloy-film with more than one atom species (such as  $A_xB_{1-x}$  with atom species  $A$  and  $B$ , where  $0 < x < 1$  indicates the atomic concentration of  $A$  species) one can follow two different strategies. On one hand, one could start from a sputter target of the same composition as the desired film. This is usually a valid strategy for creating films with the desired stoichiometry, even if optimization in terms of sputtering conditions (e.g. Ar pressure, power) is needed because of the slightly different sputter yield or efficiency that atom species  $A$  and  $B$  may possess [108]. On the other hand, one could follow the strategy of simultaneously sputtering from two different source targets made of pure  $A$  and  $B$  species. In such a case, the ratio of their deposition rates  $R_i$  ( $i = A, B$ ) has to be correctly calibrated in order to reach the desired film composition, in terms of the stoichiometry parameter  $x$ . The ratio of the deposition rates of the species  $A$  and  $B$  can be related to the ratio of film thicknesses (or, equivalently, volumes  $V_i$ ) that would result in separate deposition processes, such that

$$\frac{R_A}{R_B} = \frac{V_A}{V_B} = \frac{x}{1-x} \frac{\rho_B}{\rho_A} \frac{M_A}{M_B}, \quad (2.2)$$

where  $\rho_i$  and  $M_i$  are the density and atomic mass of the corresponding species, respectively<sup>16</sup>. A similar procedure is generally valid for ternary and quaternary alloys.

### ***Method for deposition of thin films with a wedge-profile***

For certain experiments in this thesis, it was sought to systematically vary the thickness of a single film in multilayer system to examine what is the effect of this thickness on

---

<sup>16</sup> In order to estimate the total thickness of the  $A_xB_{1-x}$  film, I assume that the total deposition rate during co-deposition is  $R = R_A + R_B$ . This is a relatively good approximation, with the typical thickness estimation error being less than 5%, as concluded from x-ray reflectivity determination of the grown films.

the magnetic, optical or magneto-optical properties of the entire multilayer stack. One way to do so consists of performing various subsequent depositions by varying the deposition time of this particular layer in the multilayer stack. However, one would be always subject to deposition-to-deposition variations in between these growth processes, which have to be taken into account despite the robust and stable operation of magnetron sputtering.

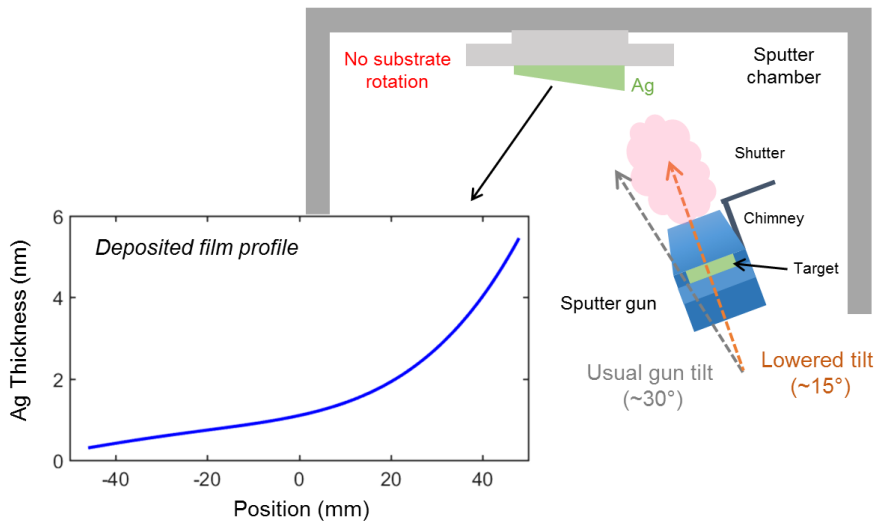


**Fig. 2.5:** Method to grow thin films with a position dependent thickness profile of a wedge-type. The inset shows the calibration of such a thickness profile done via scanning spectroscopic ellipsometry (see Section 2.4).

A convenient way to have such a batch of samples made once is usually realized by depositing films with a position dependent thickness profile, in the form of a wedge. In order to fabricate samples containing wedge-type films, we follow the method depicted in Fig. 2.5, based on the utilization of a tilted magnetron gun geometry upon maintaining the substrate azimuth orientation fixed. This creates a non-uniform thickness profile in the substrate, such that a higher thickness results in the substrate region placed closer to the gun (which is incident from one side), whereas a thinner film is formed in the substrate region located further from the sputter gun.

We take advantage of this fact by completely eliminating substrate rotation and placing an elongated wafer (e.g., Si) on the sample holder, with its long axis oriented along the projection of the normal vector of the sputter gun onto the sample holder plane. One can make this effect even more pronounced by lowering the tilt of the magnetron gun, usually placed at about  $30^\circ$  from the normal. By reducing this angle to  $15^\circ$ , films with a wedge-type profile exhibiting thickness ratios as high as  $\sim 10$ - $15$  for substrate

positions that are 80 mm apart from each other can be obtained. An exemplary wedge-type profile for a Ag deposition is shown in the inset of Fig. 2.5, with the Ag thickness ranging from 0.3 to 4 nm when going from the position  $-40$  mm to  $40$  mm. The wedge profile is nearly linear in its low-thickness region, while it shows a monotonic increase in its slope towards the high thickness end. This allows us to have now a large number of ‘different samples’ of distinct Ag thickness, if we are able to analyze them with a position-dependent probe (e.g. by scanning a laser with a  $\sim 1$ -mm-wide spot).

### 2.2 Structural characterization via x-ray diffraction

Given that diffraction of light happens when the wavelength and the obstacle size are similar, x-rays (with typical wavelengths of the order of  $\sim 1$  Å) provide an ideal method for characterizing condensed matter at the atomic scale, as the interatomic distances in solids are of the order of a few angstroms. On one hand, x-ray interference effects prove to be very powerful to characterize the layered structure of thin film and multilayer systems, including thicknesses, roughness or grading effects at interfaces [115].

On the other hand, x-rays can also probe how the regularly arranged atoms in a crystalline lattice are positioned, which gives also a way to study crystallinity and texture effects in a non-destructive way [115, 116]. Fig. 2.6(a) shows the schematic of a typical x-ray diffraction measurement. X-rays are incident on the sample at an angle  $\omega$ , while the scattering or diffraction angle  $2\theta$  is defined as the angle between the incident x-ray path and the scattered x-rays. In the kinematical diffraction approximation, it is assumed that the energy of the incident and scattered x-rays remains unchanged, such that their momenta fulfill  $k = k' = 2\pi/\lambda$ . However, because of the different relative orientation of the  $\mathbf{k}$  and  $\mathbf{k}'$  x-ray momentum vectors, there is a transfer of momentum exerted by the sample, which is defined as  $\mathbf{Q} = \mathbf{k}' - \mathbf{k}$  [see Fig. 2.6(a)]. In the particular case in which  $2\omega = 2\theta$  (symmetric diffraction condition), the momentum transfer vector  $\mathbf{Q}$  is perpendicular to the sample plane [see Fig. 2.6(a)].

The x-ray diffractometer available at CIC nanoGUNE is an *X'Pert PRO PANalytical* making use of a Cu anode for generating x-rays [Fig. 2.6(c)]. The major part of the x-ray radiation from the source corresponds to the  $K_\alpha$  and  $K_\beta$  spectral lines of Cu. For crystallinity and texture analysis, a double bounce Ge(220) monochromator selecting the  $K_{\alpha_1}$  spectral line of Cu ( $\lambda = 1.54056$  Å) is employed. An automated goniometer allows moving the source and detector arms enabling measurements for different  $\omega$ - $2\theta$  configurations where x-ray reflections from the sample are sought. Additionally, the sample holder can be tilted by varying the polar and azimuthal angles  $\chi$  and  $\Phi$  [Fig. 2.6(b)].

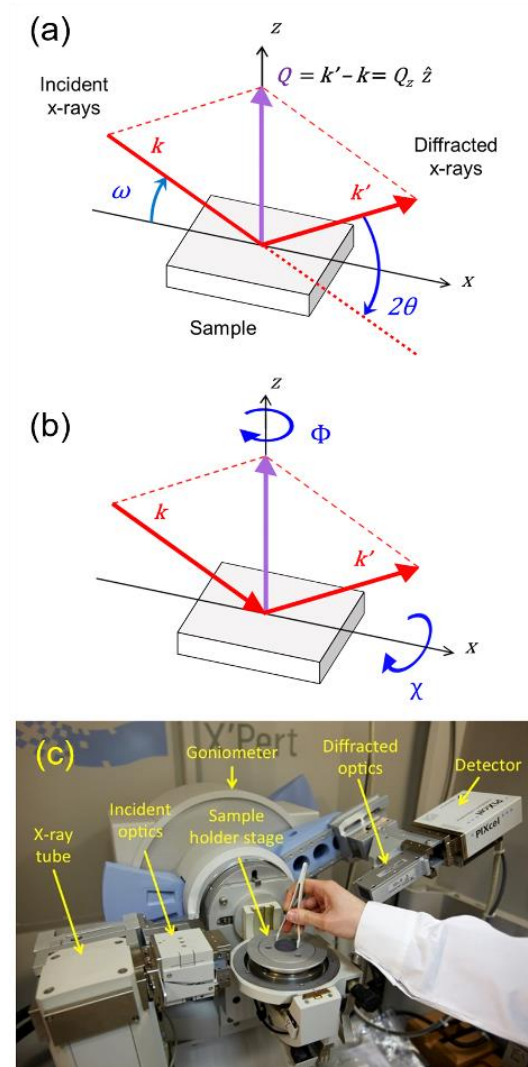


**Fig. 2.6:** (a) Schematic of an x-ray diffraction experiment, defining the incident angle  $\omega$  and the scattering angle  $2\theta$ . (b) Definition of the polar and azimuthal angles  $\chi$  and  $\Phi$ , respectively. (c) Picture and components of the x-ray diffractometer at CIC nanoGUNE.

### *Thickness calibration and layer structure determination via x-ray reflectivity (XRR)*

The index of refraction  $n$  of a material in the x-ray region can be represented as [115]

$$n = 1 - \delta + i\beta,$$

(2.3)

with the parameters  $\delta$  and  $\beta$  being the real and imaginary parts of the material dependent contribution describing the dispersive and absorptive aspects of the wave-matter interaction. As the absorption depth of x-rays in matter is of the order of millimeters, x-ray refractive indices are slightly smaller than one [115]. This leads to the phenomenon of total external reflection, upon which x-rays incident from a less dense medium into a denser one will totally reflect for incident glancing angles  $\omega$  smaller than a critical angle  $\omega_c$ . Because the refractive index is very close to one, critical angles are usually very small (0.1-0.5°), even if the exact value naturally depends on the energy of the x-rays and the media from which they are reflected.

When considering x-ray reflection from a homogeneous slab of a finite thickness placed on a semi-infinite substrate, the multiple reflections at the interfaces of the slab with the ambient and the substrate underneath must be considered [see Fig. 2.7(a)]. Each time the wave travels through the slab of thickness  $D$ , it undergoes a phase shift due to the dispersive nature of the medium. When summing the amplitudes of waves exiting the slab upon undergoing a single or multiple reflections, constructive or destructive interference may occur for different settings of the incident angle  $\omega$ . The total reflectivity can thus be computed by considering the sum of all possible reflection and transmission events at the two interfaces (ambient/slab and slab/substrate), reaching to a geometric series that can be written in the following compact form [115]

$$r_{slab} = \frac{r_{01} + r_{12} p^2}{1 + r_{01} r_{12} p^2} \quad (2.4)$$

with  $r_{ij}$  being the reflection coefficient for x-rays incident at the interface between media  $i$  and  $j$ . The indices 0, 1 and 2 refer to the ambient, slab and substrate, respectively [Fig. 2.7(a)]. The phase factor  $p^2 = e^{iQD}$  (with  $Q = 2k \sin \omega$  being the momentum transfer, and  $k = 2\pi/\lambda$ ) accounts for the phase shift added by the thin slab when travelling back and forth<sup>17</sup>. The formula is valid for angles of incidence well above  $\omega_c$ , within the kinematical approximation of x-ray scattering [115].

The oscillatory nature of the  $p$  phase factor in Eq. 2.4 leads to the appearance of reflectivity oscillations as a function of the incident x-ray angle  $\omega$ , which are termed as Kiessig fringes [see Fig. 2.7(b)]. The observable peaks and dips correspond to waves that are scattered in phase and out of phase, respectively. If represented against  $Q$ , the oscillation period of the reflectivity function is inversely proportional to the slab

---

<sup>17</sup> The formula is reached upon further considering energy conservation and that the equivalence  $r_{01} = -r_{10}$  holds. For the derivation, see Ref. [115], pages 75-76.

thickness  $D$ , with the peak-to-peak periodicity being  $\Delta Q = 2\pi/D$  (in the small  $\omega$  approximation,  $\Delta\omega \approx \lambda/2D$ ).

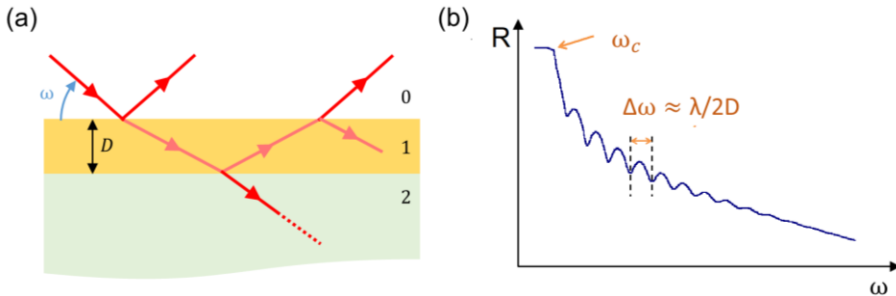


**Fig. 2.7:** (a) Schematic of x-ray reflection from a slab of finite thickness. (b) Simulated reflectivity profile for a thin slab on a substrate. The critical angle  $\omega_c$  and the Kiessig oscillations are depicted.

While the approach based on extracting the oscillation period of the Kiessig fringes is generally sufficient to obtain a reasonable estimate of the film thickness, x-ray reflectivity (XRR) profiles of thin films and multilayer structures overall display non-trivial curve characteristics that go beyond what Eq. 2.4 in particular can account for. With the aim of enabling the multilayer structure characterization of arbitrary samples, more sophisticated mathematical descriptions of XRR are often implemented. A common approach is based on the Parratt formalism, which gives a way to compute the reflectivity of an arbitrary number of strata on top of a substrate using a recursive method [115]. These mathematical descriptions are often incorporated in commercial as well as open-source software platforms<sup>18</sup>, which typically allow building customized x-ray optical models for direct comparison and fitting of experimental XRR data. Commonly the thickness, density and interfacial roughness of each layer can be optionally set as fit parameters, while occasionally, compositional gradients within layers can be considered as well. While an excessive amount of fit parameters may lead to incongruent fit results, the aforementioned software platforms enable a very detailed determination of complex multilayer structures via multiparameter fitting. This is applicable in systems ranging from single layers to complex superlattices.

In order to briefly illustrate the effect on XRR curves of the additional layer properties, a set of curves for a 15-nm-thick Co film on a Si substrate have been simulated by varying the roughness values of the ambient (air)/Co film interface (Fig. 2.8). The XRR curves with simulated Co film roughness values of 0.4, 0.8 and 1.2 nm

<sup>18</sup> Analysis of XRR curves was done via the commercial XRR fitting software from *Panalytical* (instrument manufacturer) as well as the open-source software *GenX* [117].

indicate that the reflectivity decays faster with respect to  $\omega$  for larger roughness values. Additionally, the amplitude of the Kiessig fringes also decreases faster. While the interference oscillations are very robust up to  $\omega = 4^\circ$  for a roughness of 0.4 nm, these are already suppressed for  $\omega > 3^\circ$  if the roughness is increased to 0.8 nm and even disappear at considerably lower angles of incidence ( $\omega > 1.5^\circ$ ) when it is increased to 1.2 nm. Thus, Fig. 2.8 depicts that the XRR curve features are very susceptible to sub-nanometer attribute changes of the constituent layers and interfaces in the sample.

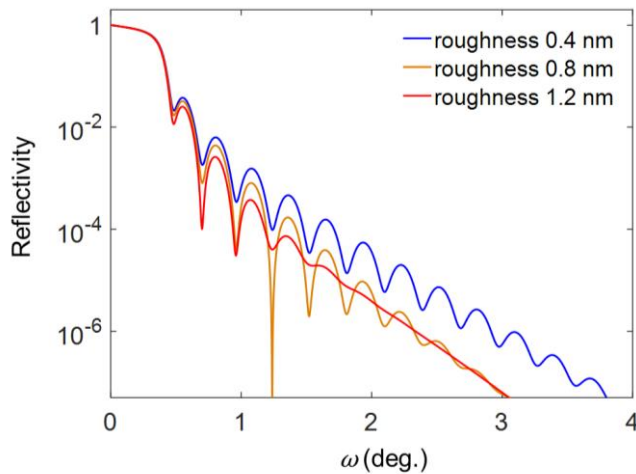


**Fig. 2.8:** Simulated XRR curves for a 15-nm-thick Co film with variable ambient/film roughness (0.4, 0.8 and 1.2 nm). The substrate/film roughness was set to 0.5 nm in all cases. The simulated curves were obtained using the free-source software GenX [117].

When calibrating the deposition rates of the materials grown via magnetron sputtering, XRR was commonly used as a way to obtain more accurate deposition rate values than those obtained from the QCM. In order to illustrate this, I compare the thickness determination of a series of Co thin films grown on Si substrates using QCM vs XRR. The nominal thicknesses of the films, as obtained from the QCM, were 5, 10 and 20 nm. The films were grown at identical conditions using a sputter power of 50 W and an Ar pressure 3 mTorr, varying only the deposition time from sample to sample. Subsequently, XRR spectra of grown Co films were measured and fitted in order to determine the actual thickness of the deposited film. Fig. 2.9(a) exhibits the measured XRR data as well as its corresponding fit for the nominally 20-nm-thick test sample. Fitting the data to an x-ray optical model resulted in the determination of a thickness value of  $26.5 \pm 0.5$  nm, considerably higher than the nominal 20 nm. The fitted roughness value of the Co film was  $1.0 \pm 0.2$  nm

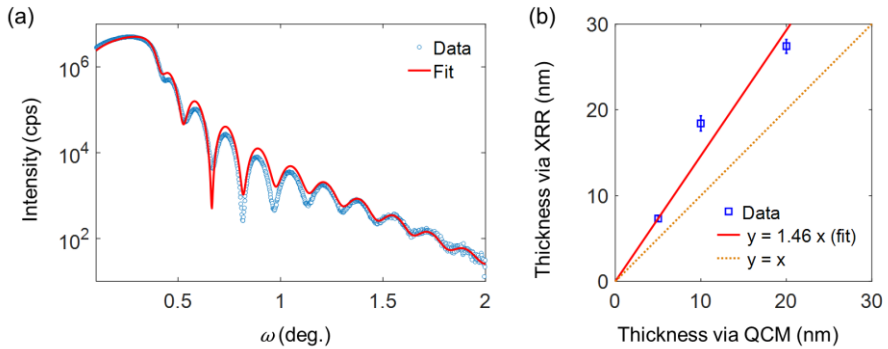


**Fig. 2.9:** (a) XRR data and corresponding fit for a 20 nm nominal thickness Co film grown by magnetron sputtering on a Si substrate (b) Comparison of measured film thicknesses vs their nominal thickness as given by the QCM.

Upon comparing the measured (XRR) and nominal (QCM) thicknesses, one can conclude that the deposited film thickness was always underestimated upon relying this quantification on the QCM method. Fig. 2.9(b) shows the measured thickness values against the nominal ones, with the solid line indicating a least squares fit of the trend to a straight line. It can be concluded that XRR proves the film thickness to be  $1.46 \pm 0.07$  times greater than the one indicated by the QCM.

This discrepancy could be related to systematic inaccuracies of the QCM, as it is known that the employed quartz crystals usually have an expiration that depends on the total amount of deposited material onto them. Due to the prolonged use of a disposable quartz crystal element in the QCM device, its reliability is reduced and the estimated thickness is susceptible to relatively large errors (even by nearly 50%, as shown here).

Consequently, we generally relied on the deposition rate values obtained from XRR measurements, since this technique measures the actual thickness of the films obtained from depositions. In any case, the use of QCM is still a useful tool for obtaining an approximate deposition rate value and for tracking its relative variations when tuning deposition parameters such as the sputter power or pressure.

Throughout this thesis, the deposition rate of a wide variety of materials (Co, NiFe, Cr, Ag, Pt, SiO<sub>2</sub>, etc.) was always checked using XRR. Whenever the thickness of a film is given, the value generally corresponds to the actual thickness as calibrated or measured via XRR, rounded to 1 nm precision.

**Texture analysis via x-ray diffraction (XRD)**

So far, we have seen how small angle x-ray scattering can provide a way to characterize the multilayered structure of our samples containing layers with characteristic thickness values ranging in between  $\sim 1$ -100 nm. In addition to this, high-angle x-ray scattering also facilitates the determination of the crystalline structure, preferential texture and even chemical composition of a thin film or multilayer sample, via a family of techniques and procedures classified within the term *x-ray diffraction* (XRD). The family of XRD methodologies are based on constructive and destructive interference effects of coherent x-rays upon scattering from ordered atomic lattice planes in crystalline or textured materials<sup>19</sup>.

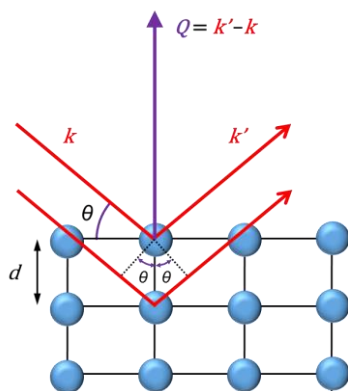


**Fig. 2.10:** Graphical representation of the Bragg law, which provides the condition for constructive interference to occur.

A schematic of x-ray scattering within the typical XRD geometry is shown in Fig. 2.10. Here, x-rays are incident onto and scattered from well-ordered atomic lattice planes where a large electronic density is concentrated [115]. The quantities of interest here are the incident angle  $\theta$  of x-rays with respect to the atomic lattice planes as well as the distance  $d$  between regularly spaced atomic planes. Since x-rays are indistinctly reflected by different atomic planes, scattering from consecutive planes will cause the waves to undergo a different path length before they meet, with the path difference being  $\Delta l = 2d \sin \theta$  (see Fig. 2.10). If this path difference matches the x-ray wavelength  $\lambda$  (or a multiple), constructive interference will occur, thus giving rise to an

<sup>19</sup> A more rigorous description of the x-ray diffraction phenomenon is given in terms of the reciprocal space description of crystals. In order to make the discussion brief, the presentation of the concepts concerning the reciprocal space is skipped and the reader is referenced to exemplary textbooks that extensively cover the topic [115, 116].

intense diffraction peak upon scanning the incidence and observation angles  $\theta$ . The interference condition is summarized by Bragg's law, which reads as [115, 116]

$$n\lambda = 2d \sin \theta, \quad (2.5)$$

where  $d$  is the interplanar distance in the lattice,  $\lambda$  is the x-ray wavelength and  $n$  is a positive integer number.

Interplanar distances in well-ordered crystals and textured samples are characteristic of a given crystal structure symmetry as well as its related dimensions, such that scattering angles can be related to databases where one can identify the material species and the relative orientation of the crystal planes with respect to the sample or substrate geometry in the laboratory frame.

Three types of experimental procedures for texture and crystallite alignment determination are briefly summarized below, namely: (i) *gonio* or symmetric  $\theta$ - $2\theta$  scans, (ii) rocking curves or  $\omega$ -scans, and (iii) azimuthal or  $\Phi$ -scans.

*i. Symmetric  $\theta$ - $2\theta$  scans (gonio scans)*

In a symmetric  $\theta$ - $2\theta$  scan, the source and detector arm are scanned in a coupled fashion such that the relation  $2\omega = 2\theta$  is always fulfilled. Upon this configuration, the angle between the source and the sample as well as the angle between the detector arm and the sample are both equal to  $\theta$  [see Fig. 2.11(a)]. This in turn means that the momentum transfer vector  $\mathbf{Q}$  is at all times perpendicular to the sample plane. Hence, the  $\theta$ - $2\theta$  x-ray scan is sensitive to the existence of well-ordered lattice planes that are (nearly) coherent with the sample plane.

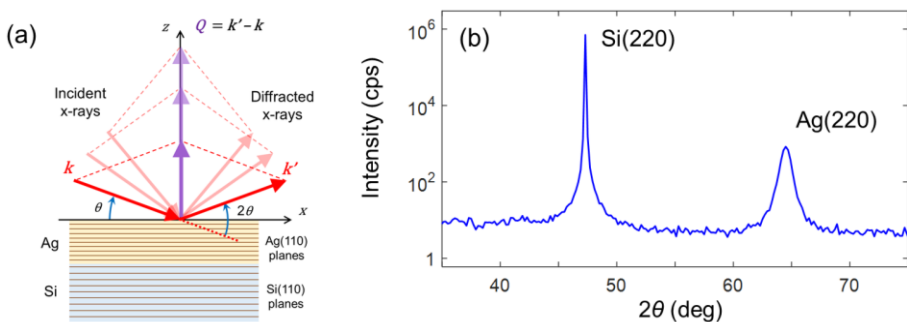


**Fig. 2.11:** (a) Schematic of the measurement configuration for a symmetric  $\theta$ - $2\theta$  scan, applied to a Ag epilayer on a Si substrate. (b) Experimental XRD data acquired in the  $\theta$ - $2\theta$  configuration for a 75-nm-thick Ag film epitaxially grown onto a Si(110) single-crystal substrate.

This measurement configuration is particularly useful for detecting the out-of-plane texture of thin film or multilayer samples grown according to an epitaxial sequence onto a substrate. Fig. 2.11(b) displays exemplary XRD data acquired in the symmetric  $\theta$ - $2\theta$  configuration for a 75-nm-thick Ag film on a Si(110) substrate in the  $35$ - $75^\circ$   $2\theta$  range [see also schematic in Fig. 2.11(a)]. Only two diffraction peaks are prominent from the scan, which correspond to the Si(220) and Ag(220) reflections, and thus confirming the (110) texture for the Ag film.

In this thesis, symmetric  $\theta$ - $2\theta$  scans have been extensively used in order to verify the epitaxial growth of the fabricated samples, as this scan constitutes a fingerprint of their out-of-plane crystalline orientation. In addition,  $\theta$ - $2\theta$  scans also facilitate the attainment of the lattice parameter values connected with the lattice planes oriented parallel to the sample plane.

ii. *Rocking curves ( $\omega$ -scans)*

Rocking curves or  $\omega$ -scans are performed in order to characterize the mosaic spread of textured samples such as thin films. Every crystalline thin film system can be thought of as an assembly of crystallites or grains (for metallic thin films, grains typically have the size of the film thickness [116]). Within each grain, the crystallographic structure of the material remains coherent, whereas at grain boundaries the lattice regularity is disrupted by defects, dislocations or stacking faults. For polycrystalline films the different grains are generally randomly oriented, whereas in textured films a certain coherence of the relative crystallographic orientation between grains is kept.

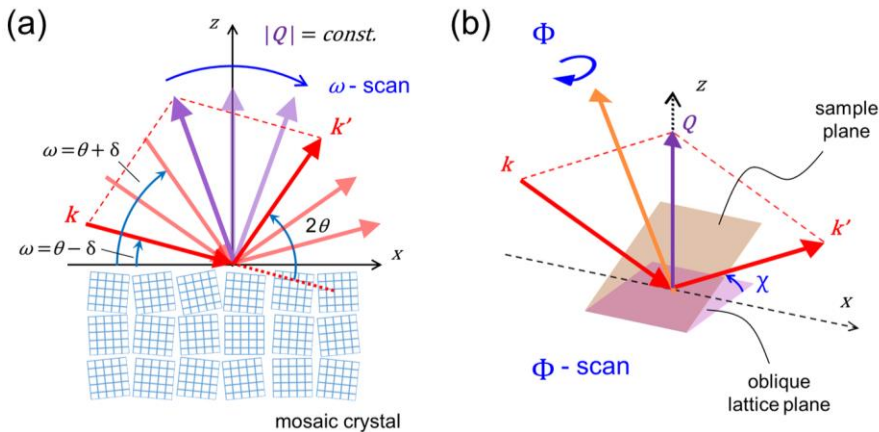


**Fig. 2.12:** Schematic representation of (a) rocking curve or  $\omega$ -scan and (b) azimuthal or  $\Phi$ -scans.

In epitaxial films, the slight misalignment between grains is termed as mosaicity or mosaic spread [see Fig. 2.12(a)]. The mosaic spread can be quantified via the rocking curve scan that is schematically represented in Fig. 2.12(a). First, the source and detector arms are oriented at a symmetric  $\theta$ - $2\theta$  configuration matching the Bragg diffraction condition. Subsequently, the  $\omega$ -axis is scanned around this central position [e.g., from  $\omega - \delta$  to  $\omega + \delta$ , see Fig. 2.12(a)], while keeping the angle  $2\theta$  between source and detector unchanged. This scan thus enables matching the orientation of the  $\mathbf{Q}$  vector with grains that are slightly misoriented with respect to the sample plane. The obtained curve can be perceived as an orientation distribution function of crystallographic grains, commonly centered around the  $\omega = \theta$  value. The full width at half maximum (FWHM) of the peak can be regarded as the quantitative estimate of the average misorientation, thus being an indication of the crystalline quality of the sample.

### iii. Azimuthal scans ( $\Phi$ -scans)

The detection of prominent peaks in the  $\theta$ - $2\theta$  scans is generally not sufficient to prove epitaxy of a film, as this could still consist of crystallites that are very well oriented in the out-of-plane direction but randomly oriented in the film plane. In order to characterize the in-plane crystallographic grain alignment, it is necessary to evaluate a diffraction condition involving lattice planes that are oblique to the sample plane. A valid strategy to do so is depicted in Fig. 2.12(b). Here, the sample (previously glued to the sample stage) is tilted by an angle  $\chi$  with respect to the plane of incidence of x-rays (applying a rotation around the  $x$ -axis). The idea consists on setting the diffraction condition for an oblique lattice plane that is oriented at an angle  $\chi$  with respect to the sample plane. Upon correctly adjusting the  $\theta$ - $2\theta$  configuration for the diffraction condition, the measurement of x-ray intensity vs the azimuthal angle  $\Phi$  ( $\Phi$ -scan) reveals the existence of periodic peaks for in-plane oriented epitaxial films, with a periodicity corresponding to the multiplicity of equivalent lattice planes in the in-plane film direction. The FWHM value of the peaks is again indicative of the in-plane alignment quality.

## 2.3 Vibrating sample magnetometry

The technique termed as vibrating sample magnetometry (VSM) allows the determination of the magnetic moment of samples, including thin films. Within this experimental setting, the sample is attached to a nonmagnetic rod, which oscillates or vibrates in an air gap between two pairs of fixed coils (termed as *pick-up coils*), as can be seen in Fig. 2.13(a) [118].

## 2. Experimental techniques

The idea behind this procedure is that the stray magnetic field arising from the magnetized sample moves together with the sample, thus producing an oscillatory, time-varying magnetic flux in the coils. The way to read the magnetization of the sample consists in tracking the voltage generated by the time-dependent magnetic flux in the coils, which is proportional to the magnetization value by virtue of Faraday's induction. The absolute scale of magnetization and the corresponding voltage calibration is done by means of a reference sample, which in our case consists of a bulk yttrium iron garnet sphere. The vibrating rod and the attached sample can be placed in an environment equipped with an electromagnet or even with a variable temperature option, such as in an oven or a cryostat. The sequential measurement of the magnetic moment of the sample in a variable applied magnetic field or temperature thus enables reconstructing field- and temperature-dependent magnetization curves (upon the knowledge of the sample volume or weight), which is an important asset in nanomagnetism.

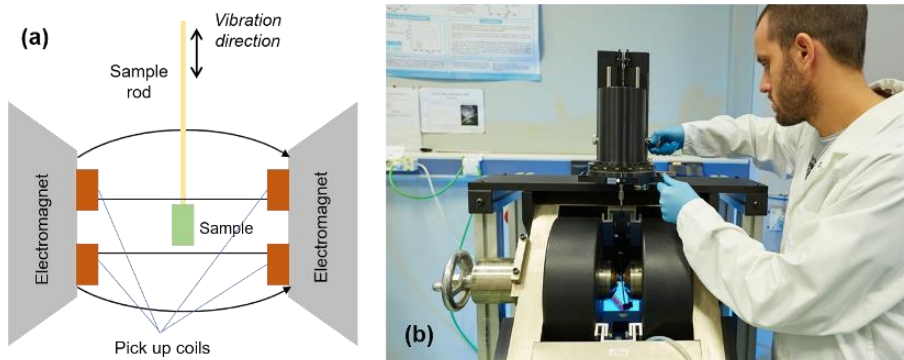


**Fig. 2.13:** (a) Schematic of the operation of the VSM method. (b) Picture of the VSM system at CIC nanoGUNE.

The VSM system at CIC nanoGUNE is a commercial *MicroMag™ Model 3900 VSM* tool from *Princeton Measurement Corporation* [see Fig. 2.13(b)], a high sensitivity instrument which can measure magnetic moments down to  $0.5 \mu\text{emu}$  upon averaging 1 second per retrieved data point. It is also equipped with an electromagnet that can apply an external magnetic field up to  $\pm 1.8 \text{ T}$  during the measurement, in order to modify the magnetic state of the sample and characterize magnetization reversal processes. The rod can be rotated around its axis in an automated way, such that the angle between the sample and the externally applied field axis can be rotated by a full  $360^\circ$ . When measuring thin films or multilayers, this allows varying the applied field angle (i) within the sample plane, or (ii) between the in-plane and out-of-plane orientations, by an appropriate choice of the sample holder.

While only room temperature measurements have been performed with the VSM tool for the results presented in this thesis, the system is also equipped with a furnace that allows magnetization measurements up to a maximum temperature of 800°C in a helium gas environment.

## 2.4 Spectroscopic ellipsometry

Ellipsometry is an optical technique for the investigation of optical (or dielectric) properties of materials. It consists of the measurement of the polarization state of light upon reflection (or transmission) from a sample and its name originates from the most common polarization state of light that ellipsometry aims to determine, namely the *elliptical* polarization state [119]. Ellipsometry is a useful and high precision tool for the determination of the physical parameters belonging to the sample under study. The experimentally accessible quantities are most often summarized by two real parameters that are defined via the complex reflectance ratio

$$\frac{r_p}{r_s} = \tan \Psi e^{i\Delta}, \quad (2.6)$$

which are namely the amplitude ratio  $\tan \Psi$  and phase shift  $\cos \Delta$ . In the above equation,  $r_p$  and  $r_s$  are the Fresnel reflection coefficients for the  $p$ - and  $s$ -polarization components of the electric field of light, which are parallel and perpendicular to the plane of incidence, respectively. Upon building an appropriate optical model of the sample under study, these experimentally determined quantities can be directly compared to the model outcome, giving a way to extract the best-match model fit for quantities such as the layer thickness, refractive index, roughness, composition or even the crystalline texture and orientation of the samples [119].

In *spectroscopic ellipsometry*, the polarization detection scheme is combined with a multiple wavelength measurement procedure. The ellipsometer is then equipped with a broad-band or tunable wavelength light source enabling measurements from the near infrared, across the visible light part of the spectrum, to the ultraviolet<sup>20</sup>. In particular, the *GES5-SEMILAB* ellipsometer at CIC nanoGUNE has a broad-band light source (230-900 nm) and a detector consisting of a spectroscopic unit detecting all wavelengths simultaneously.

---

<sup>20</sup> Nowadays, commercially available instruments include spectroscopic ellipsometry realizations from the ultraviolet to the mid-infrared region of the electromagnetic spectrum. Implementation in the Terahertz spectral range have also been demonstrated [120].

## 2. Experimental techniques

The schematic in Fig. 2.14(a) represents the measurement procedure. In ellipsometry, large angles of incidence (e.g.,  $\theta \sim 50^\circ\text{-}75^\circ$ ) are usually convenient, due to the increasing difference in the  $r_p$  and  $r_s$  Fresnel reflectivity terms upon increasing  $\theta$ . The light coming out from the broad-band source passes through a linear polarizer, such that the light incident on the sample has a well-defined polarization state. The linearly polarized beam is then reflected by the sample, with the reflected polarization becoming elliptic in the most general case. To measure the change in polarization a rotating compensator together with a fixed analyzer are utilized. The amount of light allowed to reach the detector will depend on the orientation of the compensator, an information that will then be compared to the already known input polarization to determine the polarization change upon reflection.

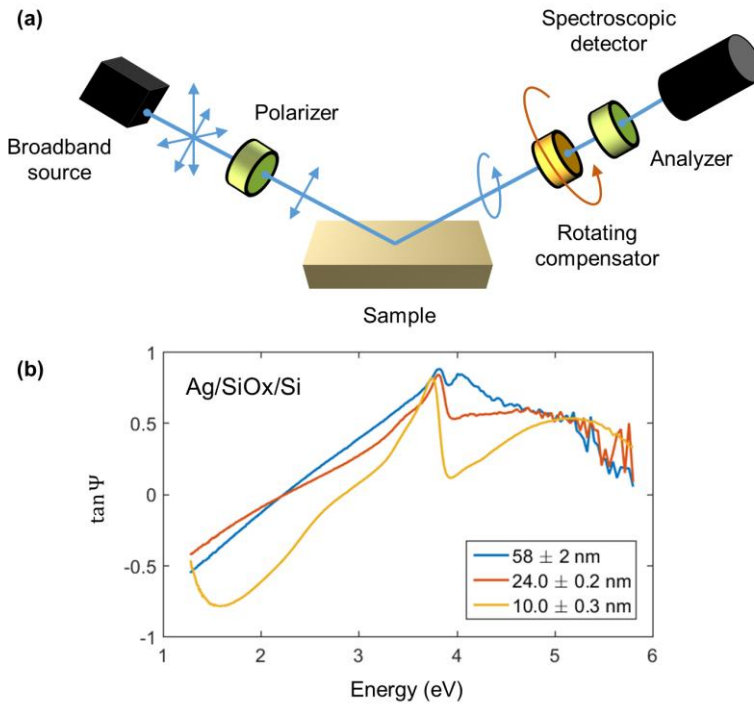


**Fig. 2.14:** (a) Schematic of the spectroscopic ellipsometry setup. The ellipsometer is equipped with a broad-band light source ranging from the near infrared to the ultraviolet, a polarizer, a rotating compensator, an analyzer and a spectroscopic detector. (b) displays spectroscopic measurements acquired at an angle of incidence of  $75^\circ$ , where the amplitude ratio  $\tan \Psi$  is shown at three different positions of a Ag-wedge grown on an elongated Si substrate. By making use of an optical model, I concluded that the Ag thickness at these three positions correspond to  $58 \pm 2$ ,  $24 \pm 0.2$  and  $10 \pm 0.3$  nm. The feature visible in the data at approximately 3.8 eV corresponds to the plasmonic resonance of Ag [121].

In this thesis, I have employed the spectroscopic ellipsometry technique for the thickness and structure determination of thin film and multilayer systems, as well as to extract the refractive index of deposited metallic and dielectric films. The optical properties (e.g. absorption) are highly dependent on film microstructure, such that refractive index values in thin films and multilayers structures may substantially differ from the bulk values reported in the literature. The tool has also been utilized to characterize material systems with uniaxial optical anisotropy by implementing a sample holder with azimuthal rotation capabilities.

The ellipsometer employed in this thesis can also perform automated position-dependent measurements with sub-mm resolution, which enabled the detailed thickness profile determination of the wedge-type samples that have been described in Section 2.1 (see Fig. 2.5). Spectroscopic ellipsometry was particularly beneficial in the case of obtaining the thickness profiles of Ag wedge-type samples, as this material possesses a distinctive plasmonic resonance at a photon energy of 3.8 eV, with the spectral feature being highly film thickness dependent [see Fig. 2.14(b)].



## Chapter 3

# Generalized magneto-optical ellipsometry as a tool for vector magnetometry

*The generalized magneto-optical ellipsometry (GME) technique is presented, with special focus on its capabilities for vector magnetometry and characterization of the magnetization reversal process. After a short review on preceding literature about magneto-optical ellipsometry, our experimental setup and measurement procedure are presented. Together with this, the consequences of the existence of optical anisotropy are identified, which may lead to an erroneous interpretation of the retrieved magneto-optical signal. The core part of the chapter is centered in demonstrating the three-dimensional vector magnetometry option of the GME technique, which results in an unprecedented precision for the determination of the magnetization angles.*

### 3.1 Introduction: review of magneto-optical ellipsometry

When aiming to investigate the optical properties of matter, the problem is usually directed towards experimentally determining the electromagnetic dielectric tensor of the material. This is often done via light reflection experiments, in which the experimentally accessible parameters encompass the polarization dependent reflectivity elements, embodied in the Fresnel coefficients. The most common technique for retrieving those is ellipsometry, which is based on the measurement of the polarization changes of light upon reflection from the sample. Ellipsometry has demonstrated to be a precise and efficient tool to retrieve not only the optical constants of a material, but also to characterize the structural details of objects such as multilayer stacks [119, 122]. In addition, it is a conceptually simple, non-invasive technique with a high versatility for its implementation.

In particular, the Generalized Ellipsometry approach is based on measuring the full reflection matrix of the sample and thus obtaining the optical constants of the

materials of interest. On the other hand, (ferro)-magnetic materials often display magneto-optical activity, which means that their optical properties and in turn their dielectric tensor as well as reflection matrix depend on magnetization. This leads to the magneto-optical Faraday and Kerr effects, phenomena which are being utilized to obtain information on the magnetization behavior of these materials, achieved by measuring their transmission or reflection properties while modifying their magnetization state.

It seems reasonable to attempt the determination of all parameters in the dielectric tensor, which in turn describe the entirety of optical properties of the material, including the purely optical activity as well as magneto-optical effects. Previously, this was usually done by two independent experiments, in which ellipsometry and magneto-optical methods were combined but separately performed. Specifically, one would measure the optical properties of the sample first by using an ellipsometric approach, and subsequently perform a magneto-optical experiment [123, 124]. In addition, early reports determining the dielectric tensor of a material including magneto-optical effects concentrated on a single Kerr geometry, accounting only for longitudinal or polar effects [125-127].

Correspondingly, Berger and Puffall devised a new method by reconsidering the problem of optical reflection from a ferromagnetic sample, in a technique termed as Generalized Magneto-optical Ellipsometry (GME) [84]. Within their approach, they solved the problem of determining the full reflection matrix of a sample featuring magneto-optical activity, by using a single experimental setup as well as a single measurement and analysis scheme. Furthermore, its implementation is not only independent from the initial knowledge of the magnetization orientation, but also allows the determination of the magnetization vector with very high precision [128]. The GME technique emerged as a powerful tool to investigate the optical, magneto-optical as well as magnetic properties of materials. Upon measurement of the full reflection matrix, one can recover the dielectric tensor elements of the material by devising an appropriate optical model of the sample and searching for the best-match model that fits the experimentally determined reflection matrix. A decade before the development of the GME methodology, Višňovský formulated the equations describing electromagnetic reflection and transmission from layered media [72] based on the seminal work of Yeh, which developed a  $4 \times 4$  matrix method to describe light propagation in optically anisotropic layered media [129]. This provided the mathematical formulation to obtain the reflection matrix of any planar medium by consideration of the dielectric tensor information of each stratum in the media. This set the grounds for magneto-optical ellipsometry, hence making GME equally applicable to bulk-like samples as well as to thin films and multilayered structures.

Since its first experimental realization, several implementations of the GME technique have been realized. Apart from its utilization for the study of magnetization reversal processes [130], it has also been employed, for instance, for the study of the temperature-dependent presence of spin-polarized electronic carriers in multiferroic materials [131, 132]. Some other works have also extended the description of the GME technique to account for depolarization effects, by utilizing the Müller matrix formalism<sup>21</sup> [133]. This approach is especially useful for the study of non-planar surfaces, where polarization is not conserved, as in the case of slanted columnar metallic media [134-136]. Throughout this thesis, polarization conservation will be always assumed and hence the Jones matrix formalism will be employed.

While magneto-optical measurement methods constitute a powerful and straightforward way to obtain component-resolved magnetization information (i.e., retrieving proportional signals to  $m_x$ ,  $m_y$  and  $m_z$ ), only a few selected MOKE studies follow a rigorous approach performing an actual vector magnetometry analysis [83, 85, 137-143] in addition to GME-type measurements. While GME showed to be a most appropriate method for this purpose, we believe that there is still a lot of room for improvement and exploration of its capabilities. This idea originates from the essence of the GME technique itself, consisting on revealing the entire reflection matrix of the sample, which entails the maximum amount of information that can be obtained from a polarization dependent optical reflection experiment. Here, we intend to take maximum advantage of the vector magnetometry capabilities of the GME technique, with the aim of obtaining a deeper insight from the optical and magneto-optical response of magnetic thin film and multilayers, as well as from the fine features of their magnetization reversal processes. We will see that GME will provide an excellent way to do so. In particular, we will demonstrate an unprecedented precision of the determined magnetization orientation, which originates from the strategic use that GME makes from the polarization dependent symmetry specificity of each of the Kerr geometries, namely, the longitudinal, transverse and polar Kerr effects.

Generally, the requirement of high precision implies a far larger number of measurements as well as a more elaborate analysis than in the case of conventional MOKE related techniques. However, this apparent disadvantage is promptly compensated by the large amount of information that is obtained within the GME methodology. Besides, we will also implement a dataset optimization study in the present chapter, in order to promote an efficient use of the measurement time. Successively, we will demonstrate the vector magnetometry capability in a variety of

---

<sup>21</sup>A data analysis procedure taking advantage of the full information in magneto-optical ellipsometry using the Müller matrix formalism, however, has not been developed so far.

thin film systems. In general, uniform states of magnetization will be assumed throughout this chapter. Obtaining information on the multi-domain structure at the microscale via MOKE signals is a challenging problem [144] and often only possible by measuring diffracted MOKE signals [93, 145]. However, GME also provides a way to estimate the relative variation of the magnetization modulus upon formation of non-uniform magnetization states during reversal [128].

Altogether, the material presented in this chapter will serve as a guide for the investigations presented in the subsequent chapters, where GME will act as the central magnetometry characterization tool.

## 3.2 Experimental setup and measurement procedure

First, the details of the experimental setup as well as the measurement procedure associated with the GME methodology are described. The practices and methods defined here will be useful for all the forthcoming chapters of this thesis.

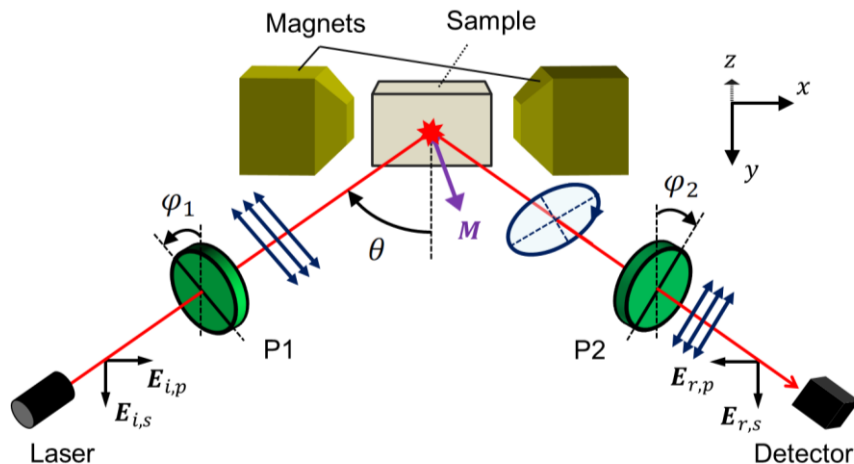


**Fig. 3.1:** Schematic of the GME setup utilized in this thesis. It consists on an optical measurement system containing a continuous wave laser, two polarizers (P1 and P2), and a photodetector. An electromagnet is used for modifying the magnetization state of the sample. The inset describes the Cartesian axes as they are defined for reflection the experiment.

A schematic view of the GME setup is depicted in Fig. 3.1. The light source consists of a continuous wave laser incident at an angle  $\theta$  onto the sample. The light passes first a linear polarizer (P1) mounted on a rotation stage, is reflected by the sample and goes through a second rotatable polarizer (P2), working as an analyzer, before reaching the photodetector. If we define the sample surface as the  $xy$  plane in the

Cartesian coordinate system of the reflection experiment, then the plane of incidence is the  $xz$  plane (see inset in Fig. 3.1). The orientations of the rotatable linear polarizers P1 and P2 are described by the angles  $\varphi_1$  and  $\varphi_2$ , defined as the counterclockwise deviations of the polarizing axis from the  $s$ -polarization orientation, when looking from the direction along the optical path. The sample is placed on a holder in the midst of an electromagnet, in order to modify its magnetization state via applied magnetic fields.

Within this setup, the electric field  $E_D$  of light arriving at the detector can be computed by using the Jones matrix formalism [67]. This is done by subsequently multiplying the  $2 \times 2$  operator matrices of the optical elements in the setup to the incident electric field  $E_I$ , such that

$$E_D = P2 \cdot R \cdot P1 \cdot E_I, \quad (3.1)$$

where the matrices  $P1$  and  $P2$  corresponding to the linear polarizers are defined as

$$P_i = \begin{pmatrix} \cos^2 \varphi_i & \cos \varphi_i \sin \varphi_i \\ \cos \varphi_i \sin \varphi_i & \sin^2 \varphi_i \end{pmatrix}, \quad (3.2)$$

while the reflection matrix  $R$  of the sample, on the basis of  $s$ - and  $p$ -polarization states, reads as [69-71]

$$R = \begin{pmatrix} r_{ss} & r_{sp} \\ r_{ps} & r_{pp} \end{pmatrix} = \begin{pmatrix} r_s & \alpha + \gamma \\ -\alpha + \gamma & r_p + \beta \end{pmatrix} = r_p \begin{pmatrix} \tilde{r}_s & \tilde{\alpha} + \tilde{\gamma} \\ -\tilde{\alpha} + \tilde{\gamma} & 1 + \tilde{\beta} \end{pmatrix} = r_p \tilde{R}. \quad (3.3)$$

In the above equation,  $r_s$  and  $r_p$  are the purely optical reflectivity coefficients with respect to incident and reflected light waves with  $s$ - and  $p$ -polarized light, respectively. In addition, the complex quantities  $\alpha$ ,  $\beta$  and  $\gamma$  correspond to the magnetically induced elements of the reflection matrix associated to the longitudinal, transverse and polar Kerr effects, at the same time proportional to the normalized magnetization components  $m_x$ ,  $m_y$  and  $m_z$ , respectively. Unless otherwise stated, uniform states of magnetization will only be considered. In a reflection experiment, the matrix  $R$  can only be determined up to a complex multiplication constant. For this reason, the reduced reflection matrix  $\tilde{R}$  and the reduced matrix elements  $\tilde{r}_s$ ,  $\tilde{\alpha}$ ,  $\tilde{\beta}$  and  $\tilde{\gamma}$  will be utilized from now on (see Eq. 3.3). Upon consideration of linear magneto-optical Kerr effects alone, we assume that the magnetically induced elements  $\tilde{\alpha}$ ,  $\tilde{\beta}$  and  $\tilde{\gamma}$  change the sign upon spatial inversion of the magnetization, which is how one can experimentally distinguish them from the purely optical complex factor  $\tilde{r}_s$ . Given that magneto-optical Kerr effects are small compared to the purely optical reflectivity terms of the materials studied throughout this

thesis, it is expected that the elements  $\tilde{\alpha}$ ,  $\tilde{\beta}$  and  $\tilde{\gamma}$  are at least two to four orders of magnitude smaller than  $\tilde{r}_s$ . Here, it is worth to underline that under the absence of any other birefringent optical activity, the only source for intermixing the  $s$ - and  $p$ -polarization states of light upon reflection arises from either the longitudinal ( $\tilde{\alpha}$ ) or polar ( $\tilde{\gamma}$ ) magneto-optical activity.

Once the multiplications in Eq. 3.1 have been done in order to obtain the electric field  $E_D$  at the photodetector, the corresponding intensity function for an arbitrary magnetization orientation is obtained as

$$I = E_D^* \cdot E_D, \quad (3.4)$$

which is now related to an experimentally measurable quantity. A minimum number of three measurements at different incoming light polarizations are needed to fully determine the reduced reflection matrix  $\tilde{R}$  [84, 119]. This is achieved in the setup presented in Fig. 3.1 by acquiring intensity data for different  $(\varphi_1, \varphi_2)$  orientation configurations of the rotatable polarizers.

By recalling the time reversal symmetry for ferromagnetic materials, we have that  $\mathbf{M}(\mathbf{H}) = -\mathbf{M}(-\mathbf{H})$ , and hence we assume that the magnetically induced reflection matrix elements  $\tilde{\alpha}$ ,  $\tilde{\beta}$  and  $\tilde{\gamma}$  change the sign upon inverse applied magnetic field values corresponding to a different field cycling history<sup>22</sup>. Thus, one can express the fractional intensity change<sup>23</sup> at the applied field  $H$  upon magnetization reversal as [84]

$$\frac{\delta I}{I}(\varphi_1, \varphi_2) = \frac{I(+H) - I(-H)}{[I(+H) + I(-H)]/2} = 4 \frac{B_1 f_1 + B_2 f_2 + B_3 f_3 + B_4 f_4 + B_5 f_5 + B_6 f_6}{f_3 + B_7 f_7 + 2B_8 f_4 + I_0}, \quad (3.5)$$

which is a quantity that depends on the reflection matrix elements via the  $B_i$  parameters

$$\begin{aligned} B_1 &= \text{Re}(\tilde{\alpha}) & B_2 &= \text{Re}(\tilde{r}_s \cdot \tilde{\alpha}^*) \\ B_3 &= \text{Re}(\tilde{\beta}) & B_4 &= \text{Re}(\tilde{r}_s \cdot \tilde{\beta}^*) \\ B_5 &= \text{Re}(\tilde{\gamma}) & B_6 &= \text{Re}(\tilde{r}_s \cdot \tilde{\gamma}^*) \\ B_7 &= |\tilde{r}_s|^2 & B_8 &= \text{Re}(\tilde{r}_s), \end{aligned} \quad (3.6)$$

---

<sup>22</sup> Meaning for complementary magnetic field cycles corresponding to the decreasing and increasing field branches.

<sup>23</sup> For the full derivation, see Appendix II of this thesis.

as well as on the polarizer angles  $\varphi_1$  and  $\varphi_2$ , via the following  $f_i$  functions

$$\begin{aligned}
 f_1(\varphi_1, \varphi_2) &= \sin^2 \varphi_1 \sin \varphi_2 \cos \varphi_2 - \sin^2 \varphi_2 \sin \varphi_1 \cos \varphi_1 \\
 f_2(\varphi_1, \varphi_2) &= \cos^2 \varphi_2 \sin \varphi_1 \cos \varphi_1 - \cos^2 \varphi_1 \sin \varphi_2 \cos \varphi_2 \\
 f_3(\varphi_1, \varphi_2) &= \sin^2 \varphi_1 \sin^2 \varphi_2 \\
 f_4(\varphi_1, \varphi_2) &= \sin \varphi_1 \cos \varphi_1 \sin \varphi_2 \cos \varphi_2 \\
 f_5(\varphi_1, \varphi_2) &= \sin^2 \varphi_1 \sin \varphi_2 \cos \varphi_2 + \sin^2 \varphi_2 \sin \varphi_1 \cos \varphi_1 \\
 f_6(\varphi_1, \varphi_2) &= \cos^2 \varphi_2 \sin \varphi_1 \cos \varphi_1 + \cos^2 \varphi_1 \sin \varphi_2 \cos \varphi_2 \\
 f_7(\varphi_1, \varphi_2) &= \cos^2 \varphi_1 \cos^2 \varphi_2.
 \end{aligned}
 \tag{3.7}$$

At the same time, the quantity  $I_0$  in the denominator of Eq. 3.5 is introduced in order to account for the background intensity offset in the experiment, as it is experimentally inaccessible to measure a zero intensity value at the photodetector<sup>24</sup>.

Thus one can now measure the intensities at the inverted applied field values  $H$  and  $-H$  for a given polarizer orientation configuration  $(\varphi_1, \varphi_2)$ . The evaluation of the experimentally obtained  $\delta I/I$  values according to Eq. 3.5 enables the determination of the  $B_i$  parameters and hence of the reflection matrix elements. This constitutes one of the main strengths of the GME technique, by which the access to the optical, magneto-optical and magnetic properties of the sample is obtained without prior knowledge of the three-dimensional magnetization orientation.

The methodology to obtain the fractional intensity change  $\delta I/I$  at an applied field  $H$  is sketched in Fig. 3.2. Intensity vs applied field cycles for different the polarizer orientations  $(\varphi_1, \varphi_2)$  are measured. The variation of the applied magnetic field will generally cause a modification of the magnetization state in the sample, which in turn modifies the magnetically induced reflection matrix elements and hence the measured intensity at the photodetector. Thus upon measuring a field cycle for each  $(\varphi_1, \varphi_2)$  pair, the light intensity at the applied fields  $H$  and  $-H$  during the decreasing and increasing field branches are picked for computing the  $\delta I/I$  value.

---

<sup>24</sup> According to Eq. 3.2, which assumes perfect polarizer efficiencies, a zero value of the sum intensity  $I(+H) + I(-H)$  should be measured for configurations  $(\varphi_1, \varphi_2) = (0^\circ, 90^\circ)$  and  $(90^\circ, 0^\circ)$ , which correspond to crossed polarizer arrangements of P1 and P2. However, a number of experimental imperfections, such as the finite polarizer efficiency, the effect of the ambient light or the contribution from dark-currents to the voltage measured at the photodetector, require the consideration of the parameter  $I_0$  at the denominator of the  $\delta I/I$  expression. For an extended discussion, see Appendix II.

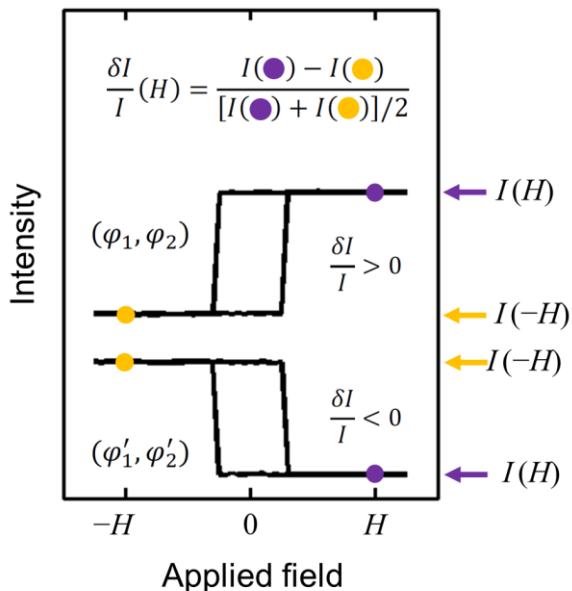


**Fig. 3.2:** Schematic representation of the  $\delta I/I$  quantity construction. The intensities at applied fields  $H$  and  $-H$  are subtracted and this quantity is divided by the half of their sum. The schematic displays simulated hysteresis cycles for two arbitrary polarizer orientation configurations  $(\varphi_1, \varphi_2)$  and  $(\varphi'_1, \varphi'_2)$ , giving rise to a positive and negative  $\delta I/I$  value at  $H$ , respectively.

The subtraction in the numerator of the  $\delta I/I$  expression in Eq. 3.5 implies that second-order magneto-optical Kerr effects arising from bilinear multiplication terms of  $\tilde{\alpha}$ ,  $\tilde{\beta}$  and  $\tilde{\gamma}$  are inherently removed during the GME data analysis procedure, thus avoiding further complications to interpret the measure data<sup>25</sup>.

In order to illustrate the character of the  $B_i$  parameters, we compute them here for a semi-infinite permalloy ( $\text{Ni}_{80}\text{Fe}_{20}$ ) slab at a light wavelength of  $\lambda = 635$  nm. The polarization dependent Fresnel coefficients are calculated assuming a  $\theta = 45^\circ$  angle of incidence, a refractive index of  $N = 1.88 + 3.62i$  and a magneto-optical coupling factor amounting to  $Q = 0.014 - 0.012i$  [131]. The results are summarized in Table 3.1, where the  $B_i$  parameters for the particular cases in which the magnetization is oriented along the  $x$ -,  $y$ - and  $z$ -axis are included.

<sup>25</sup>The presence of second order Kerr effects cannot be completely removed from the denominator in the  $\delta I/I$  expression, even if their relevance is less important for the data analysis path proposed here.

When the magnetization is aligned with the  $x$ -axis, the only non-zero magneto-optical parameters are  $B_1$  and  $B_2$ , which are related to the longitudinal Kerr effect. For magnetization orientations along the  $y$ - and  $z$ -axis, only the transverse Kerr parameters  $B_3$  and  $B_4$  or the polar Kerr parameters  $B_5$  and  $B_6$  are different from zero, respectively. Under this observation, one can anticipate that the magneto-optical parameters  $B_1$  to  $B_6$  acquire in general a finite value for an arbitrary magnetization orientation with non-zero magnetization components  $m_x$ ,  $m_y$  and  $m_z$ . Finally, the parameters  $B_7$  and  $B_8$ , which are related to the purely optical reflectivity response of the sample, possess the same value for all magnetization orientations (see Table 3.1). Their value is approximately two to four orders of magnitude larger than the magneto-optical parameters, which confirms that (at least for materials and experimental conditions considered throughout this thesis) Kerr effects are small compared to the purely optical reflectivity response of the sample.

$B_i$ parameters		$\mathbf{M} \parallel Ox$	$\mathbf{M} \parallel Oy$	$\mathbf{M} \parallel -Oz$
<i>Longitudinal Kerr</i>	$B_1 (10^{-4})$	-0.94	0	0
	$B_2 (10^{-4})$	3.30	0	0
<i>Transverse Kerr</i>	$B_3 (10^{-4})$	0	-4.60	0
	$B_4 (10^{-4})$	0	10.73	0
<i>Polar Kerr</i>	$B_5 (10^{-4})$	0	0	28.73
	$B_6 (10^{-4})$	0	0	-36.36
<i>Optical activity</i>	$B_7$	1.43	1.43	1.43
	$B_8$	-1.13	-1.13	-1.13

**Table 3.1:** Calculated reflection matrix elements  $B_1 - B_8$  for magnetization orientations along the  $x$ -,  $y$ - and  $z$ -axis for a semi-infinite permalloy slab at an angle of incidence of  $\theta = 45^\circ$  and a wavelength of  $\lambda = 635$  nm.

An additional aspect to point out in Table 3.1 consists on the fact that the polar Kerr parameters  $B_5$  and  $B_6$  are almost one order of magnitude larger than the longitudinal and transverse parameters. While this aspect largely depends on the angle of incidence employed in the experiment, the maximum amplitude of polar Kerr effects is commonly larger than the amplitudes associated with longitudinal and transverse effects [71].

### ***Kerr geometry dependent symmetry of the $\delta I/I(\varphi_1, \varphi_2)$ function***

The dependence of the  $\delta I/I$  expression on the polarizer angles  $\varphi_1$  and  $\varphi_2$  is studied in this section. This is equivalent to evaluating the symmetry of the  $f_i$  functions that are introduced in the  $\delta I/I$  expression (Eq. 3.7). By mere inspection of the reflection matrix in Eq. 3.3, it is clear that the three different Kerr geometries should exhibit distinct features in their dependency with respect to polarizer orientations in the experiment. In order to unveil the specific dependencies, we simulated  $\delta I/I$  datasets in a wide range of  $(\varphi_1, \varphi_2)$  configurations corresponding to the longitudinal, transverse or polar Kerr effects alone, which read as

$$\begin{aligned} \left(\frac{\delta I}{I}\right)^{lon} &= 4 \frac{B_1 f_1 + B_2 f_2}{f_3 + B_7 f_7 + 2B_8 f_4 + I_0} \\ \left(\frac{\delta I}{I}\right)^{trans} &= 4 \frac{B_3 f_3 + B_4 f_4}{f_3 + B_7 f_7 + 2B_8 f_4 + I_0} \\ \left(\frac{\delta I}{I}\right)^{pol} &= 4 \frac{B_5 f_5 + B_6 f_6}{f_3 + B_7 f_7 + 2B_8 f_4 + I_0}. \end{aligned} \tag{3.8}$$

where the  $B_i$  parameters in Table 3.1 and an intensity offset  $I_0 = 5 \cdot 10^{-4}$  were assumed.

Figs. 3.3(a)-3.3(c) show color-coded  $\delta I/I$  maps for all possible orientations of  $\varphi_1$  and  $\varphi_2$  under the presence of a longitudinal, transverse or polar magnetization components [see schematic in Fig. 3.3(g)]. All  $\delta I/I$  patterns depicted here possess a  $180^\circ$  periodicity in  $\varphi_1$  and  $\varphi_2$ , as expected from the uniaxial rotation symmetry of a linear polarizer. For all three maps, the maximum absolute value of the  $\delta I/I$  quantity can generally be found near the diagonal lines at which the polarizers P1 and P2 are perpendicular to each other, according to the relation  $\varphi_1 = -\varphi_2 \pm 90^\circ$ . In fact it is along these symmetry lines where the denominator in  $\delta I/I$  (Eq. 3.5) acquires its minimum values (see Fig. 3.4), which partially boost the  $\delta I/I$  quantity. Despite these similarities, each  $\delta I/I$  map associated to a different Kerr geometry exhibits distinct features in their dependence with respect to  $\varphi_1$  and  $\varphi_2$ . For instance, the longitudinal and polar Kerr  $\delta I/I$  maps [Figs. 3.3(a) and 3.3(c)] display non-zero  $\delta I/I$  values in the near region of crossed polarizer configurations in which either P1 or P2 is aligned with the plane of incidence, such as  $(\varphi_1, \varphi_2) = \{(90^\circ, 0^\circ), (0^\circ, 90^\circ), (-90^\circ, 0^\circ), (90^\circ, 180^\circ)\}$ . Opposite to this, the transverse  $\delta I/I$  map acquires its maximum absolute values at crossed polarizer configurations in which the polarizers are  $45^\circ$  away from the plane of incidence, such that  $(\varphi_1, \varphi_2) = \{(45^\circ, -45^\circ), (45^\circ, 135^\circ)\}$ . Even if transverse Kerr effects are typically measured using incident  $p$ -polarized light and then evaluating the

$p$ -polarized amplitude of reflected light [138], the map in Fig. 3.3(b) indicates that this configuration  $[(\varphi_1, \varphi_2) = (90^\circ, 90^\circ)]$  does not give rise to the maximum transverse Kerr signals. The incident  $p$ -polarization strategy, however, possess advantages such as the ability to null out any contribution from longitudinal and polar Kerr effects.

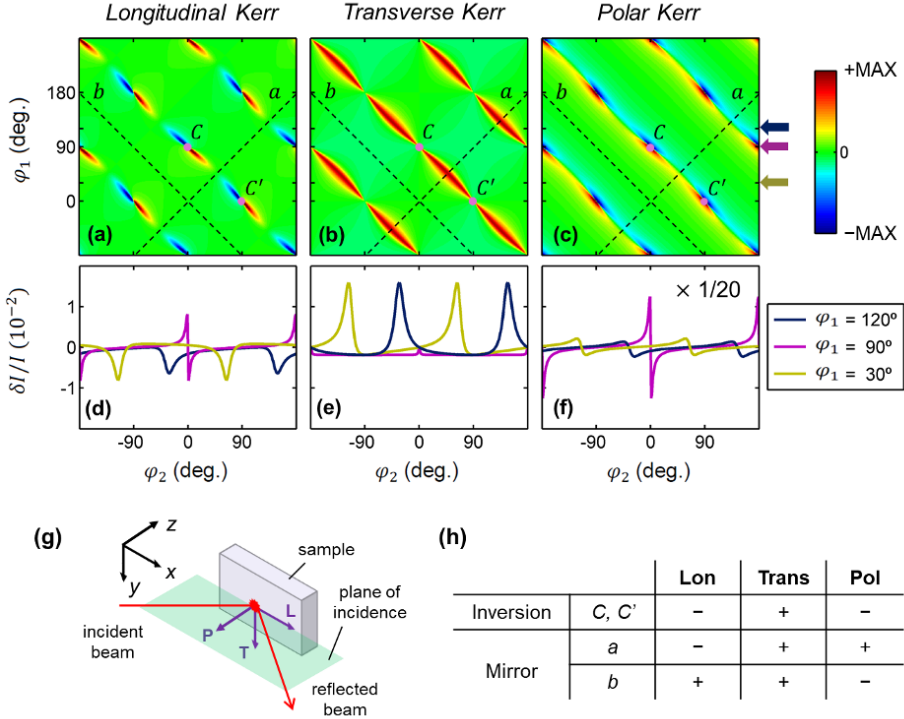


**Fig. 3.3:** Simulated color-coded  $\delta I/I$  maps vs polarizer orientations  $\varphi_1$  and  $\varphi_2$  for the (a) longitudinal, (b) transverse and (c) polar Kerr effects. The inversion symmetry points  $C$  and  $C'$  as well as the lines  $a$  and  $b$  are indicated in the maps. (d) - (f) show  $\delta I/I$  vs  $\varphi_2$  curves which correspond to horizontal cuts of the colormaps above at different  $\varphi_1$  values, depicted by the arrows in (c). (g) Schematic of the reflection experiment and definition of the longitudinal, transverse and polar magnetization orientations with respect to the plane of incidence. (h) Summary of symmetries with respect to inversion and mirror operations for each specific Kerr geometry.

The color coded  $\delta I/I$  maps for the longitudinal, transverse and polar Kerr effects can be individually classified according to few selected symmetry operations. We first define the symmetry point  $C$  located at  $(\varphi_1, \varphi_2) = (90^\circ, 0^\circ)$ . While the  $\delta I/I$  value corresponding to the longitudinal Kerr effect reverses its sign with respect to inversion operations about  $C$ , the value associated to the transverse Kerr effect remains the same

under the same operation [see Figs. 3.3(a) and 3.3(b)]. Thus, on the event of having a mixture of longitudinal and transverse Kerr effects, these can easily be separated by virtue of this distinct inversion symmetry, as long as sufficient  $\delta I/I$  data are measured around  $C$ . On the other hand, the polar Kerr effect [Fig. 3.3(c)] shares the same type of inversion symmetry about the point  $C$  with the longitudinal Kerr effect, by which the  $\delta I/I$  value reverses sign. Thus, in case of having simultaneous longitudinal and polar Kerr effects, these could not be discerned if measurements are only performed in a close proximity to the  $C$  symmetry point.

In order to overcome this difficulty, we examine symmetry operations in the  $(\varphi_1, \varphi_2)$  space that are non-equivalent for these two Kerr effects. In fact, one can observe that the longitudinal and polar Kerr effects possess opposite symmetries with respect to mirror operations with respect to lines  $a$  and  $b$  [see Figs. 3(a) - 3(c)]. Thus, it can be concluded that for cases in which an arbitrary orientation of magnetization exists in three dimensions, contributions from all three Kerr geometries can be separated if  $\delta I/I$  data is retrieved at sufficient polarizer orientation configurations  $(\varphi_1, \varphi_2)$  which according to the symmetry operations discussed above reflect the different symmetries with respect to each of the Kerr geometries.

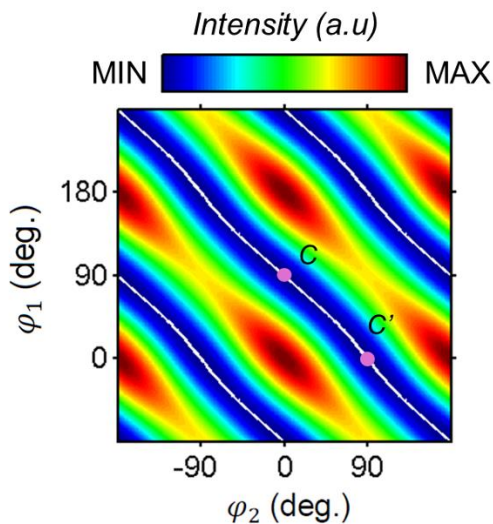


**Fig. 3.4:** Color-coded  $[I(+H) + I(-H)]$  intensity map with respect to polarizer angles  $\varphi_1$  and  $\varphi_2$ . The white ‘wiggling’ lines indicate the  $\varphi_1$  points at which the intensity is minimum for a fixed  $\varphi_2$ . These closely follow the diagonal lines  $\varphi_1 = -\varphi_2 \pm 90^\circ$  at which the polarizers have perpendicular orientations. The symmetry points  $C$  and  $C'$  are indicated.

As a plausible strategy, we propose here to measure  $\delta I/I(\varphi_1, \varphi_2)$  datasets around both inversion symmetry points  $C$  and  $C'$ , that is, around  $(\varphi_1, \varphi_2) = (90^\circ, 0^\circ)$  and  $(0^\circ, 90^\circ)$ . These lie at both sides of the mirror symmetry line  $a$  (see Fig. 3.3), hence providing a way to distinguish between longitudinal and polar Kerr effects<sup>26</sup>. In addition, the distinct inversion symmetry of the longitudinal (or polar) and transverse Kerr effects with respect to  $C$  as well as  $C'$  allows to separate all three Kerr geometries from one another. The symmetry properties of the longitudinal, transverse as well as polar Kerr geometries are summarized in the table depicted in Fig. 3.3(h).

While separating all three Kerr effects is possible by measuring a few selected datasets around (across) the symmetry points (lines) described above [139], the GME methodology employed in this thesis adopts the strategy of sampling relatively extensive regions of the  $(\varphi_1, \varphi_2)$  space, which enables differentiating specific magneto-optical contributions from noise and spurious signals, thus reaching an improved level of robustness and reliability.

### ***Experimental determination of the reflection matrix in a permalloy thin film***

For the purpose of demonstrating the feasibility of the mathematical formulation described above, we present GME measurements on an 80-nm-thick permalloy film that has been sputter deposited on top of an oxidized Si(100) substrate (see Fig. 3.5). Due to the thin-film geometry, we assume that the magnetization lies in the plane of the sample. This in turn implies that the parameters  $B_5$  and  $B_6$ , which are proportional to the polar magnetization component, are zero. Under this situation, the  $\delta I/I$  expression in Eq. 3.5 is reduced to

$$\frac{\delta I}{I}(\varphi_1, \varphi_2) = 4 \frac{B_1 f_1 + B_2 f_2 + B_3 f_3 + B_4 f_4}{f_3 + B_7 f_7 + 2B_8 f_4 + I_0}, \quad (3.9)$$

such that the remaining six  $B_i$  parameters determine the entire reflection matrix.

For the expression in Eq. 3.9 to be able to fit measured data, additional parameters that account for experimental imprecisions have to be included in the fitting process, apart from the previously mentioned intensity offset  $I_0$ . These are the polarizer orientation corrections  $\varphi_{10}$  and  $\varphi_{20}$ , accounting for slight deviations of the plane of incidence orientation with the nominal linear polarizer angles  $\varphi_1$  and  $\varphi_2$ . This means that the  $f_i$  functions must be modified as  $f_i(\varphi_1, \varphi_2) \rightarrow f_i(\varphi_1 - \varphi_{10}, \varphi_2 - \varphi_{20})$ , which

---

<sup>26</sup> The  $C$  and  $C'$  symmetry points will be subsequently named as the  $p/s$  and  $s/p$  crossing points of the polarizers.

is equivalent to introducing a translation of the  $\delta I/I$  map origin in the  $(\varphi_1, \varphi_2)$  coordinates. Hereby, the GME dataset analysis for in-plane magnetized materials consists on a nonlinear fitting process with nine fit parameters: six  $B_i$  parameters encompassing the reflection matrix and three additional parameters ( $I_0, \varphi_{10}, \varphi_{20}$ ) accounting for instrumental settings.

While it may seem that such a large amount of adjustable parameters could result into an unreliable fitting routine, the very different symmetry of the magneto-optical parameters  $B_i$  demonstrated in Fig. 3.3 ensures the correct separation of the longitudinal and transverse (as well as polar) Kerr effects in the  $\delta I/I$  expression, thus facilitating a relatively rapid convergence of the regression despite the large number of fit parameters. In the same way, the  $B_7$  and  $B_8$  parameters associated with the purely optical parameters, differ from the magnetically induced  $B_i$  in that they do not change sign upon magnetization reversal, such that they can also be separated.

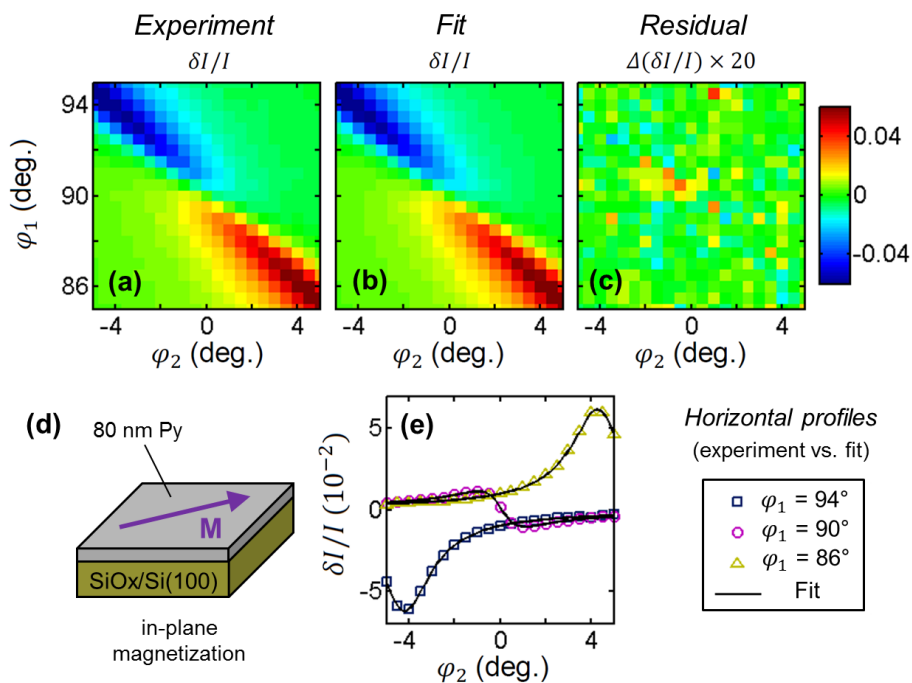


**Fig. 3.5:** (a) Measured and (b) fitted color-coded  $\delta I/I(\varphi_1, \varphi_2)$  datasets in the near region of the crossed polarizer configuration  $(\varphi_1, \varphi_2) = (90^\circ, 0^\circ)$  at  $H = 100$  Oe. A fit goodness of  $R^2 = 0.9997$  was achieved. (c) Residual of the  $\delta I/I$  maps, obtained upon subtraction of the experimental and fitted maps. All three colormaps in (a) – (c) share the same colorbar, for which the  $\Delta(\delta I/I)$  values have been multiplied by 20. (d) Schematic of the sample. (e) Measured  $\delta I/I$  vs  $\varphi_2$  line profiles for few selected  $\varphi_1$  values. The superimposed solid lines represent the fit outcome.

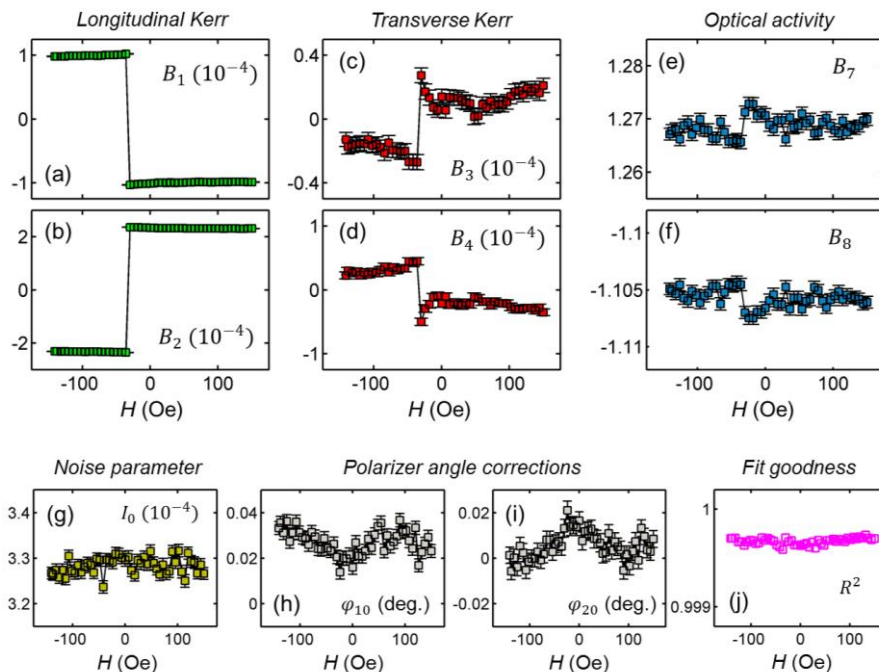
For retrieving the GME datasets, hysteresis loops in the range  $H = \pm 150$  Oe were measured for different polarizer orientation configurations. The measurements were done for a light source of  $\lambda = 635$  nm at a  $45^\circ$  angle of incidence. In particular, the data were measured around the  $C$  symmetry point named before as  $p/s$  crossing point, corresponding to incoming  $p$ - and outgoing  $s$ -polarization states,  $(\varphi_1, \varphi_2) = (90^\circ, 0^\circ)$ . We have chosen a polarizer angle grid of  $\varphi_1 \in [85^\circ, 95^\circ]$  and  $\varphi_2 \in [-5^\circ, 5^\circ]$ , with a polarizer angle step of  $\delta\varphi_i = 0.5^\circ$ . This yields a total of number of  $21 \times 21 = 441$  polarizer pair configurations and hence an equal number of hysteresis loop measurements. Under this choice of dataset, the mathematical problem of determining the reflection matrix is vastly overdetermined, while precision is gained due to the detailed mapping of the  $\delta I/I$  quantity in the  $(\varphi_1, \varphi_2)$  space.

Fig. 3.5(a) shows the experimental color-coded  $\delta I/I$   $(\varphi_1, \varphi_2)$  map built at a magnetic field value of  $H = 100$  Oe applied along the  $x$ -axis, which is sufficient to magnetically saturate the permalloy film. The dataset exhibits a maximum  $\delta I/I$  amplitude value of around 0.05. The  $\delta I/I$  pattern consists of two lobes of opposite sign that meet at the crossing point of the polarizers,  $(\varphi_1, \varphi_2) = (90^\circ, 0^\circ)$ , which we defined as the origin of the dataset. The resemblance with the symmetry properties described in Fig. 3.3 suggests that the strongest  $\delta I/I$  contribution is coming from the longitudinal Kerr effect, as expected from the applied field geometry. The colormap in Fig. 3.5(b) displays the fitted  $\delta I/I$  values according to Eq. 3.9, which correctly reproduces the experimental colormap in Fig. 3.5(a), with a fit goodness value of  $R^2 = 0.9997$ .

In order to better visualize how closely the fit reproduces the experimental data, the residual colormap  $\Delta(\delta I/I) = (\delta I/I)_{exp} - (\delta I/I)_{fit}$  was also plotted in Fig. 3.5(c). For a better comparison of the measured  $\delta I/I$  signal with residual weights, the latter quantity is multiplied by a factor of 20, employing the same color scale for all three colormaps in Figs. 3.5(a) - 3.5(c). The residuals consist of few scattered points deviating from zero value, reaching maximum values below 3% of the maximum measured  $\delta I/I$  signal. In addition, they are randomly distributed and do not show any recognizable pattern in the  $(\varphi_1, \varphi_2)$  space, thus concluding that the characteristic features described by the different Kerr geometries have been correctly fitted. Fig. 3.5(d) displays selected  $\delta I/I$  vs  $\varphi_2$  horizontal line cuts for  $\varphi_1 = 86^\circ, 90^\circ$  and  $94^\circ$ , which exhibit excellent agreement between the experimental data and the fit.

By repeating the procedure for different strengths of the applied magnetic field, one can study the magnetization reversal properties of the sample from the  $H$  dependence of the reflection matrix elements. The field dependence of all fitted  $B_i$  parameters is shown in Fig. 3.6 for the decreasing field branch of the hysteresis loop. The magneto-optical parameters  $B_1, B_2$  [Figs. 3.6(a), 3.6(b)], and  $B_3, B_4$  [Figs. 3.6(c),

3.6(d)] show a clear modulation upon magnetization reversal, due to their proportional character to the longitudinal ( $m_x$ ) and transverse ( $m_y$ ) magnetization components. On the other hand, the parameters  $B_7$ ,  $B_8$  [Figs. 3.6(e), 3.6(f)] do not show any substantial field dependent variation, given their magnetization independent character.



**Fig. 3.6:** Field dependence of the reflection matrix elements (a)  $B_1$ , (b)  $B_2$ , (c)  $B_3$ , (d)  $B_4$ , (e)  $B_7$  and (f)  $B_8$ , as well as of the experimental correction parameters (g)  $I_0$ , (h)  $\varphi_{10}$  and (i)  $\varphi_{20}$ , measured for a 80-nm-thick permalloy film. Error bars obtained in the fitting process are shown for all quantities in this figure. (j) Field dependence of the  $R^2$  fit goodness, for which all values lie above 0.9995.

Similarly, the background intensity parameter  $I_0$  [Fig. 3.6(g)] as well as the polarizer angle corrections  $\varphi_{10}$  and  $\varphi_{20}$  [Figs. 3.6(h) and 3.6(i)] also exhibit a field independent behavior, showing only minor variations comparable to their level of precision (error bars are indicated in all panels in Fig. 3.6). This is an important appreciation, as it confirms that the polarizer offsets allow for an automatic self-centering of the  $\delta I/I$  symmetry point during the fit process.

Finally, the quality of the fits is evidenced by their high  $R^2$  goodness values shown in Fig. 3.6(j), which lie above 0.9995 in the entire field region.

### ***GME setup geometries and technical specifications***

Depending on the type of properties of the sample in which we are interested in, we can conveniently choose between the two GME setup geometries developed in this thesis. These are based on the two different sample holders that either allow for: (i) *rotating* the sample about its surface normal, or (ii) *translating* the sample in the direction perpendicular to the plane of incidence. The schematic of the setup with the rotation stage for the sample holder is depicted in Fig. 3.7(a), while photographs of the actual setup are shown in Figs. 3.7(b) and 3.7(c). This setup will be useful for investigating the orientation dependent optical, magneto-optical and optical properties of the samples, such as magnetic, optical or magneto-optical anisotropies. On the other hand, the schematic and pictures of the setup with a linear translation stage are shown in Figs. 3.7(d) - 3.7(f). This configuration will be utilized for the study of wedge-like samples possessing a position dependent sample property such as composition or thickness.

We employed an ultra-low noise, continuous wave, diode laser module operating at  $\lambda = 635$  nm with an output power of 5 mW as the light source<sup>27</sup> (*Coherent, Inc.*). We also utilize two calcite Glan-Taylor, achromatic linear polarizers with an extinction ratio of 100 000:1 (*Thorlabs, Inc.*). These are mounted on a pair of motorized compact rotation stages (PR50CC by *Newport Corp.*), controlled by single-axis stepper motor controllers (SMC100 by *Newport Corp.*). For the light detection, a Si transimpedance amplified photodetector is used (*Thorlabs, Inc.*), in which a band-pass red filter ( $635 \pm 2$  nm) is placed in front of its window for getting rid of the majority of ambient light. It is worth to point out that no lock-in or light modulation techniques are employed for detection within this approach of the GME setup.

The sample holder rotation stage is based on custom-made aluminum parts mounted on a compact motorized rotary stage, identical to the ones used for rotating the Glan-Taylor polarizers. The sample is attached to the holder by pumping air through an orifice that is located at the holder edge. For the GME setup under the translation stage configuration, a travel stage with a travel range of 150 mm (*Thorlabs, Inc.*) is introduced in the setup, while the samples are placed in an aluminum holder attached to the translation stage via adhesive Kapton tape. Finally, the magnetic field is applied via a homemade electromagnet mounted on a high-load motorized rotary stage (*Zaber<sup>TM</sup>*). This stage allows for tilting the applied field axis from the  $x$ -axis (up to a maximum of  $\pm 30^\circ$ ). For the case of the setup with the linear translation stage, the magnet was mechanically fixed at a tilted position for allowing the clearance of the optical path with

---

<sup>27</sup> While not described in this chapter, an achromatic  $\lambda/4$  waveplate (*Thorlabs, Inc.*) is also utilized right in front of the laser light source. The purpose and arrangement of this optical element is thoroughly explained in Appendix II of this thesis.

### 3. Generalized magneto-optical ellipsometry (GME)

the sample stage through the space between the yokes [see inset in Fig. 3.7(e)]. The electromagnet is run by a bipolar power supply delivering up to 50 V at a maximum current of 8 A (*Kepeco BOP 50-8M*). The applied field strength is measured in real time by a single-axis Hall effect transducer (*Senis GmbH*).

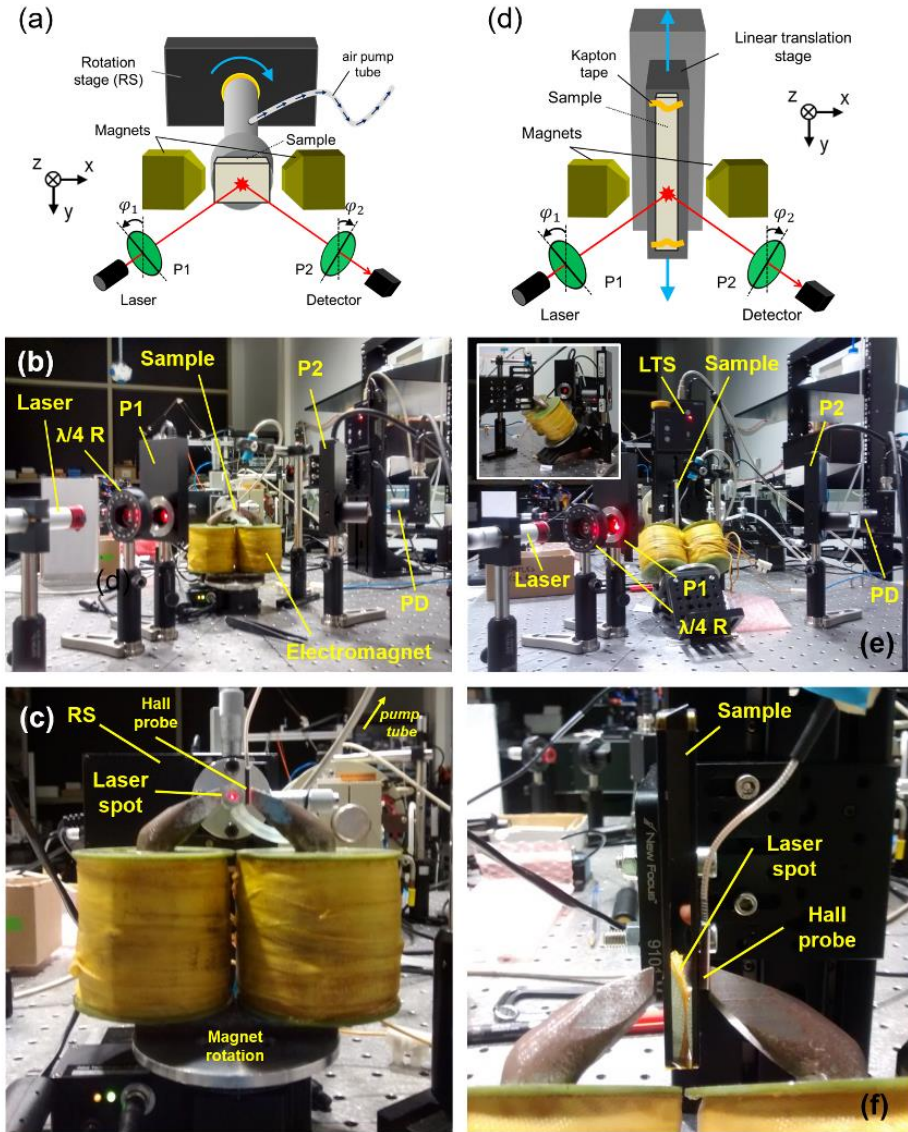


**Fig. 3.7:** (a) Schematic and (b), (c) pictures of the setup with a rotatable sample holder stage (RS). (d) Schematic and (e), (f) pictures of the setup with a linear translation stage (LTS) for the sample holder. The different parts and components are labelled in the figure.

The entire measurement and data acquisition process is automatically controlled by a computer making use of the LabVIEW software (*National Instruments Corporation*). This includes the action of all mechanical parts such as rotators or linear translation stages, as well as the power generation for sweeping the applied magnetic field. The automation of the polarizer, sample and applied magnetic field control is especially advantageous given the large amount of measurements that are needed for constructing the GME datasets leading to a high precision in the determination of the reflection matrix elements.

In this thesis, the rotation sample stage will be utilized in Chapters 3, 4 and 5, while the linear translation stage will be employed in the Section 4.4 and Chapter 6.

### 3.3 GME dataset optimization

In the previous section, it was demonstrated that the GME technique allows for the precise determination of the reflection matrix elements during magnetization reversal. The knowledge of the field dependent evolution of the optical, magneto-optical and magnetic properties of the sample constitutes a vast amount of information that can be readily accessible within the methodology presented here. However, it can also be appreciated that for a precise determination of the reflection matrix, a large amount of data has to be measured. This circumstance is linked to the discussion of Fig. 3.3, where it was explained that the longitudinal, transverse as well as polar Kerr effects can be properly separated based on the different evenness of each Kerr geometry to different symmetry operations in the  $(\varphi_1, \varphi_2)$  space. This in turn requires that the sampled polarizer angle configuration space must span wide enough regions in which these symmetry operations can be tested.

This aspect causes that a large number of hysteresis loop measurements must be performed. For instance, 441 field cycles for different polarizer angle configurations were measured to extract the data in Figs. 3.5 and 3.6. This causes the fit problem to be overdetermined, even for as many fit parameters as nine<sup>28</sup>. However, the extensive mapping of the  $(\varphi_1, \varphi_2)$  space brings an increased robustness of the fit, incrementing the precision of the determined parameters. The main time limiting factor during the measurement is usually originated from the impedance of the magnet, as it is not possible to sweep the applied magnetic field in a range of, for instance, a few kOe, in a time scale faster than  $\sim 10$  seconds. By assuming that this is the time needed for

---

<sup>28</sup> For an arbitrary magnetization orientation, the total number of fit parameters is eleven. For in-plane magnetization orientations alone, we neglect the parameters associated to the polar Kerr effect by setting  $B_5 = B_6 = 0$ .

acquiring each of the 441 field cycles in the GME dataset, the total measurement time adds up to approximately one hour and a half<sup>29</sup>.

While this is a reasonable time span for obtaining such a large amount of information, it is clear that the GME technique will often require relatively lengthy measurement times. Therefore, implementing the right choice of the  $(\varphi_1, \varphi_2)$  configuration space is most important for finding a good balance between performing reliable as well as less time consuming measurement procedures. For this reason, the most suitable dataset geometry within GME has been explored before coming to discuss magnetometry as well as optical and magneto-optical characterization capabilities. This is done by analyzing the susceptibility of the nonlinear fitting process to the presence of noise in the measured GME maps.

#### *Noise effects in the near region of the crossed polarizer configuration*

The accuracy and precision of the obtained information highly depends on the multi-parameter nonlinear least-square fitting procedure described above. During a GME experiment, the quality of the acquired data and the subsequent fit are subject to stochastic noise sources and errors. For example, these include non-ideal polarizer properties, fluctuations of the non-filtered ambient light or the presence of systematic polarizer misalignments.

As a way to examine the impact of undesired noise sources on the  $\delta I/I$  quantity and the subsequent fit, the significance of each  $(\varphi_1, \varphi_2)$  grid data point in the fitting procedure is numerically evaluated under the presence of noise, which is simulated in terms of random variables. We introduce the grid-site-specific sensitivity function  $S(\varphi_1, \varphi_2)$ , defined as the difference between the fit goodness  $R^2$  values obtained upon excluding or including a given  $\delta I/I(\varphi_1, \varphi_2)$  data point in the fitting

$$S(\varphi_1, \varphi_2) = R_{without}^2 - R_{with}^2, \quad (3.10)$$

which quantitatively assesses the significance of the data point at  $(\varphi_1, \varphi_2)$ . One has to consider that for simulated  $\delta I/I(\varphi_1, \varphi_2)$  datasets, there are no differences in  $R^2$  upon including or excluding a given data point in the regression process, as its removal would not affect the perfect least squares fit of the simulated data. Correspondingly, we computed numerical  $\delta I'/I'$  maps by a random noise implementation according to the following expressions [146]

---

<sup>29</sup> However, one acquires in reality over 100 GME-maps within 1.5h: one for each applied field value, provided that a dense-enough grid of field points is acquired.

$$\begin{aligned}
 I'(\varphi_1, \varphi_2) &= I + 10^{-5} \cdot \sqrt{I} \cdot [-0.5 + \sigma_1(\varphi_1, \varphi_2)] \\
 \delta I'(\varphi_1, \varphi_2) &= \delta I/I + 10^{-5} \cdot \sqrt{I} \cdot [-0.5 + \sigma_2(\varphi_1, \varphi_2)],
 \end{aligned}
 \tag{3.11}$$

where  $\sigma_1$  and  $\sigma_2$  are random variables in the interval  $[0, 1]$ . Within this approach, the random error of the  $\delta I'/I'$  quantity is set to be proportional to the square root of intensity. The factor  $10^{-5}$  is motivated by the magnitude of the largest residual values we see when fitting the experimental data, which typically amount to 2-3% of the largest measured  $\delta I/I$  values.

For the numerical study, we considered a semi-infinite Co slab with a refractive index of  $N = 2.1 + 4.2i$  and magneto-optical coupling factor of  $Q = 0.03 - 0.01i$ . For simplicity, we continue considering longitudinal and transverse Kerr effects alone, setting the magnetization orientation in the sample plane,  $45^\circ$  away from the  $x$ -axis ( $m_x = m_y, m_z = 0$ ). The corresponding  $B_i$  parameters are extracted and an intensity offset parameter of  $I_0 = 5 \cdot 10^{-4}$  is assumed. We computed the  $\delta I/I$  map from these quantities and added the site specific noise according to Eq. 3.11 over the whole polarizer angle grid  $\varphi_1 \in [80^\circ, 100^\circ]$ ,  $\varphi_2 \in [-10^\circ, 10^\circ]$ . Subsequently, GME maps were fitted before and after removal of each specific data point at  $(\varphi_1, \varphi_2)$  in order to extract the  $R^2$  goodness values and the sensitivity function  $S(\varphi_1, \varphi_2)$ .

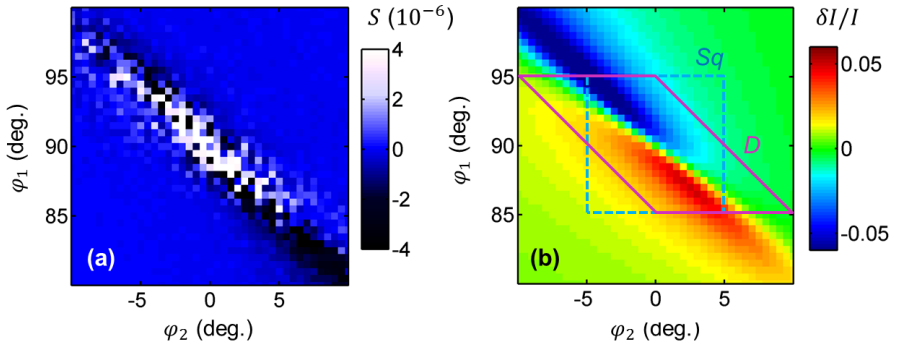


**Fig. 3.8:** (a) Color-coded  $S(\varphi_1, \varphi_2)$  sensitivity map reflecting the variation of the fit quality upon removal of an individual  $\delta I'/I'$  data point. A negative  $S$  value represents a reduction of the fit quality upon removing the  $(\varphi_1, \varphi_2)$  point. (b) Graphical definition of the square ( $Sq$ ) and diagonal ( $D$ ) datasets described throughout the manuscript text. For the exemplary dataset represented in the figure,  $(\varphi_{1c}, \varphi_{2c}) = (90^\circ, 0^\circ)$  and  $\Delta = 10^\circ$  (see text).

In order to suppress the effect of the random noise associated with each  $(\varphi_1, \varphi_2)$  grid point (which might smear out the significance of the point for the fit process) the process was repeated ten times by applying a different site-dependent noise realization in each run, subsequently averaging the value of the sensitivity  $S(\varphi_1, \varphi_2)$ .

Fig. 3.8(a) exhibits the polarizer angle dependence of the numerically calculated site specific sensitivity. A negative value of  $S(\varphi_1, \varphi_2)$ , depicted with darker colors, indicates a reduced goodness of the fit upon excluding the grid point  $(\varphi_1, \varphi_2)$ , while the brighter, positive data points denote an improvement. This is equivalent to saying that the darker colors identify particularly valuable grid points, while the brighter ones point out those polarizer configurations that are greatly susceptible to the presence of noise. Remarkably, the vast majority of points that lie near the diagonal of the dataset, for which the P1 and P2 polarizers are perpendicular, present a negative value of sensitivity. This means that their removal results into a worse fitting. In addition, we also see that the central  $(\varphi_1, \varphi_2)$  data points, for which the measured intensity is very low, are more susceptible to noise and thus their removal improves the fit goodness. Finally, the vast majority of points outside the diagonal display a characteristic blue color corresponding to sensitivity values near zero, hence being less relevant for the fit.

Based on the above discussion, we suggest to employ an improved dataset geometry entailing a larger fraction of polarizer configurations contained along the diagonal region, where the most valuable data points were found. Fig. 3.8(b) displays a color-coded  $\delta I/I$  map where the selection of two different datasets is highlighted. The square ( $Sq$ ) dataset employed so far is represented with dashed lines, with the solid lines depicting a new dataset type ( $D$ ) constructed as follows: (i) the polarizer angle  $\varphi_1$  is varied in a symmetric range between  $\varphi_{1,c} - \Delta/2$  and  $\varphi_{1,c} + \Delta/2$  around the symmetry point  $\varphi_{1,c}$ , while (ii) the  $\varphi_2$  range is dependent on the current  $\varphi_1$  value, such that  $\varphi_2$  is delimited between  $\varphi_1 - 90^\circ - \Delta/2$  and  $\varphi_1 - 90^\circ + \Delta/2$ . This will compose a diagonal dataset possessing the same amount of total data points as the square one.

By comparing the  $S(\varphi_1, \varphi_2)$  map in Fig. 3.8(a) with the definition of the two datasets in Fig. 3.8(b), it is clear that the diagonal dataset spans a larger number of  $(\varphi_1, \varphi_2)$  grid points lying in the region where the most valuable data points were found. Thus one can expect that the choice of this dataset will result into an improved data analysis scheme as well as into a more precise determination of the fit parameters. Upon comparing the outcome of the fitting procedure in square and diagonal datasets both experimentally and theoretically, we demonstrated that the diagonal dataset consistently produces a more precise determination of the reflection matrix elements. This demonstration is beyond the scope of this thesis and the interested reader is directed to Ref. [146].

### 3.4 Three-dimensional vector magnetometry of magnetic thin films

As a next step, we approach the problem of recovering the dielectric tensor starting from the reflection matrix elements that we have experimentally determined via the GME technique. This will result in an extremely valuable source of information, as material parameters that are independent of the experimental conditions (e.g. the angle of incidence) can be obtained. These are, namely, the refractive index  $N = n + i\kappa$ , the magneto-optical coupling factor  $Q = Q_r + iQ_i$ , as well as the components of the magnetization orientation vector,  $\mathbf{m} = \{m_x, m_y, m_z\}$ . All these quantities are contained in the dielectric tensor, which for an optically isotropic material reads as

$$\vec{\epsilon} = (\epsilon_{ij}) = N^2 \begin{pmatrix} 1 & iQm_z & -iQm_y \\ -iQm_z & 1 & iQm_x \\ iQm_y & -iQm_x & 1 \end{pmatrix}. \quad (3.12)$$

Our major interest is centered towards obtaining a precise determination of the magnetization vector components,  $m_x$ ,  $m_y$  and  $m_z$ . In case of having a bulk-like material (or alternatively, an opaque material with a thickness greater than the skin depth of light) one can readily use the Fresnel formulae in Section 1.4 (Eqs. 1.31). These directly relate the polarization dependent reflectivity terms to the quantities needed to construct the dielectric tensor, such as  $N$ ,  $Q$  and the magnetization components.<sup>30</sup>

In contrast, if the system under study consists of a layered material, the semi-infinite medium approach is not suitable anymore and one needs to consider the full electromagnetic problem of light reflection from a stratified media, by appropriately applying the corresponding boundary conditions at the multiple material interfaces. This is not generally a trivial problem but it can still be solved via the Transfer Matrix Method (TMM) [72-75], a rigorous mathematical formulation that can evaluate the reflection matrix of a multilayered material from the dielectric tensors of its constituent layers (see Appendix I for a more detailed description).

The strategy to recover the dielectric tensor of a material from the information provided by GME is depicted in Fig. 3.9. The TMM allows to calculate the reflection matrix of the sample under certain experimental conditions, starting from the dielectric tensor elements of the constituent layers. For simplicity, we will consider that only one type of material is magneto-optically active in our sample. The TMM provides a robust

---

<sup>30</sup> The measured magnetization properties belong in any case to a surface layer portion (about half of the skin depth), such that strictly speaking, bulk magnetization properties cannot be obtained using MOKE.

way to the path  $\{N, Q, m_x, m_y, m_z\} \rightarrow R = (r_{ij}) \rightarrow B_1 - B_8$ , but the inverse way cannot be implemented in general. For achieving this, one needs to treat the problem as a nonlinear least squares fit process, using the TMM methodology as a functional and treating the quantities  $\{N, Q, m_x, m_y, m_z\}$  as fit parameters. This is achieved via a Levenberg-Marquardt algorithm [147], which finds the minimum deviation of squares upon finding the best optical model match that mimics the experimentally determined reflection matrix elements in the best possible way.

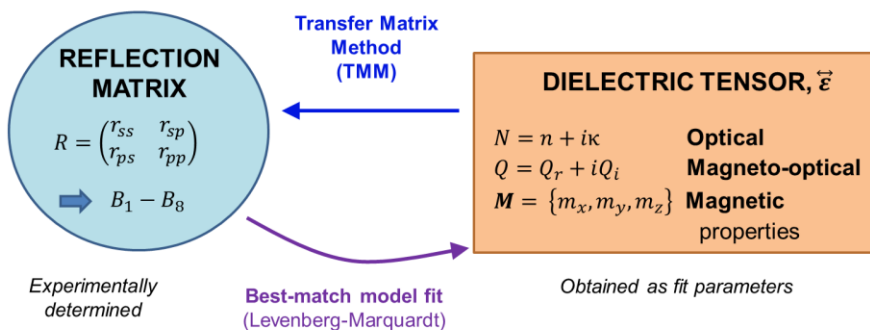


**Fig. 3.9:** Schematic of the fitting process to extract the dielectric tensor quantities from experimentally determined reflection matrix elements. The Transfer Matrix Method (TMM) is employed for obtaining the reflection matrix of any layered material from the dielectric tensor elements of its constituent materials. In order to complete the inverse path, a best-match model nonlinear fit based on the Levenberg-Marquardt algorithm is utilized, treating the dielectric tensor quantities as fit parameters.

The strength of the GME methodology to perform vector magnetometry in magnetic thin films is examined in the next sub-section and employed throughout the rest of the thesis.

### *hcp Co films with in-plane uniaxial magnetic anisotropy*

Magnetic thin films with strong in-plane magnetocrystalline anisotropy are firstly employed as a model system for showcasing the GME magnetometry capabilities, due to their relatively simple magnetization reversal process. Epitaxial hcp Co films with in-plane  $c$  axis orientation, where the  $c$  axis is the magnetic easy axis (EA) of Co, were fabricated at room temperature via sputter deposition onto hydrofluoric acid etched Si substrates. The followed epitaxial sequence was Si(110)/Ag(110)/Cr(211)/Co(10 $\bar{1}$ 0), for which 75 nm of Ag and 50 nm of Cr were deposited, as well as 30 nm of Co,

according to the procedures reported by Yang *et al.* [148] and previous work within the Nanomagnetism group at CIC nanoGUNE [112, 148, 149]. A 10-nm-thick capping layer of amorphous SiO<sub>2</sub> was also sputter-deposited on top of the Co films for oxidation protection.

Fig. 3.10 shows XRD data measured for a 30-nm-thick, Co(10 $\bar{1}$ 0) textured epitaxial hcp Co film with an in-plane oriented *c* axis (Co[0001] orientation). The symmetric  $\theta$ - $2\theta$  scans in Fig. 3.10(a) show that a good out-of-plane crystallographic texture of the different layers has been achieved throughout the epitaxial sequence, as indicated by the presence of the Co(10 $\bar{1}$ 0), Co(20 $\bar{2}$ 0), Ag(220) and Cr(211) reflections. In addition, Fig. 3.10(b) displays a rocking curve measurement of the Co(10 $\bar{1}$ 0) peak, exhibiting a full-width at half-maximum of 3.20°, which is a relatively good value for room temperature deposited epitaxial films. Complementarily, the in-plane epitaxy is confirmed by performing  $\Phi$ -scans in all layers of the sample stack. Figs. 3.10(d)-3.10(g) show the  $\Phi$ -scans for the selected Si(004), Ag(004), Cr(110) and Co(10 $\bar{1}$ 1) reflections, indicating the relative in plane orientation of the sequential layers.

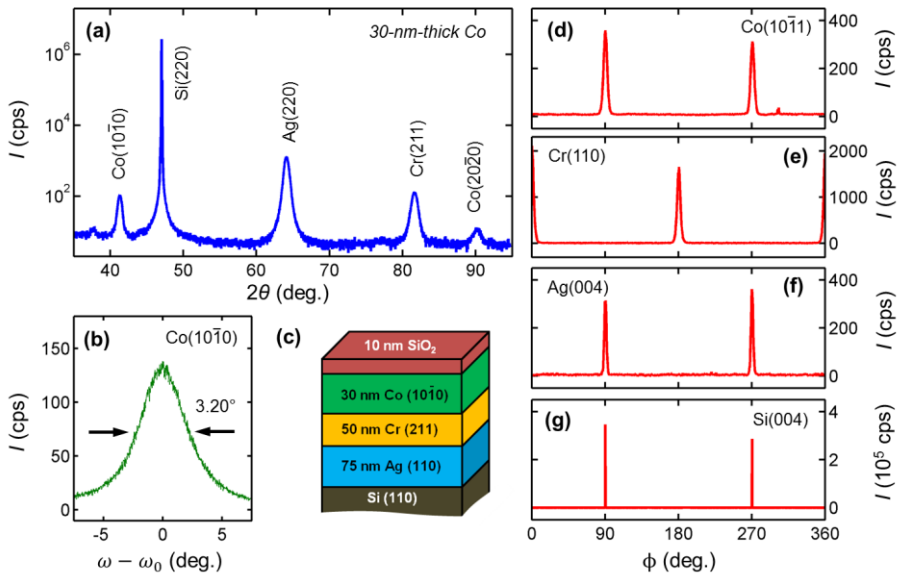


**Fig. 3.10:** Structural characterization of a 30-nm-thick epitaxial hcp Co films via x-ray diffraction. (a) Symmetric x-ray  $\theta$ - $2\theta$  scan. (b) Rocking curve ( $\omega$ -scan) of the Co(10 $\bar{1}$ 0) diffraction peak. (c) Schematic of the epitaxial sequence. (d) - (g)  $\Phi$ -scans revealing in-plane epitaxial relations.

Due to the in-plane magnetocrystalline anisotropy of the Co films, their quasi-static magnetization reversal can be described very well by means of a coherent

magnetization rotation followed by a sample-sized magnetization switch [112]. In this way, the analysis of GME datasets in terms of uniform magnetization states is straightforward. The magnetic properties of epitaxial hcp Co films are firstly checked via VSM measurements. Fig. 3.11(a) shows three  $M$  vs  $H$  magnetic hysteresis loops measured for different relative orientations  $\beta$  of the magnetic field with respect to the in-plane  $c$  axis of Co:  $0^\circ$  (EA),  $45^\circ$  and  $87^\circ$ . The magnetization value was obtained by dividing the measured magnetic moment by the 30-nm-thick film volume. The measurements reveal a square hysteresis loop for the EA case, whereas the curves for  $45^\circ$  and  $87^\circ$  suggest a prominent magnetization rotation process upon lowering the field from magnetic saturation. The hysteresis loop at  $87^\circ$  approaches a characteristic hard axis  $S$ -shaped curve. The extracted room temperature saturation magnetization value of  $1340 \pm 10$  emu/cm<sup>3</sup> is in agreement with the literature values. The high degree of magnetic uniaxial anisotropy of the sample is further confirmed by the plot of the normalized remanent magnetization  $M_r/M_s$  vs the applied field angle, which follows a regular  $180^\circ$  periodicity [Fig. 3.11(b)].

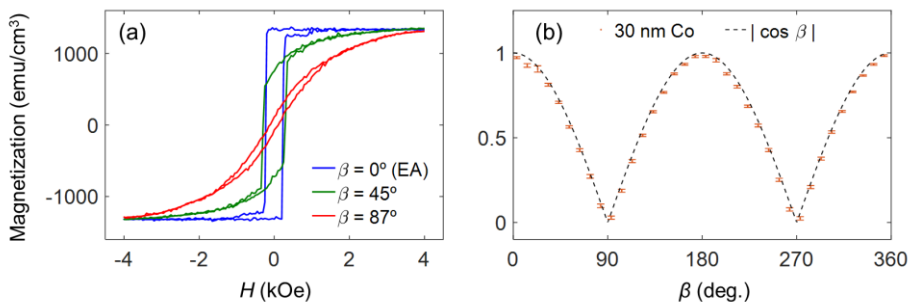


**Fig. 3.11:** (a) Exemplary VSM hysteresis loop measurements of an epitaxial hcp Co film for three different orientations of the applied field with the magnetic easy axis ( $c$  axis) of Co:  $\beta = 0^\circ$ ,  $45^\circ$  and  $87^\circ$ . (b) Normalized remanent magnetization vs applied field orientation obtained from VSM measurements (dots) and the  $|\cos \beta|$  curve expected for a material with a perfect uniaxial magnetic anisotropy.

Once the general magnetic properties of the sample are evaluated via VSM, magnetometry analysis is performed via GME. Magnetization reversal is studied by applying a magnetic field with a maximum amplitude of  $\pm 2.2$  kOe in the plane of the sample. The sample orientation with respect to the field (applied within the plane of incidence, see Fig 3.1) is also defined in the GME experiment by the angle  $\beta$ , with the orientation  $\beta = 0^\circ$  corresponding to the case in which the EA is aligned with the field.

Fig. 3.11 displays exemplary  $\delta I/I(\varphi_1, \varphi_2)$  maps acquired at an angle of incidence of  $30^\circ$  and for the different sample orientations  $\beta = 0^\circ$  (EA),  $45^\circ$ ,  $75^\circ$  and  $85^\circ$

(see schematics of the relative field-to-EA orientation in the top part of Fig. 3.12). The field-dependent snapshots during reversal are chosen such that for each sample orientation  $\beta$  four datasets are shown, which correspond to the following stages of the magnetization reversal during the decreasing field branch: (i) near positive saturation ( $H = +H_{MAX}$ ), (ii) remanence ( $H = 0$ ), (iii) the field value just before magnetization switching ( $H = H_S$ ), and (iv) near negative saturation ( $H = -H_{MAX}$ ). The field values are indicated in the inset of the GME datasets.

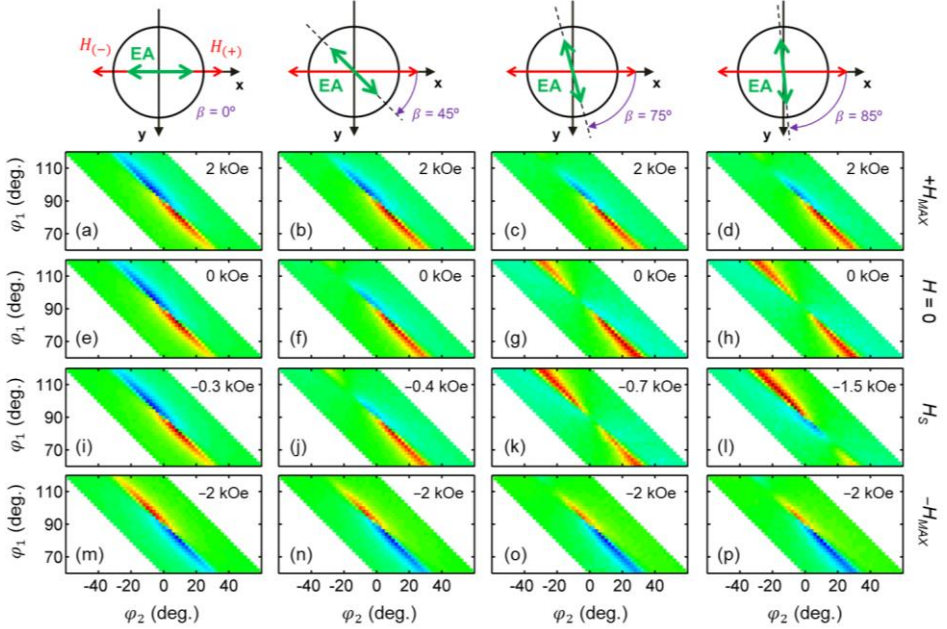


**Fig. 3.12:** A ‘movie’ of the magnetization reversal process via GME maps. Each column represents a magnetization reversal event for a given orientation  $\beta$  of the applied field with the  $c$  axis of Co, the EA of magnetization.  $\delta I/I(\varphi_1, \varphi_2)$  maps for  $\beta = 0^\circ$  (EA),  $45^\circ$ ,  $75^\circ$  and  $85^\circ$  are shown. On the other hand, each line corresponds to a configuration within the reversal event, namely (a) – (d) maximum positive field, (e) – (h) remanence, (i) – (l) the field value just before magnetization switching and (m) – (p) maximum negative field. The inset in each map displays the applied field value at which the map was acquired. The same color-code is utilized for all maps shown here, with  $\delta I/I$  values in between  $\pm 0.06$ .

When the GME data in Fig. 3.12 are visualized within the same column, one can track the symmetry change of the  $\delta I/I(\varphi_1, \varphi_2)$  maps during different stages throughout reversal. In the case of  $\beta = 0^\circ$ , it can be appreciated that the GME map remains unchanged until the switching field  $H_S$  is reached [Fig. 3.12(i)], to then invert the sign of the two lobes in the GME map for fields  $H < H_S = -0.3$  kOe. On the other

### 3. Generalized magneto-optical ellipsometry (GME)

hand, a considerable change is seen when comparing the GME maps at high positive fields [Figs. 3.12(b)-3.12(d)] and remanence [Figs. 3.12(f)-3.12(h)] for the cases  $\beta = 45^\circ$ ,  $75^\circ$  and  $85^\circ$ . In these cases, the two lobes of opposite sign are distorted as a result of the mixing of the  $\delta I/I$  signals arising from both longitudinal and transverse Kerr effects. In fact, the GME map at remanence for the  $\beta = 85^\circ$  case [Fig. 3.12(h)] shows a characteristic transverse Kerr effect symmetry, displaying two lobes of the same sign and thus suggesting that the magnetization is essentially oriented along the vertical  $y$ -axis (in fact, it is oriented only  $5^\circ$  away from the vertical, along the EA orientation).

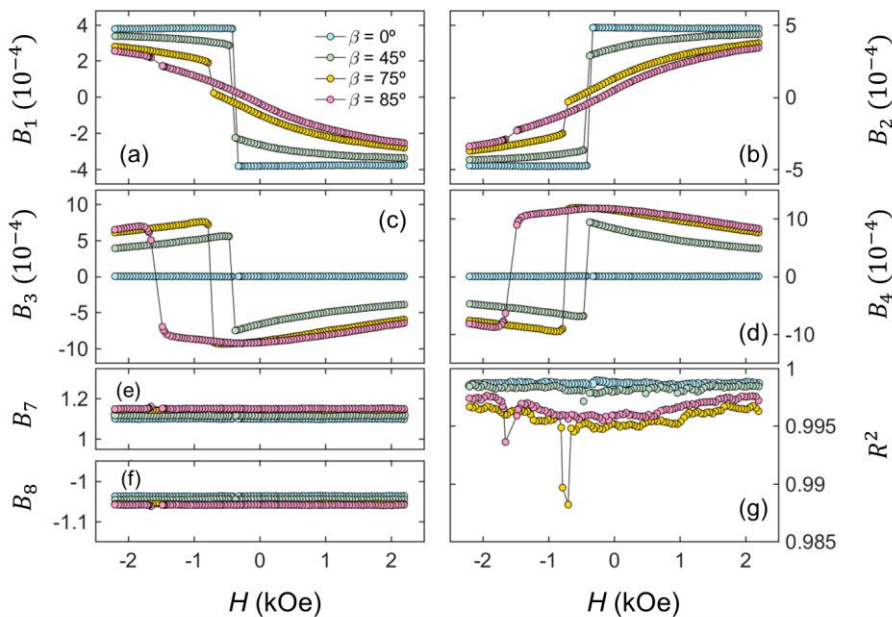


**Fig. 3.13:** Field dependent reflection matrix parameters  $B_1$ - $B_4$ ,  $B_7$  and  $B_8$  as well as the fit goodness  $R^2$  obtained from the GME maps measured for the field orientation configurations  $\beta = 0^\circ$ ,  $45^\circ$ ,  $75^\circ$  and  $85^\circ$  (datasets were acquired for a larger set of  $\beta$  configurations, but selected data are shown here). The data represent the magnetization reversal process within the decreasing field branch of the hysteresis loop.

Hereby, all field-dependent GME maps such as the ones shown in Fig. 3.12 were fitted to the  $\delta I/I$  expression in Eq. 3.9 (hence neglecting polar Kerr effects). The results are shown in Fig. 3.13, where the data for the  $\beta = 0^\circ$ ,  $45^\circ$ ,  $75^\circ$  and  $85^\circ$  cases are again shown. The  $B_i$  parameters linked to the longitudinal [Figs. 3.13(a), 3.13(b)] and transverse Kerr effect [Figs. 3.13(c), 3.13(d)] show a very different field-dependent

behavior upon changing the angle  $\beta$ , indicative of the distinct magnetization reversal processes. In particular, the case  $\beta = 0^\circ$  clearly points to a characteristic easy axis magnetization reversal, with a bi-stable field-dependent value of the parameters  $B_1, B_2$  while  $B_3, B_4$  are equal to zero for all field values. On the other hand, the purely optical parameters  $B_7$  [Fig. 3.13(e)] and  $B_8$  [Fig. 3.13(f)] do not show any field dependence, despite their values seeming to be slightly shifted for different  $\beta$  values. This aspect is further explored in Section 3.5 and Chapter 4. Finally, it is worth noting that the  $R^2$  fit goodness essentially displays values above 0.995, except for a few data points in the case of  $\beta = 75^\circ$  and  $85^\circ$  [see Fig. 3.13(g)]. These slightly worse data points are located in the reversal region, where the uniform magnetization assumption may not be fulfilled in a narrow field-range during reversal (due to the formation of magnetic domains).

With the purpose of performing magnetometry, the dielectric tensor of the Co film was recovered. This was accomplished by considering an appropriate optical model and applying the TMM to calculate the reflection matrix as a function of the optical model parameters. The optical model employed in the analysis is shown in Fig. 3.14(a). We use refractive index of  $n_0 = 1.46$  for the  $\text{SiO}_2$  cap layer (measured via spectroscopic ellipsometry) and set  $N_{Cr} = 3.13 + 3.31i$  for the Cr underlayer [151], which we consider to be the substrate in our optical model. This is because the light penetration depth at  $\lambda = 635$  nm is significantly smaller than the combined thickness of the Co (30 nm) and Cr (50 nm) films. We then assume a dielectric tensor of the form

$$\vec{\epsilon} = N^2 \begin{pmatrix} 1 & 0 & -iQm_y \\ 0 & 1 & iQm_x \\ iQm_y & -iQm_x & 1 \end{pmatrix} = N^2 \begin{pmatrix} 1 & 0 & -iQ \sin \gamma \\ 0 & 1 & iQ \cos \gamma \\ iQ \sin \gamma & -iQ \cos \gamma & 1 \end{pmatrix}, \quad (3.13)$$

where  $m_x = \cos \gamma$  and  $m_y = \sin \gamma$  (with  $m_z = 0$ ) [see the schematic of the relevant orientations between applied field, easy axis of the sample and magnetization in Fig. 3.14(b)]. For every experimentally determined reflection matrix parameters at a certain applied field value, we obtain the best-matching model parameters for the optical ( $N = n + ik$ ) and magneto-optical ( $Q = Q_r + iQ_i$ ) constants of the Co film as well as the in-plane magnetization angle  $\gamma$ . The results obtained from this second fit process are shown in the lower panel of Fig. 3.14. As an exemplary case, the fitted field-dependent values of  $n$  and  $\kappa$  [Figs. 3.14(c), 3.14(d)] as well as of  $Q_r$  and  $Q_i$  [Figs. 3.14(e), 3.14(f)] are shown for the  $\beta = 45^\circ$  case. The measured refractive index of Co at a wavelength of 635 nm is  $N = 2.06 + 4.60i$ , whereas the magneto-optical coupling factor is  $Q = 0.032 - 0.003i$ . As expected, there is essentially no field dependence of these quantities within the error bars. However, a slight field-dependent modulation can be appreciated for the quantity  $Q_i$  [Figs. 3.14(f)]. This aspect will be discussed in Chapter 4.

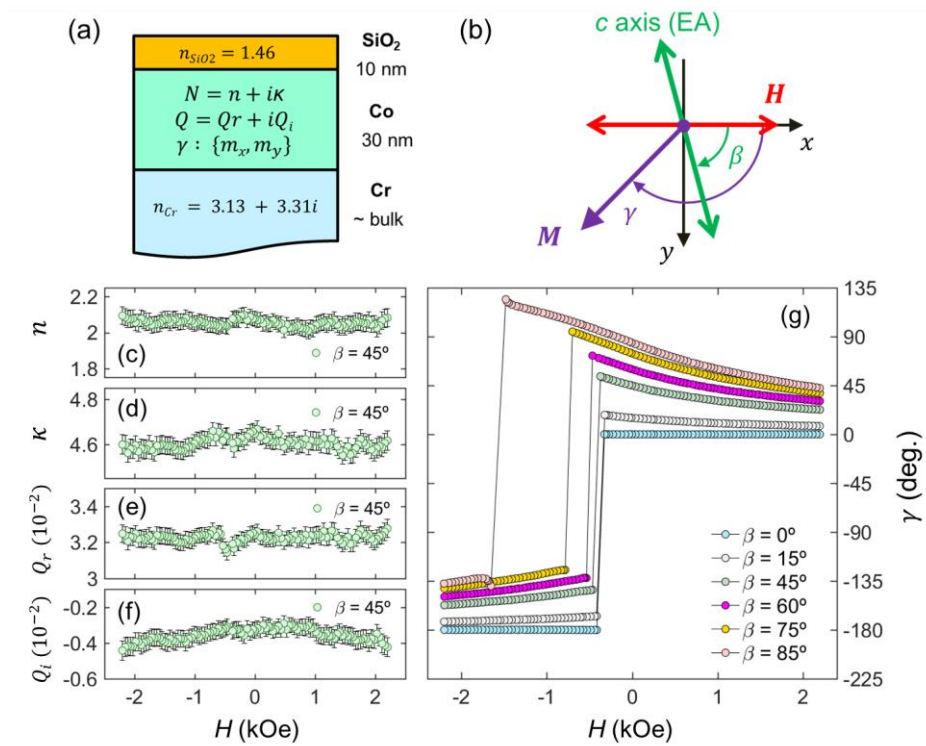


**Fig. 3.14:** (a) Sketch of the optical model employed for the 30-nm-thick hcp Co film in order to retrieve the dielectric tensor elements of the Co layer. (b) Sketch defining the relative orientations of the applied field axis (which is contained in the plane of incidence), the magnetization angle  $\gamma$  and the Co easy axis orientation  $\beta$  with respect to the plane of incidence. (c)-(f) Exemplary fitted  $N$  and  $Q$  values for the  $\beta = 45^\circ$  orientation. (g) Magnetization angle  $\gamma$  vs  $H$  during reversal (decreasing field branch) for  $\beta = 0^\circ, 15^\circ, 45^\circ, 60^\circ, 75^\circ$  and  $85^\circ$ .

Together with  $N$  and  $Q$ , the field-dependent magnetization angle  $\gamma$  is obtained in the fitting routine for each field value as well. The data are shown in Fig. 3.14(g), where the field evolution of  $\gamma$  is represented for different relative orientations between the sample (and hence the easy axis of Co) and the applied field direction.

Thus we see that GME enables the acquisition of the true magnetization vector, opposite to the vast majority of MOKE experiments which obtain a signal that is proportional to a single magnetization component. While this is often sufficient, the vector magnetometry capability can become crucial when investigating different aspects of magnetization reversal, discerning signals of optical and magneto-optical origin, or when studying the fine interplay of magnetic interactions in magnetic thin films and multilayers (see next chapters of this thesis).

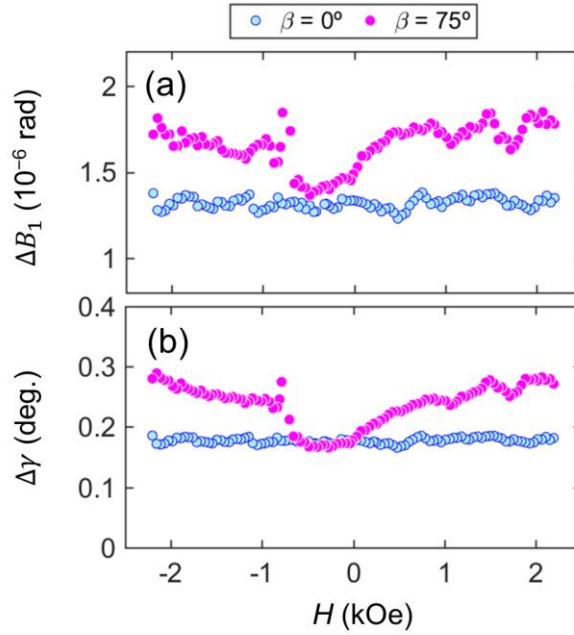


**Fig. 3.15:** (a) Field-dependent error bar quantities for the fitted  $B_1$  during magnetization reversal with  $\beta = 0^\circ, 75^\circ$ . (b) Error bar quantities for the magnetization angle  $\gamma$  as determined from the optical model fit during the same magnetization reversal processes.

While error bar quantities were plotted in Fig. 3.14(g) for the magnetization angle  $\gamma$ , these are shadowed by the plot symbols due to their small size. In order to give an account of the magnetometry precision achieved by GME, Fig. 3.15 shows error bar quantities for the  $B_1$  parameter (which for a reference, is equal to the Kerr rotation quantity for incident  $p$ -polarized light) for selected  $\beta$  datasets. It is seen that the typical precision of the Kerr rotation measurements via GME is an exceptionally low  $\sim 1 \mu\text{rad}$  (or  $\sim 0.05 \text{ mdeg}$ ) [see Fig. 3.15(a)]. The precision values in  $B_1$  during reversal are very stable, without any large field-to-field variations, and are kept always below  $2 \mu\text{rad}$ , which is a remarkably good result. These error bar values can be further lowered to a few hundreds of nanoradians by doubling the averaging time during GME data acquisition, which would then require an affordable 3-to-4-h-long experiment to record a magnetization reversal process in such a high detail.

Similarly, Fig. 3.15(b) shows the error bars associated with the  $\gamma$  values extracted from the same experiment for which the  $B_1$  error bars were shown in Fig. 3.15(b). From here, we see that typical precisions of the order of  $\sim 1 \mu\text{rad}$  in the

determination of Kerr rotation (and ellipticity) translate into a  $\sim 0.2^\circ$  precision in the determination of the magnetization angle.

One can test the effect of the high-precision knowledge in the magnetization orientation on the determination of other sample properties such as magnetic anisotropy. In order to quantify the magnetic anisotropy of this particular sample, the magnetization orientation vs field data was fitted to a Stoner-Wohlfarth model behavior including a second order term of the MCA energy. Then, the total energy density (including Zeeman and MCA energy) reads as

$$\epsilon = \epsilon_K + \epsilon_Z = K_1 \sin^2(\gamma - \beta) + K_2 \sin^4(\gamma - \beta) - HM_S \cos \gamma, \quad (3.14)$$

Fig. 3.16 exhibits the  $\gamma$  vs  $H$  data for various  $\beta$  configurations together with the corresponding fits to the Stoner-Wohlfarth model. All data for different sample orientations  $\beta$  is fitted at once, using the first- and second-order anisotropy fields  $H_{K1} = 2K_1/M_S$  and  $H_{K2} = 4K_2/M_S$  as fit parameters<sup>31</sup>. As seen from Fig. 3.16, the agreement of the data with the fit is excellent.

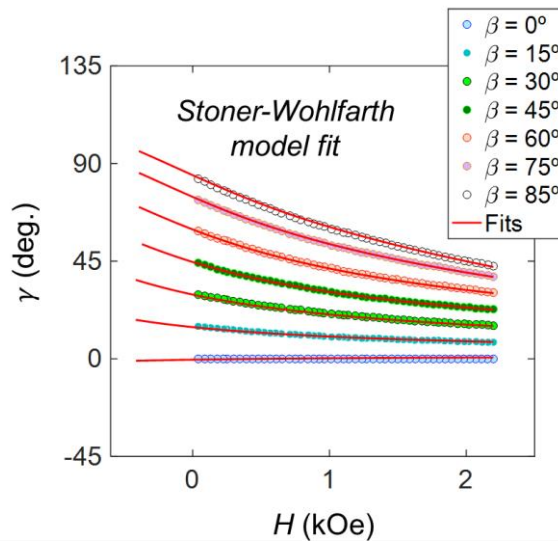


**Fig. 3.16:** Fitting of the field-dependent magnetization angle data to the Stoner- Wohlfarth model.

<sup>31</sup> The fit routine also allows adjusting the true  $\beta = 0^\circ$  orientation for which the easy axis of Co is exactly aligned with the field axis. The slightly imprecise alignment of the field axis with the optical plane of incidence can be corrected as well ( $\sim 1.5^\circ$  in our case).

The fitted values of the first and second order anisotropy field are shown in Table 3.2. The actual magnetic anisotropy energy densities  $K_1$  and  $K_2$  can also be determined if the saturation magnetization is known (values are shown in the Table 3.2).

$H_{K1}$ (kOe)	$1.07 \pm 0.01$ (0.1%)
$H_{K2}$ (kOe)	$2.12 \pm 0.04$ (2%)
$K_1$ ( $10^6$ erg/cm <sup>3</sup> )	$0.717 \pm 0.007$ (0.1%)
$K_2$ ( $10^6$ erg/cm <sup>3</sup> )	$0.71 \pm 0.01$ (2%)

**Table 3.2:** Fitted magnetic anisotropy parameters of the 30-nm-thick epitaxial hcp Co film (relative errors in parenthesis). The fit to the Stoner-Wohlfarth model gave an  $R^2$  value of 0.9998. The magnetic anisotropy energy densities  $K_1$ ,  $K_2$  are obtained from the anisotropy fields and the saturation magnetization value of  $1340 \pm 10$  emu/cm<sup>3</sup> as determined via VSM.

After showing magnetometry results for magnetization orientations in the film plane, the capability of GME to experimentally determine the **three dimensional magnetization vector** is presented. In order to obtain a non-zero  $m_z$  component in the experiment (and thus a sizeable polar Kerr effect) the applied field axis is tilted away from the Co film plane and within the plane of incidence [see Fig. 3.17(a)]. Due to the reduced gap between the poles of the electromagnet ( $\sim 1$  cm), the maximum tilt angle  $\chi$  that can be realized while allowing the laser beam path clearance to the sample (and back upon reflection) depends on the angle of incidence  $\theta$ . For example, for tilt angles up to  $\chi = 20^\circ$ , an angle of incidence of  $\theta = 30^\circ$  was chosen (as in the previous experiment in which the field was applied along the in-plane film orientation).

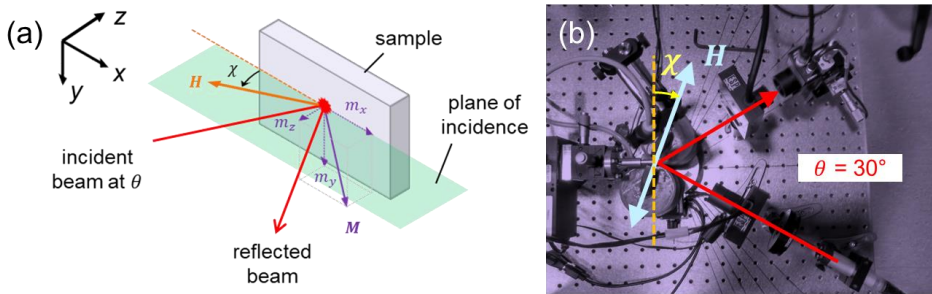


**Fig. 3.17:** (a) Schematics of the GME experiment with an applied field tilted in the plane of incidence (at an angle  $\chi$  away from the field plane). (b) Top view of the GME setup upon this configuration.

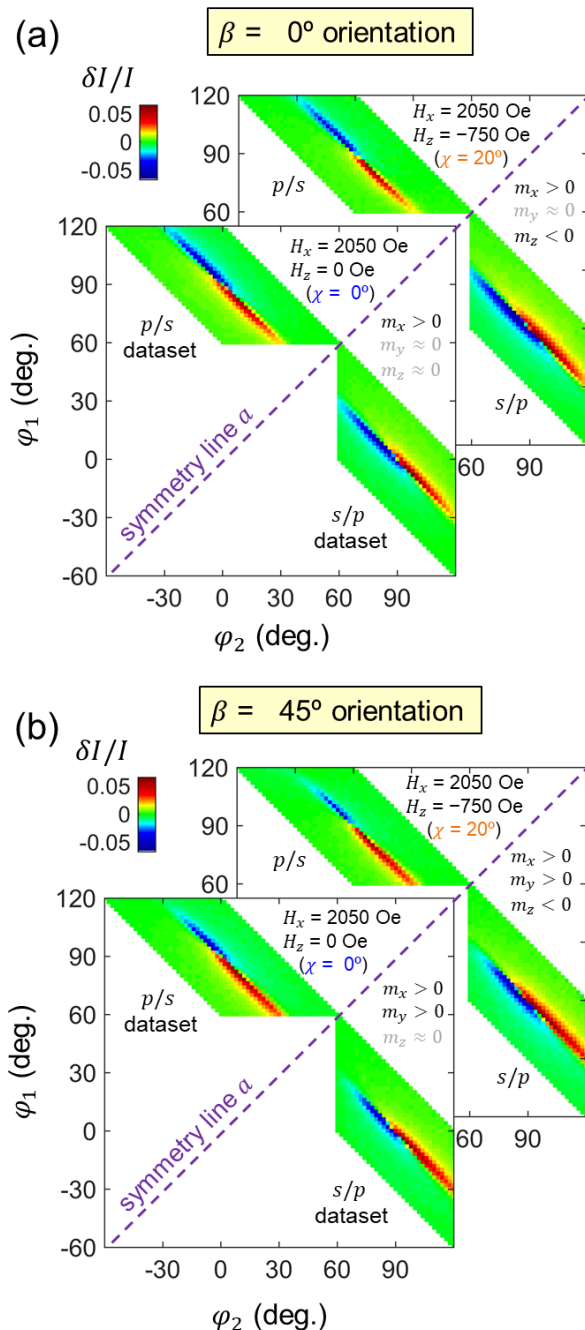


**Fig. 3.18:** GME  $\delta I/I(\varphi_1, \varphi_2)$  maps around the  $p/s$  and  $s/p$  symmetry points retrieved for different  $H_x$  and  $H_z$  field configurations, obtained via different electromagnet tilt settings:  $\chi = 0^\circ$  (no tilt) and  $20^\circ$ . Datasets for two relative orientation of the Co easy axis with the plane of incidence are shown: (a)  $\beta = 0^\circ$  and (b)  $\beta = 45^\circ$ .

Following the discussion on the symmetries of the GME (see Fig. 3.3), the measured  $\delta I/I(\varphi_1, \varphi_2)$  datasets have to be extended in order to adequately separate the  $\delta I/I$  contributions of the longitudinal, transverse and polar Kerr effect. Fig. 3.18 illustrates the type of extended datasets that were acquired within the experiment. This consists of the already described diagonal-shaped dataset around the  $p/s$  crossing point [centered around  $(\varphi_1, \varphi_2) = (90^\circ, 0^\circ)$ ], as well as of an additional diagonal-shaped region centered around the  $s/p$  crossing point [ $(\varphi_1, \varphi_2) = (0^\circ, 90^\circ)$ ], which is the mirror image with respect to the symmetry line  $a$  (see Fig 3.18).

In order to demonstrate that this dataset selection is crucial for separating the effect of the polar Kerr effect, we show extended GME maps for different magnetic states of the Co film. For the data displayed in Fig. 3.18(a), the easy axis of Co is aligned in the plane of incidence ( $\beta = 0^\circ$ ). Here, two extended maps are compared:

- (i) one in which a positive field was applied in the sample plane ( $\chi = 0^\circ$ , with  $H = H_x = 2050$  Oe), thus bringing magnetization close to saturation along the positive x-axis.
- (ii) another in which a positive field is applied in a tilted configuration, such that the difference with the first one consists on adding a field component along the z-axis while maintaining the same  $H_x$  component (i.e.  $\chi = 20^\circ$ , with  $H_x = H \cos \chi = 2050$  Oe and  $H_z = -H \sin \chi = -750$  Oe). This should lead to a similar in-plane orientation of the magnetization in the Co film, but also produce a small out-of-plane component  $m_z < 0$  upon slightly overcoming magnetostatic effects [see the schematics in Fig. 3.17(a) for the definition of the field tilting with respect to the Cartesian axes].

The effect of the slight  $m_z$  component induced via the tilted field can be clearly seen in the GME maps shown in Fig. 3.18(a). For the purely in-plane field ( $\chi = 0^\circ$ ), the  $\delta I/I$  data near the two different crossing points is the exact mirror image with respect to the diagonal symmetry line upon inverting the sign of the  $\delta I/I$  quantity. The presence of an additional  $H_z$  field component, however, breaks this mirror symmetry and the  $\delta I/I$  features at each crossing point notoriously change [see Fig. 3.18(a)].

A similar situation is shown in Fig. 3.18(b), which is equivalent to the scenario in Fig. 3.18(a) except for the fact that the sample (and hence its easy axis) has been rotated by an angle  $\beta = 45^\circ$  around the z-axis. In this case, the  $\delta I/I$  datasets near the two different crossing points have already lost their mirror symmetry even for in-plane fields ( $\chi = 0^\circ$ ), as a result of the joint presence of longitudinal and transverse Kerr effects (which possess an odd and even symmetry with respect to mirroring across the diagonal symmetry line). However, the addition of a  $H_z$  field component modifies again

notoriously the  $\delta I/I(\varphi_1, \varphi_2)$  maps around one crossing point and the other, which is the scenario we need for separating all three Kerr geometries and eventually performing three dimensional vector magnetometry.

Correspondingly, the magnetization reversal process at the field/sample orientations described in Fig. 3.18 was measured, that is, the configuration given by the angle pairs  $(\beta, \chi) = (45^\circ, 0^\circ)$  and  $(45^\circ, 20^\circ)$ . Consequently, the  $\delta I/I(\varphi_1, \varphi_2)$  maps at different field values and orientations were fitted to Eq. 3.5. The reflection matrix elements extracted from the fits are shown in Fig. 3.19, where the  $B_1 - B_8$  parameters for the two aforementioned field configurations are plotted on top of each other.

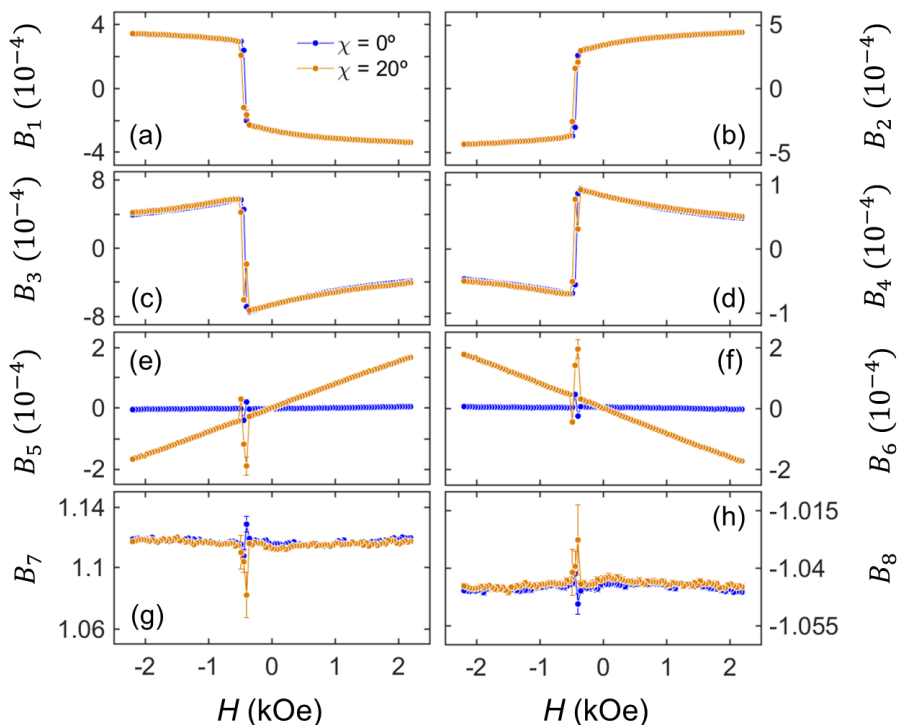


**Fig. 3.19:** Fitted reflection matrix elements  $B_1 - B_8$  for the 30-nm-thick Co film during the decreasing field branch of the magnetization reversal, obtained upon configurations  $(\beta, \chi) = (45^\circ, 0^\circ)$  and  $(45^\circ, 20^\circ)$ .

The reflection matrix parameters linked to the longitudinal [ $B_1, B_2$  in Figs. 3.19(a) and 3.19(b)] and transverse Kerr effects [ $B_3, B_4$  in Figs. 3.19(c) and 3.19(d)] show only slight variations upon tilting the field axis  $20^\circ$  towards the out-of-plane direction. However, a clear difference emerges for the parameters  $B_7$  and  $B_8$  that are proportional to the polar Kerr effect [Figs. 3.19(g) and 3.19(h)]. Specifically,  $B_7$  and  $B_8$

are nearly equal to zero in the  $\chi = 0^\circ$  case, whereas a linear dependence with field is featured when  $\chi = 20^\circ$ , corroborating the fact that the presence of an out-of-plane field  $H_z$  pulls out the magnetization slightly out-of-plane (it is worth noting that when  $H = 0$ ,  $B_7 = B_8 = 0$ ). Finally, there is no variation for the purely optical reflectivities either [Figs. 3.19(g) and 3.19(h)]. The  $R^2$  fit goodness values were always above 0.997, except for three particular datapoints in the  $\chi = 20^\circ$  dataset near the magnetization switching region. These worse fit results may arise from the existence of non-uniform intermediate states of magnetization, as well as due to the lack of the switching field reproducibility in consecutive reversal events, which effectively lowers the quality of the  $\delta I/I$  data acquired in this field region. The precision in the quantities  $B_1$  and  $B_7$ , for example, was in the range of  $\sim 0.5 \mu\text{rad}$  and  $\sim 0.05 \mu\text{rad}$ , respectively (not shown).

As a next step, the dielectric tensor of the Co film is recovered as a necessary step to perform vector magnetometry. We define the Cartesian magnetization components in terms of the in-plane magnetization angle  $\gamma$  and the polar angle  $\psi$  (angle between the magnetization and the  $z$ -axis) as  $m_x = \sin \psi \cos \gamma$ ,  $m_y = \sin \psi \sin \gamma$  and  $m_z = \cos \psi$ . Thus, the dielectric tensor reads as

$$\begin{aligned} \vec{\epsilon} &= N^2 \begin{pmatrix} 1 & iQm_z & -iQm_y \\ -iQm_z & 1 & iQm_x \\ iQm_y & -iQm_x & 1 \end{pmatrix} \\ &= N^2 \begin{pmatrix} 1 & iQ \cos \psi & -iQ \sin \psi \sin \gamma \\ -iQ \cos \psi & 1 & iQ \sin \psi \cos \gamma \\ iQ \sin \psi \sin \gamma & -iQ \sin \psi \cos \gamma & 1 \end{pmatrix}, \end{aligned} \quad (3.15)$$

where we have assumed that the magneto-optical coupling factor  $Q$  is isotropic (i.e. there is an equal strength of MOKE along all orientations).

By following the same layered optical model and procedures as before, we obtain the best-matching model parameters for the optical ( $N = n + ik$ ) and magneto-optical ( $Q = Q_r + iQ_i$ ) constants of the Co film as well as the in-plane and out-of-plane magnetization angles  $\gamma$  and  $\psi$ , respectively. We omit here the results for  $N$  and  $Q$  to avoid repetition, and focus on the magnetization orientation data. Fig. 3.20(a) shows the field-dependent in-plane magnetization angle  $\gamma$  for both  $(\beta, \chi) = (45^\circ, 0^\circ)$  and  $(45^\circ, 20^\circ)$  cases. While the data points are seemingly on top of each other in the entire field range, a zoomed in view of the  $H > 0$  region allows visualizing how the  $\gamma$  angles are the same in remanence and deviate for larger applied field values [see Fig. 3.20(b)]. This is because as the field increases in the  $\chi = 20^\circ$  case, the magnetization is

pulled out more and more by the augmenting  $H_z$  field component, thus impeding the slight better alignment of magnetization towards the  $x$ -axis configuration promoted by the  $H_x$  field component. In the  $\chi = 0^\circ$  case, the in-plane magnetization is about  $1.5^\circ$  closer at 2.2 kOe upon the existence of a single applied field component along the  $x$ -axis. On the other hand, the out-of-plane angle  $\psi$  for  $\chi = 0^\circ$  seems to be well aligned around the  $\psi = 90^\circ$  line (Co film plane), but the curve displays a small linear slope caused by the non-ideal ( $\sim 0.5^\circ$ ) alignment of the  $\chi = 0^\circ$  electromagnet position with the Co film plane [see Fig. 3.20(c)]. In addition, the out-of-plane magnetization tilting is clear for the  $\chi = 20^\circ$  dataset, revealing that an  $H_z = H \cos \chi$  field of about  $\sim 700$  Oe pulls out the magnetization about  $\psi \sim 1.5^\circ$  from the magnetostatic- and magnetocrystalline-anisotropy-promoted in-plane magnetization configuration.

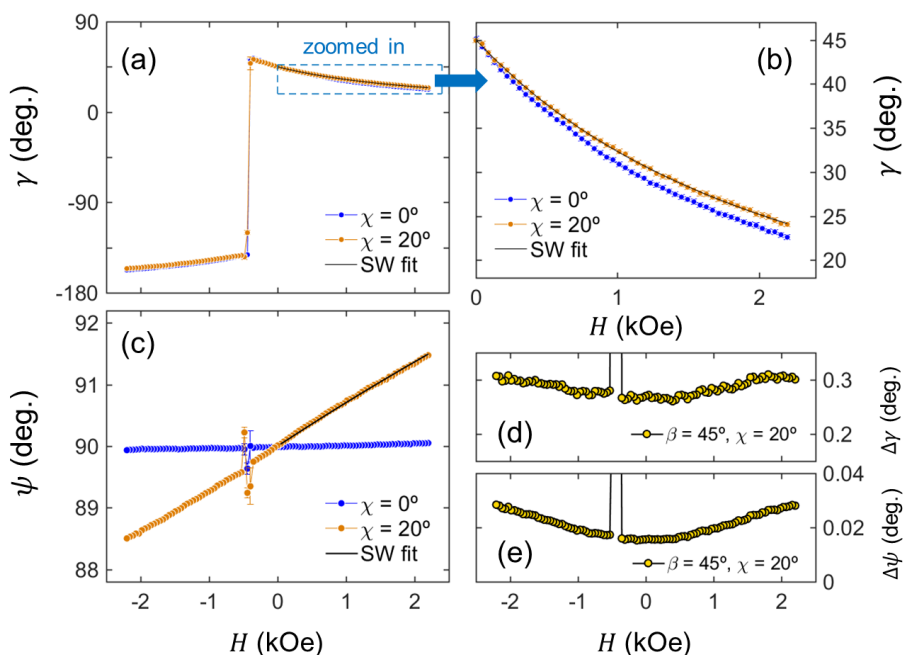


**Fig. 3.20:** Three-dimensional vector magnetometry of a 30-nm-thick epitaxial Co film performed via GME. Field dependent (a), (b) in-plane magnetization angle  $\gamma$  and (c) out-of-plane angle  $\psi$  during magnetization reversal. (d) and (e) show the precision in the determination of the magnetization angles  $\gamma$  and  $\psi$ , respectively, achieved during the fitting process. These amount to  $\sim 0.1^\circ$  and  $\sim 0.01^\circ$  for  $\gamma$  and  $\psi$ , respectively.

Thus with this experimental test, we demonstrate the feasibility to perform three-dimensional vector magnetometry via the GME technique, as the full field-dependent magnetization vector information during magnetization reversal was obtained via the analysis presented here. In addition, Figs. 3.20(d) and 3.20(e) display the error bar quantities for the fitted  $\gamma$  and  $\psi$  angles, respectively. A remarkable precision of the order of  $0.1^\circ$  and  $0.01^\circ$  is obtained for the in-plane and out-of-plane magnetization orientations, respectively.

To conclude with the magnetometry section, it is worth to point out that the knowledge of the three magnetization vector components contains very advantageous implications to characterize material properties, such as magnetic anisotropy energy densities and the exact orientation of the anisotropy axes in the laboratory frame. What it is even more, the magnetization dependent energy density for a thin film considering all three components of  $\mathbf{M}$  can now be written as

$$\epsilon = \epsilon_K + \epsilon_Z + \epsilon_M = K_1 \sin^2 \alpha + K_2 \sin^4 \alpha - M_S \mathbf{m} \cdot \mathbf{H} + 2\pi M_S^2 \cos^2 \psi, \quad (3.16)$$

where  $\alpha$  is the angle between the magnetization vector and the  $c$  axis of Co, and the magnetostatic energy term for a thin film has been added, which depends on the square of  $M_S$ . Due to this, one can now compare the experimental data in Fig. 3.20 to the energy model in Eq. 3.16, and attempt to fit the saturation magnetization value. The fit attempt reproduces very well the  $\gamma$  and  $\psi$  data for the  $\chi = 20^\circ$  case in the positive field range [see the fits represented in Figs. 3.20(a)-3.20(c) by the black solid lines]. The value of the fitted  $M_S$  for the Co sample in the experiment is slightly larger than the value obtained using VSM measurements, despite both being close to literature values. The discrepancy could be explained by the relatively large error made when estimating the film volume (especially in the case when the film is non-uniformly covering the substrate, such as on its edges) impacting the value obtained from VSM.

$M_S$ (emu/cm <sup>3</sup> ) via VSM	1340 ± 10 (0.7%)
$M_S$ (emu/cm <sup>3</sup> ) via GME	1522 ± 3 (0.2%)

**Table 3.3:** Comparison of room temperature saturation magnetization values obtained for a 30-nm-thick epitaxial Co film via conventional VSM and within the GME approach presented here. Both values are close to the room temperature reported values of  $M_S = 1440$  emu/cm<sup>3</sup> [54].

### 3.5 Optical anisotropy effects in epitaxial Co/CoO bilayers

The effect of different overcoats on the optical and magneto-optical properties of epitaxial hcp Co films was also investigated. Correspondingly, 30-nm-thick Co films were grown following the same procedure as in the previous section, but instead of depositing a SiO<sub>2</sub> protective layer, the uncapped Co film was exposed to ambient conditions for several days and let it oxidize. This process yielded 3-nm-thick strained CoO layers of crystalline character, as corroborated using transmission electron microscopy [152].

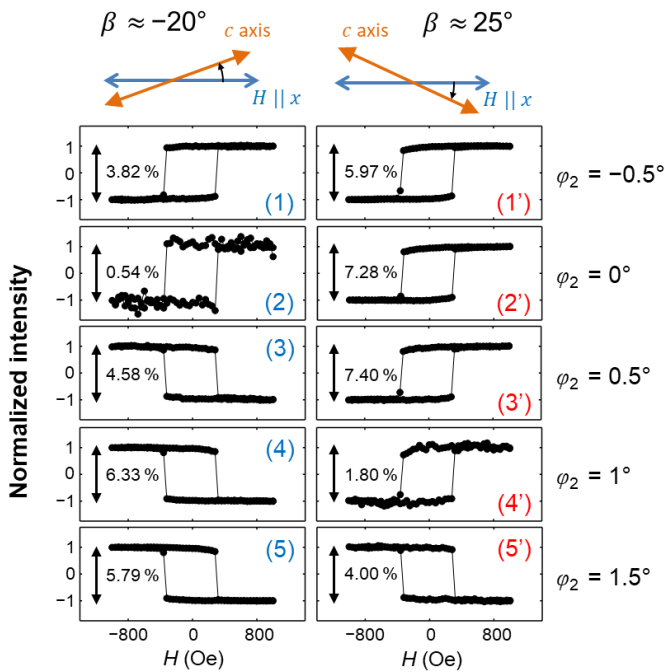


**Fig. 3.21:** MOKE hysteresis loops measured for an epitaxial hcp Co film with an ultrathin (3 nm), naturally oxidized epitaxial overcoat of CoO. Loops for different values of the analyzer angle  $\varphi_2$  are shown for two different orientations of the c-axis of Co with respect to the plane of incidence (right and left panels, see schematics of orientation on the top).

Subsequently, several hysteresis loop measurements were performed for different  $\varphi_2$  orientations while maintaining  $\varphi_1 = 90^\circ$ , until the signal-to-noise ratio is maximized. Examples of this procedure are depicted in Fig. 3.21, where sets of normalized hysteresis loops for two different sample orientations are shown. The magnetically-induced relative light intensity change is indicated by the bars that are shown to the left of each loop. For the first sample orientation, the angle between the

easy axis of magnetization and the direction of the magnetic field is about  $\beta \approx -20^\circ$ . The set of hysteresis loops corresponding to this particular sample orientation shows a minimum of the reflected light intensity near  $\varphi_2 = 0^\circ$ , in which the analyzer is nearly perpendicular to the reflected light polarization. This is also the orientation, for which the hysteresis loop signal inverts due to the symmetry of the magneto-optical response.

For a second experiment, the sample orientation was changed by  $45^\circ$  with respect to the first sample orientation, such that  $\beta \approx 25^\circ$ . The relative angle between applied field and easy axis is very similar to the first case, with the only difference that the angle is now positive. So, we expect that all the loops will show an equivalent hysteresis behavior and shape in both columns. Since the measurement configuration did not change, one should expect to find the compensation point at the same  $\varphi_2$  orientation, which is not the case: the smallest light intensity loop occurs at a shifted angular position,  $\varphi_2 = 1^\circ$ . This result represents an anomalous MO behavior, inconsistent with the general conventional descriptions of the MOKE effect.

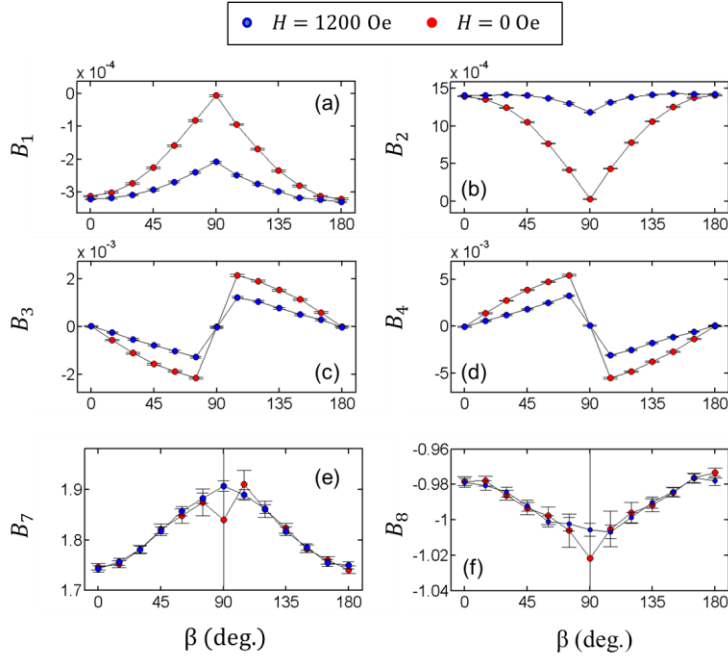


**Fig. 3.22:** Sample orientation dependent fitted (a)  $B_1$ , (b)  $B_2$ , (c)  $B_3$ , (d)  $B_4$ , (e)  $B_7$  and (f)  $B_8$  reflection matrix elements for  $H = 1200$  and  $0$  Oe, obtained for a 30-nm-thick epitaxial Co film capped with CoO.

The origin of this anomalous effect was explored by using the GME technique. Fig. 3.22 shows the fitted reflection matrix elements at 1200 and 0 Oe during reversal, for samples orientations  $\beta$  between 0 and  $180^\circ$ . For  $\beta = 0^\circ$ , the c-axis of Co is aligned

with the plane of incidence in the experiment. The data reveals that the optical reflectivity parameters  $B_7$  and  $B_8$  show a sinusoidal modulation in  $\beta$  with  $180^\circ$  periodicity [Figs. 3.22(e) and 3.22(f)], where a minimum and a maximum of their amplitude is observed for  $\beta = 0$  and  $90^\circ$ , respectively. One can conclude that this sample orientation dependence observation is indicative of an uniaxial optical anisotropy or birefringence, as the parameters  $B_7$ ,  $B_8$  are related to a purely optical effect.

The  $\beta$ -dependence of the additional fit parameters, which allow for systematic corrections of the GME datasets, are shown in Fig. 3.23. These are the polarizer angle corrections  $\varphi_{10}$  and  $\varphi_{20}$ , as well as the intensity offset parameter  $I_0$ . The fit goodness  $R^2$  is also included in Fig 3.23(d). The polarizer correction angles  $\varphi_{10}$  and  $\varphi_{20}$  [Figs. 3.23(a) and 3.23(b)] show a clear sinusoidal modulation with the same  $180^\circ$  periodicity, similar to the optical reflectivity parameters  $B_7$  and  $B_8$ . This shift of the  $(\varphi_1, \varphi_2)$  symmetry point in the  $\delta I/I$  maps (reaching values up to  $0.5^\circ$ ) is too large for being originated from the sample rotation wobble or typical misalignments of the plane of incidence, which typically amount to  $\pm 0.05^\circ$ . Furthermore, the shift cannot be ascribed to misalignments of the optical elements in the experimental setup, since a small tilt of the sample plane with respect to the incident light plane should cause a  $360^\circ$  variation of the structure instead of the observed  $180^\circ$  periodicities.

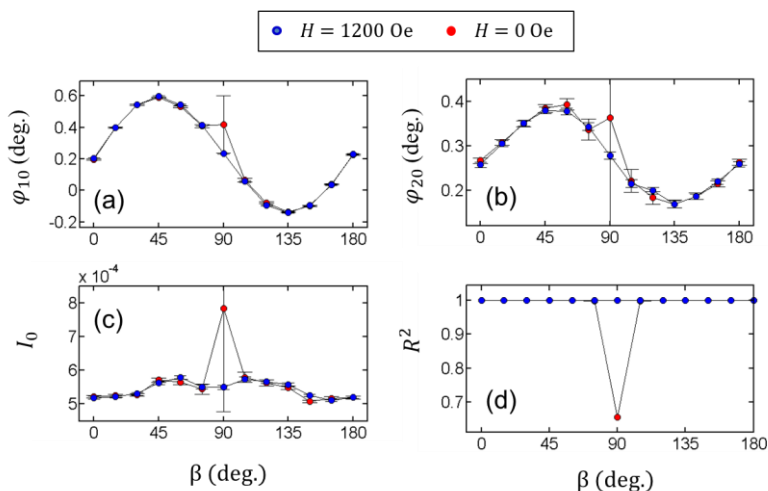


**Fig. 3.23:** Sample orientation dependent fitted correction parameters (a)  $\varphi_{10}$ , (b)  $\varphi_{20}$ , (c)  $I_0$ , as well as (d) fit goodness  $R^2$  the  $H = 1200$  and  $0$  Oe, cases, obtained for a 30-nm-thick epitaxial Co film capped with CoO.

Thus, one can conclude that optical anisotropy induces a shift of the origin of the  $\delta I/I(\varphi_1, \varphi_2)$  maps, such that a sample orientation dependent  $(\varphi_{10}, \varphi_{20})$  correction pair is introduced in the magneto-optical signal, depending on the relative angle between

the uniaxial axis and the plane of incidence [153]. This happens as a result of the anisotropic purely optical part of the dielectric tensor, which intermixes the incoming  $s$ - and  $p$ -polarization states even in the absence of magneto-optical effects. Yet the GME methodology still works [as illustrated by the high  $R^2$  values of the fits in Fig. 3.23(d)], in that one can fit the  $\delta I/I$  maps if a polarizer angle correction pair is assumed. This feature will be taken into account when studying the presence of optical anisotropy in epitaxial and patterned magnetic films (in Chapter 4 and 5, respectively).

Comparison of epitaxial hcp Co films with an oxidized overcoat and those in which a protective 10-nm-thick Ag layer confirmed that the strong uniaxial optical anisotropy originates from the CoO overcoat. In particular, angular dependent spectroscopic ellipsometry measurements of Co/Ag and Co/CoO samples reveal an isotropic angular dependence of the  $\tan \Psi = |r_p/r_s|$  quantity for Co/Ag, while a large uniaxial anisotropy is observed for Co/CoO (see Fig. 3.24).

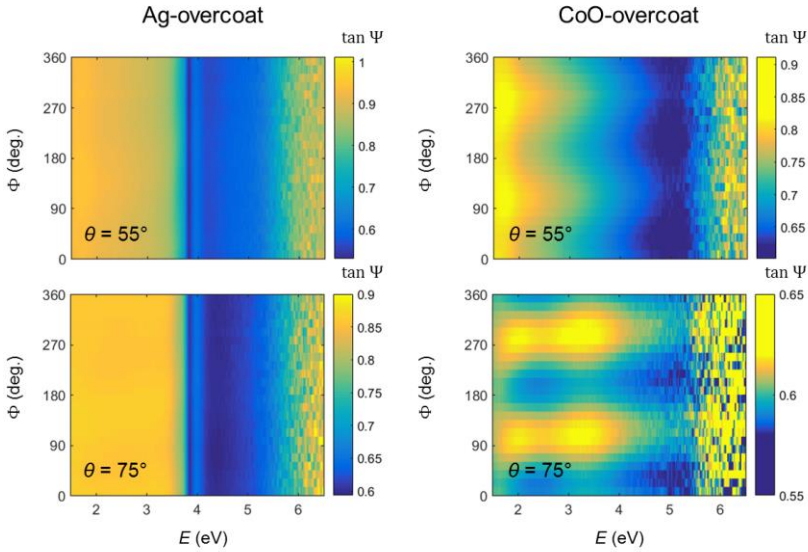


**Fig. 3.24:** Azimuthal angle-dependent spectroscopic ellipsometry measurements (in terms of  $\tan \Psi = |r_p/r_s|$ ) in the 1.5-6.5 eV photon energy range for 30-nm-thick epitaxial hcp Co films capped with a 10-nm-thick Ag overcoat (left panel) and a naturally oxidized CoO layer (right panel). Datasets for angles of incidence of  $55^\circ$  and  $75^\circ$  are included. The angle  $\Phi = 0^\circ$  corresponds to the setting in which the  $c$  axis of Co is contained in the plane of incidence. The strong feature at the photon energy of  $E = 3.8$  eV for the Ag-capped Co film (left panel) corresponds to the bulk Ag plasmon [121].

### 3.6 Measurement of non-uniform magnetization states

So far, uniform states of magnetization have been always considered during GME analysis. This allows to describe the reversal properties of the samples in terms of the magnetization rotation and switching mechanisms alone. However, it is a most common fact that multi-domain, intermediate states of magnetization can arise even in Stoner-Wohlfarth-like magnetic objects, such as the epitaxial hcp Co films with in-plane magnetic anisotropy that are investigated here. Even these highly oriented magnetic films display non-uniform magnetization states in the form of lateral ripple domains [112] when the field is applied near the magnetization hard axis orientation.

Such intermediate states were often observed in Section 3.4 as data points characterized by a typically low  $R^2$  value of the GME fit, since the  $\delta I/I$  expression in Eq. 3.5 cannot account for magnetization states other than a single-domain system with a well defined, unique magnetization orientation. Thus, it may at first seem like GME cannot generally deal with such non-uniform states of magnetization. Nevertheless, the large amount of information that we obtain in terms of the entire reflection matrix provides a way to circumvent this initial inconvenience of GME. It was shown by Berger and Pufall that a reduction of the net magnetization  $M$  due to the presence of non-uniform magnetization states is perceived as a commensurate reduction of the magneto-optical coupling factor  $Q$  [128].

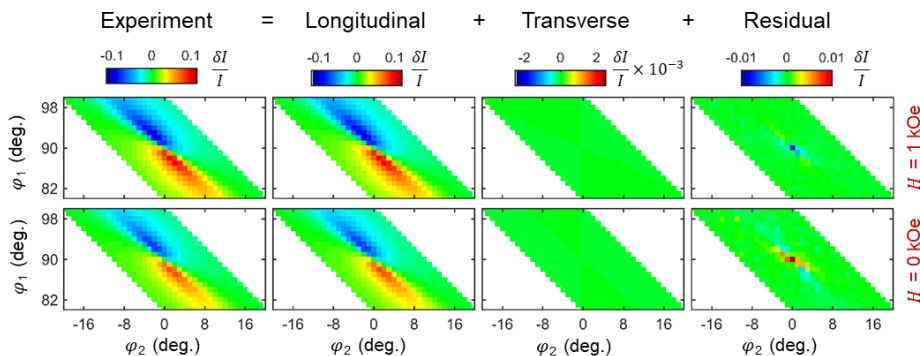


**Fig. 3.25:** Experimental color-coded  $\delta I/I$  datasets as well as the corresponding separation into longitudinal and transverse MOKE contributions enabled by the fitting process. Data acquired for 100-nm-thick polycrystalline sample deposited onto oxidized Si(001) substrates. A remarkable fit goodness of  $R^2 > 0.999$  is obtained in both cases. In this case, the data suggest that there is no appreciable transverse signal even at remanence, thus coherent magnetization rotation processes being absent.

In order to test that this result can be replicated with the setup employed in this thesis, GME measurements for a 100-nm-thick polycrystalline Co film are presented here. The uncapped Co film was sputter deposited on a Si/SiO<sub>x</sub> substrate. This growth process results into a granular film where hcp Co crystallites of few-tens-of-nm in size are randomly oriented and thus possess an even distribution of the preferential axis of magnetization. Due to magnetostatic effects, we expect the magnetization to be confined in the sample plane. Fig. 3.25 shows experimental  $\delta I/I$  maps (left column) for field values of 1 and 0 kOe (top and bottom). By following the fitting process, each map is separated into its longitudinal and transverse contribution. The residual maps indicating the difference between the experimental data and the fit are indicated as well. It is found that there is no apparent transverse magnetization signal in remanence, thus suggesting the absence of any transverse magnetization component  $m_y$ .

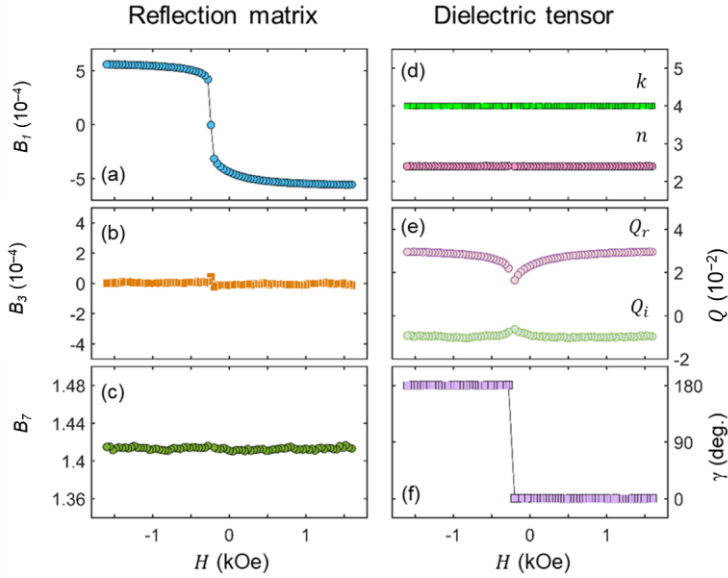


**Fig. 3.26:** In the left panel, field dependent reflection matrix elements (a)  $B_1$ , (b)  $B_3$ , and (c)  $B_7$ , measured for a 100-nm-thick polycrystalline Co film at an angle of incidence of  $\theta = 45^\circ$ . In the right panel, field dependence of the (d) refractive index, (e) magneto-optical coupling factor and (f) magnetization angle for the same polycrystalline 100-nm-thick Co film.

The complete field-dependent fitting results of the experiment are plotted in Fig. 3.26. The left panel shows the experimentally determined reflection matrix elements  $B_1$ ,  $B_3$  and  $B_7$  during magnetization reversal. The quantity  $B_1$  [Fig. 3.26(a)], which is proportional to the longitudinal magnetization  $m_x$ , undergoes a reduction of about 20% when going from magnetic saturation to remanence. On the other hand, the

parameter  $B_3$  associated with transverse MOKE is zero for the entire field range, pointing to the absence of coherent magnetization rotation processes during reversal [Fig. 3.26(b)]. The reflectivity term  $B_7$  in Fig. 3.26(c) is field-independent, as expected.

The field-dependent dielectric tensor of the sample is recovered by performing a best-match model fit to an optical model consisting of a semi-infinite single Co layer. While the refractive index  $N = n + ik$  is constant in the entire field range [Fig. 3.26(d)], both the real and imaginary part of the magneto-optical coupling factor  $Q$  undergo a slight reduction in their absolute value as the field is lowered towards the switching field,  $H_S \sim -200$  Oe [Fig. 3.26(e)]. The magnetization angle  $\gamma$  vs  $H$  plotted in Fig. 3.26(f) shows a bi-stable behavior, being fully aligned along the positive field axis ( $0^\circ$ ) before switching and with the negative field axis ( $180^\circ$ ) after switching.

This outcome can be explained in terms of the non-coherent magnetization rotation process during reversal. This effectively lowers down the longitudinal magnetization component as the field is lowered (and thus its associated longitudinal MOKE signal) by deflecting the magnetization of different grains in the film to both sides of the applied field axis with equal probabilities. The resulting multi-domain state of magnetization, despite the uniform magnetization assumption during the GME analysis, is perceived as a decrease of the  $Q$  modulus [128]. This observation thus allows quantifying the effective reduction of the coherently aligned magnetization vector, and in turn distinguishing coherent and non-coherent magnetization rotation processes. This way to measure the size of magnetization  $M$  will be implemented when investigating multilayer samples in Chapter 6.

## 3.7 Conclusions

In this chapter, the generalized magneto-optical ellipsometry (GME) technique was presented as a versatile and powerful tool to investigate the optical, magneto-optical and magnetic properties of thin films and multilayer structures. Special emphasis was put on the vector magnetometry capabilities of the technique, which yielded an unprecedented precision in the determination of the reflection matrix elements and magnetization angles. In particular, it was shown that polarization changes of the order of 10-to-100 nanoradians could be measured in terms of magnetization induced Kerr rotation. It is consequently demonstrated that such a narrow uncertainty on the knowledge of the polarization dependent reflectivity variables is translated to a precision of about  $\sim 0.1^\circ$  and  $\sim 0.01^\circ$  for the in-plane and out-of-plane magnetization vectors, respectively. This level of detection sensitivity was reached without any use of light modulation or lock-in techniques.

Throughout the chapter, the followed methodology was explained in detail, commenting aspects such as the mathematical formulation behind the GME technique and the improvements behind specific dataset choices in connection to uncertainties originated by the presence of noise. It was also found out that certain complications may arise when interpreting magneto-optical signals from materials featuring optical anisotropy or birefringence. A plausible data analysis route based on GME, however, has been provided to circumvent these difficulties.

The validity of the magnetometry strategy via GME was also tested on different magnetic thin films and multilayer samples, such as in sputter deposited Co/Pd multilayers and ferrimagnetic CoTb alloys with perpendicular magnetic anisotropy. The description in this chapter, however, is limited to the illustrative case of epitaxial hcp Co films, which possess a simpler magnetization reversal process and thus are an appropriate study case to highlight the capabilities of the GME technique.

Lastly, it is important to point out that it is not possible to obtain such a large amount of magnetization information with a conventional MOKE technique. Thus, GME proved to be an extremely useful and powerful magnetometry tool with state-of-the-art precision. The capabilities demonstrated throughout this chapter will set up the basis for the investigation of the physical phenomena described in the forthcoming chapters.



# Chapter 4

## Strain-induced magneto-optical anisotropy in epitaxial hcp Co films

*Based on the demonstrated vector magnetometry capabilities of the GME technique, the existence and origin of magneto-optical anisotropy in epitaxial hcp Co films is investigated in this chapter. The early observations of magneto-optical anisotropy are summarized prior to presenting measurements for our hcp Co films, which show a minimum of the magneto-optical coupling constant  $Q$  for magnetization orientations along the crystallographic  $c$  axis. By modifying the strain state of the films via a thickness dependent approach, it is demonstrated that relevant magneto-optical anisotropy exists and that its amplitude is strongly connected with epitaxial strain. The magnetocrystalline anisotropy of the samples is also studied in detail, as earlier reports identified a correlation of this quantity with magneto-optical anisotropy. A strategy is explored to control the magneto-optical properties of a film by its strain state modification, based on an underlayer crystal tuning approach.*

### 4.1 Introduction: early observations of magneto-optical anisotropy

In the vast majority of MOKE studies, it is assumed for the sake of simplicity that the strength of the magneto-optical coupling factor  $Q$ , which defines the magnetization dependent elements in the dielectric tensor, is independent from the magnetization orientation. While such a description may hold for homogeneous bulk-like magneto-optical properties, it does not consider the crystallographic structure and symmetry of the material. This aspect acquires crucial importance in the case of nanomagnetic entities, where the presence of surfaces, film-interfaces and crystal imperfections, such as dislocations and lattice distortions, play a major role in defining their physical properties. The influence of the symmetry reduction in nanometer thick scale magnetic films is corroborated, for instance, by the Néel's surface anisotropy in metallic multilayers. Here, the different energy landscape of the atoms located near the interface enables ultrathin film systems to develop an out-of-plane magnetic anisotropy, to the extent of being able to overcome the magnetostatic and magnetocrystalline anisotropy

energy contributions dominated by the bulk [154]. Indeed, it has been theoretically formulated that the local inter-atomic structure and bonding have a great influence on a broad variety of spin-orbit coupling related properties of magnetic materials [155]. In this way, such effects are expected to modify not only magnetic, but also optical and magneto-optical properties.

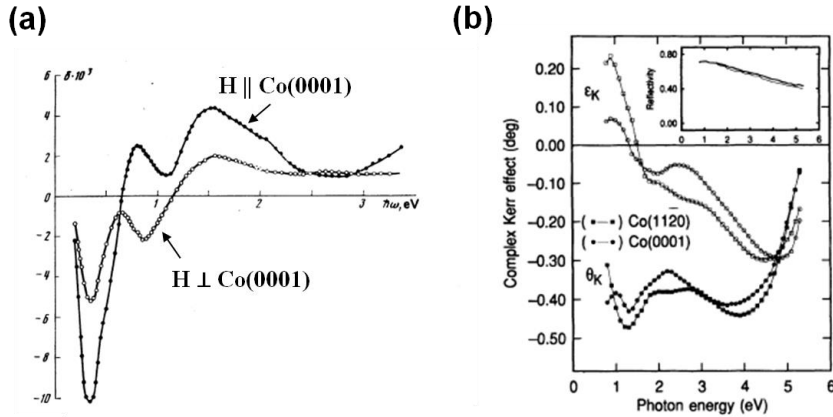


**Fig. 4.1:** (a) Wavelength-dependent transverse Kerr effect for a bulk Co-crystal for different relative orientations of the  $c$  axis and the applied field, (Ganshina *et al.* [156]). (b) Polar Kerr spectra for hcp Co films with different crystallographic textures (Weller *et al.* [157]).

Yet the consideration of isotropic magneto-optical effects is understood to be a reasonable assumption for metallic systems, where optical anisotropies overall are weak [158], and very few experimental studies have observed only modest deviations from this assumption in crystalline materials. More than 40 years ago, Krinchik and coworkers reported on an anisotropic magneto-optical signal in bulk-like FeSi and Ni single-crystal faces upon measuring the transverse Kerr effect for different orientations of the sample with respect to the applied field [159, 160]. The same group reported in 1980 an alike observation, named at the time as ‘orientation magneto-optic effect’, for crystalline hcp Co in the infrared and visible regions of the electromagnetic spectrum [156] [see Fig. 4.1(a)]. Following the early works on single-crystalline ingots, Weller and coworkers found dissimilar Kerr rotation and ellipticity spectra for epitaxial hcp Co films having  $(11\bar{2}0)$  and  $(0001)$  preferential crystallographic textures [Fig. 4.1(b)] [157]. A variation of up to 20% in Kerr rotation was found in between the two samples for the spectral range investigated (0.8-5.3 eV). Additional theoretical and experimental works regarding anisotropic MOKE spectra on uniaxial  $\text{CrO}_2$  [161] and Fe/Au superlattices [162, 163] have also been published.

All these prior works relied on different MOKE-setup geometries or even different samples in order to obtain  $Q$  values along different magnetization orientations. Moreover, measuring just the Kerr rotation or ellipticity does not directly allow a full understanding on the origin of the anisotropy. For instance, the complex polar Kerr effect for an optically thick magnetic film at near-normal incidence reads as [71]

$$\theta_K + i\varepsilon_K = \pm \frac{iNQ}{(N^2 - 1)}, \quad (4.1)$$

where the positive or negative sign is chosen depending on the polarization state of the incident light ( $p$ - or  $s$ -polarized, respectively). As both the refractive index  $N$  and the magneto-optical coupling factor  $Q$  are involved here, the anisotropic Kerr effect could originate from either optical or magneto-optical anisotropy. This drawback is also present in the case of the work reported by Osgood III *et al.*, which lacked a simultaneous optical and magneto-optical characterization method<sup>32</sup> despite being able to reproduce the results for hcp Co on a single sample [164]. Additionally, as all these experimental studies were performed in magnetic saturation conditions, none of them had measured the  $Q$  value along more than two magnetization orientations, the magneto-optical anisotropy being just evaluated from a two-point measurement without the estimation of error bars. Among more recent works, one reports on magneto-optical anisotropy for permalloy films with slanted columnar topography [135]. However, the authors did not separate magnetization orientation effects from  $Q$  anisotropy, so that magneto-optical anisotropy in the sense given here was not actually measured.

This has caused severe limitations for the accurate determination of magneto-optical anisotropy (MOA) so far, and more importantly it has prohibited the investigation of MOA in conjunction with other materials properties, so that its underlying physical origin is unexplored. For instance, relatively recent *ab-initio* calculations highlight the importance of the crystallographic texture (from the polycrystalline to single-crystal level) in the case of low symmetry ferromagnets such as hcp Co, CrO<sub>2</sub> or FePt [165].

Correspondingly, the quantitative accuracy and reliability of magneto-optical magnetometry, being a very common and widely utilized form of magnetometry, can be certainly compromised if MOA is not taken into account. This problematic is often mentioned [166] but at the same time circumvented in the literature, due to the more complicated analysis demanded by the presence of anisotropic magneto-optical effects.

---

<sup>32</sup> In the experiment by Osgood III *et al.*, the optical constants were measured via spectroscopic ellipsometry from a different polycrystalline Co film [164].

If MOA exists, the conversion of MOKE data into magnetization vector information is not trivial anymore, and can lead to an inaccurate real-space description of the magnetization. MOKE magnetometry has been utilized to obtain the canting angle of magnetization during the thickness-dependent spin reorientation transition of an ultrathin Co film [140]. Similarly, Vomir and coworkers show the projections of the longitudinal, transverse and polar Kerr effects during the ultrafast demagnetization process of an epitaxial Co film [167]. These and many other studies claim that the real space trajectories of the magnetization are obtained by following an isotropic  $Q$  dielectric tensor analysis. However, the presence of MOA, if overlooked, can lead to severe misinterpretations of the MOKE data upon extracting the magnetization vector information, so that care must be taken to avoid complications arising from MOA. In this regard, it is interesting to explore the origin and interplay of MOA with other sample parameters, in order to avoid complications whenever vector information of the magnetization needs to be investigated.

In view of this, a proper data analysis and measurement path description under these effects is crucial at the present time. In particular, advantage will be taken from the vector magnetometry capability of the GME-technique demonstrated in the previous chapter. This will enable to retrieve multiple  $Q$  vs magnetization angle data, leading to a more robust quantification of MOA. Moreover, the employed methodology can also identify separate the contributions from optical anisotropy and MOA, giving a more accurate description of MOA solely in terms of  $Q$ .

## 4.2 Observation of magneto-optical anisotropy via GME methodology

In the preceding chapter, I have shown that the GME allows the determination of the refractive index  $N = n + i\kappa$ , the magneto-optical coupling factor  $Q = Q_r + iQ_i$  and the vectorial information of magnetization, all within a single measurement scheme. However, all these quantities were shown with respect to the applied field strength.

I recover the data measured for the 30-nm-thick epitaxial hcp Co film for different relative orientations of the applied field and the  $c$  axis of Co within the plane of the sample. In Chapter 3, the obtained field dependent  $N$ ,  $Q$  and magnetization angle  $\gamma$  data were determined using the following form of the dielectric tensor

$$\vec{\epsilon} = (n + i\kappa)^2 \begin{pmatrix} 1 & iQm_z & -iQm_y \\ -iQm_z & 1 & iQm_x \\ iQm_y & -iQm_x & 1 \end{pmatrix}, \quad (4.2)$$

that is, assuming that the strength of magneto-optical coupling in the material is magnetization orientation independent. We prove the validity of such an approximation by looking more carefully into the magneto-optical coupling factor  $Q$  data fitted upon using the dielectric tensor in Eq. 4.2.

Fig. 4.2 shows the best-matching model parameters for the optical and magneto-optical constants of the 30 nm thick Co film directly vs the magnetization orientation data, which is also obtained from the best-matching optical model fit. Results are shown for sample orientations<sup>33</sup>  $\beta = 0^\circ, 45^\circ, 55^\circ, 65^\circ, 75^\circ$  and  $85^\circ$ .

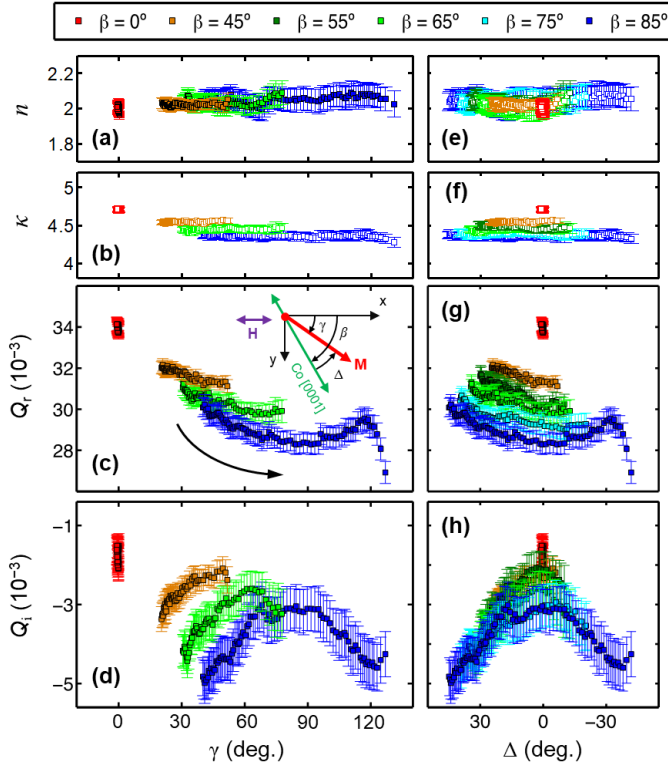


**Fig. 4.2:** Magnetization orientation dependence of refractive index  $N = n + ik$  and MOKE coupling factor  $Q = Q_r + iQ_i$ . (a)  $n$  and (b)  $\kappa$ , (c)  $Q_r$  and (d)  $Q_i$  vs magnetization angle  $\gamma$  as defined in the laboratory frame for different sample orientations  $\beta$ . The inset in (c) defines the angles between the  $c$  axis, the magnetization orientation, and the applied field. The curved arrow in the inset of (c) indicates the magnetization rotation direction prior to magnetization switching. (e)  $n$ , (f)  $\kappa$ , (g)  $Q_r$ , and (h)  $Q_i$  vs the magnetization angle  $\Delta$ , which is defined in the crystal frame as the deviation from the  $c$  axis of Co.

<sup>33</sup> The datasets for  $\beta = 0^\circ, 45^\circ, 65^\circ$  and  $85^\circ$  are only shown in the left panel for clarity.

The data in this figure correspond to the range in between maximum applied field strengths of 2 kOe and the field value right before the switching field, which varies as a function of  $\beta$  between  $-0.4$  and  $-1.5$  kOe. The left panel of the figure shows the dependence of the optical and magneto-optical constants on the magnetization orientation  $\gamma$ , which is defined in the laboratory frame. As it can be expected, the datasets with larger  $\beta$  values have also a larger extension on the  $\gamma$ -axis range, given the more pronounced rotation process during reversal. This fact is illustrated by the  $\beta = 0^\circ$  dataset, which has a nearly zero extension along the horizontal axis. This is because the magnetization reverses here by means of the switching mechanism alone and with the absence of the rotation process, such that it covers practically no range in  $\gamma$  when the field is applied along the easy axis of the film.

Both  $n$  and  $\kappa$  data [Figs. 4.2(a) and 4.2(b)] are independent of  $\gamma$  within our level of precision. In contrast, the  $Q_r$  [Fig. 4.2(c)] and  $Q_i$  [Fig. 4.2(d)] values show a clear modulation with respect to the magnetization orientation  $\gamma$ . The data in Fig. 4.2(c) is accompanied by an arrow that indicates the course of the magnetization angle during reversal. The high field data corresponds to the low  $\gamma$  values in each of the datasets. Upon reducing the field, the magnetization rotates by increasing its  $\gamma$  value. The  $Q_r$  and  $Q_i$  data lower their absolute value together with this rotation process, reach a minimum and start to increase again until the  $\gamma$  value at which magnetization switching occurs is reached in the horizontal direction.

This observation is a clear indication of magneto-optical anisotropy, that is, the measured  $Q$  amplitude is not equal when the magnetization is oriented along different directions in the material. The minimum values of the real and imaginary part of  $Q$  do not seem to happen around the same  $\gamma$  value for different  $\beta$  datasets. Correspondingly, different  $\beta$  datasets do not overlap and therefore indicate that  $\gamma$ , which is defined by the plane of incidence (or by the laboratory frame), is not a good variable to describe this anisotropy. In fact, it is seen that each dataset reaches the minimum value of  $Q$  approximately at  $\gamma = \beta$ . Hence, a consistent description is achieved, if one uses the sample's crystallographic orientation as a reference. Figs. 4.2(e)-4.2(h) show the experimental data again, but now vs  $\Delta$ , which is the magnetization angle with respect to the crystallographic  $c$  axis. The relation between the angles  $\gamma$ ,  $\beta$  and  $\Delta$  is explained in the inset of Fig. 4.2(c), which reads as  $\Delta = \gamma - \beta$ .

While the trend of the optical constants is unaffected by this change in representation [Fig. 4.2(e) and 4.2(f)], the  $Q_r$  [Fig. 4.2(g)] and  $Q_i$  [Fig. 4.2(h)] vs  $\Delta$  data now exhibit a consistent behavior by collapsing onto the same center point and showing symmetric behavior with respect to  $\Delta = 0^\circ$ . This confirms that the existence of a magneto-optical anisotropy effect originating from the specific crystal symmetry. It is

interesting to point out that in the case of  $\beta = 85^\circ$  a further reduction on the absolute value of  $Q_r$  and  $Q_i$  happens right before magnetization switching, at the high end of the  $\Delta$  values. This weak reduction in  $Q$  is explained by the appearance of regions with non-uniform magnetization states, corresponding to ripple domain structures, appearing for applied field orientations near the hard-axis of uniaxial ferromagnets [88].

The data in Fig. 4.2 do not only reveal the anisotropic behavior of MOKE in our Co films, but also gives a signature of the presence of optical anisotropy. This is most evident from the refractive index data, where the  $\kappa$  data are shifted for different  $\beta$  datasets. A similar thing can be said for the  $Q_r$  and  $Q_i$  values, given that the data for different sample orientations  $\beta$  do not collapse on top of each other when represented vs  $\Delta$ , but are instead vertically shifted from dataset to dataset, despite keeping the same functional form. Although the simultaneous presence of optical and magneto-optical anisotropy in our samples builds up a complex scenario, this example is actually very illustrative in the sense that one can exactly distinguish what is the effect of each of the anisotropies, given the ability of the GME-methodology to characterize all  $n$ ,  $\kappa$ ,  $Q_r$ ,  $Q_i$  and  $\Delta$  simultaneously. The presence of the optical anisotropy is reflected as a vertical shift of the  $N$  and  $Q$  for different  $\beta$  values, whereas the signature of MOA is reflected in the unequivocal modulation of  $Q$  vs  $\Delta$  for each sample orientation  $\beta$ . The symmetric behavior of  $Q$  around the  $\Delta = 0^\circ$  symmetry point ( $c$  axis of Co) also confirms that the modulation can be regarded as a crystal symmetry induced anisotropy. This is a big advantage with respect to the previous works reporting MOA on hcp Co films [157, 164], as the lack of a simultaneous optical and magneto-optical characterization does not allow to resolve MOA from optical anisotropy.

As in the case of Co films capped with a strained Co-oxide layer which exhibit a considerably high optical anisotropy [153], the here observed optical anisotropy is attributed to the overcoat as well. Although  $\text{SiO}_2$  generally grows in its amorphous form (being homogeneous and transparent for visible light) a very thin Co-oxide might have formed during its deposition. Upon considering a birefringent  $\text{SiO}_2$  capping layer, its uniaxial anisotropic dielectric tensor read as

$$\vec{\epsilon}_{\text{SiO}_2} = \begin{pmatrix} N_e^2 & 0 & 0 \\ 0 & N_o^2 & 0 \\ 0 & 0 & N_o^2 \end{pmatrix}, \quad (4.3)$$

where  $N_e = n_e + i\kappa_e$  and  $N_o = n_o + i\kappa_o$  are the refractive indices of  $\text{SiO}_2$  along the extraordinary and the ordinary optical axes of the uniaxial overlayer, respectively.

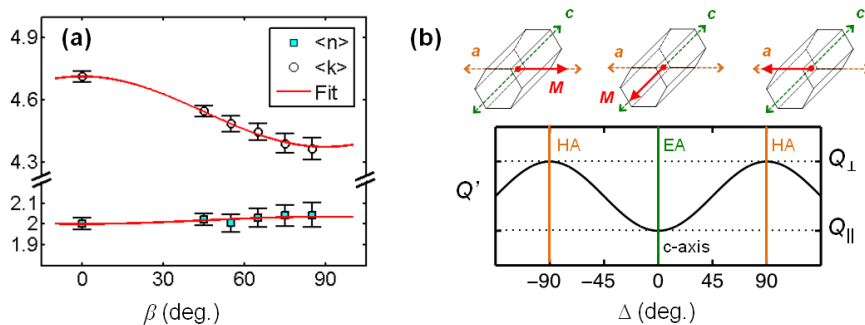


**Fig. 4.3:** (a) Correction of optical anisotropy realized by assuming a birefringent SiO<sub>2</sub> capping layer. (b) Dependence of the perceived magneto-optical coupling factor  $Q'$  with the magnetization angle  $\Delta$ , under the assumption of uniaxial MOA. The schematic represents the magnetization orientations along the easy axis (EA,  $\Delta = 0^\circ$ ) and hard axis (HA,  $\Delta = \pm 90^\circ$ ) of the hcp Co lattice.

Fig. 4.3(a) shows the  $\beta$ -dependent  $\langle n \rangle$  and  $\langle \kappa \rangle$  values, which are the averaged values measured in each  $\beta$  dataset. The symmetry of the dielectric tensor in Eq.4.3 can now be applied to extract what are the optical constants of SiO<sub>2</sub> along the extraordinary and ordinary axis, by fitting the  $\langle n \rangle$ ,  $\langle \kappa \rangle$  data to a sinusoidal behavior with  $2\beta$  periodicity<sup>34</sup>. The best-match model fit is shown in the figure as the solid lines superimposed to the data. The extraordinary axis of the overcoat is well aligned with the  $c$  axis of Co. The refractive indices  $N_e$  and  $N_o$  for the overcoat are obtained in this way, finding that the absolute anisotropy values  $\Delta n = n_e - n_o$  and  $\Delta \kappa = \kappa_e - \kappa_o$  amount  $-0.13$  and  $0.32$ , respectively.

Complementarily, the presence of MOA reflects the need for considering a dielectric tensor for Co with dissimilar magneto-optical coupling strengths for different orientations of magnetization in the material. If defined in the crystal lattice reference frame, this reads as

$$\vec{\epsilon} = (n + i\kappa)^2 \begin{pmatrix} 1 & iQ_z \cos \psi & -iQ_\perp \sin \psi \sin \Delta \\ -iQ_z \cos \psi & 1 & iQ_\parallel \sin \psi \cos \Delta \\ iQ_\perp \sin \psi \sin \Delta & -iQ_\parallel \sin \psi \cos \Delta & 1 \end{pmatrix}, \quad (4.4)$$

<sup>34</sup> A slightly absorptive SiO<sub>2</sub> overcoat needs to be considered here, given that the modulation in  $n$  and  $k$  perceived for Co are not of the same size. This could be caused by the presence of slightly Si-rich parts in the overcoat, which in its amorphous form has an imaginary part of the refractive index of  $\kappa_{\text{SiO}_2} = 0.42$  [168].

which represents an optically isotropic Co layer, but has the most general form to account for uniaxial MOA. In our experiment, the angle  $\psi$  between the z-axis and the magnetization is  $90^\circ$ , while the in-plane angle  $\Delta$  varies during magnetization reversal. Hence, we access a two-dimensional projection of the dielectric tensor<sup>35</sup>, while not measuring  $Q_z$ . The quantities  $Q_{\parallel}$  and  $Q_{\perp}$  denote the magneto-optical coupling strength for magnetization orientations parallel and perpendicular to the crystallographic  $c$  axis [see the schematic in Fig. 4.3(b)]. Under the presence of such an anisotropic dielectric tensor, and for in-plane magnetization orientations in the employed experimental geometry, the perceived magneto-optical coupling factor  $Q'$  can be expressed as<sup>36</sup>

$$Q'(\Delta) = \frac{Q_{\perp} + Q_{\parallel}}{2} \left( 1 - \frac{\tau}{2} \cos 2\Delta \right), \quad (4.5)$$

which is an oscillatory function of periodicity  $2\Delta$ , taking values in between the boundaries  $Q_{\parallel}$  and  $Q_{\perp}$ . The fractional modulation amplitude of  $Q'$  has been defined as

$$\tau = \frac{Q_{\perp} - Q_{\parallel}}{(Q_{\perp} + Q_{\parallel})/2}, \quad (4.6)$$

which is a measure of the magneto-optical coupling strength variation upon magnetization orientation changes in the crystal. The functional form of Eq. 4.5 has been reproduced in Fig. 4.3(b) by assuming a positive value of  $\tau$ . For this choice,  $Q'$  takes its minimum value when the magnetization lies along the  $c$  axis of Co ( $Q_{\parallel}$ ), increasing upon deviating the magnetization away from this orientation and towards the basal plane of Co, where the maximum magneto-optical coupling strength occurs ( $Q_{\perp}$ ).

Fig. 4.4 shows the optical and magneto-optical constants for the measurements performed on the 30-nm-thick epitaxial hcp Co film (as in Fig. 4.2), upon including a birefringent overcoat in the optical model. As exemplary cases, the  $\beta = 65^\circ$ ,  $75^\circ$ , and  $85^\circ$  datasets are shown here, where  $n$ ,  $\kappa$ ,  $Q_r$  and  $Q_i$  are represented vs both  $\gamma$  (left panel) and  $\Delta$  (right panel). Now, it is seen that the  $Q_r$  and  $Q_i$  datasets with distinct  $\beta$  collapse on top of each other. Given that the existing optical anisotropy is now captured by the overcoat in the sample, the Co film purely shows the effect of MOA alone, such

---

<sup>35</sup> For the hcp Co crystal structure, it is expected  $Q_z$  and  $Q_{\perp}$  to be nearly identical, because both describe magneto-optical coupling for basal plane orientations of magnetization.

<sup>36</sup> While  $Q$  is a complex quantity, the modulation function in Eq. 4.5 is understood to mimic the behavior of one of its real projections, such as the real or imaginary part and its modulus.

that  $Q$  datasets display a modulation of their magnitude with magnetization angles, without exhibiting any shift from one  $\beta$ -dataset to another.

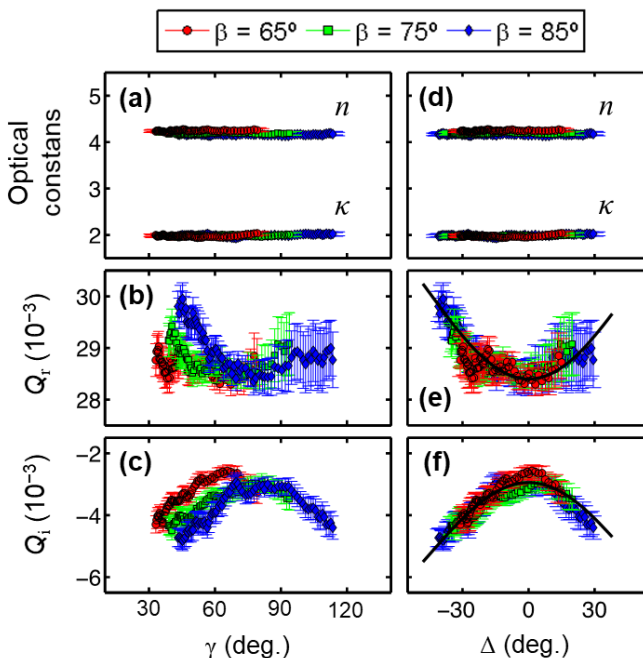


**Fig. 4.4:** Magnetization angle dependence of the optical constants and the magneto-optical coupling factor, upon consideration of an optically anisotropic overcoat. (a)  $n$  and  $\kappa$ , (b)  $Q_r$  and (d)  $Q_i$  vs  $\gamma$ , for the datasets with  $\beta = 65^\circ, 75^\circ$  and  $85^\circ$ . (d)  $n$  and  $\kappa$ , (e)  $Q_r$  and (f)  $Q_i$  vs the angle  $\Delta$ . The solid lines in (e), (f) represent the least-squares fits of the data to Eq. 4.5.

Given the rather low maximum applied field provided by the electromagnets (approximately  $\pm 2.3$  kOe, with  $\pm 2.0$  kOe in this experiment) as compared to the anisotropy field of the Co films ( $> 3$  kOe), one cannot measure the full modulation of the perceived magneto-optical coupling factor  $Q'$  as it is depicted in the Fig. 4.3(b). As seen in Figs. 4.4(e) and 4.4(f), the maximum  $\Delta$  range that can be accessed is of around  $70^\circ$ . However, a considerable amount of datapoints in this range are obtained, which is enough to reliably extract all the relevant parameters such as  $Q_{\parallel}$ ,  $Q_{\perp}$  and the modulation  $\tau$  by fitting the experimental data to Eq. 4.5. We find the data to be fully consistent with this crystal symmetry induced  $Q$  anisotropy, as demonstrated by the overlap of the experimental data with the least-squares fits represented by the solid lines in Figs. 4.4(e) and 4.4(f). It is found that the anisotropy amplitude for  $Q_r$  is 11.1%, and 88.1% for  $Q_i$ . The percentage in modulation is particularly large given that  $Q_i$  in hcp Co inverts its sign near the 1.95 eV photon energy employed for this study [164].

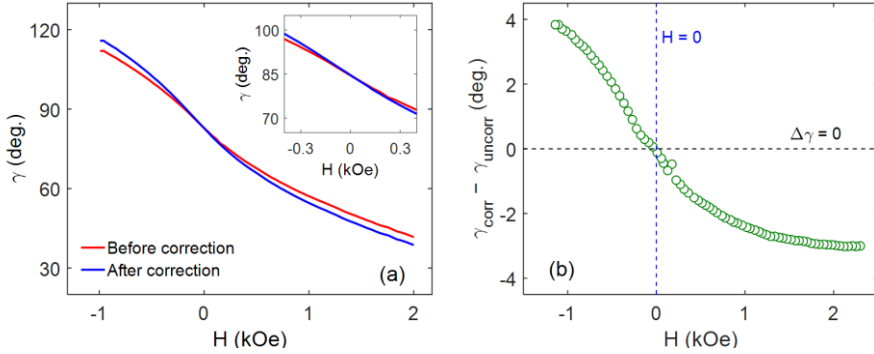


**Fig. 4.5:** (a) Magnetization angle  $\gamma$  vs applied field  $H$  during magnetization reversal at the  $\beta = 85^\circ$  orientation showing both the uncorrected and corrected  $\gamma$  values. The inset highlights their coincidence at  $H = 0$ ,  $\gamma = \beta = 85^\circ$ . (b) Difference  $\Delta\gamma = \gamma_{corr} - \gamma_{uncorr}$  vs  $H$ .

A relevant conclusion to derive from this study consists on the impossibility to determine the anisotropic  $Q$  and the magnetization angle from an individual  $\delta I/I$  map alone. Instead, complete datasets sampling several magnetization orientations over an extended range are needed, in order to retrieve  $Q$  values along different orientations. This in turn implies that the magnetization angles  $\gamma$  and  $\Delta$  retrieved from individual  $\delta I/I$  map fits have to be corrected by implementing the magneto-optically anisotropic dielectric tensor of Eq. 4.4 in the optical model.

Upon analyzing the data on a second iteration, the corrected magnetization angle values are obtained. The outcome of this second iteration is displayed in Fig. 4.5(a), where  $\gamma$  vs  $H$  magnetization reversal data for the  $\beta = 85^\circ$  sample orientation are presented. Both uncorrected (the values used so far) and corrected  $\gamma$  vs  $H$  are shown here. The differences from one dataset to the other can reach up to  $4^\circ$  [see Fig. 4.5(b)]. It is also seen that both datasets coincide at  $\gamma = \beta = 85^\circ$ , which furthermore happens at zero field,  $H = 0$ .

It is reasonable to find that the magnetization angle values do not need to be corrected at  $H = 0$ , when the magnetization points along the  $c$  axis of Co, this being one of the two principal axes in the material. In such a case, all magneto-optical effects are solely defined by  $Q_{||}$ , as any magnetization component along the basal plane of Co nulls out. Upon this configuration, the hcp Co film is ‘momentarily magneto-optically isotropic’, as only one of the two dissimilar magneto-optical coupling factors has influence on MOKE effects.

### 4.3 Study of Co films with varying thickness

For the purpose of investigating the general relevance and the origin of MOA, this type of measurement and data analysis scheme is repeated for an entire series of epitaxial hcp Co films with thicknesses of 5, 15, 50, 100 and 150 nm. The good epitaxial quality in the entire thickness range is clearly demonstrated by Fig. 4.6, where symmetric  $\theta$ - $2\theta$  scans for the different samples are shown. While the Ag- and Cr-peaks look virtually the same for all samples, the first and second order Co-peaks change substantially in their relative intensity due to the varying Co film thickness.

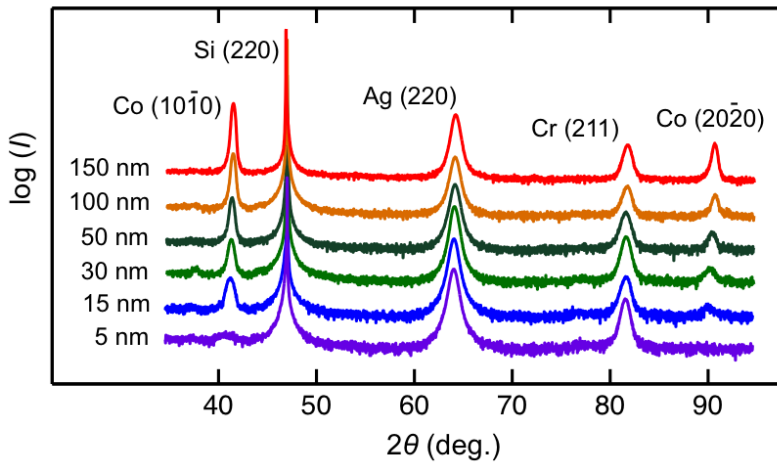


**Fig. 4.6:** X-ray diffraction  $\theta$ - $2\theta$  scans for the sample series with varying Co-thickness. The datasets are vertically shifted for clarity.

GME measurements revealed that the magneto-optical coupling factor is magnetization orientation-dependent for all the sample series with different Co thickness. In order to summarize the representation of the data, the coupling factor is expressed as  $Q = \tilde{Q}e^{i\theta}$ , focusing on the orientation dependence of the modulus  $\tilde{Q}$ . Figs. 4.7(a)-4.7(c) display the magnetization orientation dependence of  $\tilde{Q}$  for the Co films with 15 nm, 50 nm and 150 nm thickness. The  $\beta = 75^\circ$  case is only shown here for clarity of the plot. As for the 30-nm-thick sample, the modulus of the coupling factor  $\tilde{Q}$  takes its minimum value when the magnetization is oriented along the easy axis. It is seen that the thinner Co films (15 and 50 nm thickness) show a more pronounced modulation with magnetization orientation as compared to the thicker film (150 nm). The solid lines in Fig. 4.7 represent the fits to Eq. 4.5, from which the modulation amplitude  $\tilde{\tau}$  of the  $Q$  modulus is determined to be 18.8%, 12.0%, and 2.9% for the 15, 50 and 150 nm thick Co films, respectively. Thus, a remarkable reduction of MOA with increasing film thickness is observed here.

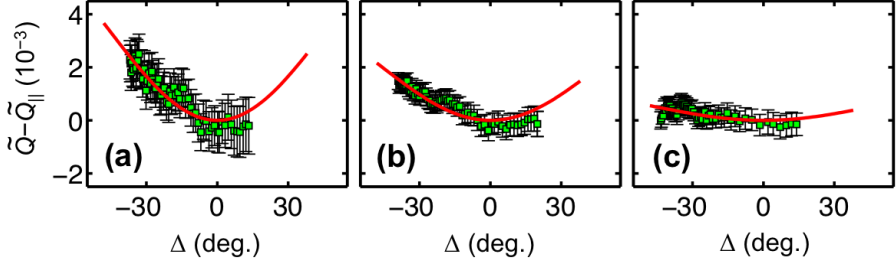


**Fig. 4.7:** Magneto-optical coupling constant  $\tilde{Q}$  vs  $\Delta$  for samples with (a)  $t_{Co} = 15$  nm, (b) 50 nm and (c) 150 nm. For all datasets,  $\beta = 75^\circ$  was used. The solid lines show the least-squares fits of the general dielectric tensor, Eq. 4.5, to the data.

Aiming to understand the observed thickness dependence of MOA, a more detailed structural study of the films is realized. Fig. 4.8(a) displays zoomed in x-ray diffraction data around the Co(10 $\bar{1}$ 0) reflection. It is observed that not only the relative height of the peak but also the peak position  $2\theta$  varies from sample to sample. In particular, the Co(10 $\bar{1}$ 0) peak position shifts towards higher values as the Co film thickness is increased. Furthermore, it is obvious that the peak position approaches  $2\theta_{bulk} = 41.56^\circ$  for thicker films. As the peak position can be directly related to the corresponding interplanar distance associated with the x-ray reflection, it can be concluded that the lattice constant in the basal plane of the hcp Co [see the inset in Fig. 4.8(a)] gradually reduces for increasing film thickness<sup>37</sup>.

Hence the x-ray data reveals that the hcp Co films grown are positively strained in the out-of-plane direction of the sample. This strain is thickness dependent as it tends to relax for increasing film thickness. This phenomenon is interpreted in terms of a thickness dependent strain relaxation process of the Co lattice. As the hcp Co is being grown on top of the bcc Cr underlayer, it is necessary for the Co film to first adopt the structure of the Cr lattice plane as a result of the heteroepitaxial matching of the two lattices, which possess different lattice constants [see the schematic in Fig. 4.8(b)]. In the low thickness regime of Co, the film is exerted to a strong mechanical coupling with the underlayer, being fully strained and thus deviating from their most stable bulk-like arrangement. However, as the film grows thicker, it is energetically more favorable to generate stacking faults in the Co crystal (in the form of a missing or dangling bond in the lattice) than preserving the lattice dimensions imposed by the underlayer [169, 170]. These defects, termed as misfit dislocations, are in general mobile and they propagate towards the interface where the mismatch occurs, since it is here where the stress needs

<sup>37</sup> For bulk hcp Co, we have  $a = 2.51 \text{ \AA}$  and  $a = 4.06 \text{ \AA}$  [171].

to be relieved. This reflects the fact that the lattice mismatch between Cr and Co causes the thin Co films to be more distorted, while this strain state is relaxed as the Co film thickness increases.

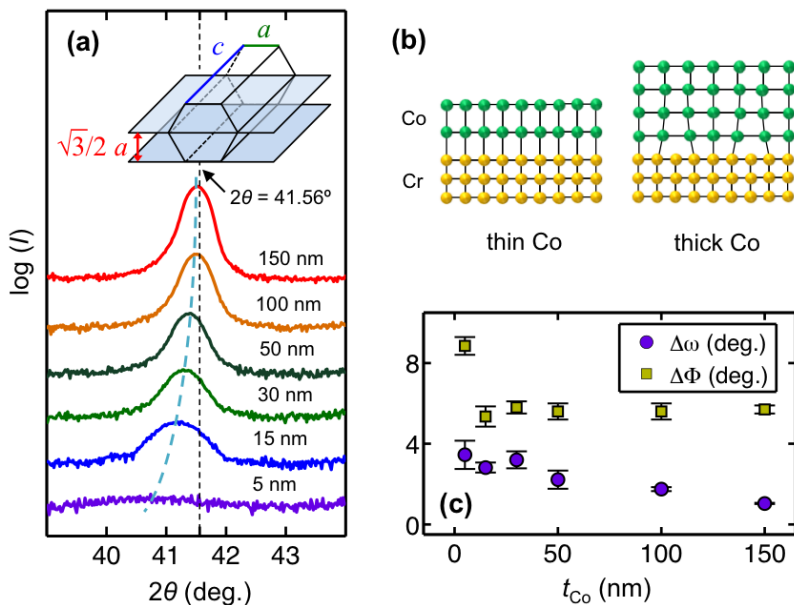


**Fig. 4.8:** Strain relaxation in hcp Co films. (a)  $\theta$ - $2\theta$  x-ray diffraction data for the Co(10 $\bar{1}$ 0) reflection in samples with varying Co thickness. The vertical dashed line indicates the peak position corresponding to bulk Co,  $2\theta = 41.56^\circ$ . The curved dashed line is a guide to the eye. The inset shows the particular interplanar distance of Co measured at this reflection. (b) Schematic of the Co film relaxation mechanism by forming dislocations during growth. (c) Co-thickness dependence of the rocking curve FWHM and phi-scan measurements performed for the Co(10 $\bar{1}$ 0) and Co(10 $\bar{1}$ 1) reflections, respectively.

It is also necessary to make an evaluation of the crystalline quality of the samples, in order to verify that the thickness dependent strain relaxation is triggered by the natural formation of misfit dislocations during growth, rather than due to accidental, non-repeatable deposition-related events (such as dirty or oxidized substrates, presence of impurities, etc.). For this purpose,  $\omega$ -scan (rocking curve) as well as  $\Phi$ -scan measurements for the Co(10 $\bar{1}$ 0) and Co(10 $\bar{1}$ 1) reflections, respectively, have been performed for the entire thickness series. The measured diffraction peaks are fitted to a Gaussian curve to extract the peak widths  $\Delta\omega$  and  $\Delta\Phi$ . The results are exhibited in the Fig. 4.8(c) which corroborate the sample independent good level of the out-of-plane and in-plane crystallographic alignment. The width of the rocking curve  $\Delta\omega$  shows a weak

linear decrease in Co film thickness, ranging in between  $1.04^\circ$  and  $3.45^\circ$  values. We attribute this thickness dependence to the apparent depth-dependent strain gradient of the samples. On the other hand, the  $\Delta\Phi$  is kept relatively constant around the average value of  $5.6^\circ$ , this being true for all films except for the 5 nm thick one, which possesses a slightly higher value of  $8.8^\circ$ . In any case, these results confirm the good crystalline quality and epitaxial alignment of all films independent of their thickness.

For a quantitative analysis, I have determined the strain level of the epitaxial Co films from their lattice constant  $a$  in the basal plane as

$$e_{zz}(\%) = 100 \times \frac{a - a_{bulk}}{a_{bulk}}. \quad (4.7)$$

The thickness dependence of the Co(10 $\bar{1}$ 0) peak position and the associated out-of-plane strain as calculated from Eq. 4.7 are shown in Fig. 4.9(a). It is seen that the  $2\theta$  peak position approaches the bulk value for the thickest films, while the corresponding strain value varies from a positive 1.5% to nearly zero as the Co film thickness is increased. In our case, the film thickness ( $t$ ) dependent strain decay, in opposition to the ultrathin film limit  $\sim 1/t$  law found by Chappert and Bruno [172], is better represented by [173]

$$e_{zz} = \frac{A}{t} \ln\left(\frac{e}{b}t\right) + e_{zz}^0, \quad (4.8)$$

where the amplitude  $A$ , the length of the Burgers vector  $b$  and the residual strain  $e_{zz}^0$  are treated as fit parameters. The fit to the strain data, displayed as the dashed line in Fig. 4.9(a) reveals a virtually zero residual strain and a fitted Burgers vector value of  $0.5 \pm 0.1$  nm. The agreement of the strain data with this equation<sup>38</sup> reflects on the fact that considerable strain values can still remain even in of few-tens-nm-thick films. This is the case of the samples studied here, where strain is largely diminished upon exceeding Co film thicknesses above 50 nm.

For the sake of comparison to the strain data, Fig. 4.9(b) shows the thickness dependent MOA amplitude  $\bar{\tau}$ . It is evident that both quantities show a very similar thickness dependent behavior. This becomes blatantly evident if the two quantities are plotted against each other, as it has been done in the inset of Fig. 4.9(b). The data display a clear linear correlation between both quantities, and thus provide evidence that the increase of MOA is strongly connected to epitaxial strain in our hcp Co films. The least-

<sup>38</sup> Caution is needed to assess the reliability of the fit parameters, as the introduction of misfit dislocations as a strain relaxation mechanism is highly temperature dependent [173].

squares fit of these data to a straight line reveals a  $\tilde{\tau}$  slope of  $16.8 \pm 1.4\%$  for every 1% strain increase, as well as an estimated residual MOA of  $3.3 \pm 0.8\%$  upon the absence of strain.

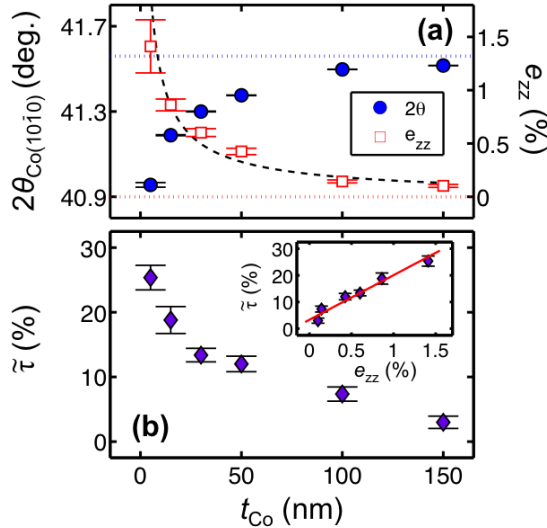


**Fig. 4.9:** Thickness dependent Co film properties; (a) x-ray diffraction peak position (circles) and associated  $e_{zz}$  strain values (squares). The dotted lines indicate the bulk values. The dashed lines represent the fit of the strain data to Eq. 4.8. (b) Magneto-optical anisotropy amplitude  $\tilde{\tau}$ ; the inset shows  $\tilde{\tau}$  vs  $e_{zz}$ .

From this correlation, it can be concluded that strain potentially induces a relevant MOA in epitaxial films, with a large value of up to 25% for the 5 nm Co film detected here. These observations show very clearly that MOA effects are not generally small, even in only weakly strained metallic films, for which the  $Q$  isotropy assumption is very widely utilized. This means that special care must be taken even for materials of high symmetry possessing barely any intrinsic MOA, as non-cubic lattice distortions may cause the dielectric tensor to be anisotropic. This is especially true for most common thin and ultrathin epitaxial films, for which strains far in excess of the 1.5% range explored here are typical. Thus the translation of the measured longitudinal, transverse and polar Kerr effects into magnetization vector components is not a trivial task under this situation. In fact, the assumption of an isotropic  $Q$  can lead to large misinterpretations of the real space trajectory of magnetization during reversal.

This study also permits to identify strain as a source for MOA. Previous works on this topic had (from the perspective of this thesis) a number of limitations which did not allow a complete and systematic study of the MOA, in particular when coming to

its joint investigation together with other physical properties, such as with structural properties. It is still worth to compare the main lines that can be concluded from this study with the insights that are found in literature. Motivated by the early experiments by Grinchik *et al.* for Ni [159], Parker offered a phenomenological explanation for MOA suggesting that its appearance was related to either second-order magneto-optical effects or magnetostriction [174]. We find these interpretations to be contrary to our results. Despite the fact that second-order Kerr effects can be anisotropic even in materials with cubic symmetry [175], the employed GME-methodology removes any second-order Kerr effects from the data, so that the here observed MOA cannot be caused by them. Magnetostriction, on the other hand, should show a thickness dependence opposite to what it has been found here, since thicker epitaxial films would undergo larger shape changes than thinner ones due to the reduced relevance of the mechanical coupling to the substrate.

It has also been reported that MOA could arise from third-order magneto-optical Kerr effects [176]. While this hypothesis deserves a cautious consideration, it is very unlikely that the third-order effects can possess such a considerable strength to explain magnetization orientation dependent variations of the MOKE response as big as a quarter of the total signal. Extended experiments on second-order Kerr effects in Co proved that their strength is at least one to three orders of magnitude smaller than the first-order Kerr effects [177]. We thus expect the third-order contributions to be insufficient to explain MOA values in the range from 3-to-25%.

Driven by the fact that earlier studies (both theoretical and experimental) reporting the appearance of MOA put a considerable emphasis on the correlation with magnetocrystalline anisotropy (MCA) [157, 162, 164, 178, 179], this aspect of the samples has also been investigated in conjunction with their structure and magneto-optical properties. Furthermore, the joint investigation of MOA and MCA can assist giving a deeper insight of the spin-orbit coupling phenomenon, from which both effects originate. It is also well established that strain induces magnetic anisotropy by means of magnetoelastic coupling [36, 170, 173]. As already discussed in the preceding chapter, one can fit the field dependent magnetization angle data to quantify the magnetic anisotropy energy density parameters of the material. A Stoner-Wohlfarth model with first- and second-order magnetic anisotropy energy terms is considered

$$\epsilon_K = K_1 \sin^2 \Delta + K_2 \sin^4 \Delta = K_1 \sin^2(\gamma - \beta) + K_2 \sin^4(\gamma - \beta), \quad (4.9)$$

to mimic the uniaxial in-plane magnetic properties of the hcp Co films. The magnetization angle vs  $H$  data comparison to the above equation enables obtaining the

first- and second-order anisotropy fields  $H_{K1} = 2K_1/M_S$  and  $H_{K2} = 4K_2/M_S$ , as well as locating the exact orientation of the magnetic easy axis ( $c$  axis) of Co in the sample.

Figs. 4.10(a) and 4.10(b) exhibit magnetization angle vs applied field data for 15-nm- and 100-nm-thick samples, respectively, in the range from 2.3 kOe to remanence for applied field angles  $\beta = 0^\circ, 45^\circ, 65^\circ$  and  $75^\circ$ . These data have been fitted to the Stoner-Wohlfarth model (solid lines in Fig. 4.10), the sample dependent anisotropy fields  $H_{K1}$  and  $H_{K2}$ .

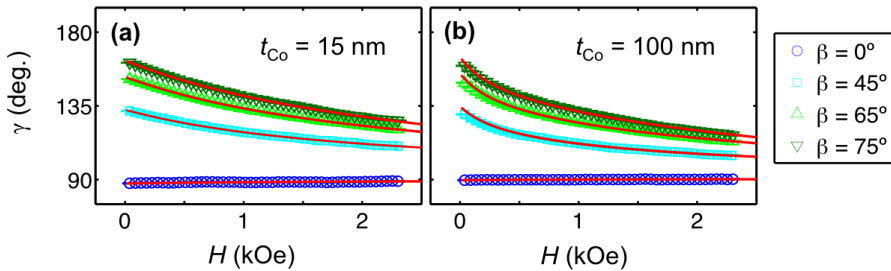


**Fig. 4.10:** Magnetization angle  $\gamma$  vs applied field strength  $H$  for the (a) 15 nm and (b) 100 nm thick Co films, for different applied field angles  $\beta$ . The red solid lines indicate the Stoner-Wohlfarth model fit.

While in principle the data for the 15-nm- and 100-nm-thick Co films seems very similar, a significant difference can be observed in terms of their curve shapes, the magnetization vs field datasets being noticeably more curved for the thicker film. This aspect reflects the different magnetic anisotropy properties of the samples, as confirmed by the fitted values of the first- and second-order anisotropy fields. In particular  $H_{K1} = 1.46 \pm 0.01$  kOe and  $H_{K2} = 1.54 \pm 0.04$  kOe was obtained for the 15-nm-thick film, whereas for the 100-nm-thick film, the values were  $H_{K1} = 0.54 \pm 0.01$  kOe and  $H_{K2} = 2.70 \pm 0.02$  kOe. Thus a thickness dependent redistribution of the first and second order anisotropy fields is observed, while the total anisotropy field  $H_K = H_{K1} + H_{K2}$  (which is a measure of the field needed to saturate the film along the hard-axis direction) remains relatively similar in both cases ( $3.00 \pm 0.04$  kOe and  $3.24 \pm 0.04$  kOe for the 15 nm and 100 nm film thicknesses, respectively).

These observations are reproduced in the entire thickness series of the samples, as can be observed from Fig. 4.11(a), where  $H_{K1}$  and  $H_{K2}$ , as well as their sum  $H_K$ , are plotted against the Co film thickness.  $H_{K1}$  is above 2 kOe for the thinnest film, which possesses a nearly zero  $H_{K2}$  value, but  $H_{K1}$  steadily decreases its value for larger film thicknesses, while  $H_{K2}$  shows an increasing trend. Accordingly, it is found that the  $H_{K1}$  and  $H_{K2}$  values reshuffle in a thickness dependent fashion, with their sum  $H_K$  being kept

relatively constant around the 3 kOe value. By this means, we see that the field needed to saturate all Co films along the hard axis orientation is equivalent, while magnetization rotation paths during reversal are variable from sample-to-sample due to the different relative strength of  $H_{K1}$  and  $H_{K2}$ .

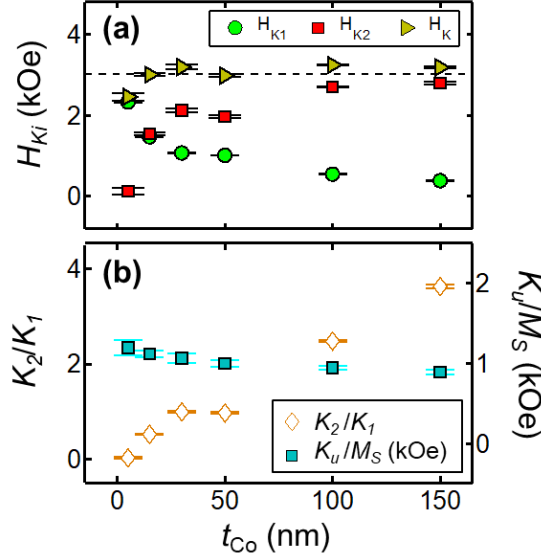


**Fig. 4.11:** (a) Anisotropy fields  $H_{K1}$  (circles),  $H_{K2}$  (squares) and  $H_K$  (triangles) for the Co films with different thickness. The dashed line indicates the  $H_K$  average value of all samples. (b) Ratio of the second to first order magnetic anisotropy energy density,  $K_2/K_1$  (diamonds), and the total uniaxial magnetic anisotropy energy divided by the saturation magnetization,  $K_u/M_s$  (squares).

Correspondingly, an appropriate quantity to illustrate the relative strength of  $H_{K1}$  and  $H_{K2}$  is the ratio between the first and second order magnetic anisotropy energy densities  $K_2/K_1$ , which read as

$$\frac{K_2}{K_1} = \frac{H_{K2}}{2H_{K1}}, \quad (4.10)$$

and is an independent quantity of the saturation magnetization  $M_S$ . The  $K_2/K_1$  ratio vs the Co films shown in Fig. 4.11(b), where a linearly increasing trend with the film thickness is revealed, ranging from the very low value of 0.03 at  $t_{Co} = 5$  nm to a remarkably large value of 3.62 for  $t_{Co} = 150$  nm. Thus, the ratio  $K_2/K_1$  undergoes a dramatic change upon varying the thickness of the epitaxial Co films investigated here.

It has been often found that the MCA energy densities  $K_1$  and  $K_2$  depend on the microstructure of the film. This includes factors such as the density of stacking faults, dislocations, and defects [180, 181]. It has also been reported that there is a dependence of the total magnetic anisotropy energy density on the hcp lattice constants (and hence on strain) in epitaxial Co and Co-alloy films<sup>39</sup>. In particular, experiments indicate that the magnetic anisotropy energy is increased upon reducing the  $c/a$  ratio in Co and Co-alloy materials [182-184]. Existing theoretical works explain this MCA increase in terms of the strong correlation between the  $c/a$  ratio and the splitting of the electronic  $d$ -bands, which in turn lower the band filling factor [185, 186].

An alternative quantity for evaluating the magnetic anisotropy energy density is

$$K_u = K_1 + K_2 = \frac{M_S}{2} \left( H_{K1} + \frac{H_{K2}}{2} \right), \quad (4.11)$$

which can be defined as the energy difference between the easy-axis and hard-axis magnetization configurations in the absence of applied magnetic fields. Fig. 4.11(b) displays this quantity divided by the saturation magnetization<sup>40</sup>. A drop of the order of 25% in the entire thickness range is observed for the quantity  $K_u/M_S$ , as it goes from 1.2 kOe to 0.9 kOe upon increasing the film thickness. This drop can arise from two distinct contributions, namely (i) the introduction via misfit dislocations of small portions with face-centered cubic (fcc) ordering in the hcp crystal, the former possessing a considerably lower MCA energy than the latter, and (ii) by the decline of the MCA energy due to strain, in particular because of the decrease of the  $c/a$  ratio with increasing thickness.

So far, the relation between epitaxial strain and MCA for Co has been extensively studied for epitaxial films in the limit of few monolayer thicknesses [187-189]. Such ultrathin-film systems feature thickness dependent phenomena as, for instance, the enhancement of MCA, the spin-reorientation transition and changes of the integral magnetic anisotropy symmetry. However, it is demonstrated here that the strain is also strongly connected to further features of the magnetic anisotropy, which can also

---

<sup>39</sup> In the case of the Co-alloys, it is difficult to obtain a comprehensive understanding from experiments on the combined effects of the hybridization between different atomic species (such as Co and Pt) and the effect of the  $c/a$  ratio. Thus we limit ourselves to the comparison with earlier works on epitaxial hcp Co alone.

<sup>40</sup> The saturation magnetization of each of the samples is determined by VSM measurements to be between 1350-1450 emu/cm<sup>3</sup>, confirming the lack of large variations in  $M_S$  from sample to sample.

vary at considerably larger thicknesses and moderate strains: while the  $H_K$  value is kept fixed and the MCA energy  $K_u$  is also sensitive to the density of dislocations and defects, the  $K_2/K_1$  ratio dramatically changes its value upon modifications of the strain state in the film.

#### 4.4 Strain engineering of magneto-optics

In spite of the convincing correlation between epitaxial strain and MOA in Co films, it would still be preferable to decouple the effects of the thickness and strain. For doing so, the exact origin of strain and further options to control its strength have been investigated, as a way to control the magneto-optical properties of the hcp Co films. A platform for tuning the distortion state of the Co films is envisaged and realized here.

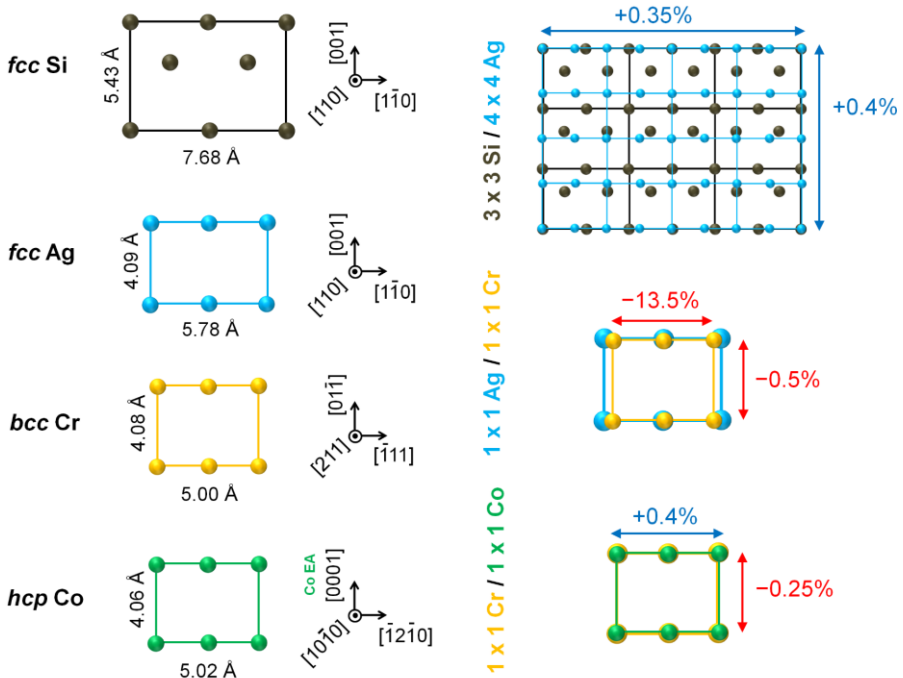


**Fig. 4.12:** Atomic lattice planes that take part in the epitaxial sequence of the samples grown for this study (left panel) and the mismatch situation at the Si/Ag, Ag/Cr, and Cr/Co interfaces (right panel).

The detailed epitaxial sequence to grow hcp Co films with in-plane uniaxial magnetic anisotropy [148, 190] is depicted in Fig. 4.12. The sequence reads as Si(110)[001]/Ag(110)[001]/Cr(211)[011]/Co(1010)[0001]. The left panel in Fig. 4.12



deformation of the hcp unit cell, an increase of the  $a$  lattice constant may also bring a reduction of the lattice constant  $c$  along the  $c$  axis orientation of Co.

Thus we assume that the strain in Co originates as a by-product of the strain state of the Cr layer underneath. This means that if one were able to precondition the strain state of the Cr layer, it would also be possible to control the strain state of the Co film grown on top. Now, one can think attempting to tune the strain state of the Cr layer by varying its thickness, which would then adjust its strain level according to the thickness-dependent strain relaxation we earlier found for Co.

With the purpose of following this strategy, the tilted sputter-gun deposition method described in Section 2.1 was utilized to grow wedge-type samples with a Cr-layer thickness between 15 and 100 nm. This allows us to explore Cr thicknesses above and below the usual 50 nm standard that was fixed in the recipe utilized up to now. A schematic of the suggested sample structure is shown in Fig. 4.14(a). The Ag layer thickness is fixed at the usual 75 nm and a compromise of 20 nm is chosen for Co in order to ensure that (i) the mechanical coupling to the Cr underneath is still strong enough as well as (ii) large enough signals for x-ray diffraction and GME-measurements are obtained. Finally, a 10-nm-thick SiO<sub>2</sub> overlayer is deposited on top of the sample as a protection capping layer. This approach provides a way to grow a large set of samples with many Cr-thicknesses in one, due to the fact that the Cr-thickness is modified as a function of the wedge-sample position. This brings in several advantages from the point of view of the sample fabrication and the measurement procedure. On one hand, it assures that the deposition conditions for all the layers except Cr are kept the same at all the positions of the wedge, so that the Ag, Co and SiO<sub>2</sub> layer thicknesses do not vary while the Cr thickness is changed. In this way, sample-to-sample systematic errors are avoided. On the other hand, the concept is also advantageous for GME-measurements, as one can use the translation-stage of the GME-setup described in the Section 3.2 to perform position-dependent measurements on the wedge-type sample.

The wedge-type samples are grown on top of 90-mm-long and 5-mm-wide elongated substrates that are cut from 4-inch diameter Si-wafers. The relatively large length of the stripe-like substrate allows having a quasi-linear wedge profile with Cr-thickness gradients below 1-1.5 nm/mm, which is smooth enough for a reliable position-dependent measurement using a 1 mm diameter laser spot. An important aspect to take into account when cutting the wafer is the relative orientation of the direction along the wafer stripe and the eventual orientation of the crystallographic  $c$  axis of Co. In the GME-setup, the magnetic field is applied perpendicular to the elongated direction of the stripe-shaped substrate. As the determination of MOA is facilitated by ampler magnetization rotation processes, the cutting direction in the wafer should be preselected such that the resulting angle  $\beta$  between the applied field and the magnetic

easy axis of Co is ideally above  $45^\circ$ . As a way to ensure this condition, the primary flat of the wafer was taken into consideration, which defines the crystalline in-plane orientation of Si. 4-inch Si-wafers from *Virginia Semiconductor Inc.* with  $\{110\}$  crystalline orientation and  $\langle 110 \rangle$  primary flat are utilized in this study. Fig. 4.14(b) exhibits the cubic unit cell of Si, highlighting the  $(110)$  plane<sup>41</sup>, the primary flat  $[110]$  orientation (red arrow), as well as the  $[001]$  orientation (green arrow) corresponding to the  $c$  axis of Co within the envisioned epitaxial sequence. Thus for obtaining a stripe-orientation that will lead, for instance, to  $\beta = 75^\circ$  in the experiment, the stripes must be cut in a direction that is  $15^\circ$  away from the Si $[001]$  axis, as depicted in Fig. 4.14(c). An equivalent argument is followed for alternative  $\beta$  orientations.

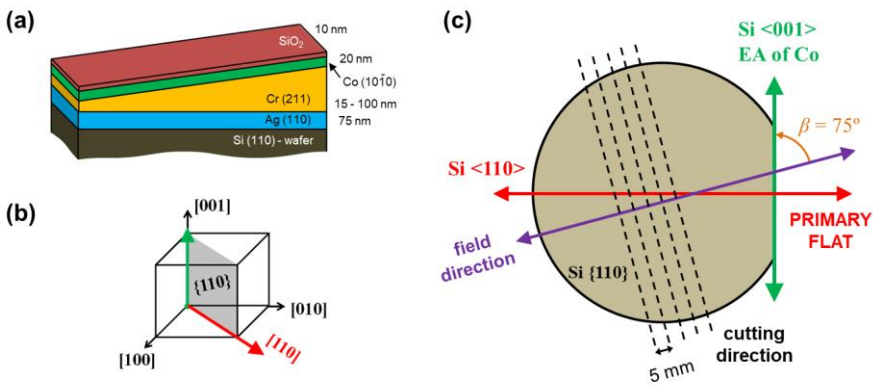


**Fig. 4.14:** Structure of the epitaxial hcp Co film sample upon implementing a Cr-thickness wedge in the epitaxial sequence. Crystallographic unit cell of Si, indicating the relevant planes and vectors. (c) Schematic of the Si-wafer cutting geometry to obtain the desired in-plane orientation along the wedge-direction (here,  $\beta = 75^\circ$ ).

Epitaxial hcp Co films including a Cr-thickness wedge were fabricated in order to have applied field directions of  $\beta = 45^\circ$  and  $75^\circ$  in the GME experiments. For each epitaxial wedge-type structure, two identical samples are grown at the same time, which will be separately used for x-ray diffraction GME experiments. Given that the x-ray diffractometer utilized in this study lacked the option to perform position dependent measurements, we cut one of the sister samples in pieces of approximately 10 mm in length, thus getting 8-9 pieces from the elongated 90-mm-long wedge-samples.

<sup>41</sup> The plane that is drawn in the schematic in Fig. 4.14(b) is actually the  $(\underline{1}10)$  plane, given its equivalency to the  $(110)$  plane within the  $\{110\}$  family.

Fig. 4.15 exhibits x-ray  $\theta$ - $2\theta$  scans from each of the 8 pieces cut from the sample corresponding to a  $\beta = 45^\circ$  cutting angle. The pieces have been labeled from 1 to 8, with 1 being the piece with the lowest Cr thickness ( $\sim 18$  nm at its center) and 8 having the thickest Cr layer ( $\sim 95$  nm). A good epitaxial quality of the Ag, Cr and Co layers has been achieved for all sample pieces. It is also clear that the Cr(211) peak increases its height when going from piece No. 1 towards No. 8, as a result of the Cr-thickness increase. The Ag(220) and Co(10 $\bar{1}$ 0) peaks look similar for all the datasets.

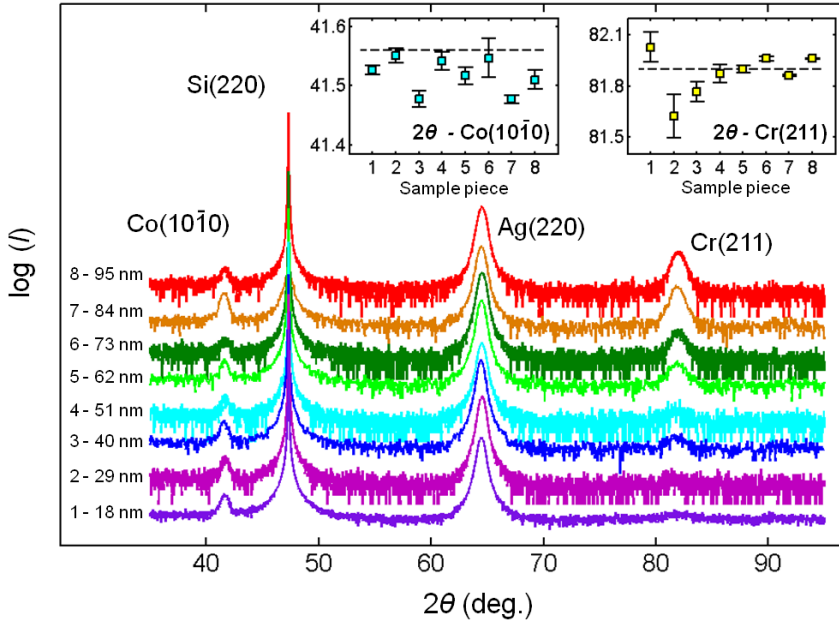


**Fig. 4.15:** X-ray diffraction  $\theta$ - $2\theta$  scans for different pieces of the epitaxially grown wedge-type samples with varying Cr-thickness ( $\beta = 45^\circ$ ). The thickness at the center of the sample piece and the sample identifier are indicated in the left of each dataset. The plot in the insets display the  $2\theta$  positions of the Co(10 $\bar{1}$ 0) and Cr(211) peaks. The dashed lines in the inset plots indicate the bulk  $2\theta$  value of Co or Cr.

Correspondingly, the strain state of the layers has been analyzed by extracting the  $2\theta$  peak positions of Cr and Co by fitting them to a Gaussian profile. The insets in Fig. 4.15 show the fitted peak positions for Cr and Co. Indeed, the peak position of Cr seems to increase its value in approximately  $0.3^\circ$  as the Cr thickness rises<sup>42</sup>. In addition, it is asymptotically approaching the bulk value for Cr(211), such that the assumption of a thickness dependent strain relaxation process is fulfilled here. Opposite to this, the

<sup>42</sup> The data for the piece No. 1 does not follow this trend, as the reduced peak height did not result into a reliable fit.

data regarding the Co-peak position is less interesting, as it shows little dependence on the Cr-underlayer thickness. In view of this, it can be concluded that the strain relaxation process occurring in the Cr-layer is either not being transferred to the Co-layer on top, or its strength is instead rather weak to create a notorious effect on the strain state of Co.

A striking feature of the diffraction data in Fig. 4.15 consist on the apparently low peak height of the Co reflection. As an example, Fig. 4.16(a) shows the Co(10 $\bar{1}$ 0) peak measured in sample No. 2 (~27 nm of Cr) and the peak height barely surpasses 30 cps (counts per second) for a 20-nm-thick Co film, when in the previously grown samples we had approximately 50 cps and 100 cps for 15-nm and 30-nm-thick films, respectively. This leads to think that the quality of the Co films grown within this strategy is not optimal. In order to get additional insights on the crystalline quality of the films, rocking curve measurements have been performed for the Co-peak. Fig. 4.16(b) shows measurements for piece No. 2 at the azimuthal orientation at which the  $\theta$ - $2\theta$  data in Fig. 4.16(a) was acquired ( $\Phi = 0^\circ$ ). Surprisingly, it is observed that the rocking curve is considerably shifted towards the left, its center being located at  $-2.4^\circ$  as compared to  $\omega_0$ . The peak height reaches a considerably larger 60 cps. Even more, if the sample is reversed in the azimuthal plane ( $\Phi = 180^\circ$ ), the rocking curve measurement is now shifted towards the right by  $2.3^\circ$  as compared to  $\omega_0$ .

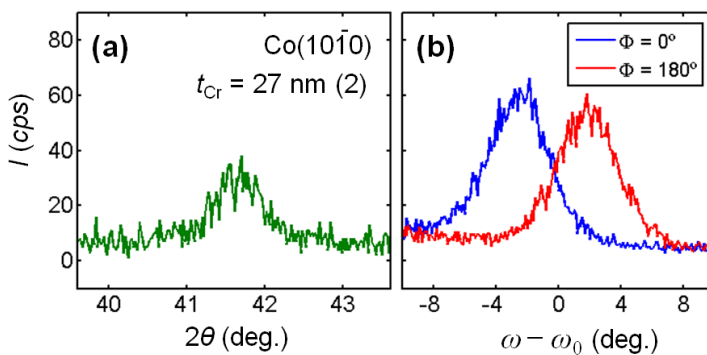


**Fig. 4.16:** (a) Zoomed in  $\theta$ - $2\theta$  scan near the Co(10 $\bar{1}$ 0) reflection for the sample piece No. 2 ( $t_{Cr} = 27$  nm) for different pieces. Rocking curve measurements realized on the same peak of the same sample at azimuthal orientations  $\Phi = 0^\circ, 180^\circ$ .

These relatively large shifts in the rocking curves for different azimuthal sample orientations suggests that the sample's surface normal (which is also the  $\Phi$ -rotation axis) and the vector normal to the Co(10 $\bar{1}$ 0) crystallographic plane are appreciably misaligned. While a small shift ( $\sim 0.3^\circ$ ) could be originated by the fact that

the sample is not placed on a completely smooth, planar surface, a misalignment over  $2^\circ$  points out to a real tilt of the crystallographic plane of Co.

In order to confirm this, rocking curve measurements have been performed for different sample azimuthal orientations not only for the Co-reflection, but also for the rest of the visible peaks in the  $\theta$ - $2\theta$  scans.

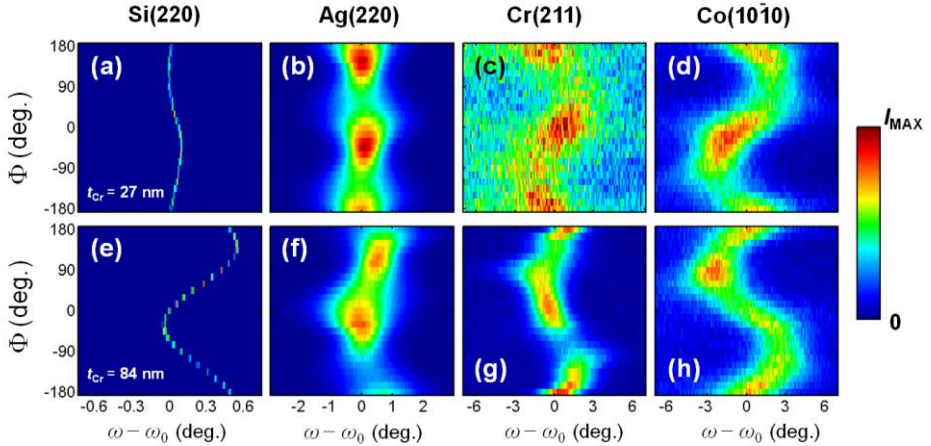


**Fig. 4.17:**  $\Phi$ -dependent  $\omega$ -scans for the (a) Si(220), (b) Ag (220), (c) Cr (211) and (d) Co(10 $\bar{1}$ 0) reflections measured from the sample piece No. 2 ( $t_{Cr} = 27$  nm). (e)-(h) display the same data for the sample piece No. 7 ( $t_{Cr} = 84$  nm).

The data retrieved for the sample piece No. 2 ( $t_{Cr} = 27$  nm) is displayed in Figs. 4.17(a)-(d), which show color-coded maps of the measured x-ray intensity upon varying the angles  $\omega$  and  $\Phi$  at the Si(220), Ag(220), Cr(211) and Co(10 $\bar{1}$ 0) reflections<sup>43</sup>. From the color-coded maps shown here, the  $\Phi$  dependence of rocking curve scans is studied. First, it is seen that the rocking curves for the Si [Fig. 4.17(a)] and Ag-peak [Fig. 4.17(b)] show a slight dependence on  $\Phi$ . Nonetheless, the maximum deviation in  $\omega_0$  does not reach to be more than few tenths of a degree, which is of the order of the sample alignment precision of the equipment. However, a completely different level is seen for the Cr- and Co-peaks, which display deviations from  $\omega_0$  up to approximately  $1.5^\circ$  and  $3^\circ$ , respectively. Furthermore, it looks like these deviation values reach their maximum at the  $\pm 90^\circ$  azimuth orientations. Figs. 4.17(e)-(h) show equivalent datasets for  $\Phi$ -dependent rocking curves acquired for the sample piece No. 7 ( $t_{Cr} = 84$  nm), where the same behavior as for sample piece No. 2 is recognized.

<sup>43</sup> Here, the  $\Phi = 0^\circ$  azimuth orientation of the sample is chosen so that the x-rays travel in the direction of the increasing Cr-thickness direction.

The data in Fig. 4.17 suggest that the Cr(211) and Co(10 $\bar{1}$ 0) crystallographic planes are tilted with respect to the Si(110) and Ag(110) crystallographic planes, which are, to a very good approximation, contained in the plane of the sample. Fig. 4.18 shows a schematic representation of the rocking curve x-ray reflection geometry, in which the meaning of having measured peak positions off the  $\omega_0$  value is explained. In particular, it is seen that for a tilt of the crystallographic planes of an angle  $\delta$ , the  $\omega$  value at which the rocking curve maximum is retrieved undergoes a corresponding displacement of  $\Delta\omega = 2\delta$ . It also follows from Figs. 4.18(a) and 4.18(b) that by rotating the sample azimuth by 180°, the sign of the tilt angle reverses its sign, so that depending on  $\Phi$ , the rocking curve peak displacement  $\Delta\omega$  takes both positive and negative signs, which agrees with the situation we found in Fig. 4.16(b).

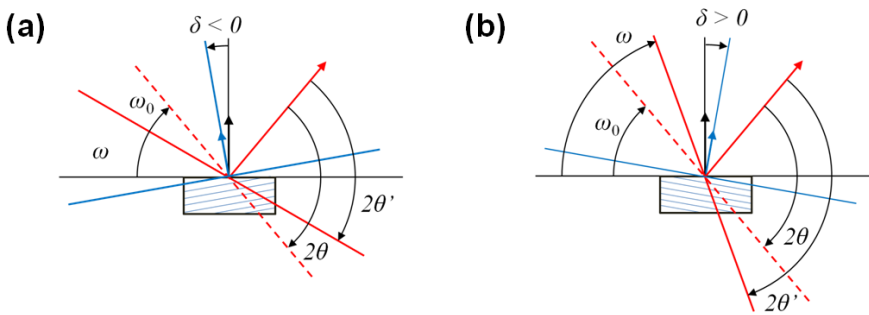


**Fig. 4.18:** Schematic representation of rocking curve measurements under the presence of (a) positively and (b) negatively tilted crystallographic planes. The two situations are interchangeable by rotating the azimuth  $\Phi$  of the sample by 180°.

One can also notice that the Cr and Co rocking curve data follow the same deviation trend in  $\Phi$  [Figs. 4.17(c)–4.17(d) and Figs. 4.17(g)–4.17(h)], meaning that the Cr(211) and Co(10 $\bar{1}$ 0) plane tilts are interrelated and most probably originated from a physical process introduced upon growth of the Cr-wedge. The subsequently grown Co film then basically adopted the lattice tilt introduced in the Cr-layer underneath, and even more, incremented this tilt in a complex scenario which may involve anisotropic strain relaxation process in both Cr and Co films.

An alternative origin of the crystallographic plane tilt could lie on the specific strategy followed to grow the Cr-thickness wedge, based on the oblique sputtering deposition method. It has been observed that the oblique deposition of metals has a strong influence on their microstructure, due to shadowing phenomena during growth [191, 192]. Despite the deposition angle we used was not considerably high, this might

be an influential factor as control samples deposited by rotating the sample during growth did not show this tilt behavior of the Cr and Co crystallographic planes.

Given that we did not achieve a full understanding of the crystallographic plane tilt in our samples with a Cr-thickness wedge, a representative portion alone of the GME measurements is shown here. Figs. 4.19(a)-4.19(c) display the modulation in the magnetization angle  $\Delta$  of the magneto-optical coupling factor modulus  $\tilde{Q}$ , measured for Co films with Cr-wedge thicknesses equal to 18.4 nm, 48.9 nm and 77.2 nm underneath. The angle between the applied field and the easy axis of Co was  $\beta = 45^\circ$  in this case.

It was found that the modulation amplitude in Co varies depending on the Cr-thickness underneath. In particular, the modulation shows a positive [Fig. 4.19(a)], nearly zero [Fig. 4.19(b)] or negative amplitude [Fig. 4.19(c)] at different Cr-thicknesses. The data were fitted to Eq. 4.5 in order to quantitatively evaluate the modulation amplitudes, which are, from thinner to thicker Cr, 16.7%, 0.6% and -13.8%.

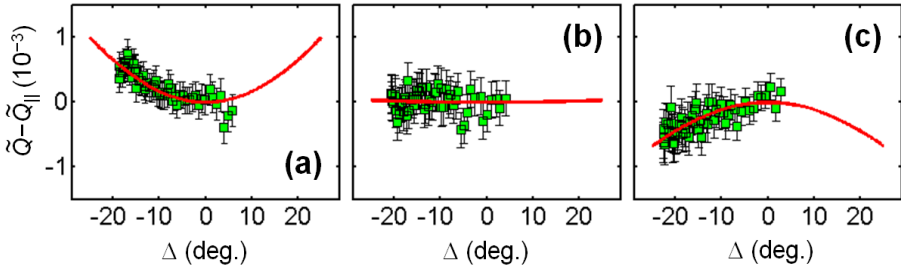


**Fig. 4.19:**  $\tilde{Q}$  vs  $\Delta$  measurements obtained from GME-experiments at different positions of the wedge-type Co film sample with varying Cr-thickness, corresponding to Cr-thicknesses of (a) 18.4 nm, (b) 48.9 nm and (c) 77.2 nm.

While it seems that the Cr thickness wedge approach can effectively modify the MOA properties of the hcp Co films deposited on top (via an effective transfer of strain from the Cr to the Co layer), the exact strain situation of the Co films has not been well understood in this study, as the Cr lattice seems to overcome the mismatch with the Ag underlayer by tilting approximately  $1^\circ$  its preferential Cr(211) texture with respect to the plane of the sample. This causes the Co film on top to adopt a tilted growth as well, such that the interpretation of strain levels in this sample are not straightforward.

Correspondingly, the Cr-thickness dependent inversion of the MOA amplitude (Fig. 4.19) might be associated to other factors such as the existence of a slight out-of-plane magnetization component, for instance. It is also worth to point out that the rocking curve data for Co in Figs. 4.17(d) and 4.17(h), corresponding to Cr-thicknesses of 27 nm and 84 nm, reflect opposite  $\Phi$ -dependent oscillatory trends of the rocking

curves, such that dissimilar Co crystallographic plane tilts could cause a different amplitude of the MOA as well.

In summary, further studies would be needed in this direction to understand the validity of this approach when coming to control the strain state of hcp Co films via the underlayer crystal tuning strategy. While the work shown here indicates that an active modification of the structural properties of Co is achieved, the mechanisms involved here turned out to be more complex than what it was foreseen in the beginning.

### 4.5 Conclusions

In conclusion, we observe magneto-optical anisotropy (MOA) in epitaxial hcp Co films and find a direct correlation between the MOA amplitude and the film strain [193]. The GME-methodology allowed identifying and thus discerning the contributions from the optical and magneto-optical anisotropies in the retrieved data. One can observe that MOA effects are not small in general, as quite modest strains below 1.5% are already able to be the source of relevant MOA of the order of 25%. Thus caution is needed when assuming that bulk homogeneous descriptions adequately describe real systems. In fact, this can seriously compromise, under these very common conditions, the reliability of magnetometry data under the usual isotropic  $Q$  analysis. Relevant corrections to existing MOKE experiments may need to be contemplated.

Together with this, the magnetocrystalline anisotropy (MCA) properties of the hcp Co films have been analyzed. Contrary to previous reports, we have seen that the MOA and MCA do not have to be correlated in size, but that the features of both properties are connected to structural properties, such as the level of epitaxial strain. In this sense, it was found that the ratio of the second- and first-order magnetic anisotropy energy densities  $K_2/K_1$  is highly strain dependent, which comes to complement the literature regarding the correlation of structural properties and magnetic anisotropy of magnetic materials. The precision of the GME-technique to measure the  $H_{K1}$  and  $H_{K2}$  anisotropy fields proved to be essential regarding this aspect.

Additionally, a strategy was envisioned in order aim for modification of MOA in hcp Co films by using an underlayer crystal tuning approach. Even if the preliminary results show to be promising, a more complex strain relaxation scenario is found when growing samples in the wedge-type geometry. Along these lines, further work is needed in order to perform a continued test on the validity and versatility of this approach.

## Chapter 5

# Magneto-optical ellipsometry of permalloy gratings in reflection and diffraction

*The GME technique is employed to investigate the optical, magneto-optical and magnetic properties of one-dimensional patterned magnetic structures (magnetic gratings) of permalloy. First, the context for the interest in artificially tailored systems and magnetic gratings is placed. A brief explanation on the fabrication procedure and morphological characterization of the grating samples is followed by the study on their orientation dependent optical and magneto-optical properties. An effective optical and magneto-optical anisotropy of uniaxial character, whose strength scales linearly with the height modulation of the surface topography, is found. These results demonstrate that both optical and magneto-optical properties can be tuned by controlling the profile depth of a periodic structure. In addition, full ellipsometric characterization of diffraction signals is carried out. The longitudinal and transverse magneto-optical Kerr effects in diffraction preserve the symmetry of the conventional reflection matrix, at least for light polarization states that are not too far from specific symmetry points.*

### 5.1 Introduction: technological interest of artificially tailored materials and the concept of form birefringence

Recent work in the field of artificially tailored materials has generated a large interest in metamaterial fabrication platforms on the micro- and nanoscale, in which electronic, magnetic, optical, magnonic or other ferroic properties are fine-tuned or even interrelated to act jointly in multifunctional devices [194, 195]. The simultaneous incorporation of these multiple degrees of freedom can enable reprogrammable devices that allow control during operation. Some of the candidates suggested as reconfigurable metamaterial platforms are magnonic [196] and magneto-photonics [197], which allow for the preselection of frequency band gaps and highly anisotropic spin wave or light dispersion relations. For simplicity reasons, much of the work on magnonic and magneto-photonics properties of materials has been centered onto one-dimensional

periodic ferromagnetic structures, also known as magnetic gratings. Apart from the mere reporting on the frequency band gaps and spin-wave propagation characteristics [198, 199], several studies have also demonstrated the control of these properties via magnetic fields [200] and electric currents [201]. Magnetic gratings also exhibit the enhancement of magneto-optical effects by plasmonic activity [202]. In addition, their dispersive character makes them suitable for the spatial separation of spectra from pulsed light produced via high harmonic generation [203].

Characterization techniques based on MOKE prove to be useful in order to understand the field- and time-dependent evolution of magnetization in this kind of periodic magnetic structures. Although MOKE on patterned or rough surfaces may present complications in terms of understanding diffuse and diffracted light signals [204], it may also give additional opportunities for magnetization characterization. Nowadays, the applicability of MOKE is not limited to thin-film analysis, as focused MOKE-type scanning-type approaches are readily employed to study selected regions of individual nanostructures [24, 205]. In the case of magnetic arrays with well-defined periodicities, it is seen that diffracted MOKE signals are especially sensitive to magnetization inhomogeneities, enabling the determination of fine features in the magnetization reversal of periodic magnetic arrays [93, 206].

Hereby, the overwhelming majority of studies concerning the optical and magneto-optical properties of magnetic grating systems work within an isotropic dielectric tensor formulation. Despite this often being a reasonable assumption, it has already been reported that homogeneous dielectric materials can effectively act as anisotropic metamaterials systems, developing uniaxial or biaxial dielectric properties [207-209]. This phenomenon, termed as *form birefringence*, leads to the appearance of uniaxial anisotropic dielectric properties for one-dimensional periodic structures such as gratings. Fig. 5.1(a) shows the schematic of such a grating system with periodicity  $D$ , composed by alternating lamellas of refractive indices  $n_1$  and  $n_2$ .

In general, the electromagnetic properties of gratings depend on various quantities such as the profile geometry, thickness or the line-to-space ratio, as well as on the wavelength  $\lambda$  of light. For  $D < \lambda/2$ , the effective dielectric properties of the ordinary and extraordinary axes depend on the grating filling factor  $q = w/D$  [210]

$$\begin{aligned}
 n_o &= [n_1^2(1 - q) + n_2^2q]^{\frac{1}{2}} \\
 n_e &= \left[ \frac{1 - q}{n_1^2} + \frac{q}{n_2^2} \right]^{-1/2}
 \end{aligned}
 \tag{5.1}$$

which gives to the grating system in Fig. 5.1(a) the character of a negative uniaxial crystal ( $\Delta n = n_e - n_o < 0$ ). Fig. 5.1(b) depicts the calculated difference between the effective refractive indices along the two optical axes, which can be as large as  $\Delta n = 1$  for a sufficiently large  $n_2$  value. Thus, it is demonstrated both theoretically and experimentally [208] that artificially materials of this kind can have values of the anisotropy strength as large as  $\Delta n/n \sim 0.5$ , exceeding the values found in naturally occurring materials<sup>44</sup>. This finding led to the design of versatile optical components for manipulating the polarization state of light [211, 212].

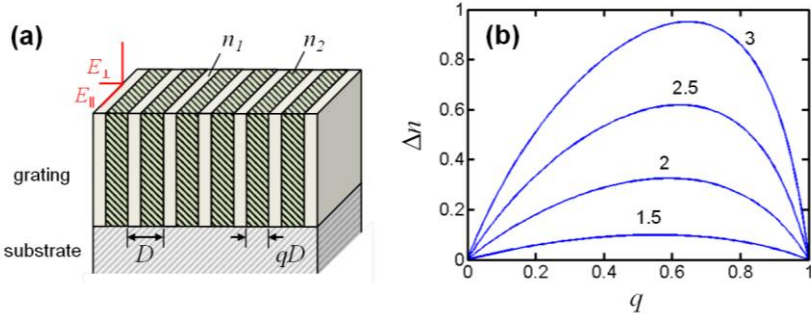


**Fig. 5.1:** (a) Illustration of a square profile grating system on a substrate. The grating periodicity  $D$ , and the filling factor  $q$  are represented. (b) Calculated  $\Delta n$  vs the filling factor  $q$  for different values of  $n_2$  ( $n_1 = 1$  is assumed). Adapted from the work by Flanders [208].

In this chapter, the orientation dependence of the optical and magneto-optical properties of magnetic gratings of  $\text{Ni}_{80}\text{Fe}_{20}$  (permalloy, Py) is investigated. For the gratings studied here,  $D > \lambda$  holds, such that the effective medium approximation is not valid anymore and there is no way to obtain an analytical form of the dielectric tensor quantities. In particular, we focus on the optical and magneto-optical properties in grating samples with different topographic depth. Combining GME measurements and optical modeling, we find that both optical and magneto-optical anisotropy exist in Py gratings, with their amplitude being correlated with the surface topography depth. While theoretical investigations of nanostructured metal-dielectric metamaterials suggest the existence of highly anisotropic optical and magneto-optical properties [213], the lack of experimental studies so far motivates the present study.

Complementarily, the magneto-optical properties of the Py gratings have been studied in the diffraction geometry. While it is well established that valuable information can be obtained by measuring the magneto-optical signal of periodic magnetic structures, the vast majority of experiments in which magneto-optics in

<sup>44</sup> For instance,  $\Delta n/n \sim \pm 0.1$  for calcite [214] or rutile [215].

diffraction is measured deals only with one incident polarization of light [145, 216-220]. While an early study of Azzam and Bashara [221] assessed the polarization characteristics of diffracted light signals from (non-magnetic) grating systems, an attempt to look into this problem including magneto-optical effects is made here. It is shown that the GME methodology allows identifying the symmetry properties of the diffracted Kerr effect with respect to the polarization states of the incident and diffracted light beams.

### 5.2 Sample description and measurement configuration

The samples employed in this study have been fabricated by Nastassia Soriano and Beatriz Mora, from the Department of Chemical-Physics in Leioa (University of the Basque Country). I also acknowledge Olatz Idigoras (CIC nanoGUNE) for assistance with the scanning electron microscope (SEM).

Glass/Ta (5nm)/Py (100nm) thin films were deposited by ion beam sputtering (IBS) in a vacuum chamber with a base pressure of  $6 \times 10^{-8}$  Torr and an Ar working pressure of  $4.5 \times 10^{-5}$  Torr. Py gratings were fabricated by interference lithography using a Lloyd's mirror interferometer [see Fig. 5.2(a)] and a He-Cd laser ( $\lambda = 325$  nm) as the light source [222]. The antireflective coating WIDE-8B and the negative resist TSMR-IN027 were exposed and developed in AZ 726 MIF. A soft- and post-bake was performed before and after exposition, respectively. Then, a Ti hard mask was deposited by IBS [223] and photoresists were removed by lift-off in 1-methyl-2-pyrrolidinone. Subsequently, grooves were etched by  $\text{Ar}^+$  plasma, controlling their depth by adjusting the etching time. The Ti layer thickness was calculated from the Ti and Py etching rates for each Py groove depth in order to keep a 5-nm-thick Ti overcoat.

The schematics in Fig. 5.2(b) illustrates the grating geometry of the samples, depicting the grating periodicity  $D$ , stripe width  $w$ , inter-stripe distance  $a$  and Py groove depth  $h$ . The three former parameters were kept constant for all samples investigated here, while the groove depth  $h$  was varied from sample to sample. A set of gratings was fabricated with the following parameters:  $D = 1.9 \mu\text{m}$ ,  $w = 1.2 \mu\text{m}$ ,  $a = 0.7 \mu\text{m}$  and  $h = 10, 15, 25$  and  $52$  nm. For all the grating samples, the topography was characterized by atomic force microscopy (AFM) and scanning electron microscopy (SEM). AFM data retrieved on the patterned samples confirm their one-dimensional periodic structure [Fig. 5.2(c)]. Fig. 5.2(d) shows the AFM data of the sample with the highest groove depth ( $h = 52$  nm) over an area of  $9.5 \times 9.5 \mu\text{m}^2$ , corroborating the stripe geometry with sharp edges. In addition, the inset in Fig. 5.2(d) shows a scanning electron micrograph of the same sample over a wider area, verifying its high-quality grating character. The sample quality was tested by making comparable SEM images at different locations

distributed over the whole patterned area (several  $\text{mm}^2$ ) of the samples. The profile drawn in Fig. 5.2(e) from the path marked with the red line in Fig. 5.2(c) further supports a regular periodicity of  $D = 1.9 \mu\text{m}$  and a total step height of approximately 57 nm, corresponding to the sum of the Py groove depth  $h$  and the 5-nm-thick Ti overcoat. The parameters  $h$  and  $D$  extracted from the AFM data are visible in the Table 5.1 for all samples in this study.

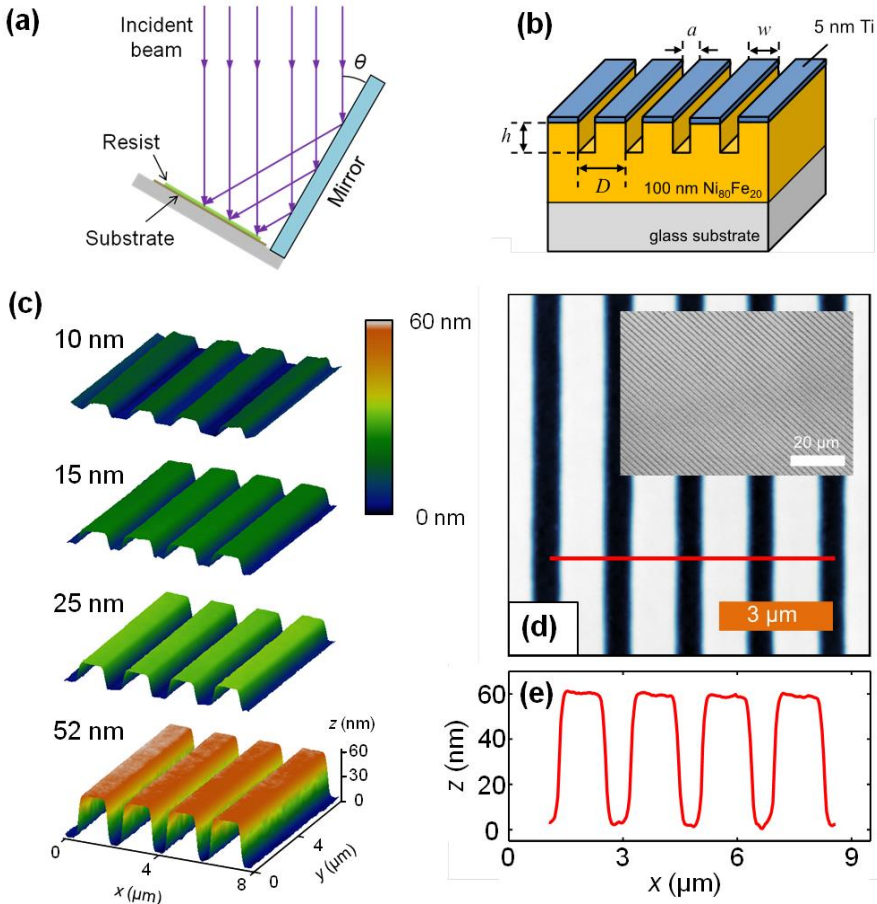


**Fig. 5.2:** (a) Sketch of the interference lithography technique by means of the Lloyd's mirror, which is used to create interference fringes on the resist. (b) Grating structure defining the relevant topographic parameters. (c) 3D-profile AFM images of the series of samples investigated here. The height profile color-code depicted by the colorbar applies to all samples here. (d) AFM image of the sample with  $h = 52 \text{ nm}$  over a  $9.5 \times 9.5 \mu\text{m}^2$  area. The inset displays a SEM image of a wider area of the same sample. (e) Topography profile along the red line depicted in (d).

$h$ (nm) [Nominal]	$h$ (nm) [AFM]	$D$ ( $\mu\text{m}$ ) [AFM]
10	$9.2 \pm 0.5$	$1.91 \pm 0.01$
15	$17.2 \pm 0.4$	$1.89 \pm 0.01$
25	$23.1 \pm 0.6$	$1.92 \pm 0.01$
52	$52.0 \pm 0.4$	$1.90 \pm 0.01$

**Table 5.1:** Experimentally determined dimensions of the Py grating samples via AFM measurements.

In order to investigate the optical and magneto-optical response of the Py gratings, the GME technique is utilized. Fig. 5.3(a) depicts the usual setup employed for this kind of study, indicating the well known polarizer (P1) and analyzer (P2) detection scheme of the reflection experiment. The angle of incidence is chosen to be  $45^\circ$  and the magnetic field is applied in the plane of the sample. Here, the sample orientation  $\beta$  is defined as the angle between the vertical  $y$ -axis and the Py lines. Due to the thin-film and in-plane stripe geometry of the samples, as well as the in-plane orientation of the applied magnetic field, the presence of out-of-plane magnetization components and thus polar Kerr effects can be neglected.

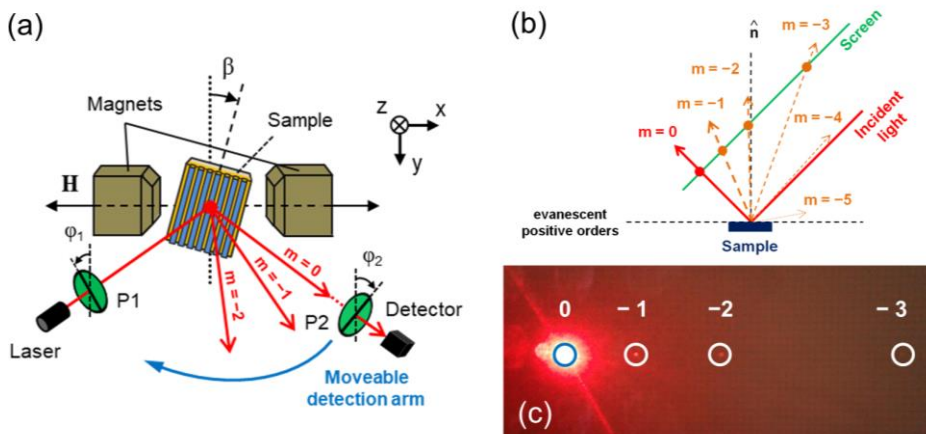


**Fig. 5.3:** (a) Schematic of the setup employed for the magneto-optical characterization. The orientations of the first (P1) and the second polarizer (P2) are indicated by the angles  $\varphi_1$  and  $\varphi_2$ , respectively. The angle between the vertical axis and the Py lines of the sample is represented by  $\beta$ . (b) Representation of the reflection and diffraction beam geometry for the experimental conditions indicated in the text. (c) Picture of the screen indicated in (b), where the beams with order  $m = 0, -1, -2$  and  $-3$  are captured.

With a grating periodicity of  $D = 1.9 \mu\text{m}$ , the wavelength to periodicity ratio approximately fulfills  $\lambda/D \sim 1/3$  for the incident light at  $\lambda = 635 \text{ nm}$  in our setup. Hereby, diffracted spots can also be expected, their multiplicity depending on the relative orientation of the grating vector (perpendicular to the Py lines) and the plane of incidence. In the  $\beta = 0^\circ$  case, the grating vector is contained into the plane of incidence and thus all diffracted beams lie on this plane, together with the reflected beam. This is known as the *in-plane* diffraction<sup>45</sup> configuration and the scattering angle  $\theta_m$  of the  $m$ -th diffracted order is given by the grating equation

$$\sin \theta_m = \sin \theta_i + m \frac{\lambda}{D}, \quad (5.2)$$

with  $\theta_i$  being the angle of incidence. For  $\theta_i = 45^\circ$ , up to five diffracted spots corresponding to negative diffraction orders exist, with no positive order being observable. The diagram in Fig. 5.3(b) depicts the scattering angles of the reflected/diffracted beams, as concluded from Eq. 5.2. A first hint about the relative intensities of the scattered orders can be obtained by placing a screen in the plane perpendicular to the reflected beam [Fig. 5.3(b)]. The 0<sup>th</sup> as well as the first three negative orders have been captured here. The picture in Fig. 5.3(c) shows that the reflected spot<sup>46</sup> is considerably brighter than the diffracted ones, which also reduce its relative intensity the higher is the diffracted order.

Apart from the mere visualization of the reflected and diffracted beams, the placement of the screen allows the fine tuning of the sample alignment in the setup, in order to experimentally achieve the sample orientation  $\beta = 0^\circ$ . This is realized by lining up the visible diffraction spots within the plane of incidence with a precision in  $\beta$  of  $\pm 0.1^\circ$ . This alignment exercise is of crucial importance for the subsequent measurement of the magneto-optical signal within GME. Specifically, a new implementation of the setup is the incorporation of a movable detection arm that allows to switch the measurement geometry in between reflected and diffracted spots [Fig. 5.3(a)]

---

<sup>45</sup> For any other relative orientation of the stripes with respect to the plane of incidence, the reflected and diffracted beams are not contained in the same plane, but are rather arranged in a cone, this configuration being named as *off-plane* or *conical* diffraction [224].

<sup>46</sup> As the screen is made of squared paper, diffuse scattering of the reflected beam is seen in the picture. However, all beams are similar in size with an approximate diameter of 1 mm.

### 5.3 Optical and magneto-optical properties in reflection

As a starting point, multiple hysteresis loops at different sample orientations  $\beta$  have been measured for the entire set of gratings. For this purpose, the polarizer configurations were varied in a region near  $\varphi_1 = 90^\circ$  (incoming  $p$ -polarization) and  $\varphi_2 = 0^\circ$  (outgoing  $s$ -polarization). Fig. 5.4 shows exemplary hysteresis loops of the samples with  $h = 15$  and 52 nm for sample orientations  $\beta = 0^\circ, 45^\circ$  and  $90^\circ$ . For all loops shown here, the configuration of the polarizers was set to  $(\varphi_1, \varphi_2) = (85^\circ, 0^\circ)$ . While the sample with  $h = 15$  nm does not exhibit any substantial difference in the hysteresis loop shape as a function of the orientation angle  $\beta$  [Figs. 5.4(a), 5.4(c) and 5.4(e)], the sample with  $h = 52$  nm shows a clearly visible orientation dependence. The hysteresis loop for  $\beta = 0^\circ$  shows a visible reduction of the magnetization in remanence [Fig. 5.4(b)] that is less apparent at  $\beta = 45^\circ$  [Fig. 5.4(d)], and changes to a rectangular hysteresis loop when the stripes are aligned with the field at  $\beta = 90^\circ$  [Fig. 5.4(f)]. From here, it is straightforward to understand that the magnetization reversal behavior of the samples relies on the shape anisotropy induced by the stripe geometry, causing the preferential axis of the magnetization to be oriented along the Py lines. The increase in topographic profile, in terms of the groove depth  $h$ , is identified as the responsible for boosting the uniaxial magnetic anisotropy of the sample.

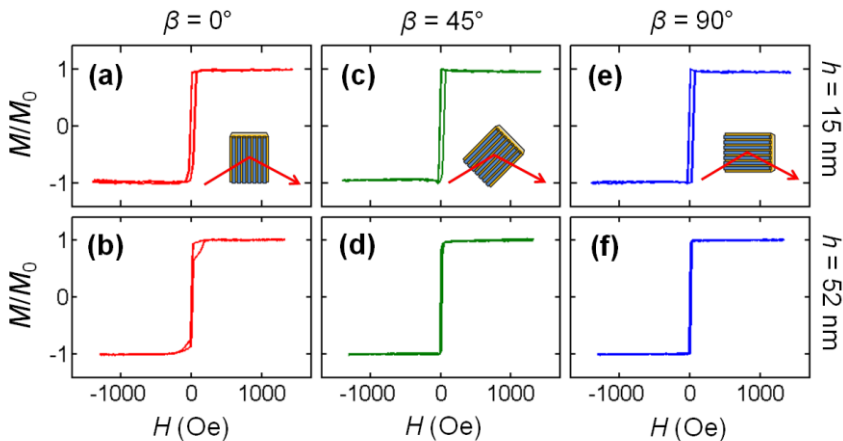


**Fig. 5.4:** Normalized hysteresis loops measured for the sample with  $h = 15$  nm (top panel) and  $h = 52$  nm (bottom panel) for sample orientations of (a)-(b)  $\beta = 0^\circ$ , (c)-(d)  $\beta = 45^\circ$  and (e)-(f)  $\beta = 90^\circ$ . The insets in (a), (c), (e) show the relative orientation of the sample during the measurement.

While from the loops in Fig. 5.4 it seems that an applied field of around 200 Oe is enough to magnetically saturate the Py gratings, we use the GME technique in order to corroborate this. Exemplary measurements for the magnetic grating with  $h = 52$  nm are

shown in Fig. 5.5, for a sample orientation of  $\beta = 0^\circ$ . This particular sample orientation (corresponding to the magnetic hard axis case) is shown as the case in which the most prominent field dependence of the measured quantities can be expected. In particular, Figs. 5.5(a), 5.5(c) and 5.5(e) show color-coded experimental  $I/I(\varphi_1, \varphi_2)$ -maps for applied field strengths of 1000, 250 and 10 Oe, respectively. The maps corresponding to field values of 1000 Oe and 250 Oe, show a well-defined two lobe structure with sign inversion at the  $p/s$ -polarization crossing point. In contrast, the map at 10 Oe displays a very different pattern with an almost vanishing negative lobe and a clearly weaker amplitude for the positive one. As usual, the variation of the  $\delta I/I$  pattern can be understood in terms of the modification of the magnetization state of the material, given the different symmetry of the longitudinal and transverse magneto-optical Kerr effects with respect to the polarization crossing point: while the data in Figs. 5.5(a) and 5.5(c) are indicative of nearly pure longitudinal effects at high fields, the map in Fig. 5.5(e) arises from the coexistence of longitudinal and transverse Kerr effects, as a result of the magnetization rotation process upon reducing the applied field. Figs. 5.5(b), 5.5(d) and 5.5(f) display the fitted  $\delta I/I$  maps below the experimental ones. The fitted maps exhibit an excellent agreement with the measured data, as demonstrated by the  $R^2$  values indicated in the inset of the fitted maps.

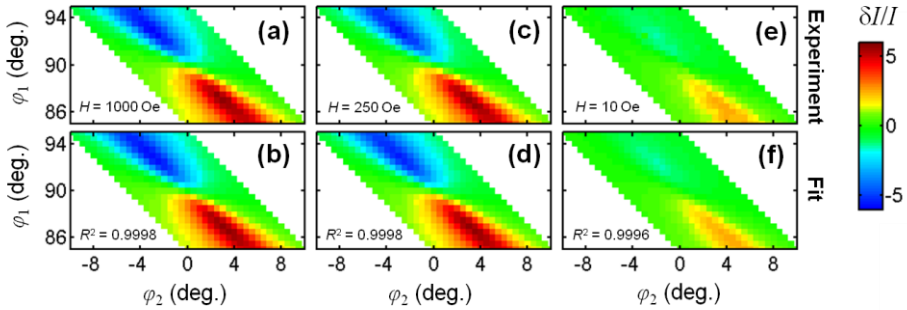


**Fig. 5.5:** Color-coded  $\delta I/I(\varphi_1, \varphi_2)$ -maps measured in reflection for the sample with  $h = 52$  nm oriented at  $\beta = 0^\circ$  at applied field strengths of (a)-(b) 1000 Oe, (c)-(d) 250 Oe and (e)-(f) 10 Oe. The top panel shows the experimental data, while the fitted maps are shown right below to the data in the bottom panel. The colorbar displays the  $\delta I/I$  scale used for all maps in the figure.

Similar to the few field snapshots shown in Fig. 5.5, all  $\delta I/I(\varphi_1, \varphi_2)$  datasets for the complete field series in between 1200 Oe and remanence were fitted to extract the reflection matrix elements for the sample with  $h = 52$  nm at the  $\beta = 0^\circ$  orientation. The fit results for the  $B_1$  and  $B_3$  parameters vs  $H$  are displayed in Fig. 5.6(a). For sufficiently high fields, the  $B_1$  parameter saturates at a negative value, while  $B_3$  remains equal to zero. In contrast, as the field is decreased towards remanence,  $B_1$  decreases its

absolute value, with  $B_3$  synchronously departing from zero. This behavior can be understood if one considers that the parameter pairs  $B_1, B_2$  and  $B_3, B_4$  are proportional to the longitudinal and transverse components of the magnetization, respectively. Hence the modification of the  $\delta I/I(\varphi_1, \varphi_2)$  map pattern occurs as a result of the relative signal decrease (increase) of the longitudinal (transverse) magneto-optical effects, caused by a magnetization rotation upon reducing the applied field.

The fitted GME parameters indicate, however, that magnetization saturation is not achieved in practice until field strengths well above 500 Oe are reached. This observation is in contrast to the mere visual inspection of the hysteresis loop in Fig. 5.4(b), for which the magnetization seems to be fully saturated above 200 Oe. Yet the  $B_i$  parameters, and especially the transverse parameters  $B_3$  and  $B_4$  demonstrate that fields amounting to  $H > 500$  Oe are needed, due to the additional energy required to overcome the magnetostatic effects originating from the stripe-like topography profile. It is also worth to point out that the parameters  $B_7$  and  $B_8$ , encoding the purely optical part of the reflection matrix, should not show any field dependence, which is confirmed by the  $B_7$  vs  $H$  data shown in Fig. 5.6(b). The excellent fit quality with  $R^2 > 0.999$  in the entire field range is confirmed in Fig. 5.6(c).

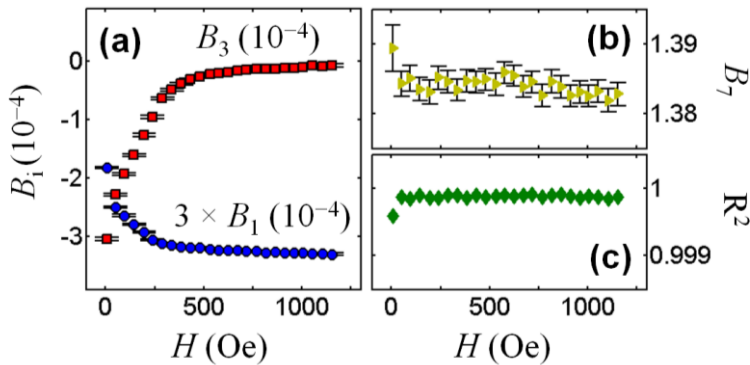


**Fig. 5.6:** (a) Fitted  $B_1$  and  $B_3$  parameters vs  $H$ . The  $B_1$  data has been magnified for clarity. (b) Fitted  $B_7$  parameter vs  $H$ . (c)  $R^2$  vs  $H$ .

In order to perform a comprehensive study of optical and magneto-optical properties including possible anisotropies in Py gratings,  $\delta I/I(\varphi_1, \varphi_2)$  maps were measured every  $5^\circ$  in the sample orientation range  $\beta \in [0^\circ, 180^\circ]$  for all samples. To ensure magnetic saturation, the maps were acquired at an applied field strength of 1 kOe and subsequently fitted to determine the reflection matrix elements. The results are summarized in Fig. 5.7, where the  $\beta$  dependence of the six  $B_i$  parameters ( $B_5, B_6 = 0$  is assumed in the absence of polar Kerr effects), as well as of the polarizer offsets  $\varphi_{10}$  and  $\varphi_{20}$ , is presented for the entire sample series. Figs. 5.7(a) and 5.7(b) exhibit a clear

$\beta$ -dependent modulation of the longitudinal  $B_1$  and  $B_2$  parameters. Specifically, both parameters reach their highest absolute value at  $\beta = 0^\circ$  and  $180^\circ$ . Even if relatively weaker for the samples with  $h = 10$  and  $15$  nm, the modulation is also present, becoming increasingly more noticeable as the groove depth  $h$  is augmented to  $25$  and  $52$  nm. Besides the observed modulation increase in  $h$ , the absolute values of  $B_1$  and  $B_2$  appear to increase as well, meaning that the magneto-optical signal is enhanced for bigger groove depths. The  $\beta$ -dependent  $B_1, B_2$  feature a more complex structure for increased  $h$  values, with a second local maxima appearing at  $\beta = 90^\circ$  as well as the sharp discontinuities emerging at  $\beta = 45^\circ, 135^\circ$  for the  $h = 52$  nm sample. In Figs. 5.7(c) and 5.7(d), the  $B_3$  and  $B_4$  parameters related to the transverse magneto-optical signal remain equal to zero independent of  $\beta$  within the precision of the measurements. This is the expected result as we are magnetically saturating the sample along the longitudinal direction, resulting in a (nearly) vanishing transverse magnetization. The purely optical parameters  $B_7, B_8$  shown in Figs. 5.7(e) and 5.7(f) also display a  $\beta$  dependent modulation, reaching their maximum absolute value when the stripes are perpendicular to the plane of incidence and featuring a minimum value at  $\beta = 90^\circ$ . The size of the modulation also scales with the groove depth  $h$ , similar to  $B_1$  and  $B_2$ .

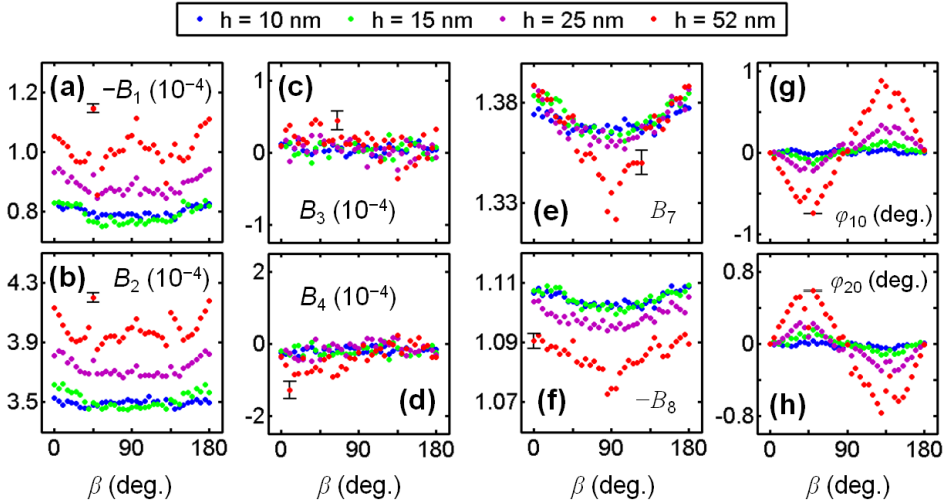


**Fig. 5.7:** Results obtained by the GME-technique for Py gratings with  $h = 10, 15, 25$  and  $52$  nm as a function of the sample orientation  $\beta$ . Extracted (a)  $-B_1$ , (b)  $B_2$ , (c)  $B_3$ , (d)  $B_4$ , (e)  $B_7$  and (f)  $-B_8$  parameters, as well as the correction angles (g)  $\varphi_{10}$  and (h)  $\varphi_{20}$  of the polarizer orientations for different angles  $\beta$ . For the data shown here, one error bar is given in each plot for the dataset with  $h = 52$  nm (red circles), which is representative for the precision of all data points.

The observed orientation dependence of the reflection matrix elements  $B_1$ ,  $B_2$  and  $B_7$ ,  $B_8$  clearly suggests the existence of a uniaxial optical and magneto-optical anisotropy, which develops as the topographic surface features increase with the groove depth  $h$ . Furthermore, there is another aspect of the experimental data that confirms the presence of optical anisotropy. Figs. 5.7(g) and 5.7(h) show the  $\beta$  dependence of the fitted  $\varphi_{10}$  and  $\varphi_{20}$  polarizer orientation corrections. The parameters show an unequivocal sinusoidal modulation of  $180^\circ$  periodicity, with increasing amplitude for larger groove depth  $h$ , reaching values up to  $0.6^\circ$  for  $\varphi_{10}$  and  $0.7^\circ$  for  $\varphi_{20}$ . The size of these corrections, which in principle account for the differences in the polarizer orientations in between the optical table reference frame and the plane of incidence frame of the experiment, is considerably larger than the polarizer angle offsets that can originate from experimental error sources<sup>47</sup>. Moreover, the corrections become zero every  $90^\circ$ , corresponding to the cases, in which the Py lines are parallel ( $\beta = 90^\circ$ ) or perpendicular ( $\beta = 0^\circ, 180^\circ$ ) to the plane of incidence.

As previously shown in Section 3.5 for the epitaxial Co/CoO bilayer system, these offsets can compensate for the translation of the  $\delta I/I$  ( $\varphi_1, \varphi_2$ ) function symmetry point under the presence of uniaxial optical anisotropy. In principle, the isotropic formulation of the reflection matrix considered in Eq. 3.3 cannot accommodate the optical anisotropy effects of the sample. However, it can be shown that the optical anisotropy primarily causes a shift of the  $(\varphi_1, \varphi_2)$  symmetry point as the orientation between the optical axes and the plane of incidence is varied, yet the functional form of  $\delta I/I$  being conserved around the shifted symmetry point in a quasi-isotropic optics approximation [153].

In the following, the optical and magneto-optical constants of the system are quantified in order to assess the anisotropic dielectric tensor of the samples. A relatively simple optical model is considered here to map the reflection matrix data onto an effective dielectric tensor for the samples. The first step to do when elaborating the optical model of these samples is to take into account their topographic features. As a consequence of the dimensions of the grating samples and the wavelength utilized in the study, the consideration of an effective medium theory is not appropriate here, given that the approximation  $D \ll \lambda$  is clearly not valid ( $D = 1900$  nm and  $\lambda = 635$  nm, such that  $D/\lambda \sim 3$ ). Instead, one can find a more accurate pathway to describe the optical properties of the samples by contemplating their shallow character ( $h < D, \lambda$ ) and thus applying the local mode method (LMM) to describe the reflection matrix of a grating sample. The LMM approximation is based, in the case of shallow gratings, on the far-

---

<sup>47</sup> For instance, the misalignments produced by the sample wobble upon its rotation are usually of the order of  $0.05^\circ$  in our experimental setup.

field Fourier analysis of the amplitude reflectance distribution, where the grating's surface is evaluated assuming local lateral uniformity [225-227]. In this way, the edge internal diffraction effects and consequently, multiple scattering processes, can be neglected, as concluded by Suzuki *et al.* [228]. Then the complex reflection coefficients in reflection can be written as the weighted reflection matrices of the alternating media. For a grating filling factor equal to  $w/D$ , this can be expressed as

$$R_{ij} = \frac{w}{D} R_{w,ij} + \left(1 - \frac{w}{D}\right) R_{g,ij}, \quad (5.3)$$

where  $R_{w,ij}$  and  $R_{g,ij}$  are the reflection coefficients at the wire and the groove positions, respectively. Thus, in order to employ the LMM approximation, two distinct layered optical systems have to be taken into account, which lead to the reflection matrices at the wire and the groove. Fig. 5.8(a) shows a sketch of the grating system, displaying the regions of the grating surface where each of the reflection matrices  $R_{w,ij}$  and  $R_{g,ij}$  apply. From here, the layered optical model at the wire region will consist of 100 nm of Py with a 5-nm-thick Ti capping layer. On the other hand, the optical model at the groove region only consists of a Py film of 100-nm thickness. An isotropic, non-magnetic dielectric tensor  $\vec{\epsilon}_{Ti}$  is considered for the Ti capping layer, for which a refractive index of  $N_{Ti} = 2.71 + 3.77i$  [151] is assumed. When coming to model the Py, a distinction is made between the patterned thickness portion of height  $h$  and the unpatterned film underneath, for which the different dielectric tensors  $\vec{\epsilon}_{wire}$  and  $\vec{\epsilon}_{film}$  are considered, respectively. First, the Py film portion (present in both the wire and groove regions) will be treated as an optically and magneto-optically isotropic material, given that the same measurement procedure realized on a continuous 100-nm-thick Py film confirmed its isotropic nature. Such a test measurement was performed in order to discard any possible anisotropic properties that could be caused by the film structure itself. A refractive index value of  $N_{Py} = 1.88 + 3.62i$  and a magneto-optical coupling factor  $Q_{Py} = 0.014 - 0.012i$  were evaluated, excluding any sample orientation dependence<sup>48</sup>. Therefore, these measured values are assigned to  $\vec{\epsilon}_{film}$  [see Fig. 5.8(a)].

In contrast, an *artificial material* approach will be taken to construct the dielectric tensor of the Py wires. For doing so, an optically and magneto-optically anisotropic dielectric tensor  $\vec{\epsilon}_{wire}$  is defined. Associated to this, the extraordinary and ordinary optical axes of the system are introduced, which are perpendicular and parallel to the Py lines, respectively [Fig. 5.8(a)]. The optical and magneto-optical constants

<sup>48</sup> For instance, the polarizer deviation corrections upon realizing orientation dependent GME measurements on continuous Py films never exceeded  $\pm 0.04^\circ$  in our experiments.

along the extraordinary axis are given by  $N_e = n_e + i\kappa_e$  and  $Q_e = Q_{e,r} + iQ_{e,i}$ , respectively, with  $N_o$  and  $Q_o$  being analogously defined for the ordinary axis. Thus the dielectric tensor of the Py grating system within this approach is given by

$$\vec{\epsilon}_{wire} = \begin{pmatrix} N_o^2 & 0 & -iN_e^2 Q_e m_y \\ 0 & N_e^2 & iN_o^2 Q_o m_x \\ iN_e^2 Q_e m_y & -iN_o^2 Q_o m_x & N_z^2 \end{pmatrix}, \quad (5.4)$$

when the extraordinary axis is aligned with the vertical  $y$ -axis, and the ordinary axis lies within the plane of incidence<sup>49</sup> (i.e.,  $\beta = 90^\circ$ ). A simple and elegant strategy to determine the dielectric tensor in Eq. 5.4 consists on taking advantage of the fact that for sample orientations  $\beta = 0^\circ, 90^\circ$  either the ordinary or the extraordinary optical axis is aligned with the plane of incidence. In these two cases, the cross-polarization terms arising from birefringence are zero and specific projections of the dielectric tensor intersect the plane of incidence, such that their measurement is more straightforward [229, 230]. The validity of this idea is supported by the vanishing polarizer corrections along these two distinct orientations [see Fig. 5.7(g) and 5.7(h)]. Thus, a two-point measurement along the extraordinary/ordinary axis is already sufficient to quantify the degree of optical and magneto-optical anisotropy of the samples. Moreover, the nearly complete magnetic saturation ensures  $m_x = 1$  and  $m_y = 0$ , facilitating the measurements of one  $Q$  component at a time.

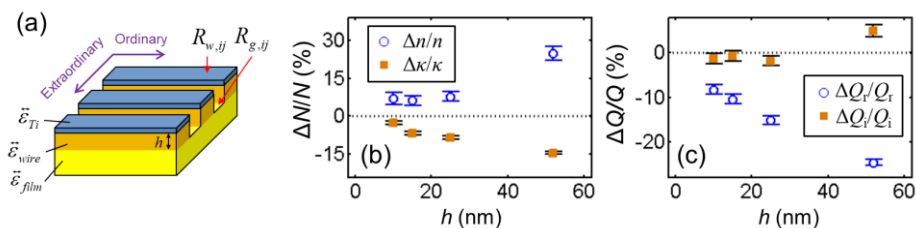


**Fig. 5.8:** Quantitative analysis of the optical and magneto-optical anisotropy of the samples. (a) Schematic of the grating sample, indicating the different reflection matrices at the wire/groove regions, as well as the different material dielectric tensors involved in the optical modeling. The orientations of the extraordinary and ordinary optical axes are also indicated. (b)  $\Delta n/n$  and  $\Delta \kappa/\kappa$  vs  $h$ . (c)  $\Delta Q_r/Q_r$  and  $\Delta Q_i/Q_i$  vs  $h$ . The dotted lines in (b), (c) indicate the zero anisotropy level.

<sup>49</sup> Upon assuming an optically uniaxial material,  $N_z = N_o$  is used without limiting the generality of the observations here.

By following this strategy, the Transfer Matrix Method [74, 75] is applied to calculate the reflection matrix coefficients at the wire and the groove regions ( $r_{w,ij}$  and  $r_{g,ij}$ ) as a function of the optical model parameters. In this way, the best-matching model parameters of dielectric tensor  $\vec{\epsilon}_{wire}$  at the Py wire are obtained from the experimental data. In particular, the optical and magneto-optical constants along the extraordinary and ordinary axis are obtained from the data measured at  $\beta = 0^\circ$  and  $\beta = 90^\circ$ , respectively, as projections of the dielectric tensor in Eq. 5.4.

Furthermore, we define the relative anisotropy of the optical constants as  $\Delta n/n = (n_e - n_o)/[(n_e + n_o)/2]$  and  $\Delta\kappa/\kappa = (\kappa_e - \kappa_o)/[(\kappa_e + \kappa_o)/2]$ . The relative anisotropies of the magneto-optical constant  $\Delta Q_r/Q_r$  and  $\Delta Q_i/Q_i$  are defined correspondingly. Fig. 5.8(b) presents the experimentally determined  $\Delta n/n$  and  $\Delta\kappa/\kappa$  values as a function of groove depth  $h$ . The real part of the refractive index  $n$  shows a positive anisotropy increase as the grating depth is augmented, up to a value of around 25%, with  $\Delta n/n > 0$  in all cases. The absolute value of  $\Delta\kappa/\kappa$  also increases with  $h$ , having  $\Delta\kappa/\kappa < 0$  for all cases. Hence, the extraordinary axis case (the stripes oriented within the plane of incidence) is the less absorptive one. Both trends are found to be approximately linear with  $h$ . Fig. 5.8(c) displays the relative anisotropy values of the magneto-optical coupling factor  $\Delta Q_r/Q_r$  and  $\Delta Q_i/Q_i$  for different  $h$ . Here, we find a strong linear negative trend of  $\Delta Q_r/Q_r$  reaching a relative value of  $-25\%$  for  $h = 52$  nm, while the anisotropy in  $Q_i$  is nearly zero for all  $h$  except for the  $h = 52$  nm, for which it is slightly positive (5%). Thus, the magneto-optical activity is decreased along the extraordinary axis in comparison to the activity along the ordinary axis.

These results demonstrate that optical and magneto-optical properties of our grating samples show an effective anisotropic behavior governed by their surface topography. While the stripe geometry develops an anisotropic behavior of uniaxial nature, the degree of this anisotropy is linearly correlated with the groove depth  $h$ , at least in the  $h$  range investigated here. If looking to the real part of the refractive index  $n$ , Py gratings behave as a positive uniaxial material ( $n_e - n_o > 0$ ). In addition, it was found that they are decreasingly less absorptive for augmenting  $h$  along the extraordinary axis. These samples also show magneto-optical anisotropy, meaning that the magnitude of the magneto-optical activity changes with the relative orientation of the Py grooves with respect to the plane-of-incidence. The anisotropy of the magneto-optical coupling factor  $Q$  is generally associated, as treated in detail in the Chapter 4, with the crystallographic structure of magnetic samples [157, 164, 193]. A relatively recent work on magnetic thin-films with growth-induced slanted columnar geometry found magneto-optical anisotropy as well [135], which is consistent with our experimental observations here.

### 5.4 Polarization analysis of magneto-optical effects in diffraction

The diffracted magneto-optical signal of the permalloy grating samples has been also studied in this work. The results displayed here are limited to the samples with  $h = 25$  and  $52$  nm for the in-plane diffraction configuration ( $\beta = 0^\circ$ ), so that all the scattered beams lie within the plane of incidence. While up to five negative order diffracted spots are observed for a  $\theta_i = 45^\circ$  angle of incidence, only the first two have been measured, their observation angles being,  $\theta_{-1} = 22^\circ$  and  $\theta_{-2} = 2.5^\circ$  as measured from the sample normal. Figs. 5.9(a) and 5.9(b) show magnetic hysteresis loops retrieved at the  $m = -1$  diffraction order for the samples with  $h = 25$  nm and  $52$  nm, respectively, while Figs. 5.9(c) and 5.9(d) display hysteresis loops corresponding to the  $m = -2$  diffracted order. For all loops shown here, the polarizer orientations were set to  $(\varphi_1, \varphi_2) = (80^\circ, 10^\circ)$ . The first and second order loops were averaged over 20 and 40 loop cycles, respectively, without any use of lock-in detection or any other noise reduction method.

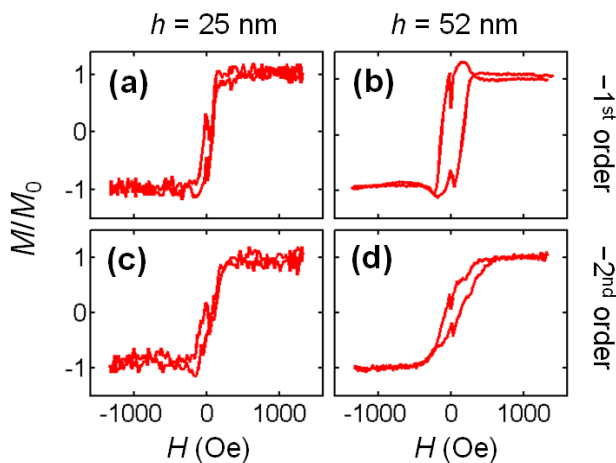


**Fig. 5.9:** Exemplary diffracted-MOKE hysteresis loops, measured for polarizer settings  $\varphi_1 = 80^\circ$  and  $\varphi_2 = 10^\circ$  for samples with  $h = 25$  nm (left panel) and  $h = 52$  nm (right panel); in (a)-(b) first order and (c)-(d) second order diffraction signals are shown for the in-plane diffraction case, with  $\beta = 0^\circ$  sample orientation.

It is visible that the signal-to-noise ratio decreases for higher diffraction orders<sup>50</sup> (Fig. 5.9), while it increases with the grating depth  $h$ . Additionally, one can see that the characteristic fields at which magnetization seems to approach saturation differ

<sup>50</sup> While some studies report the same trend [231], others only find an enhancement of the magneto-optical signal for particular diffraction orders [232].

significantly from the loops acquired in reflection geometry (Fig. 5.4). This is due to the particular sensitivity of the diffracted magneto-optical signal to magnetization inhomogeneities [145, 220], which emerge as the stripe geometry induced magnetostatic effects cause non-uniform magnetization states to exist. The field strengths at which these processes occur (such as magnetic saturation of the stripe edges) are in general larger than those describing the average reversal behavior, which is what we measure in the reflected spot geometry. The loops also display sharp features near remanence, which are related to the existence of non-uniform magnetization states originating from the prevailing magnetostatic effects at the stripes at zero applied field [233, 234].

In the case of the sample with  $h = 52$  nm, multiple hysteresis loops are also measured for different  $(\varphi_1, \varphi_2)$  polarizer configurations, with the purpose of testing the viability of the GME methodology in diffraction geometries. As the specific polarization-dependent symmetry of the scattering matrix (analogous to the reflection matrix) is unknown in diffraction, separate attention will be given onto the longitudinal and transverse Kerr effects. In order to do so,  $\delta I/I(\varphi_1, \varphi_2)$ -maps will be analyzed at appropriate field strength values, so that one particular Kerr geometry prevails the magneto-optical signal retrieved in the experiment. In particular, predominant longitudinal (transverse) Kerr effects are obtained when the magnetization is in the saturation (remanence) state at an applied field of 1000 Oe (0 Oe), given that for the  $\beta = 0^\circ$  sample orientation, the stripes are perpendicular to the applied magnetic field and the reversal nearly mimics that of the hard-axis case for a uniaxial magnet<sup>51</sup>.

The results of this GME-study are put together in Fig. 5.10. The top panel here presents the results for the longitudinal effect, while the bottom panel shows data for the transverse Kerr effect. For the longitudinal case, Figs. 5.10(a)-5.10(c) show experimental  $\delta I/I$  data at 1000 Oe measured for the reflected, first order diffracted and second order diffracted spots. The  $\delta I/I$ -map in reflection displays the familiar two-lobe geometry with opposite sign [Figs. 5.10(a)]. However, the patterns for the first and second order diffraction maps [Figs. 5.10(b) and 5.10(c)] differ significantly from the former, with the two lobes apparently moving away from the symmetry point and broadening significantly. This broadening motivated the use of a polarizer angle range that is four times wider in  $\varphi_1$  and  $\varphi_2$  than in the previous experiments in reflection, in order to capture the maximum  $\delta I/I$  signals in diffraction. As a first observation, the absolute  $\delta I/I$  amplitude of the maps is also lowered considerably as the diffraction order increases, as can be seen from the scale bars employed in the plots.

---

<sup>51</sup> For the investigation of the (nearly) pure transverse Kerr signal, a field strength of 10 Oe is chosen in practice, as a way to avoid the non-uniform magnetization states happening at 0 Oe (remanence).

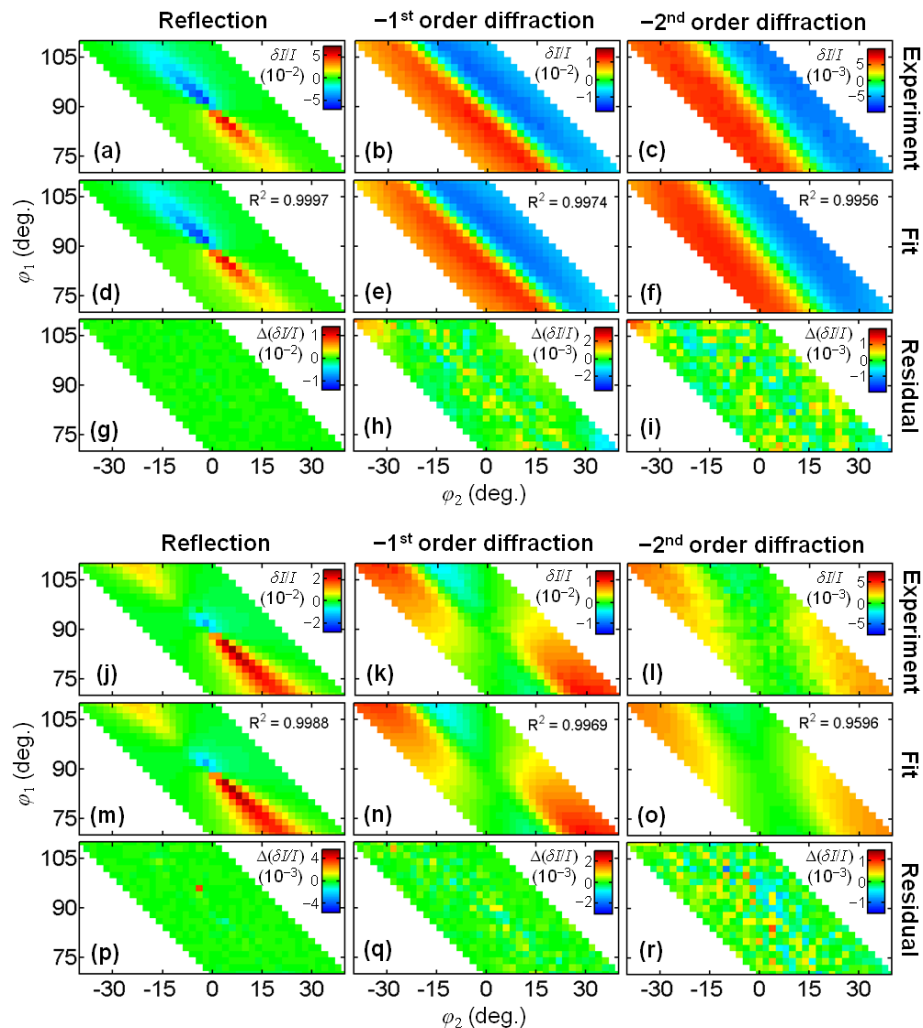


**Fig. 5.10:** Color-coded  $\delta I/I(\varphi_1, \varphi_2)$ -maps for the  $h = 52$  nm sample ( $\beta = 0^\circ$ ) measured in reflection and diffraction ( $m = 0, -1, -2$ ). The top panel displays maps for the saturated magnetization state ( $H = 1000$  Oe), while the bottom panel corresponds to the maps near remanence ( $H = 10$  Oe). The experimental data, the fitted maps and the fit residuals are displayed in consecutive rows from the top to the bottom. The first column shows reflection data, while the second and third columns display first- and second-order diffraction data, respectively. The  $R^2$  values reflect the goodness of the fits. The inset colorbars indicate the scale employed for each map, with the same colorbars being employed for the experimental data and the respective fit.

Even if measurements in diffraction are carried out by measuring light beams with a largely reduced absolute intensity level, we tested the ability of the reflection optics GME-method to fit diffraction data as well. Figs. 5.10(d)-5.10(f) display the fit

results right below the corresponding experimental datasets. Also, the residual maps displaying the difference between the experimental data and the fits,  $\Delta(\delta I/I)$ , are shown in Figs. 5.10(g)-5.10(i). The scale of the residual maps was kept at the 20% level of the corresponding  $\delta I/I$  data amplitude. In the reflection geometry, the fitted map in Fig. 5.10(d) matches the measured data almost exactly with a high  $R^2$  value of 0.9997. Correspondingly, the map in Fig. 5.10(g) shows very low values for the residual, with no points deviating visibly from the fit.

Even if it is not initially clear whether the diffraction data can be fitted within the reflection optics  $\delta I/I$  expression, it was found that the same equations are actually able to reproduce the functional form of the maps measured in diffraction. The fitted maps in Figs. 5.10(e) and 5.10(f) reproduce very well the first- and second-order diffraction maps in Figs. 5.10(b) and 5.10(c) with remarkably high  $R^2$  values of 0.9974 and 0.9956, respectively. Furthermore, the suitability of the GME analysis approach is supported by the corresponding residual maps in Figs. 5.10(h) and 5.10(i), displaying randomly distributed deviations at arbitrary  $(\varphi_1, \varphi_2)$  positions (indicating increased noise, yet the absence of systematic deviations). This increased noise level is easily understood by the considerable decrease in the signal-to-noise ratio for the diffracted spots when compared to the reflection spot.

The same procedure is repeated for the investigation of the transverse Kerr effect. Figs. 5.10(j)-5.10(l) show experimental  $\delta I/I$  data at 10 Oe, measured for the reflected, as well as first- and second-order diffracted spots. Although the two-lobe structure is present again in these maps, the lobes have the same sign rather than the opposite one, which is a characteristic fingerprint of the transverse Kerr effect in reflection. Again, the fitted maps are shown right under the experimental maps in Figs. 5.10(m)-5.10(o). The  $R^2$  values of the fits are very good here too, even if they are slightly lower than for the longitudinal case, with 0.9988, 0.9969 and 0.9506 for the reflected, first- and second-order diffracted maps, respectively. The residual maps in Figs. 5.10(p)-5.10(r) just show randomly distributed deviations at arbitrary polarizer angles, thus further supporting the fact that the functional form of the reflection matrix is able to reproduce the  $\delta I/I$  maps correctly, even for the diffracted spots.

These results imply that the symmetry of the polarization matrix describing diffraction under the existence of longitudinal and transverse Kerr effects is equivalent to the reflection matrix in Eq. 3.3 (at least for polarization configurations near the crossing point), which constitutes a remarkable experimental observation. The fit results are summarized in Table 5.2 in terms of the extracted  $B_i$  parameters, the background intensity  $I_0$  and the fit goodness  $R^2$ . Firstly, it is seen that the magneto-optical parameters  $B_1$ ,  $B_2$  (linked to longitudinal magnetization) and  $B_3$ ,  $B_4$  (linked to the transverse magnetization), are markedly enhanced for the diffracted orders. Evidently,

the obtained  $\delta I/I$  values decrease the higher the diffraction order: as a lower level of light intensity is measured, the background intensity offset becomes increasingly more important, resulting into a rise of the relative offset parameter  $I_0$  by about 50 times between the reflected and the first-order diffracted spot measurements. Moreover, the transverse parameters  $B_3, B_4$  seem to be reversing their sign when going from the reflected order to the diffracted ones. This fact might correspond to the specific phase shift introduced upon diffraction, as well as due to the particular sensitivity of the diffractive magneto-optical signal to magnetization inhomogeneities at the micron-sized Py-stripe edges.

	$H = 1000 \text{ Oe}$			$H = 10 \text{ Oe}$		
	$m = 0$	$m = -1$	$m = -2$	$m = 0$	$m = -1$	$m = -2$
$B_1 (10^{-4})$	-1.21	-8.7	-8.4	-0.63	0.0	-1.0
$B_2 (10^{-4})$	4.42	10.1	7.2	2.43	0.3	0.9
$B_3 (10^{-4})$	-0.14	-0.1	1.8	-3.11	13.4	8.1
$B_4 (10^{-4})$	0.33	0.2	-1.7	8.5	-13.7	-6.5
$B_7$	1.385	1.32	0.77	1.393	1.26	0.72
$B_8$	-1.089	-1.168	-0.68	-1.091	-1.11	-0.81
$I_0 (10^{-3})$	0.480	21.0	73	0.517	19.2	63
$R^2$	0.9997	0.9974	0.9956	0.9988	0.9969	0.9506

**Table 5.2:** Extracted fit parameters ( $B_1$ -  $B_4$ ,  $B_7$ ,  $B_8$  and  $I_0$ ) and  $R^2$  fit goodness for  $\delta I/I$ -maps measured in reflection and diffraction geometry. The last digit of the displayed quantities corresponds to the last significant digit. Positive and negative values of the  $B_1$  -  $B_4$  magneto-optical fit parameters are represented in green and red color, respectively.

Upon evaluating the residual maps in Figs. 5.11(h) and 5.11(i) in more detail, one can observe slight systematic deviations appear for in the  $(\varphi_1, \varphi_2)$  regions that are furthest (by about  $30^\circ$  away) from the crossing point of the polarizers. This slight discrepancy may be originated from the fact the functional form of the reflection matrix employed here starts to fail away from the near region of the crossing point. Such systematic errors, however, can also be ascribed to the large light intensities obtained for polarizer configurations that are very far away from the crossing point. A plausible explanation could also be based on the fact that the background intensity offset produced as a result of the voltage amplification settings at the photodetector have a nonlinear

behavior when measuring for large light intensity signals, thus distorting the  $\delta I/I$  values retrieved at this particular polarizer configurations<sup>52,53</sup>.

For the purpose of obtaining a better insight on the validity of the reflection matrix to fit ellipsometric measurements in diffraction,  $\delta I/I$ -maps were measured over an extended  $(\varphi_1, \varphi_2)$  configuration space, by varying  $\varphi_1$  in the range from  $-90^\circ$  to  $90^\circ$ . The longitudinal and transverse Kerr effect were distinguished by choosing an appropriate field (1000 and 10 Oe), as before<sup>54</sup>.

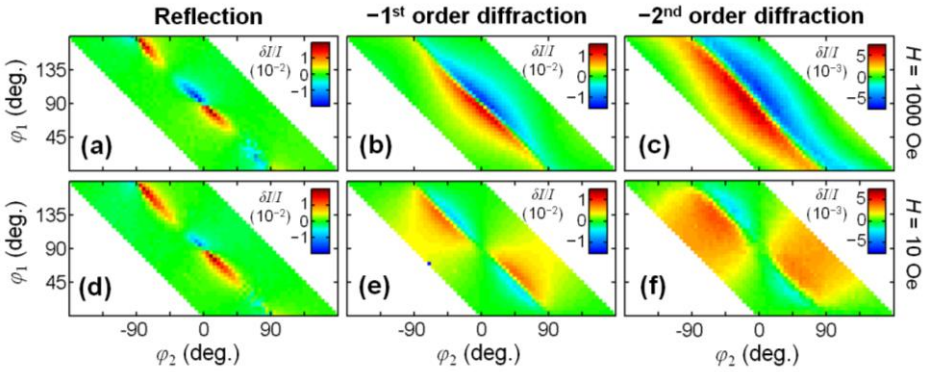


**Fig. 5.11:** Color-coded  $\delta I/I(\varphi_1, \varphi_2)$ -maps for the sample with  $h = 52$  nm ( $\beta = 0^\circ$ ) in reflection and diffraction geometries. The top panel display maps for the saturated magnetization state ( $H = 1000$  Oe), while the low panel corresponds to the maps in remanence ( $H = 0$  Oe). The range of  $\varphi_1$  has been extended to cover the entire  $180^\circ$  angle range, using  $5^\circ$  steps in both  $\varphi_1, \varphi_2$ .

Figs. 5.11(a)-5.11(c) show experimental  $\delta I/I$  data at 1000 Oe for the reflected, first- and second-order diffracted spots. The data measured at 10 Oe is also presented in Figs. 5.11(d)-5.11(f). The failure of the symmetry of the reflection matrix when coming to explain the magneto-optical signal of the samples in diffraction is made evident by the direct comparison of the reflection and diffraction data. In particular, the lobes located around the symmetry points  $(\varphi_1, \varphi_2) = (90^\circ, 0^\circ)$  and  $(180^\circ, -90^\circ)$  undergo a substantial broadening in the maps measured in diffraction, as compared to  $\delta I/I$ -maps obtained in reflection. In fact, convergence cannot be reached upon attempting to fit the extended diffraction  $\delta I/I$  datasets shown in Figs. 5.11(b), 5.11(c), 5.11(e) and 5.11(f)

<sup>52</sup> The voltage amplification gain of the Si-photodetector is usually set to 40 dB during reflection measurements in GME, while it was set to 50 and 60 dB for the measurements at the first- and second-order diffraction spots, respectively.

<sup>53</sup> For an explanation on the role of the background intensity offset, see Appendix II.

<sup>54</sup> A photodetector amplification gain of 20 dB was used for all data in Fig. 5.11.

using the formula for reflection optics. Thus, one can see that while for polarizer configurations near the  $(90^\circ, 0^\circ)$  crossing point, the  $\delta I/I(\varphi_1, \varphi_2)$  function in reflection is valid as a ‘small angles approximation’ for the diffraction data, the equivalence seems to fail for polarizer angles sufficiently far away from this symmetry point.

### 5.5 Conclusions

In summary, the optical and magneto-optical properties of Py grating samples with varying groove depth  $h$  have been investigated in reflection and diffraction geometries [235]. Laterally extended high-quality samples with one-dimensional stripe geometry and uniform height profiles were provided by collaborators from the Chemical Physics Department at the University of the Basque Country, and quality checks were performed using AFM and SEM. The optical and magneto-optical properties have been characterized by means of the GME technique, which allowed determining the orientation dependent reflection matrix of the samples. It is demonstrated that such magnetic gratings function as an artificial material, for which uniaxial optical and magneto-optical anisotropies are tunable via the groove depth  $h$ . Specifically, a linear correlation of the optical and magneto-optical anisotropy with  $h$  is observed, for the groove depth range investigated here.

Moreover, the viability of applying the GME technique to determine the reflection matrix of samples with (shallow) periodic surface patterns has been tested, even if it was initially developed for the study of planar surfaces, such as films and multilayers. The methodology is in principle applicable, even if the microscopic meaning of the reflection matrix coefficients have to be treated within an appropriate optical modeling strategy, such as in the framework of the local mode method (LMM).

Last but not least, the GME-technique has also been utilized to study the magneto-optical response of the Py gratings in diffraction, leading to the conclusions that the approach is experimentally feasible and that the polarization dependent diffraction signals under magneto-optical effects share the same basic symmetry as the conventional reflection matrix, at least for angles that are sufficiently close to the polarization crossing point.

## Chapter 6

# Oscillatory Dzyaloshinskii-Moriya type magnetic interlayer exchange coupling in Co/Ag/Co multilayers

*The optical, magneto-optical and magnetic properties of polycrystalline Co/Ag/Co multilayers with an ultrathin variable thickness Ag-wedge are studied. By using the GME technique, the quantitative separation of coherent and non-coherent magnetization rotation processes is achieved as a function of the applied field strength, which allows the identification of an anomalous transverse magnetization component, which is furthermore Ag thickness dependent. We find that the only plausible interpretation of this behavior requires the existence of a Dzyaloshinskii-Moriya type magnetic interlayer exchange coupling, which is a new phenomenon in ultrathin film magnetism. We discuss its physical origin and estimate the strength of the interaction, which is approximately one order of magnitude smaller than that found in asymmetric multilayer stacks featuring skyrmions and asymmetric domain wall dynamics.*

### 6.1 Introduction: spin polarize quantum size effects in magnetic ultrathin films and multilayers

The development of modern deposition and fabrication techniques in the last decades has made possible to produce materials that are structured at the nanometer scale, including sub-nanometer interface precision, which gave birth to the field of layered magnetic structures [236, 237]. Quantum size effects become increasingly relevant at these short length scales, having a marked impact on the relevant physical properties of the material (optical, magnetic, etc.). This means that one can design and engineer solids in which the response of the electrons to external forces such as magnetic fields or electric currents is significantly influenced by the presence and geometry of surfaces and interfaces.

One of the prominent examples that made a most relevant technological impact is the discovery of the bilinear magnetic interlayer exchange coupling through non-magnetic interlayers [8]. This finding ultimately led to the observation of the giant magnetoresistance (GMR) effect [9, 10], which was awarded with the Nobel Prize in Physics in 2007 and caused a revolution in magnetic recording technology.

Engineering ultrathin films and interfaces allows one to tune the interference effects of the electron waves in solids. For instance, in a ferromagnet/noble-metal/ferromagnet (FM/NM/FM) multilayer stack, this interference can be made constructive or destructive as a function of the noble-metal spacer thickness. In fact, it was found that interlayer exchange coupling and GMR are modulated in an oscillatory fashion with the spacer thickness [47, 48, 238, 239], a phenomenon that is explained by the formation of quantum well states mediating interlayer exchange coupling [240-243]. The role of electron quantum interference effects was also confirmed via photoemission experiments [244]. These results motivated intense research in ultrathin film structures with the purpose of optimizing trilayer geometries and maximizing the observed effects. Soon after the discovery of bilinear interlayer exchange coupling, which favors either the parallel or antiparallel alignment of magnetizations across the non-magnetic spacer, the biquadratic interlayer coupling was unveiled, which promotes a perpendicular configuration of magnetization between layers [50, 51].

Apart from magnetic coupling and magnetoresistance effects, a significant variation of the magneto-optical Kerr effect including oscillatory behavior of the Kerr rotation and ellipticity was also observed in ultrathin film structures such as the aforementioned sandwich structures [245, 246], or magnetic overlayers on noble metal films (and vice versa) [247-250]. Finally, oscillations in the magnetic anisotropy of ultrathin multilayer and overlayer structures can also exist under certain special conditions [251, 252]. Many of these studies concentrated on measuring quantities such as the Kerr rotation and ellipticity. However, as we earlier found in this thesis, such quantities depend in all optical, magneto-optical and magnetization dependent properties. The main goal of this thesis chapter is to take advantage of the capabilities of the GME technique in order to separate the optical, magneto-optical as well as magnetic properties, for the purpose of obtaining a deeper insight into the previously reported rich physical phenomena related to quantum size effects in ultrathin magnetic films and multilayers.

The present chapter contain the fabrication and the magneto-optical characterization of multilayer stacks of the type of FM/NM/FM, consisting of two adjacent magnetic films that are separated by means of a non-magnetic film of varying thickness. In particular, the focus will be put on Co/Ag/Co trilayers with a variable

thickness of the Ag interlayer. Due to the presence of this ultrathin non-magnetic interlayer, the electron wave functions and spin densities of the magnetic layers are separated even though they are not isolated from each other due to the delocalized and wave-like nature of the electrons. The existence of spin-polarized electronic wave functions interacting across this thin interlayer leads to non-trivial optical and magneto-optical responses that cannot be explained by without assuming quantum mechanical modifications of the (quasi-)local optical properties.

## 6.2 Anomalous magnetization behavior in Co/Ag/Co multilayers

Co/Ag/Co structures with a sufficiently thick bottom FM layer will be considered for this study, so that the light penetration depth at visible wavelengths does not exceed the total multilayer thickness and thus the substrate/bottom-FM interface does not need to be considered in the optical analysis treatment.

Correspondingly, Co/Ag/Co multilayers were sputter deposited on elongated Si(100) substrate pieces (80 mm  $\times$  5 mm). For the fabrication process, we first deposited 100 nm of Co as the bottom FM layer. This deposition step was made by rotating the substrate holder in order to obtain good film thickness uniformity. However, when coming to deposit the subsequent Ag layer, the substrate was aligned with its long axis towards the direction of a tilted sputter gun, such that a position dependent Ag-thickness  $t_{Ag}$  ranging between 0.5 and 3.5 nm could be obtained<sup>55</sup>. Finally, the topmost FM layer consisting of either 10 or 15 nm of Co as well as a protective SiO<sub>2</sub> overcoat of 10 nm were deposited by rotating the substrate holder again. Given that the native oxide of the Si-substrates was not removed prior to deposition, the multilayers grown here are of polycrystalline character, lacking any preferential crystallographic texture. In this case, epitaxial growth of the layers is avoided, such that the resulting samples can be magnetically saturated under modest applied field values.

Among all the fabricated samples, results are shown for just two chosen trilayer structures, which have  $t_T$  thicknesses of the topmost Co layer equal to 10 and 15 nm, and are labeled as *CoAgCo10* and *CoAgCo15*, respectively. A schematic of the multilayer structure is shown in Fig. 6.1, depicting the wedge-type interlayer geometry, the thicker bottom Co layer and a thinner topmost Co layer. In addition, the main multilayer stack parameters are summarized in Table 6.1.

---

<sup>55</sup> The Ag-wedge thickness profile was calibrated via spectroscopic ellipsometry in calibration samples. Additional details on the fabrication and calibration of wedge-type samples can be found in Chapter 2.

Sample	CoAgCo10	CoAgCo15
$t_T$ (nm)	10	15
$t_B$ (nm)	100	100
$t_{Ag}$ (nm)	0.5 - 3.2 nm	0.6 - 3.5 nm
$\frac{dt_{Ag}}{dy}$ (nm mm <sup>-1</sup> )	< 0.05	< 0.08

**Table 6.1:** Specifications of the Co/Ag-wedge/Co samples employed in this study.  $t_T$  and  $t_B$  refer to the thickness of the top and bottom Co layers, respectively, while the Ag-interlayer thickness is labeled as  $t_{Ag}$ . The maximum Ag-thickness gradient is given as an upper limit for  $dt_{Ag}/dy$ .

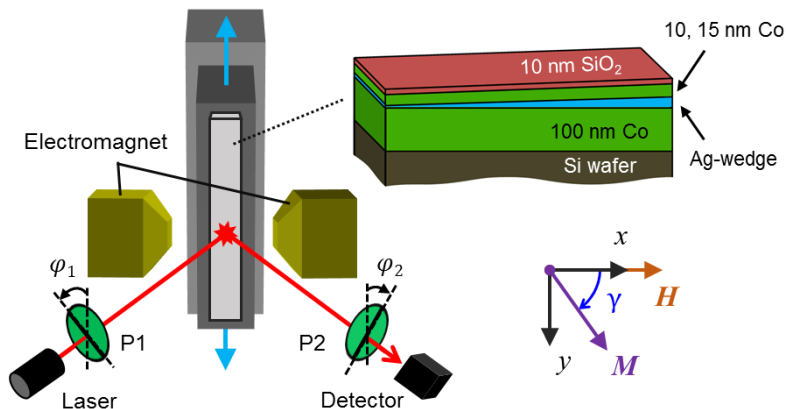


**Fig. 6.1:** Schematic of the Co/Ag-wedge/Co sample as well as the GME setup with an incorporated translation sample-stage for position-dependent magneto-optical measurements. The sample position is vertically varied along the  $y$ -direction. The relevant axes and angles are defined in the inset.

The advantage of the wedge-type sample lies in the fact that a large number of ‘samples’ are accessible using a single fabrication step. Specifically, we will perform position dependent optical experiments, thus selecting a given Ag-thickness by illuminating a narrow area of the elongated wedge-type sample. This permits one to evaluate in a quasi-continuous fashion what is the effect of the Ag thickness onto the optical, magneto-optical as well as magnetic properties of the Co/Ag/Co multilayer. Furthermore, given that the bottom and topmost Co layers have been deposited under the same conditions for the entire wedge, we avoid possible sample-to-sample variations that even occur if multiple Co/Ag/Co samples with nominally identical interlayer

thickness are grown in individual deposition processes. Instead, our fabrication process ensures that the modification of the measured properties at each position along the wedge to be the result of the Ag thickness variation alone.

One should also pay attention to the gradient of the Ag-thickness profile. In our setup, the laser spot possesses a nearly circular shape of 1 mm of diameter. This means that a certain distribution of Ag-thicknesses will be probed in the optical experiment when illuminating the sample. However, by choosing the correct substrate geometry (at least 80 mm long) and a  $t_{Ag}$  range limited to approximately 3 nm, we assure that the maximum variation of Ag-thickness with respect to the position along the long axis of the wedge,  $dt_{Ag}/dy$ , is below always 0.08 nm per mm (see Table 6.1), hence setting an upper limit for the thickness resolution in our measurements.

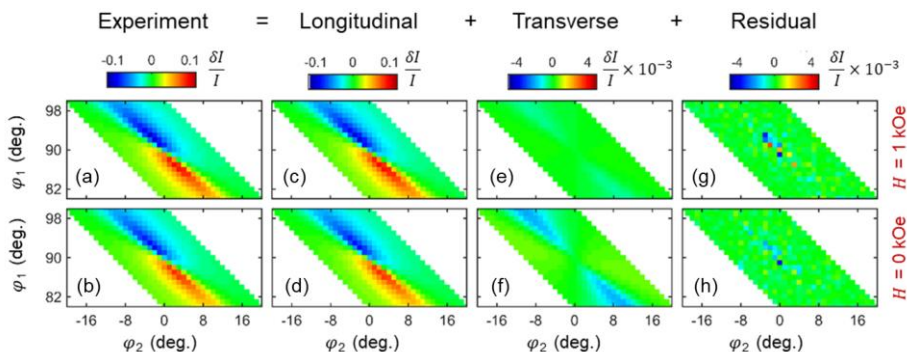
In order to perform GME measurements the Co/Ag/Co samples are placed in the setup, in which an automatic linear translation stage has been incorporated<sup>56</sup>. (see schematic in Fig. 6.1). The magneto-optical probe is scanned along the  $y$ -axis, parallel to the wedge long axis, in order to evaluate the Ag-thickness dependent variation of the optical, magneto-optical and magnetic properties. For our experiment, we took advantage of the high precision and repeatability of the translation stage positioning, by which we performed GME measurements in steps as small as 0.5 mm, corresponding to  $t_{Ag}$  variations<sup>57</sup> of the order of 0.01 nm. An applied magnetic field  $H$  of up to 1250 Oe is used along the  $x$ -axis by means of an electromagnet, with the purpose of modifying the magnetization state of the Co/Ag/Co stack.

Fig. 6.2 shows the results of an exemplary measurement that have been done on the *CoAgCo10* sample at the position corresponding to a Ag thickness of  $t_{Ag} = 0.77$  nm. In particular, Figs. 6.2(a) and 6.2(b) exhibit experimental GME maps at applied fields of 1000 and 0 Oe. By fitting these experimental maps to the  $\delta I/I$  expression (in the absence of polar Kerr effects), one can separate the  $\delta I/I$  contributions arising from longitudinal [Figs. 6.2(c) and 6.2(d)] and transverse [Figs. 6.2(e) and 6.2(f)] Kerr effects, as well as the residual maps that are the subtraction of the experimental maps and the whole  $\delta I/I$  expression [Figs. 6.2(g) and 6.2(h)]. The maps in Figs. 6.2(c) and 6.2(d) exhibit the well-known opposite sign lobe structure for the longitudinal Kerr effect, and while not clearly visible in the figure, one can observe a slight reduction of the map intensity upon lowering the applied field. Correspondingly, the transverse maps in Fig. 6.2(e) at  $H = 1000$  Oe reflects an almost null transverse Kerr effect, confirming

<sup>56</sup> See Section 3.2 of this thesis for additional details of the setup.

<sup>57</sup> Thickness variations of the order of 0.01-0.1 nm must be understood here as the statistical average variation over a sufficiently large lateral area.

at a first glance that for sufficiently high values of  $H$ , the magnetization of the Co/Ag/Co stack is well saturated along the applied field orientation. On the other hand, a weak but still appreciable signal (of the order of  $\delta I/I \sim 0.004$ ) corresponding to the transverse Kerr effect is seen in Fig. 6.2(f) at  $H = 0$ , indicating the existence of a coherent magnetization reversal process upon lowering the field. Finally, the residual maps in Figs. 6.2(g) and 6.2(h) only display scattered noisy data points near the crossing point of the polarizers ( $\varphi_1 = 90^\circ$ ,  $\varphi_2 = 0^\circ$ ). Thus we conclude that a small magnetization rotation away from the  $x$ -axis has occurred in the sample upon lowering the field.



**Fig. 6.2:** (a), (b) show GME-datasets for applied field values of 1000 and 0 Oe (remanence) measured at the *CoAgCo10* sample for an Ag-thickness of  $t_{Ag} = 0.77$  nm. The fitted  $\delta I/I$  maps originated from longitudinal Kerr effects alone are (c), (d), whereas the maps corresponding to transverse Kerr effects alone are displayed in (e), (f). The residual maps obtained by subtracting the fitted maps to the experimental ones are shown in (g), (h).

By taking into account the polycrystalline nature of the Co films in the stack, one indeed expects some level of reduction of the longitudinal magnetization component (and thus of its associated longitudinal Kerr effect) upon lowering the field. This can be anticipated as a result of the non-coherent rotation of the magnetization vectors in the grains forming the Co films, which possess a distribution of the magnetization easy axis orientations. Upon lowering the field, a fanning process of magnetization occurs, which causes a reduction of the net magnetization of the sample as weakly non-uniform states of magnetization are generated. Opposite to this, a decrease of the longitudinal component by means of a coherent magnetization rotation process must also be accompanied by a simultaneous increase of the transverse magnetization (for in-plane reversal processes). By measuring the entire reflection matrix by the GME-technique, one can also study the appearance of non-uniform states of magnetization by quantifying the relative weight of coherent and non-coherent magnetization rotation processes during reversal. This is accomplished by following the exact proportion at which the longitudinal and transverse (as well as polar) Kerr effects

vary with respect to each other, such that the magnetization orientation as well as its normalized modulus can be determined in a field-dependent fashion [128].

Fig. 6.3 shows the field dependent evolution of the magnetization angle  $\gamma$  and modulus  $M/M_0$  during the decreasing field branch of the magnetization reversal, as extracted from experimental GME datasets such as the ones shown in Fig. 6.2. As a first approximation to understand the magnetization reversal properties of the Co/Ag/Co stack, we used an optical model of a semi-infinite Co slab covered with 10 nm of SiO<sub>2</sub>, and extracted  $\gamma$  and  $M/M_0$  as fit parameters<sup>58</sup>.

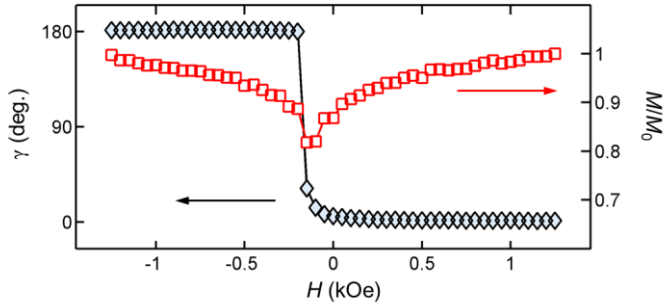


**Fig. 6.3:** Field-dependent evolution of the magnetization angle  $\gamma$  and the modulus  $M/M_0$  upon considering the Co/Ag/Co stack as a semi-infinite Co slab capped with 10 nm of SiO<sub>2</sub>.

$H$ (Oe)	$\gamma$ (deg.)	$M/M_0$
1000	$1.6 \pm 0.3$	$0.98 \pm 0.02$
0	$5.6 \pm 0.5$	$0.87 \pm 0.01$

**Table 6.2:** Determined magnetization angle  $\gamma$  and modulus  $M/M_0$ , based on the measurements in Fig. 6.2, for applied magnetic fields of  $H = 1000, 0$  Oe, in the case of the sample *CoAgCo10* at  $t_{Ag} = 0.77$  nm.

<sup>58</sup> As the magnetization component  $m_i$  ( $i = x, y, z$ ) is proportional to the sum of the magnetization components in each of the non-uniformly magnetized regions ( $|m_i^j| < 1$ ) in the material, we can assume that this sum rule is fulfilled for each MOKE contribution. Each of these local magnetizations  $m_i^j$  contribute to the dielectric tensor by the same magneto-optical coupling strength  $Q$ . However, when taking the uniform magnetization state assumption within the GME analysis procedure, this non-uniformity in  $m_i$  is translated into the perceived coupling strength, such that an effective  $Q^{eff} < Q$  emerges from the GME analysis, which can now be related to the magnetization modulus  $M/M_0$  and its reduction (see Section 3.6 and Ref [128]).

As can be seen in Fig. 6.3, the magnetization is aligned near the  $\gamma = 0^\circ$  orientation (along the  $x$ -axis) for high fields. It subsequently rotates away from the field axis towards positive  $\gamma$  values, which is in accordance with the increase of the transverse  $\delta I/I$  signal observed at remanence in Fig. 6.2(f). The magnetization then switches at about  $H_S = -200$  Oe and orients itself close to  $\gamma = 180^\circ$  for sufficiently large negative fields. On the other hand, it is seen that while the modulus of the magnetization vector is relatively uniform for high field values, it features a considerable reduction of about 20% just before switching, due to the non-coherent magnetization rotation processes we have previously mentioned. The  $M/M_0$  value reaches a minimum at  $H_S$  and starts increasing again upon application of stronger negative fields, approaching saturation for  $H < -1000$  Oe. Table 6.2 shows exemplary values of  $\gamma$  and  $M/M_0$  determined at  $H = 1000$  and  $0$  Oe, which specifically correspond to the GME datasets shown in Figs. 6.2(a) and 6.2(b). The precision in the magnetization angle is in accordance with the magnetometry results presented in the Chapter 3, where the error bars of the in-plane magnetization angles remained around  $0.2^\circ$  during reversal.

Despite the semi-infinite Co slab model being too simplistic to describe our multilayered sample, the choice can be justified by the fact that the light penetration depth at  $\lambda = 635$  nm is very similar to the thickness of the top Co film. Hence one can argue that the magneto-optical signal arising from the bottom layer is substantially smaller, such that we are mainly sensitive to magnetization effects of the topmost layer [253]. We will use this argument for an initial inspection of the Co/Ag/Co wedges we have grown, by introducing a gradual level of complexity in the optical and magnetic modeling of our samples throughout the next steps.

It should be mentioned that the measured results of the *CoAgCo10* sample at the  $t_{Ag} = 0.77$  nm thickness exhibit a remarkable feature, namely the appearance of a coherent magnetization rotation upon lowering the magnetic field, which was identified via the increase of the transverse Kerr effect. This result is in principle unexpected, because given the polycrystalline nature of the Co films in the multilayer stack, we expect no preferential orientation to which the magnetization is prone to rotate. This characteristic will be studied in detail in the following subsection.

### ***Ag-thickness dependent helicity of the transverse magnetization component***

After describing the measurement and analysis strategy for an individual Ag-thickness spot above, we proceed to study the effect of the Ag interlayer thickness in Co/Ag/Co multilayers. For doing so, we have scanned the laser spot along the *CoAgCo10* and *CoAgCo15* wedge type samples in order to perform GME measurements.

Fig. 6.4(a) exhibits the decreasing field branch evolution of the parameter  $B_3$ , proportional to the transverse magnetization component  $m_y$ , for interlayer thicknesses of  $t_{Ag} = 0.77, 1.28$  and  $2.59$  nm measured for *CoAgCo10*. For all Ag thicknesses,  $B_3$  approaches zero at high applied magnetic fields ( $|H| > 500$  Oe). As mentioned above, this is because the applied field aligns the magnetization of the Co/Ag/Co stack along the  $x$ -axis and thus causes a nearly null transverse component of magnetization  $m_y$ .

However, as the applied field is lowered, a Ag-thickness dependent sign of the departure of  $B_3$  from zero is found. In particular,  $B_3$  acquires an increasing trend when releasing the field at an interlayer thickness of  $t_{Ag} = 0.77$  nm (associated with an increase of the magnetization angle  $\gamma$  away from the  $x$ -axis, clockwise rotation). Contrary to this,  $B_3$  acquires negative values at  $t_{Ag} = 1.29$  nm, exhibiting a field dependent decreasing trend and thus representing a departure of the magnetization from the field-axis towards decreasing  $\gamma$  values (counterclockwise rotation). Finally, we also find Ag thickness cases in which the parameter  $B_3$  remains nearly zero for all applied field values, such as for  $t_{Ag} = 2.59$  nm, which is towards the thicker end of the Ag interlayer. Therefore, the coherent rotation process of magnetization manifested by the appearance of a transverse component  $m_y$  possesses a Ag thickness dependent nature.

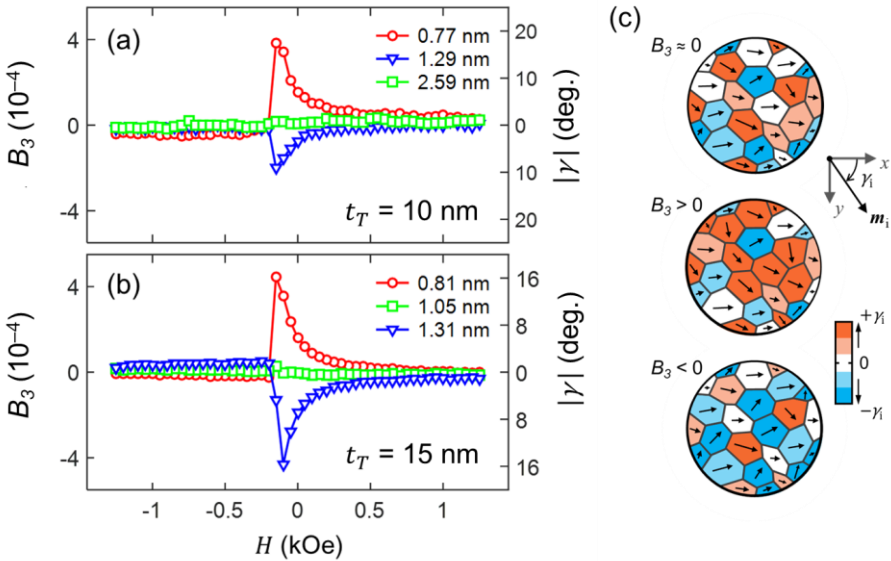


**Fig. 6.4:** Field dependent evolution of the transverse Kerr effect parameter  $B_3$  for three different Ag interlayer thicknesses, for the samples (a) *CoAgCo10* and (b) *CoAgCo15*. (c) Schematic of the magnetization configuration of the top Co layer in remanence, dependent on the measured sign of the parameter  $B_3$ .

In order to check for consistency, the *CoAgCo15* sample was also measured, which possesses a thicker top Co film and a similar Ag thickness wedge profile (see Table 6.1). As can be seen in Fig. 6.4(b), this sample exhibits qualitatively the same thickness dependent anomalous behavior of the transverse magnetization component we found in *CoAgCo10*. For a Ag thickness of 0.81 nm, the  $B_3$  parameter exhibits an increasing behavior upon lowering the field, indicative again of a clockwise magnetization rotation component. On the other hand, the  $B_3$  vs  $H$  data reveal a counter-clockwise rotation process of magnetization for a Ag interlayer thickness of 1.31 nm. Finally, one can see that for an intermediate Ag-thickness value of 1.05 nm,  $B_3$  remains nearly zero for all applied field values.

For the purpose of quantifying the amount of coherent rotation acquired by the magnetization, we have employed the same semi-infinite Co slab optical model as before. The absolute values of the magnetization angle  $\gamma$  obtained within this approximation are shown on the right axes of Figs. 6.4(a) and 6.4(b), side-by-side to the corresponding measured  $B_3$  values<sup>59</sup>. As can be observed, the maximum coherent rotation angle in remanence is around  $5^\circ$  for the cases presented here, which constitutes a slight but still appreciable magnetization deviation<sup>60</sup>.

Hereby, we conclude that the Co/Ag/Co multilayers studied here feature a Ag thickness dependent helicity of magnetization during reversal, where the existence of a coherent rotation process and its preferred circular motion (i.e., *clockwise* vs *counterclockwise*) are predefined by the interlayer thickness between the two ferromagnetic Co layers. At this point, it is worth to point out that we obtained consistent results in the two samples with different thicknesses of the topmost Co layer, such that we can attribute the predefined helicity behavior to the Ag thickness variation alone. On the other hand, it is also very important to stress the fact that the observed helicity is a deterministic behavior, because the  $B_3$  vs  $H$  values are extracted from GME-map measurements, in which  $21 \times 21 = 441$  independent magnetization reversal events are measured. This can be further checked, for instance, by inspection of Fig. 6.2(f), where the  $\delta I/I$  signal in remanence corresponding to the transverse Kerr effect alone is represented for the sample *CoAgCo10* at 0.77 nm Ag thickness. The sign of the  $\delta I/I$  quantity consistently follows the structure expected for a specific sign of the transverse magnetization component, as there are no scattered points of opposite sign suggesting

---

<sup>59</sup> For the right axes in Figs. 6.4(a)-6.4(b),  $\sin \gamma \sim \gamma$  was assumed for small angles.

<sup>60</sup> The magnetization angles increase above  $5^\circ$  upon lowering the field below remanence. However, the value in remanence is highlighted as there must be an interaction promoting this slight tilt of magnetization on average.

that magnetization rotation occurs in both circular directions with a given probability for each of them.

In order to qualitatively understand how magnetization reversal occurs as a function of the interlayer Ag thickness, the remanence states of a polycrystalline Co film for the cases in which  $B_3$  is nearly zero, positive or negative are illustrated in Fig. 6.4(c). The configuration at the top, for which  $B_3 \approx 0$ , represents a polycrystalline magnetic film in which the grains possess a distribution of preferential axes of magnetization. This leads to a remanent state after saturation along the  $x$ -axis, in which one portion of crystallographic grains lacks a substantial deviation from the applied field axis [white colored grains in Fig. 6.4(c)], while some other grains acquire a positive (orange colored grains) or negative (blue colored grains)  $\gamma_i$  rotation. For a fully disordered polycrystalline film without any texture effects, the number of grains that deviate to both sides of the  $x$ -axis upon removing the field is the same, due to the randomly oriented magnetization easy axes (approximately equal number of blue and orange colored grains). Within this situation, the magnetization reversal is governed by non-coherent rotation processes alone and the resulting state at  $H = 0$  corresponds to a ‘fanned’ magnetization configuration.

In fact, this is the remanence magnetization configuration that one would expect for our polycrystalline Co/Ag/Co multilayers. Correspondingly, one should observe a null transverse magnetization component for all applied magnetic field values within this situation. However, we see that for certain Ag interlayer thicknesses a coherent rotation of magnetization occurs in addition to magnetization fanning, as depicted in the medium and bottom illustrations in Fig. 6.4(c). These correspond to magnetization configurations, in which  $B_3$  acquires positive or negative values, respectively. In these situations, an increased number of grains are rotated clockwise ( $B_3 > 0$ ) or counter-clockwise ( $B_3 < 0$ ), as represented by the majority of orange or blue colored grains in Fig. 6.4(c). Under these situations, the Co/Ag/Co multilayers undergo the magnetization reversal process by means of a combination of coherent and non-coherent rotation processes.

In order to characterize this unexpected behavior, we have realized extensive measurements on our samples, where we have extracted the Ag thickness and applied magnetic field dependence of all reflection matrix parameters via the GME technique. The results are shown in Figs. 6.5 and 6.6 for the sample *CoAgCo10* and *CoAgCo15*, respectively. Specifically, Figs. 6.5(a)-6.5(c) show the Ag thickness dependence of the  $B_2$ ,  $B_3$  and  $B_8$  parameters for different strengths of the applied field ( $H = 1250, 250$  and  $0$  Oe). One can see that the  $B_2$  parameter in Fig. 6.5(a), proportional to the longitudinal  $m_x$  magnetization component, shows principally a small linear decrease with  $t_{Ag}$  due to

the fact that upon introducing a thicker Ag interlayer, less magneto-optical signal from the bottom layer is being observed. Together with this, a reduction of  $B_2$  also happens upon lowering the field, which is consistent with the magnetization fanning process we have described above. On the other hand, the transverse component  $B_3$  in Fig. 6.5(b) and which is proportional to  $m_y$ , exhibits a completely different behavior as a function of the Ag thickness. For large applied fields, its value is nearly zero for all Ag thicknesses. However, as the field is reduced to  $H = 0$  Oe, an oscillatory behavior emerges, as  $B_3$  features sign changes as well as an attenuation of its amplitude down to zero with increasing Ag thickness.

Finally, the purely optical reflection matrix parameter  $B_8$  in Fig. 6.5(c) displays a linear Ag thickness dependent variation (at least above  $t_{Ag} > 0.5$  nm), as the introduction of a thicker Ag interlayer modifies accordingly the optical reflectivity of the Co/Ag/Co stack. One can also observe that  $B_8$  is not modified by the applied field, in accordance with its magnetization independent nature.

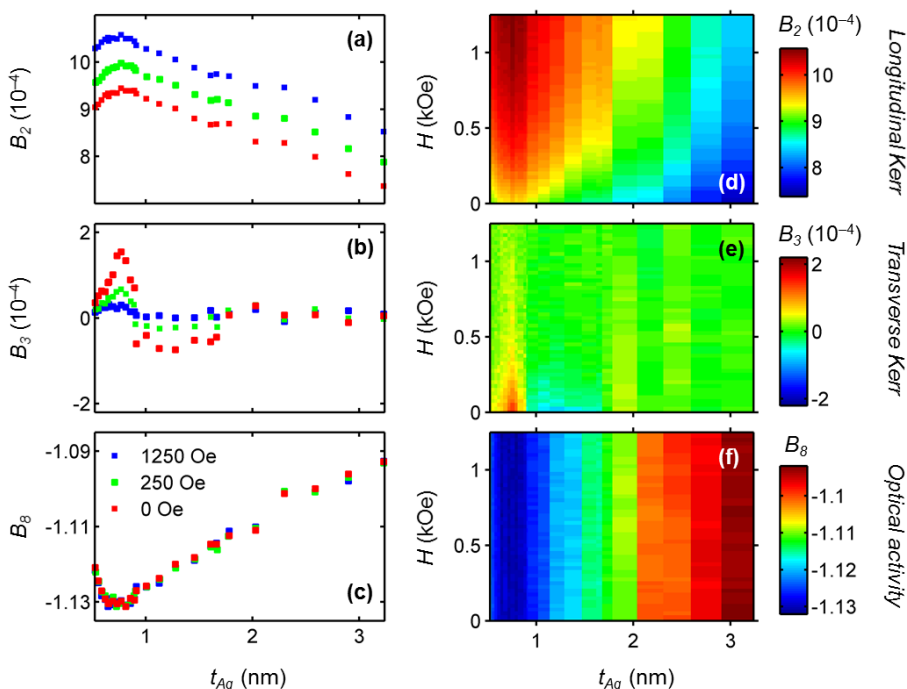


**Fig. 6.5:** Ag-thickness and applied magnetic field dependent GME data for the *CoAgCo10* sample. (a)  $B_2$ , (b)  $B_3$  and (c)  $B_8$  parameters vs  $t_{Ag}$  for applied magnetic field strengths of 1250, 250 and 0 Oe. (d), (e) and (f) display color-coded maps of the same quantities vs  $t_{Ag}$  and  $H$ .

It is worth commenting that the low Ag thickness regions of Figs. 6.5(a) and 6.5(c) show a kink in the parameters  $B_2$  and  $B_8$ , opposite to the linear behavior observed for  $t_{Ag} > 0.5$  nm. This might come from optical interference effects at the ultrathin Ag interlayer limit. In any case, one can assume that this is a modest, nonmagnetic effect that does impact the observed behavior in  $B_3$ .

Figs. 6.5(d)-6.5(f) exhibit color-coded Ag thickness and field dependent maps of the aforementioned parameters, where the complete data of the reflection matrix parameters can be found. The oscillatory behavior of the transverse Kerr effect is evidenced in Fig. 6.5(e) by the horizontally alternating red (positive) and blue (negative) colors by which  $B_3$  is represented. Together with this, one can also perceive that this transverse Kerr effect is attenuated for higher Ag thicknesses, as well as how smaller fields are needed to make this transverse Kerr effect disappear as  $t_{Ag}$  increases.

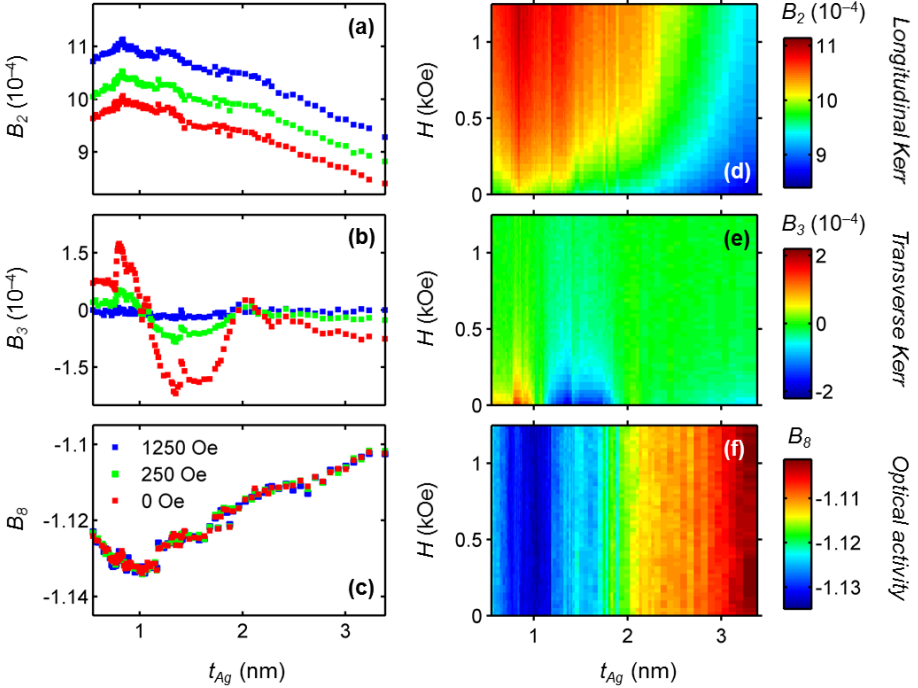


**Fig. 6.6:** Ag-thickness and applied magnetic field dependent GME data for the *CoAgCo15* sample. (a)  $B_2$ , (b)  $B_3$  and (c)  $B_8$  parameters vs  $t_{Ag}$  for applied magnetic field strengths of 1250, 250 and 0 Oe. (d), (e) and (f) display color-coded maps of the same quantities vs  $t_{Ag}$  and  $H$ .

A qualitatively equivalent situation is seen for the *CoAgCo15* sample in Fig. 6.6, where a finer grid of the Ag thickness was chosen. The same reduction in the longitudinal Kerr effect  $B_2$  upon decreasing the field and the emergent oscillatory behavior of the transverse Kerr effect are visualized in Figs. 6.6(a) and 6.6(b), respectively. It is also seen that the transverse Kerr effect  $B_3$  is strongly diminished towards the thick end of the Ag interlayer wedge, in accordance with the results found in the sample *CoAgCo10*. Finally, the purely optical reflection matrix parameter  $B_8$  in Fig. 6.6(c) also shows a linear trend which is field independent. It is remarkable that with a finer Ag thickness grid, a finer structure of the oscillations is revealed, which is most evident for the  $B_3$  data, but also for  $B_2$  and  $B_8$ , where more subtle oscillations can be seen. Finally, Figs. 6.6(d) – 6.6(f) show color coded maps of the reflection matrix elements for all Ag thickness and applied magnetic field values studied here.

Eventually, the data in Figs. 6.5 and 6.6 demonstrate that the anomalous thickness dependent helicity of the transverse magnetization component is present in both samples. The two experiments realized on different samples share the very same properties, such as (i) the oscillatory behavior of the transverse Kerr effect parameter  $B_3$ , (ii) the reduction of the longitudinal Kerr effect parameter  $B_2$  against  $H$  and  $t_{Ag}$ , and (iii) the reduction of the purely optical, field independent parameter  $B_8$ .

Therefore, one can conclude that there must exist an anisotropic energy contribution to the magnetic moments in Co/Ag/Co, favoring the deviation of the top Co layer magnetization towards one side or another of the field axis upon removing the field. This energy contribution must be, as shown above, interlayer thickness dependent, as well as needs to promote a predefined helicity for the magnetization reversal path of the topmost Co film.

In fact, one could first think that the observed phenomenon is a result of local variations, in terms of crystallite alignment effects, in the magnetocrystalline anisotropy of the Co layers. However, such a situation seems most unlikely, as the deposition process employed assures a high level of uniformity of the Co over the entire wedge. From our previous observation, the deposition of single Co films on oxidized Si substrates leads to magnetic films with no preferential orientation of magnetization (see Section 3.6). It is also difficult to find any reason why the presence of a wedge-like Ag interlayer would cause such an oscillatory variation of the Co film deposited on top. It is also important to mention that we did not see any substantial change in the switching field upon Ag thickness variation, which remained the same for all Ag thicknesses measured here within a resolution of around 20 Oe.

Given the strong dependence of magnetization reversal on the Ag-interlayer thickness, it is sensible to consider that the reversal behavior is determined by magnetic

interlayer exchange coupling. The vast majority of interlayer exchange coupling interactions are of two types: bilinear and biquadratic. The first promotes parallel or antiparallel alignment of the resulting magnetizations of the top and bottom ferromagnetic layers, while the second favors their perpendicular alignment [51]. This second type of coupling possesses a necessary ingredient for generating a deviation between the magnetization vectors in the top and bottom layers, in the form of a scissor type state. Furthermore, given that the tilt angles of magnetization that we observe are of the order of only few degrees in remanence, the underlying mechanism could consist of a combination of bilinear and biquadratic coupling, which would compete. However, none of these two interactions could explain the measured predefined helicity of the transverse magnetization component during reversal, as the two interacting magnetization are completely interchangeable within their energy expressions.

Upon these premises, a conceivable interaction that could lead to the observed magnetization configurations is the *Dzyaloshinskii-Moriya* (DM) interaction, which couples two magnetic moments via the vector cross product

$$\epsilon_{DM} = -\mathbf{D} \cdot \mathbf{m}^T \times \mathbf{m}^B, \quad (6.1)$$

in which the magnetization vector of the top and bottom layers,  $\mathbf{m}^T$  and  $\mathbf{m}^B$ , are not interchangeable. This energy expression now produces a pre-determined chirality of the angle between the magnetizations of the interacting ferromagnets based on the orientation of the vector  $\mathbf{D}$ . From here, one can now interpret the interlayer thickness oscillations in the transverse magnetization component as a sign change of  $D$ . Thus, a simple magnetic model assuming a DM-type interlayer coupling between the two ferromagnetic layers will be developed, as well as the physical origin and plausibility of such an interaction will be explored in more detail.

### ***Macrospin model with Dzyaloshinskii-Moriya type interlayer exchange coupling***

In the following, a simple macrospin model is presented, in order to understand the magnetization reversal behavior observed in sputter deposited polycrystalline Co/Ag/Co multilayers. Specifically, the model needs to include the following ingredients to be at least qualitatively realistic:

- (i) Two ferromagnetic layers that possess an isotropic distribution of easy axes of magnetization in terms of crystallographic grain misalignment. However, upon considering a finite amount of grains in the model, the anisotropy axes of the grains have to be oriented symmetrically with respect to the field axis.

- (ii) The intralayer exchange coupling interaction that regulates the inter-granular magnetization alignment in each Co layer. The strength of this interaction will be chosen to be the same in the bottom and topmost Co layers.
- (iii) The interlayer exchange coupling interaction across the non-magnetic spacer between the resulting magnetization vectors of the two magnetic layers. This interaction should favor the perpendicular alignment of the magnetization vectors.
- (iv) In addition, the interlayer coupling should reproduce the preferential helicity of the transverse component of magnetization, as observed in the experiment.

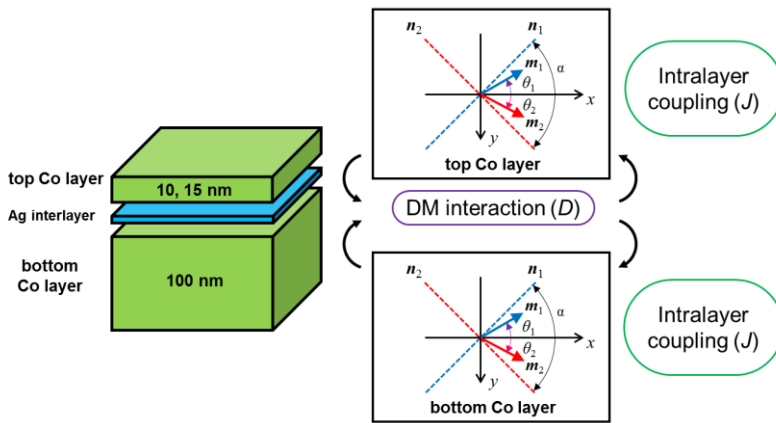


**Fig. 6.7:** Schematic of the developed macrospin model for mimicking the behavior of Co/Ag/Co multilayer stacks. Each ferromagnetic layer is modeled by two misaligned spins consisting of Stoner-Wohlfarth grains. Intralayer ferromagnetic coupling between the sub-spins is considered. On the other hand, the Ag-interlayer is considered to be the mediator of the chiral interlayer coupling between the ferromagnetic layers, via the Dzyaloshinskii-Moriya interaction.

Thus the simplest model that fulfills the requirements above was considered, a schematic of which is represented in Fig. 6.7. For doing so, each ferromagnetic layer is modeled by two Stoner-Wohlfarth particles with uniaxial in-plane magnetocrystalline anisotropy. The easy axes of the two particles are misaligned by an angle  $\alpha$  and evenly distributed around the applied field orientation (parallel to the  $x$ -axis). The magnetic anisotropy energy *per unit area* of the top ( $T$ ) and bottom ( $B$ ) Co layers are then<sup>61</sup>

<sup>61</sup> This energy term includes the contribution from the magnetocrystalline energy density, as well as from the magnetostatic energy term, which favors an in-plane orientation of magnetization due to the thin film geometry.

$$\begin{aligned}\epsilon_K^T &= -\frac{K}{2}t_T \cos^2\left(\theta_1^T - \frac{\alpha}{2}\right) - \frac{K}{2}t_T \cos^2\left(\theta_2^T + \frac{\alpha}{2}\right) \\ \epsilon_K^B &= -\frac{K}{2}t_B \cos^2\left(\theta_1^B - \frac{\alpha}{2}\right) - \frac{K}{2}t_B \cos^2\left(\theta_2^B + \frac{\alpha}{2}\right).\end{aligned}\tag{6.2}$$

Here,  $\theta_i^T$  and  $\theta_i^B$  ( $i = 1, 2$ ) are the magnetization angles of magnetic grains in the bottom and top ferromagnetic layers, while  $K$  is the magnetic anisotropy energy density. The anisotropy axes of the two grains forming each layer are misoriented by an angle  $\alpha$ , and  $t_T$ ,  $t_B$  are the thicknesses of the top and bottom Co layers, respectively.

Next, a bilinear exchange coupling term is considered in between the magnetic grains of each layer, favoring their parallel alignment. Again, by writing the energy per unit area, we have that

$$\begin{aligned}\epsilon_J^T &= -J t_T \cos(\theta_1^T - \theta_2^T) = -J t_T (m_{1x}^T m_{2x}^T + m_{1y}^T m_{2y}^T) \\ \epsilon_J^B &= -J t_B \cos(\theta_1^B - \theta_2^B) = -J t_B (m_{1x}^B m_{2x}^B + m_{1y}^B m_{2y}^B),\end{aligned}\tag{6.3}$$

where  $J > 0$  for ferromagnetic coupling<sup>62</sup>, and the in-plane magnetization components along the  $x$ - and  $y$ -axis for each magnetic grain are defined as  $m_{ix}^l = \cos \theta_i^l$  and  $m_{iy}^l = \sin \theta_i^l$  (with  $i = 1, 2$  and  $l = T, B$ ).

Moreover, the energy per unit area of the Zeeman interaction takes the form

$$\begin{aligned}\epsilon_Z^T &= -\frac{M_0 t_T H}{2} (\cos \theta_1^T + \cos \theta_2^T) = -\frac{M_0 t_T H}{2} (m_{1x}^T + m_{2x}^T) \\ \epsilon_Z^B &= -\frac{M_0 t_B H}{2} (\cos \theta_1^B + \cos \theta_2^B) = -\frac{M_0 t_B H}{2} (m_{1x}^B + m_{2x}^B),\end{aligned}\tag{6.4}$$

where  $H$  is the applied magnetic field along the  $x$ -axis and  $M_0$  represents volume averaged magnetization density.

Finally, a DM type interlayer exchange coupling interaction between the resulting magnetization vectors of the two magnetic layers is added, favoring their perpendicular alignment. Here, we define a coupling vector  $\mathbf{D} = D\hat{\mathbf{k}}$  which couples the resulting magnetization vectors of the top and bottom layers via

---

<sup>62</sup> Here,  $J$  is not the inter-atomic exchange coupling but a volume energy density interaction strength.

$$\begin{aligned}
 \epsilon_{DM} &= -\frac{D}{4} \cdot \mathbf{m}^T \times \mathbf{m}^B = -D\hat{\mathbf{z}} \cdot (\mathbf{m}_1^T + \mathbf{m}_2^T) \times (\mathbf{m}_1^B + \mathbf{m}_2^B) \\
 &= -\frac{D}{4} [(m_{1x}^T + m_{2x}^T)(m_{1y}^B + m_{2y}^B) - (m_{1x}^B + m_{2x}^B)(m_{1y}^T + m_{2y}^T)],
 \end{aligned} \tag{6.5}$$

where the sign of the factor  $D$  determines the right- or left-handed helicity of the interaction, and the  $\frac{1}{4}$  factor accounts for the multiplication of 2 time 2 spins in the interaction term. This specific interaction, through the cross product of the two interacting magnetization vectors, adds to the model the two key ingredients needed to qualitatively reproduce the outcome of our experiments via the interaction term  $E_{DM}$ , as it (i) favors the perpendicular alignment of the resulting moments of the layers, and (ii) introduces a preferred helicity of the magnetization configuration, due to the non-commutative property of the cross product.

Thus one can now build the total energy per unit area by summing up the contributions from the different interactions, namely

$$\epsilon_{TOT} = \epsilon_K^T + \epsilon_K^B + \epsilon_J^T + \epsilon_J^B + \epsilon_Z^T + \epsilon_Z^B + \epsilon_{DM}, \tag{6.6}$$

where only the last term involves the intermixing of the magnetization components belonging to the magnetic moments in both layers. Although the present model might be very simplistic, in particular in terms of its lateral sample structure, it captures the main ingredients of the physics that is present in our Co/Ag/Co samples, constituting a first good approximation towards a better understanding of their magnetization reversal properties. Furthermore, it does not only give a qualitative explanation of the observed anomalous transverse magnetization component behavior, but it also allows for a quantitative determination of the DM interaction in our samples, as will be shown below.

In order to solve the magnetic field dependent evolution of the magnetization configuration for a given set of parameters  $\{K, J, D\}$ , we recall that the free energy of a macrospin assembly can be expressed as  $F = -\sum_i \vec{m}_i \cdot \vec{H}_i^{eff}$ , by summing all the terms over all magnetic moments. The effective field  $\vec{H}_i^{eff}$  acting on the magnetic moment  $\vec{m}_i$  is then defined as

$$(\vec{H}_i^{eff})^l = -\frac{1}{M_0} \left( \frac{\partial \epsilon_{TOT}}{\partial m_{ix}^l} \hat{i} + \frac{\partial \epsilon_{TOT}}{\partial m_{iy}^l} \hat{j} \right), \tag{6.7}$$

where  $i = 1, 2$  and  $l = T, B$ . From here, the metastable magnetization configuration for each applied field  $H$  can be obtained self-consistently by requiring that each magnetic moment has to be aligned with its effective field vector, hence minimizing the free energy of the system. It is convenient to introduce the following reduced parameters:

- Ratio between bottom and top thicknesses,  $r = t_B/t_T$
- Anisotropy field,  $H_K = 2K/M_0$
- Dimensionless applied magnetic field,  $h = H/H_K = \frac{H}{2K/M_0}$
- Reduced intralayer exchange coupling strength,  $j = J/2K$
- Reduced interlayer exchange coupling strength,  $d = D/2K$

Macrospin configurations for different applied field  $h$  values are evaluated given the dimensionless coupling strengths  $j$  and  $d$ , by setting a misalignment  $\alpha = 90^\circ$  between the grains in each layer, such that there is effectively no net uniaxial anisotropy. We also chose a bottom-to-top thickness ratio of  $r = 10$ .

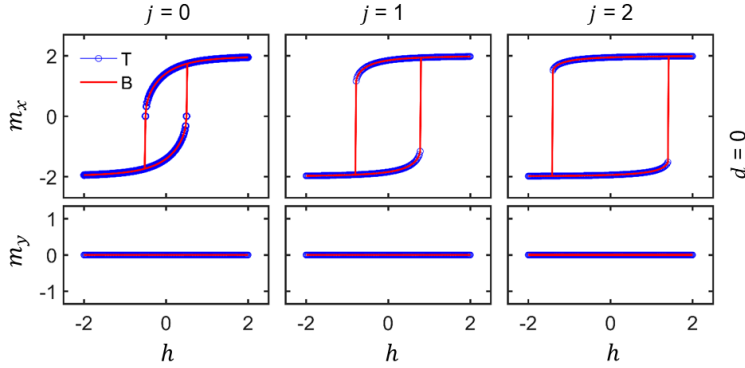


**Fig. 6.8:** Field dependence of the magnetization components  $m_x$  and  $m_y$  for different strengths  $j$  of the intralayer coupling at zero interlayer coupling,  $d = 0$ . The magnetization components are given in units of each layer magnetization,  $M_0$ .

Fig. 6.8 shows the field dependent evolution of the  $m_x$ ,  $m_y$  magnetization components of the top as well as bottom Co layers for intralayer coupling strengths  $j = 0, 0.5$  and  $1$ , as well as zero DM type interlayer coupling,  $d = 0$ . One of the most immediate results is the fact that the  $m_x$  and  $m_y$  vs  $h$  curves are identical for the top and bottom FM layers, as they act completely independently while sharing the very same magnetic properties. One can observe that while the  $m_x$  component follows a field

dependent hysteresis curve, the transverse component of magnetization  $m_y$  is zero for all field values. This is because upon lowering  $h$ , the magnetic moments in each layer rotate away in opposite directions, behaving as mirror images with respect to the  $x$ -axis. Thus we see that the system follows a magnetization fanning process upon lowering the field. It is worth pointing that the intralayer strength  $j$  controls the squareness and width of the  $m_x$  hysteresis loops (Fig. 6.8), as it has a direct consequence on the restoring force exerted by the anisotropy axes onto the magnetic moments against the action of the applied magnetic field. For the subsequent simulations, we choose the intralayer coupling strength to be  $j=1$ , which reproduces a  $m_x$  remanence value of about 90% as compared to the saturation magnetization, in accordance with our experiments on Co/Ag/Co multilayers.

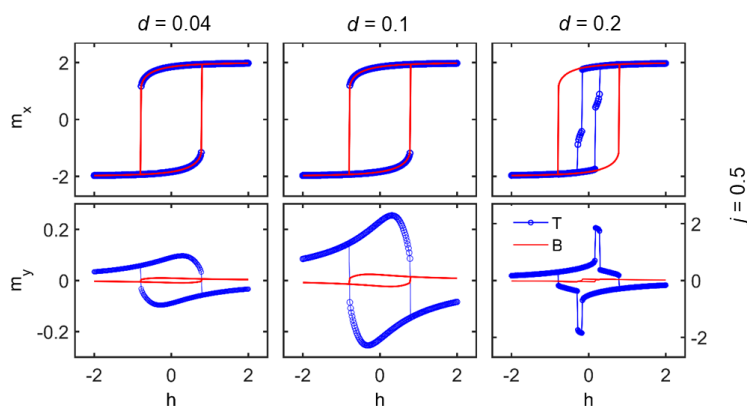


**Fig. 6.9:** Field dependent magnetization evolution for different DM interlayer coupling strengths  $d$  (with  $j = 1$ ).

In the same way, one can see that the transverse magnetization  $m_y$  is zero for every  $h$  value when  $d = 0$  (see Fig. 6.8), given that there is no interaction breaking the symmetry of the system around the applied field axis ( $x$ -axis). The situation is different when the interlayer exchange coupling between magnetic layers is introduced ( $d \neq 0$ ). Fig. 6.9 shows the field dependent magnetization evolution for a system with interlayer coupling strengths  $d = 0.04, 0.1$  and  $0.2$ . For low DM coupling strength values ( $d < 0.15$ ), the  $m_x$  components of the top and bottom layers have exactly the same field dependence, as in the case in which the DM type interlayer coupling was not present. However, a nonzero DM type coupling term gives rise in each layer to a deviation of the magnetization orientation from the  $x$ -axis, in which the tilt angles and hence the  $m_y$  magnetization components have opposite signs for the top and bottom layers. This means that apart from the magnetization fanning process described before, a net

magnetization rotation also takes place upon lowering the field in both ferromagnetic layers. Specifically, the magnetization of the top layer deviates from the  $x$ -axis on the order of few degrees, while the bottom layer magnetization is tilted by a significantly smaller but still appreciable angle in the opposite direction. This also results into an hysteretic  $m_y$  vs  $h$  behavior in both layers (see Fig. 6.9). Hereby, we find the DM type interlayer coupling, which promotes the perpendicular alignment between two FM magnetizations, is in competition with both the magnetic anisotropy energy of the grains in each layer, as well as with the intralayer coupling within them. While the interlayer coupling may not be capable to align both magnetizations perpendicular, the system still gains sufficient energy by partially adapting to this interaction, via deflecting the magnetizations of each layer to both sides of the applied field axis. This results into a configuration of the top and bottom layers in which the respective magnetizations are canted on the order of a few degrees in a scissor state, thus setting a plausible scenario for explaining our experimental observations in Co/Ag/Co films.

On the other hand, when the DM coupling strength exceeds  $d = 0.16$  (see Fig. 6.9), the tilt angles between the two layer magnetizations become increasingly larger, as perpendicular alignment is strongly favored. The field dependence of magnetization components becomes more complex and features several intermediate states of magnetization during reversal. Thus this high  $d$  regime is discarded given the stark dissimilarity with the experiment.

By comparing the  $d = 0.04, 0.1$  cases in Fig. 6.9, one can conclude that  $d$  determines the magnetization tilt amplitude from the  $x$ -axis. However, the ratio  $m_y^T/m_y^B$  is identical for every  $d$  value, being equal to the negative ratio of the magnetic film thicknesses,  $-r = -10$ . This can be understood via an energetic argument, as all energy terms scale with volume except for the DM-type interlayer coupling, which is an interfacial interaction, causing the interlayer coupling to have a bigger net effect onto the top thinner layer by giving rise to a more prominent magnetization tilt.

Given this relation between the top and bottom layer thickness ratio and the amplitude of  $m_y^T, m_y^B$ , the total net magnetic moment of the structure along the  $y$ -axis is zero during the entire reversal, such that a volume averaging measurement technique such as vibrating sample magnetometry would not be able to measure the opposite tilt of the Co layers in an experiment. However, using a probe with the appropriate depth sensitivity, such as MOKE/GME, the signal is largely dominated by the top Co layer magnetization rotation, being only minimally impacted by the bottom Co rotation. This fact allows the detection of the anomalous transverse magnetization behavior in the Co/Ag/Co samples, thus unveiling the chiral interlayer coupling mechanism.

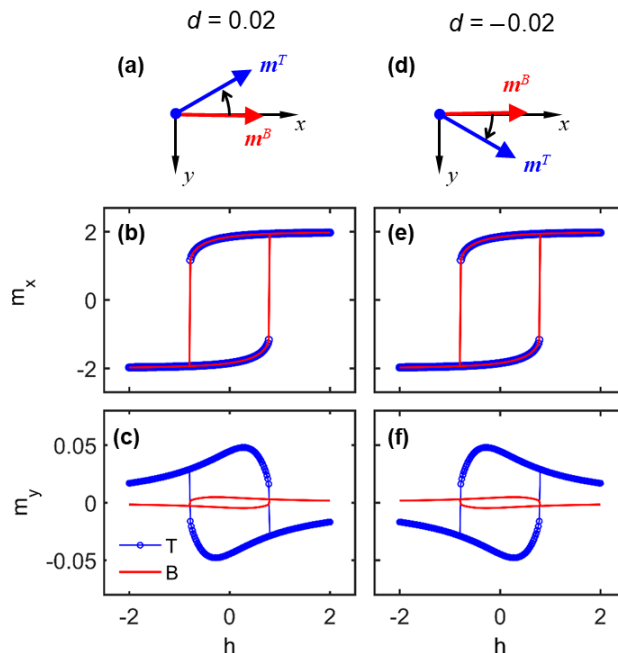


**Fig. 6.10:** (a) Decreasing field branch magnetization configuration of the top and bottom magnetization vectors  $\mathbf{m}^T$  and  $\mathbf{m}^B$  at remanence, for  $j = 1$  and  $d = 0.02$ . The field dependent evolution of the magnetization components is shown in (b), (c). (d)-(f) show the same for the opposite sign of  $d$ . The magnetization vector angles in (a), (d) are multiplied by 10 for clarity.

Finally, the role of the sign in  $d$  is evaluated within the model. This sign defines the clockwise or counterclockwise character of the angle between the top and bottom layer magnetizations, as it sets the sign of the prefactor multiplying the cross product in Eq. 6.5 and thus defines the preferred helicity for this interaction. In order to confirm this numerically, Fig. 6.10 exhibits the outcome of simulations with opposite interlayer exchange couplings  $d = \pm 0.02$ . While the  $m_x$  components of the top and bottom layers follow the same field dependent reversal path in the two cases, the field dependent  $m_y$  values of both layers change their sign upon inverting the sign of  $d$ .

Thus by the simple magnetic model described above, we can mimic qualitatively all features that have been observed in the experiment. This fact permits the direct comparison of the experimental data with this model, hence bringing a pathway to quantify the strength of the DM type interlayer exchange coupling, as it will be shown below.

### Optical modeling of Co/Ag/Co multilayers

In order to mimic the optical, magneto-optical, as well as the magnetic properties of our Co/Ag/Co multilayers, we also need to develop a more sophisticated optical model than the semi-infinite Co slab approach that has been used before. For this, one needs to match the Ag-thickness dependence of the optical and magneto-optical parameters to a plausible set of optical and magneto-optical constants of the system. First, we choose  $N = 1.46$  for the SiO<sub>2</sub> overcoat, which we measured via spectroscopic ellipsometry on Si/SiO<sub>2</sub> samples. Additionally, we employ the refractive index  $N = 2.4 + 4.0i$  as well as the magneto-optical coupling factor  $Q = (2.95 - 0.96i) \cdot 10^{-2}$  for the Co layers, which we also measured for polycrystalline Co films in a separate experiment.

From here, the dielectric tensor of each separate layer is constructed and light propagation in the entire multilayer structure (see Fig. 6.11) is described in the framework of the Transfer Matrix Method [74, 75], which allows the calculation of the reflection matrix elements of arbitrary anisotropic multilayer media, including magneto-optical effects.

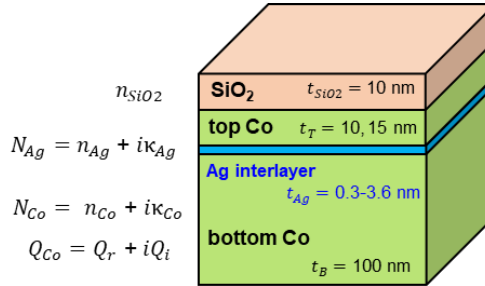


**Fig. 6.11:** Layered optical model of the Co/Ag/Co samples, indicating the relevant thicknesses as well as optical and magneto-optical parameters.

Having fixed these aspects of the optical model, we can fit the Ag thickness dependence of the longitudinal parameters  $B_1$  and  $B_2$  and the purely optical reflection matrix parameters  $B_7$  and  $B_8$  in magnetic saturation (that is, assuming  $m_x = 1$  and  $m_y = 0$ ) to the optical parameters of the Ag interlayer. The data and corresponding fits are shown in Figs. 6.12(a)-6.12(d) and 6.12(e)-6.12(h) for the samples *CoAgCo10* and *CoAgCo15*, respectively. While the optical model can closely mimic the data, it is seen that the properties in the interlayer thickness region below 1 nm are not correctly described, as a result of quantum mechanical effects near the interface for such ultrathin structures (which we neglect here by setting a thickness independent Ag refractive index). However, for the sake of simplicity, we have limited the description to

incorporate a single, thickness independent  $N_{Ag} = n_{Ag} + i\kappa_{Ag}$  value. A summary of the optical and magneto-optical parameters that were fixed or fitted in the optical model fits illustrated in Fig. 6.12 are summarized in Table 6.3.

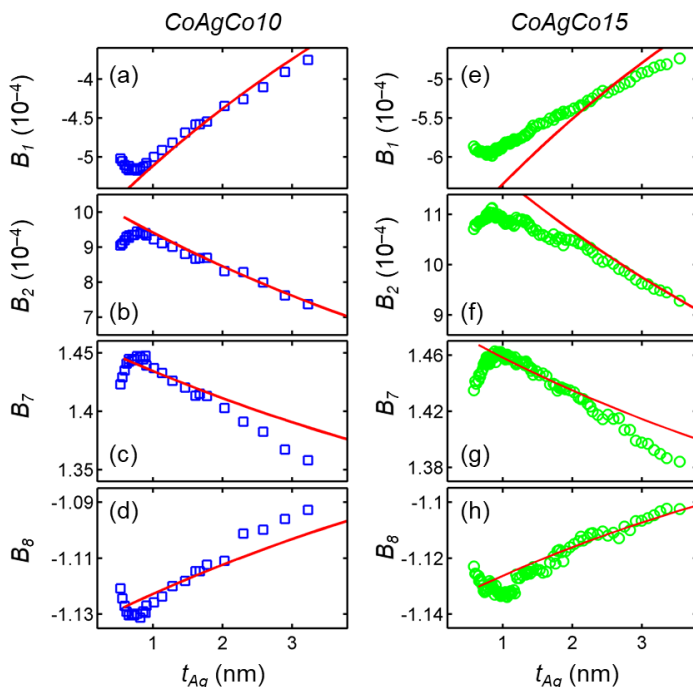


**Fig. 6.12:** Matching of the optical and magneto-optical parameters to the Ag-thickness dependence. In the left panel, experimentally measured (a)  $B_1$ , (b)  $B_2$ , (c)  $B_7$  and (d)  $B_8$  for the sample *CoAgCo10* measured at  $H = 1250$  Oe, together with the optical model fit (red solid line). In the right panel, data and fits are shown for the sample *CoAgCo15*.

Material	<i>CoAgCo10</i>		<i>CoAgCo15</i>	
	$N$	$Q \times 10^2$	$N$	$Q \times 10^2$
SiO <sub>2</sub>	1.46 (*)	-	1.46 (*)	-
Co	$2.4 + 4.0i$ (*)	$2.95 - 0.96i$ (*)	$2.4 + 4.0i$ (*)	$2.95 - 0.96i$ (*)
Ag	$0.14 + 6.01i$	-	$0.15 + 6.41i$	-

**Table 6.3:** Optical and magneto-optical parameters of the optimized optical model for the Co/Ag/Co samples. The quantities with an asterisk (\*) are fixed.

### Determination of the Dzyaloshinskii-Moriya interaction strength

Once the complete optical model has been refined to match Ag interlayer thickness dependence of the experimentally determined reflection matrix elements  $B_1$ ,  $B_2$ ,  $B_7$  and  $B_8$  in magnetic saturation (see Fig. 6.12), the field dependence of the reflection matrix elements is now entirely determined by the magnetization configuration in Co/Ag/Co. This can in turn be entirely described by the magnetic model presented above, which is dependent on the few magnetic model systems parameters  $\{K, J, M_0\}$  (assumed to be Ag-thickness independent) and  $D$  (which is Ag-thickness dependent).

The main quantity of interest we want to extract is the strength of the DM interlayer interaction  $D$ , which according to our description above should have an oscillatory behavior with respect to the Ag-interlayer thickness and change sign across the Ag-wedge.

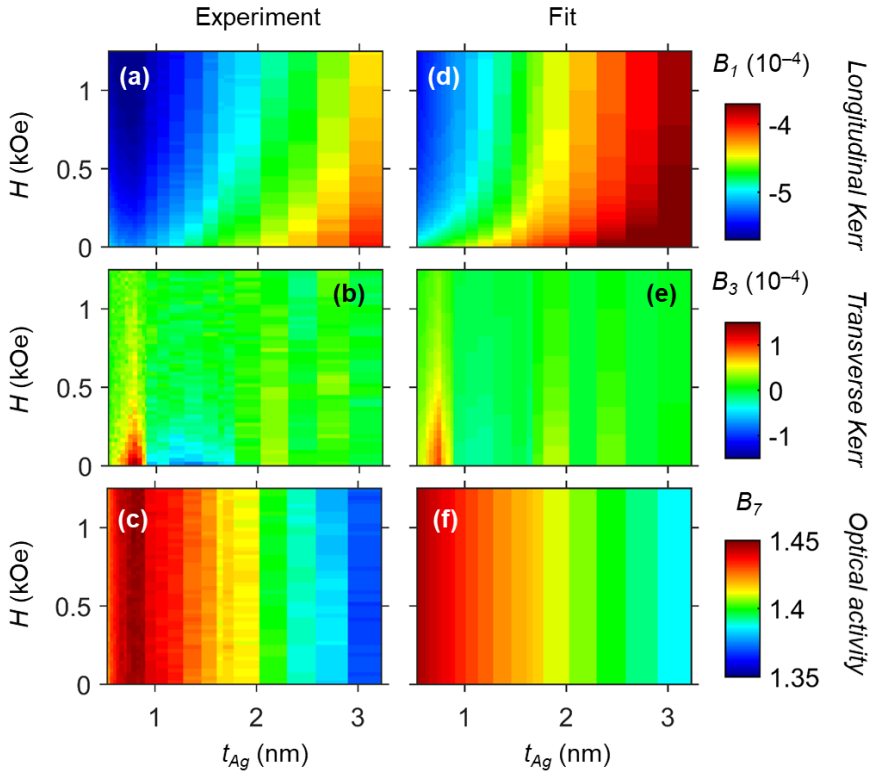


**Fig. 6.13:** Color-coded experimentally determined (a)  $B_1$ , (b)  $B_3$  and (c)  $B_7$  maps of the *CoAgCo10* sample vs the applied field and the Ag interlayer thickness. (d) – (f) show the same fitted quantities according to the optical and magnetic model developed throughout the text.

Thus we have fitted the field and Ag-thickness dependence of the experimentally determined optical and magneto-optical reflection matrix parameters previously shown in Figs. 6.5 and 6.6. It is worth mentioning that there are no adjustable parameters other than the parameters we already defined in the combined optical and magnetic model.

Figs. 6.13 and 6.14 show the experimental color-coded maps of the optical and magneto-optical reflection matrix parameters, side-by-side with the fits obtained from comparison to the combined optical and magnetic model. It is seen that this combined model is able to reproduce all relevant experimental features to a very high degree, although the slight mismatch in the optical modeling (see Fig. 6.12) causes some of the Ag thickness trends not to be so accurate in the ultrathin Ag wedge region.

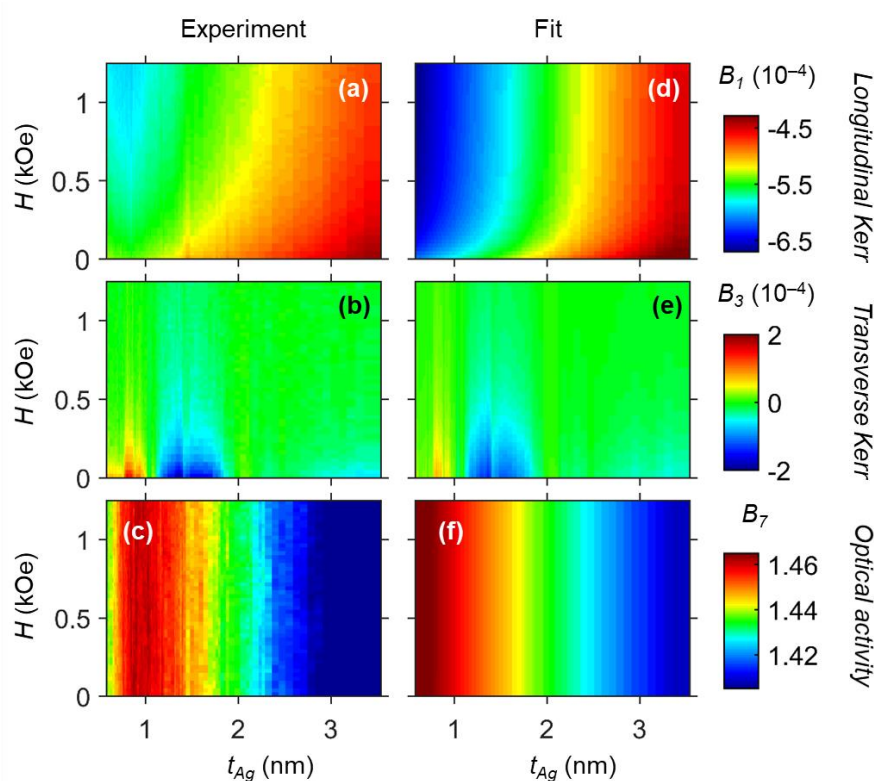


**Fig. 6.14:** Color-coded experimentally determined (a)  $B_1$ , (b)  $B_3$  and (c)  $B_7$  maps of the *CoAgCo15* samples vs the applied field and the Ag interlayer thickness. (d) – (f) show the same fitted quantities according to the optical and magnetic model developed throughout the text.

The Ag-thickness dependent (scalar) Dzyaloshinskii-Moriya coupling factor  $D$  was extracted from the fits and shown in Fig. 6.15 for the two samples studied here. As anticipated, the coupling factor shows an oscillatory behavior in the two cases, alternating positive and negative values in the entire wedge range. In addition, one can see that there is an onset in Ag thickness, at which the coupling first departs from zero, which is approximately  $t_{Ag} = 0.6$  nm. In the same way, the coupling factor  $D$  also shows an attenuation towards the thick end of the interlayer, confirming the fact that the coupling between the two Co layers should disappear for a sufficiently thick non-magnetic spacers.

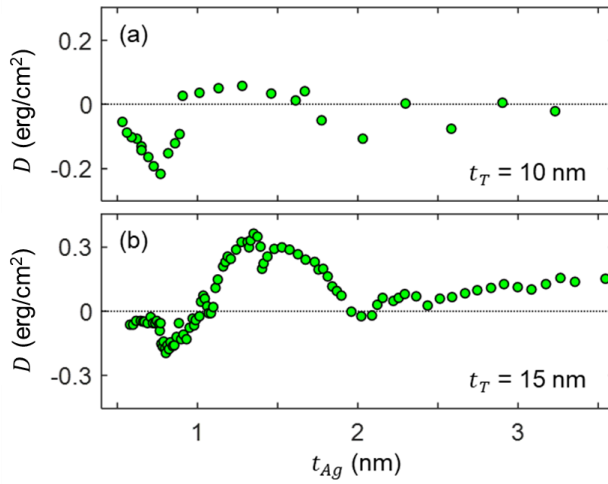


**Fig. 6.15:**  $t_{Ag}$  dependence of the DM type interlayer coupling strength  $D$ , as obtained from the fit to the combined optical and magnetic model of the multilayer system, for the sample with (a)  $t_T = 10$  nm, (b) 15 nm.

The interaction strength is of the order of  $0.1 \text{ erg/cm}^2$  or  $0.1 \text{ mJ/m}^2$ , which is one order of magnitude smaller than the DM interaction strength found in heavy-metal/ferromagnet/heavy-metal stacks such as Pt/Co/Ir, although the numbers are not directly comparable given that an intralayer DM coupling occurs in these asymmetric multilayer stacks. These multilayer systems often exhibit strong manifestations of the antisymmetric exchange, including the presence of skyrmion phases or antisymmetric domain bubble expansion [45, 46, 254]. Importantly, we obtained a direct magnetometric estimation of the DM interaction, since this is not a trivial issue, as its determination is usually made via indirect methods. While for the Co/Ag/Co samples here it shows subtle effects such as a  $5^\circ$  magnetization rotation angle in remanence, its influence is still detectable by using an appropriate depth-dependent probe (such as MOKE/GME).

*Impurity-mediated mechanism for Dzyaloshinskii-Moriya type interlayer coupling*

While the anisotropic exchange of the kind of the DM interaction was first suggested in bulk materials with lack of inversion symmetry, a seminal work by Fert suggested that the same interaction could exist in thin films and multilayer systems as a result of the inversion symmetry breaking at interfaces [41]. In this work, it is suggested that: “*DM interaction could reach 20-30% of the exchange interaction in the presence of elements contributing with high spin-orbit coupling*”.

Given that the DM interaction is mediated between two ferromagnetic atoms by a third non-magnetic atom, we can consider that the interaction between Co atoms from the top and bottom ferromagnetic layers is mediated by asymmetrically placed, isolated non-magnetic Co atom impurities in the Ag spacer. In fact, Fert and Levy suggested in 1980 while studying the magnetization reversal properties of bulk spin glasses that the DM interaction arises as a higher order term of the Ruderman–Kittel–Kasuya–Yosida (RKKY) interaction [39]. Thus for our Co/Ag/Co samples, a nonmagnetic Co impurity, asymmetrically placed<sup>63</sup> between the Co layers at the Ag interlayer site  $l$ , can break the symmetry and act as a mediator for the coupling between ferromagnetic spins  $\mathbf{S}_i$  and  $\mathbf{S}_j$  at the top and bottom interface sites  $i$  and  $j$  of the Co layers (see schematic in Fig. 6.16). The antisymmetric exchange energy term then obeys the three-site DM interaction model proposed by Levy and Fert [39]

$$E_{DM} = - \sum_{i,j} \mathbf{D}_{ij} \cdot \mathbf{S}_i \times \mathbf{S}_j = -\lambda_0 \sum_{i,j} \frac{(\mathbf{R}_{li} \cdot \mathbf{R}_{lj})(\mathbf{R}_{li} \times \mathbf{R}_{lj})}{R_{li}^3 R_{lj}^3 R_{ij}} \cdot \mathbf{S}_i \times \mathbf{S}_j, \quad (6.8)$$

where the sum over the atoms at the top and bottom interface is taken.  $\mathbf{R}_{li}$  is the vector going from the position of the impurity  $l$  to the spin  $i$ , while  $\lambda_0$  is the energy coefficient of the interaction. The above Hamiltonian can actually lead to a net interlayer exchange coupling such as the one that was considered in the magnetic model introduced here.

In collaboration with Prof. Elena Vedmedenko (University of Hamburg), we have recently shown theoretically that an effective interlayer coupling based on the DM interaction can emerge under the presence of disorder in heterostructures consisting of two ferromagnets separated by a nonmagnetic spacer, where nontrivial three-dimensional spin textures of chiral character can arise [255]. The atomistic model

---

<sup>63</sup> The asymmetric placement of an isolated, nonmagnetic Co impurity in the Ag interlayer matrix is likely to occur, given that the layers are sequentially deposited and thus intermix in different ways.

developed in this context shows that a slight non-uniformity of the magnetic state in each Co layer is required for the DM-type interlayer coupling to be effective. This situation is straightforwardly accomplished in the Co/Ag/Co samples here because their polycrystalline nature leads to non-uniform magnetization configurations even without considering DM-type interactions. These non-uniformities of magnetization are only suppressed by applying very large magnetic fields, a situation at which the magnetizations of the two Co layers are aligned anyway.

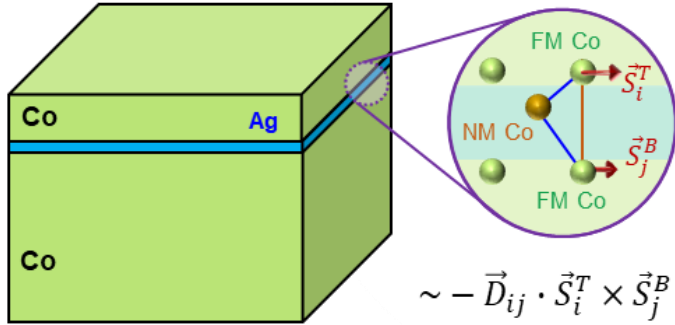


**Fig. 6.16:** Schematic representation of the impurity model, indicating an asymmetrically placed Co impurity atom in the Ag interlayer, which breaks the spatial inversion symmetry and acts as a mediator for the coupling between spins  $\mathbf{S}_i$  and  $\mathbf{S}_j$  at the top and bottom interface sites.

Recently, Khajetoorians and coworkers have reported the tuning of the DM coupling between two magnetic atoms placed on a metallic substrate with high spin orbit coupling. For doing so, they vary the distance between the atoms by manipulating them with a scanning tunneling microscope. They find the presence of a long-range DM interaction between the spins of the ferromagnetic atoms, in which the amplitude and orientation of the DM vector change in an oscillatory fashion with the atom separation [256]. The observations here confirm that the position dependent inter-atom oscillatory DM coupling can also lead to an oscillatory interlayer type DM coupling, in which vast numbers of spins are simultaneously coupled via local, nonmagnetic impurities in the spacer. The situation is similar as for bilinear coupling, in which the atom-to-atom RKKY interaction and its oscillatory behavior survive up to the case of two infinite-like interacting layers [49].

The concept of a chiral interlayer magnetic exchange coupling is very new, and the first works in the literature showing evidence of such an interaction have appeared only very recently, which report a chiral exchange bias effect in synthetic antiferromagnet systems [257, 258].

### 6.3 Conclusions

In conclusion, the existence of a coherent magnetization rotation process with a predefined helicity in the top ferromagnetic layer of polycrystalline Co/Ag/Co stacks was investigated via detailed GME measurements. It was found that the sign and strength of the interaction varies in an oscillatory fashion with the spacer thickness, attenuating considerably for values above 2 nm. We demonstrate that bi-linear or bi-quadratic interlayer exchange coupling cannot account for such an observation, while instead our findings are indicative of the existence of a Dzyaloshinskii-Moriya type interlayer exchange coupling, which promotes a scissor state between the magnetization vectors of the two Co layers of predefined chirality, i.e. clockwise or counterclockwise.

Here, we constructed an appropriate optical model for the sample and combined it with simple magnetic modeling that can mimic the magnetization reversal properties of our samples, assuming a Dzyaloshinskii-Moriya type interlayer exchange coupling whose thickness dependence is oscillatory. The entirety of the measured magneto-optical and optical data can be described in a quantitatively accurate and consistent way. This in turn allowed to extract the strength of the interaction and in an interlayer thickness dependent fashion, its strength being the order of  $D \sim 0.1$  mJ/m<sup>2</sup>. It is worth noticing that the volume averaged magnetization of the entire stack does not exhibit a net rotation, because the rotation of the top layer is compensated by the rotation of the bottom layer. Due to the use of GME, however, the detected signal is dominated by the top layer magnetization, so that this relative rotation and its helical nature could be observed, classified and quantified.

Additional preliminary experiments in Co/Au/Co and Co/Pt/Co multilayer stacks did not show the interlayer coupling behavior observed here.

# Chapter 7

## Summary & Outlook

The implementation and optimization of the generalized magneto-optical ellipsometry (GME) technique to perform ellipsometry and magnetometry of fundamentally interesting magnetic thin film and multilayer systems has been presented in this thesis. I have shown that this technique allows the precise and accurate determination of the optical, magneto-optical and magnetic properties of nanomagnetic entities, all in a single setup and analysis scheme. Quantities of interest such as the refractive index, magneto-optical coupling factor and magnetization orientation in three dimensions are obtained within the methodology presented here, which are not usually retrieved in typical MOKE experiments. The most remarkable strength of the technique consists on its ability to distinguish true polarization effects from additional reflection phenomena (e.g. birefringence), such that the evolution and origin of the different polarization-dependent modifications can be robustly separated.

A general introduction to nanomagnetism and magnetic materials at the nanoscale has been given in **Chapter 1**, pointing to the historical importance of this research field in the development of computer memory and recording media technologies. Then, the relevant interactions and energy terms in nanomagnetic systems and their magnetization reversal behavior, as well as the fundamentals of magneto-optical effects were discussed. Finally, the context in which magneto-optical characterization techniques are becoming increasingly important for actual research in nanomagnetism and spintronics is placed, highlighting the ability of MOKE to study ultrafast magnetization phenomena or spin transport at the nanoscale, for example. In this sense, and fully aligned with one of the main goals in the present thesis, it is important pointing out that obtaining reliable information from MOKE experiments is crucial at the present moment, in such a way that magnetically induced true polarization

effects can be distinguished from additional purely optical phenomena in order to reach a correct interpretation of experiments.

In **Chapter 2**, the main experimental techniques that were employed for sample fabrication, as well as structural, magnetic and optical characterization were presented. These include magnetron sputtering, x-ray diffraction, vibrating sample magnetometry and spectroscopic ellipsometry. Given that magneto-optical Kerr effect measurements constitute the backbone of the experimental results presented in this thesis, these are treated in dedicated forthcoming chapters.

The generalized magneto-optical technique (GME) is introduced in **Chapter 3** as a versatile and powerful tool to investigate the optical, magneto-optical and magnetic properties of thin films and multilayer structures. A fully computer controlled setup allowing automated measurements for different sample orientation or position along a wedge-type sample was built. The setup implementation and measurement optimization specifics are included in this chapter as well as in the **Appendices** of this thesis. The three-dimensional vector magnetometry capability of the technique was tested and demonstrated on a variety of magnetic thin film systems. Analysis in terms of multi-parameter nonlinear least-squares fitting and description of polarization effects in stratified media within the framework of the transfer matrix method are carried out. This resulted into an unprecedented precision to measure polarization changes of the order of 10-to-100 nanoradians. This is then translated to a precision of about  $0.1^\circ$  and  $0.01^\circ$ , for the in-plane and out-of-plane magnetization vectors, respectively.

Despite all magneto-optical magnetometry studies here being performed at a single wavelength, upgrading the setup by incorporating a multi-wavelength light source is a most natural extension for the GME technique. This would allow to execute spectroscopic analysis of the optical, magneto-optical and magnetic properties of the sample [259, 260]. This increased capability has several advantages that go beyond resolving the wavelength dependence of the refractive index or the magneto-optical coupling. It has already been shown that the combination of magneto-optical measurements carried out at different wavelengths allows resolving the magnetization behavior of physically separated magnetic films in multilayer stacks [261] or buried interfaces [87], as a result of the energy dependent skin depth of visible light in metals. This ultimately opens up the possibility to attempt depth profiling of magnetization [86], which could be extremely useful for characterization of nanoscale magnetic objects showing a vertical gradient of the magnetization orientation [262, 263]. It is also possible to pursue depth- and layer- resolved magnetometry by a variable angle of incidence approach, although its implementation is less versatile and more cumbersome

as compared to the spectroscopic approach. Lastly, the multi-wavelength measurement capability can occasionally allow for element resolved magnetization information in rare earth-transition metal alloys such as FeTb [264], while this option could not be extended so far to a wide variety of alloy-materials, at least in the visible light region.

Another aspect that has not been treated here in detail consists on the option to apply the GME data analysis for structure determination (i.e. the determination of thin film or multilayers thicknesses), in a similar way as it is accomplished within spectroscopic ellipsometry [122]. Any parameter within the optical model (e.g., film thicknesses) can be optimized via the best-match model fit, provided that sufficient experimental data have been acquired with respect to the number of fit parameters.

In **Chapter 4**, the observation of magneto-optical anisotropy (MOA) in epitaxial hcp Co films was presented. While the first observations of this effect in hcp Co dates more than 20 years back, the experiments here found a direct correlation between the MOA amplitude and epitaxial strain, thus revealing a possible origin of this effect. The analysis of samples with a more complicated, anisotropic dielectric tensor was possible due to the ability of GME to identify and thus discern purely optical and magneto-optical anisotropies in the retrieved data. It was shown that MOA effects are not small in general, as quite modest strains of the order of  $\sim 1\%$  can lead to MOA amplitudes of the order of 25%.

A relevant conclusion from these results consist on the fact that care must be taken when assuming bulk homogeneous descriptions of magnetic materials, as the reliability of magnetometry data obtained from MOKE experiments may be compromised under the presence of MOA. The strain-dependent magnetocrystalline anisotropy (MCA) properties of the hcp Co films were also investigated, as previous work had highlighted an interrelation between MOA and MCA. Finally, a strategy aimed at actively modifying MOA in epitaxial hcp Co films by using an underlayer crystal tuning approach was developed. Even if preliminary results show to be promising, confirming the validity of this approach would require further experimental work.

Once again, spectroscopic-GME measurements are straightforward to implement within the methodology employed here and can add up to interesting experimental platforms for the joint investigation of spin-orbit induced phenomena such as MOA and MCA in epitaxial magnetic thin films. Spectroscopic measurements would constitute an adequate option to further investigate the interrelation of MOA and MCA, because while magnetic anisotropy is an energy integrated property involving all occupied electronic orbitals, magneto-optical effects will arise from certain electronic states that match the specific wavelength dependent electronic transitions. It can be

envisioned that GME-type measurements could bring a complete avenue of novel characterization techniques to investigate very diverse physical processes. The methodology presented here could be beneficial for a better understanding of the interplay between structural (symmetry, strains and stresses, etc.) and dielectric properties of materials. A couple of examples postulating strong correlations between these two include the optical Voigt and Faraday effects [155] or the Anomalous Hall Effect (AHE) [265].

Patterned permalloy films with grating geometry were the subject of study in **Chapter 5**, where the optical and magneto-optical properties of the samples were investigated in reflection and diffraction. By determining the orientation dependent reflection matrix of the samples via GME, it was demonstrated that magnetic gratings can be considered as an artificial material platform possessing uniaxial optical and magneto-optical anisotropies. It was found that the amplitude of these anisotropies scales in a linear fashion with the groove depth, at least for topographical features that are small in comparison to the wavelength of light (i.e., in the shallow grating approximation). This anisotropic artificial material concept can be of interest, for instance, when designing one-dimensional magnonic and magneto-photonics crystals.

In addition, the magneto-optical response of the permalloy gratings samples was investigated in the diffraction geometry. It was concluded that the polarization dependent diffraction matrix shares the same symmetry as the conventional reflection matrix, at least in a region which is sufficiently close to a symmetry point corresponding to the polarization crossing point. This opens up the possibility to utilize magneto-optical ellipsometry in the diffraction geometry and hereby develop novel characterization methods for samples with periodic surface topographies, extending the capabilities of diffraction MOKE experiments in which the incident light is limited to one polarization state alone. The approach of using a single incident polarization state greatly simplifies the treatment of the magneto-optical response (which otherwise must include intermixed contributions from the groove features and the complex dielectric tensor elements of the material [93, 119]), but novel information on inhomogeneous magnetization states and magneto-optical activity in nanostructure arrays could be obtained employing the ellipsometric approach. More complex theoretical frameworks such as the rigorous coupled-wave analysis (RWCA) [266] could facilitate the data analysis in this case.

Finally, **Chapter 6** focused on the magnetization reversal behavior investigation of polycrystalline Co/Ag-wedge/Co multilayers upon modification of the Ag interlayer thickness in the sub-nanometer regime. By identifying coherent and non-

coherent magnetization rotation processes during the formation of non-uniform states, as well as taking advantage of the inherent depth dependence of MOKE (and GME), an anomalous Ag thickness dependent behavior of the transverse component of magnetization was discovered, which showed a predefined reversal helicity. As an explanation to the observed behavior, it was argued that a Dzyaloshinskii-Moriya (DM) type interlayer exchange coupling must exist, promoting a scissor state between the magnetization vectors of the two Co layers and thus setting a predefined chirality on their relative orientation, i.e., clockwise or counterclockwise. It was found that the transverse magnetization component with a predefined helicity in remanence depends on the Ag thickness in an oscillatory fashion, and moreover, vanished at large enough interlayer thicknesses, thus supporting the mechanism of a chiral interlayer coupling. A simple magnetic model was able to explain the magnetization reversal properties of the samples, allowing to quantify the strength of the interaction, which is of the order of  $D \sim 0.1 \text{ mJ/m}^2$  for the samples studied here.

The origin of the interaction was briefly explained based on the earlier work by Levy and Fert, who concluded that an anisotropic antisymmetric exchange arises from the higher order terms of the RKKY interaction when studying spin glass materials with diluted nonmagnetic impurities [39]. The same mechanism can also be produced by nonmagnetic Co impurities in the Ag interlayer matrix, which can mediate the DM interaction between Co atoms at the bottom and top layer interfaces. Recently, atomistic calculations and Monte Carlo simulations of model heterostructures consisting of two ferromagnets separated by a nonmagnetic spacer have confirmed that nontrivial three-dimensional spin textures of chiral character can arise via this mechanism [255].

The concept of a chiral interlayer magnetic exchange coupling is very new, and the first works in the literature showing evidence of such an interaction have appeared only very recently, which report a chiral exchange bias effect in synthetic antiferromagnets [257, 258]. The work presented in this thesis confirms the interlayer coupling nature of the interaction, observing an unequivocal oscillatory behavior vs the nonmagnetic space thickness and its vanishing towards its thick side.

An extensive search for adequate ferromagnet/nonmagnetic-spacer/ferromagnet systems from the material and interface engineering point of view could lead to new strategies to manipulate magnetization and interfacial spin textures in multilayers. In this sense, the chirality between magnetizations of closely spaced layers separated by an ultrathin film can play a new functional role. For instance, one could engineer in-plane magnetized, coupled multilayers which behave as an exchange spring magnet system with a predefined helicity. In fact, it has already been pointed out that the combination of intralayer and interlayer DM interactions would enable the manipulation of chirality in nanomagnetic systems in every spatial direction [267].

Further exploration of the DM interlayer coupling type in systems with out-of-plane magnetic anisotropy could lead to the design of functional magnetic tunnel junctions with a slightly tilted perpendicular magnetic anisotropy, a strongly desired property to be implemented in spin transfer torque MRAM devices in order to achieve deterministic reproducibility and short switching times [268].

In summary, this thesis demonstrates the capabilities of magneto-optical ellipsometry (and in particular, of the GME technique) to perform optical, magneto-optical and magnetic characterization of fundamentally interesting nanomagnetic entities. The experimental procedures and analysis pathways developed here show how to retrieve the maximum information in an optical reflection experiment from a material showing magneto-optical activity. It was proven throughout the thesis that retrieving the entire reflection matrix of the sample, and from here, the full magnetization vector information, is of great advantage to study a variety of physical phenomena including magnetization reversal, optical and magneto-optical anisotropy, and interlayer exchange coupling. The framework of the GME technique can provide an unprecedented high degree of precision when obtaining the quantities of interest in a MOKE experiment. This is currently highly desirable due to the inherent difficulty to measure very weak polarization-dependent effects in optical experiments, such as in the case of the MOKE detection of the spin Hall effect in heavy metals [104, 269].

A full magneto-optical ellipsometric approach as the one shown here could also result beneficial for tackling challenging experiments in the fields of laser-induced ultrafast magnetization dynamics and spin transport detection at the nanoscale, as well as for characterizing antiferromagnetic spin textures via magneto-optical effects quadratic in magnetization.

# Appendix I

## Polarization optics in stratified media

### A. Sign conventions in magneto-optics

Multiple sign conventions appear in the literature concerning the theoretical and experimental description of magneto-optical effects. The variety originates from the sign choices made in the equations that describe (i) the solutions to the wave equation of light propagation (Maxwell equations) and (ii) the off-diagonal elements of the dielectric tensor, where magnetization-dependent elements appear for linear magneto-optical Kerr effects.

The lack of consistency across the existing MOKE research in general makes difficult to compare theoretically or experimentally obtained values of the magneto-optical coupling factor  $Q$  as well as Kerr rotation and ellipticity values. In order to perform a comprehensive classification of the MOKE quantities reported in the literature, Atkinson and Lissberger summarized the different sign convention schemes and described for each scheme the sense of rotation for Faraday or Kerr rotation and ellipticity quantities in the laboratory frame (with respect to the viewing direction of the observer), albeit only upon considering polar Kerr effects [270].

In this thesis, the time-dependent part of the solution for the wave equation is set as  $e^{-iat}$ , which yields  $N = n + ik$  and  $Q = Q_r + iQ_i$  [270] for the complex refractive index and magneto-optical coupling factor, respectively. The MOKE coupling factor is defined as  $Q = -i\varepsilon_{xy}/\varepsilon_{xx}$  for  $m_z = 1$ . The convention for the sign of  $Q$  employed here agrees with the one chosen by Qiu and Bader [58, 59], while it is the opposite to the one followed by You and Shin [71]. The sign convention summary by Atkinson and Lissberger is shown in Table I.1 for all three Kerr geometries, where the choice for representing all results within the present thesis is indicated.

Time dependence	$e^{i\omega t}$	$e^{-i\omega t}$
Optical, MO constants	$N = n - i\kappa$ $Q = Q_r - iQ_i$	$N = n + i\kappa$ $Q = Q_r + iQ_i$
$\epsilon_{xy}$ Scheme 1	$\vec{\epsilon} = N^2 \begin{pmatrix} 1 & -iQm_z & iQm_y \\ iQm_z & 1 & -iQm_x \\ -iQm_y & iQm_x & 1 \end{pmatrix}$	$\vec{\epsilon} = N^2 \begin{pmatrix} 1 & iQm_z & -iQm_y \\ -iQm_z & 1 & iQm_x \\ iQm_y & -iQm_x & 1 \end{pmatrix}^a$
$\epsilon_{xy}$ Scheme 2	$\vec{\epsilon} = N^2 \begin{pmatrix} 1 & iQm_z & -iQm_y \\ -iQm_z & 1 & iQm_x \\ iQm_y & -iQm_x & 1 \end{pmatrix}$	$\vec{\epsilon} = N^2 \begin{pmatrix} 1 & -iQm_z & iQm_y \\ iQm_z & 1 & -iQm_x \\ -iQm_y & iQm_x & 1 \end{pmatrix}$

<sup>a</sup> Convention utilized in this thesis

**Table I.1:** The alternative sign convention schemes as summarized by Atkinson and Lissberger, indicating the choice for this thesis. Adapted from [270].

## B. Transfer Matrix Method (TMM)

When considering magneto-optical Kerr effects from a semi-infinite medium of a material (i.e., a bulk specimen), the experimentally accessible Fresnel complex reflectivities can be written in rather compact expressions upon considering linear magneto-optical Kerr effects, even for an arbitrary orientation of magnetization. For an optically isotropic material, the reflectivity matrix has the form [58, 69, 71]

$$R = \begin{pmatrix} r_{ss} & r_{sp} \\ r_{ps} & r_{pp} \end{pmatrix} = \begin{pmatrix} r_s & \alpha + \gamma \\ -\alpha + \gamma & r_p + \beta \end{pmatrix} \propto \begin{pmatrix} r_s & Am_x + Bm_z \\ -Am_x + Bm_z & r_p + Cm_y \end{pmatrix}, \quad (\text{I.1})$$

where well defined analytical expressions of the complex quantities ( $r_s$ ,  $r_p$ ,  $A$ ,  $B$ ,  $C$ ) exist as a function of the material quantities  $N$ ,  $Q$  as well as experimental settings such as the wavelength of light, the angle of incidence and the dielectric properties of the light incidence medium (see Section 1.4 of this thesis).

The description becomes more complicated if the specific sample of interest consists of arbitrary layered media that are magneto-optically active or optically anisotropic. The mathematical problem is usually focused on obtaining the normalized Jones matrix elements of the reflection matrix in Eq. I.1. Early works by Berreman [271] and Yeh [129] devised a pathway based on a  $4 \times 4$  matrix formalism for treating propagation of light in linear, arbitrarily anisotropic materials incorporated in a multilayer stack. Following the work by Yeh, Višňovský derived explicit formulas enabling the calculation of the reflection matrix under the presence of longitudinal,

transverse and magneto-optical Kerr effects, and thus enabling magneto-optical ellipsometry [72]. The  $4 \times 4$  matrix method was further popularized by the works of Zak, Moog and Bader [73] to derive magneto-optical Kerr effects in multilayer stacks containing a combination of ultrathin magnetic/non-magnetic layers. In all of the works mentioned above, reasonable approximations were taken at some point as the rigorous treatment of the mathematical problem involves solving the roots of quartic non-linear equations [75]. On the other hand, works from 1996 and 1999 from Schubert and coworkers worked out on the exact, analytical explicit solutions for the calculation of the normalized Jones reflection matrix arising from arbitrarily anisotropic and homogeneous layered systems [74, 75].

The central idea behind the  $4 \times 4$  matrix method focuses on the quantity termed as the transfer matrix  $\mathbf{T}$ , which takes care of the adequate description for light propagation across the boundaries of the multilayer stack, where continuity conditions according to Maxwell's equation must be fulfilled. A stack of layers can then be represented as a system matrix, which is defined altogether as a product of matrices belonging to each of the distinct layers composing the multilayer stack. The knowledge of the system's transfer matrix allows recovering the reflection and transmission coefficients that are accessible in an experimental setting.

The laboratory frame definition in this thesis is equivalent as the one proposed in the works by Schubert *et al.* [74, 75]. Light is incident at an angle  $\theta_a$  from the incident medium or ambient (index  $a$ ,  $z < 0$ ). The  $z$ -component of the incident wave-vector of light is positive ( $k_{a,z} > 0$ ), while the plane of incidence is defined by the intersection of the  $x$ - and  $z$ -axes (see Fig. I.1).

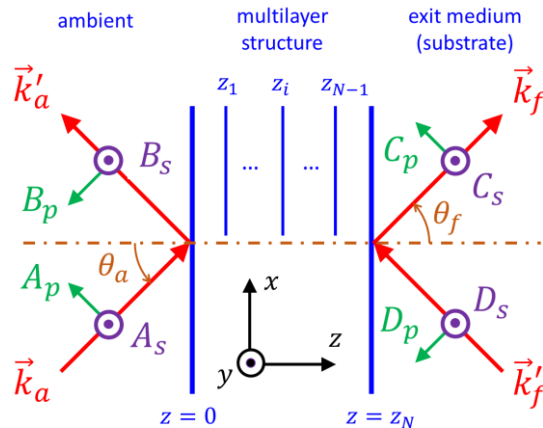


**Fig I.1:** Schematics of the light propagation phenomenon for an arbitrary multilayered structure. The graph represents the incident, reflected and transmitted  $s$ - and  $p$ -polarized components of the electric field of light. Figure adapted from Schubert *et al.* [75].

The considered multilayer structure of an arbitrary number of  $N$  layers is defined within the  $0 < z < z_N$  region, ending at the exit medium or substrate which does not have a back side ( $z_N < z < \infty$ ). The complex amplitudes of the  $p$ - and  $s$ -polarized incident and reflected electric fields are termed as  $A_p, A_s$  and  $B_p, B_s$ , respectively (see Fig. I.1). Transmitted modes alone ( $C_p, C_s$ ) are allowed in the exit medium, such that electric fields corresponding to back-traveling modes ( $D_p, D_s$ ) are set equal to zero.

Upon these considerations, the  $4 \times 4$  transfer matrix  $\mathbf{T}$  is defined as the quantity relating the electric field amplitudes in the ambient medium to those in the exit medium [75]

$$\begin{pmatrix} A_s \\ B_s \\ A_p \\ B_p \end{pmatrix} = \mathbf{T} \begin{pmatrix} C_s \\ 0 \\ C_p \\ 0 \end{pmatrix}, \quad (\text{I.2})$$

thus describing the propagation of monochromatic plane waves across the entire layer system<sup>64</sup>. The electric field amplitudes in Eq. I.2 are related to the reflection ( $\mathbf{r}$ ) and transmission ( $\mathbf{t}$ ) Fresnel matrices we aim to obtain as<sup>65</sup>

$$\begin{aligned} \begin{pmatrix} B_s \\ B_p \end{pmatrix} &= \mathbf{r} \begin{pmatrix} A_s \\ A_p \end{pmatrix} = \begin{pmatrix} r_{ss} & r_{sp} \\ r_{ps} & r_{pp} \end{pmatrix} \begin{pmatrix} A_s \\ A_p \end{pmatrix} \\ \begin{pmatrix} C_s \\ C_p \end{pmatrix} &= \mathbf{t} \begin{pmatrix} A_s \\ A_p \end{pmatrix} = \begin{pmatrix} t_{ss} & t_{sp} \\ t_{ps} & t_{pp} \end{pmatrix} \begin{pmatrix} A_s \\ A_p \end{pmatrix}. \end{aligned} \quad (\text{I.3})$$

The way to obtain  $\mathbf{r}$  and  $\mathbf{t}$  from  $\mathbf{T}$  consists on considering Eq. I.3 as an algebraic equation system [74].

The general transfer matrix  $\mathbf{T}$  is built from partial transfer matrices connecting the constituent layers in the stratified optical medium. The partial matrix  $\mathbf{T}_{ip}$  connects the  $i$ -th layer with thickness  $d_i$  and located at  $z = z_i$  with the next layer at  $z = z_i + d_i$ . The consecutive product of all  $N$  partial matrices hence connects the in-plane field components of the first interface ( $z = 0$ ) with the last substrate interface ( $z = z_N$ ). In addition, two more ingredients are needed for forming the complete transfer matrix  $\mathbf{T}$ .

---

<sup>64</sup> The matrix  $\mathbf{T}$  here is termed as  $\mathbf{M}$  in the original work by Yeh [129].

<sup>65</sup> Here, the symbols  $\mathbf{r}$  and  $\mathbf{t}$  are employed for the reflectivity and transmittivity matrices to avoid confusion with the transfer matrix  $\mathbf{T}$ .

These are the incident and exit matrices  $\mathbf{L}_a$  and  $\mathbf{L}_f$ , which project the transmitted amplitudes of the waves from the ambient to the first interface and from the last interface to the exit medium (substrate), respectively. The matrix  $\mathbf{T}$  is then mathematically obtained as the following product

$$\mathbf{T} = \mathbf{L}_a^{-1} \prod_{i=1}^N [\mathbf{T}_{ip}(d_i)]^{-1} \mathbf{L}_f = \mathbf{L}_a^{-1} \prod_{i=1}^N \mathbf{T}_{ip}(-d_i) \mathbf{L}_f. \quad (\text{I.4})$$

where the inversion symmetry with respect to the z-axis facilitates the calculation without the need of computing the inverse  $\mathbf{T}_{ip}$  matrices.

Finally, the reflection matrix elements<sup>66</sup> are obtained by the relations given by Yeh [129]

$$\begin{aligned} \frac{r_{pp}}{r_{ss}} &= \frac{T_{11}T_{43} - T_{41}T_{13}}{T_{21}T_{33} - T_{23}T_{31}} \\ \frac{r_{ps}}{r_{pp}} &= \frac{T_{11}T_{23} - T_{21}T_{13}}{T_{11}T_{43} - T_{41}T_{13}} \\ \frac{r_{sp}}{r_{ss}} &= \frac{T_{41}T_{33} - T_{43}T_{31}}{T_{21}T_{33} - T_{23}T_{31}}. \end{aligned} \quad (\text{I.5})$$

The advancement by Schubert and coworkers, and from which use is made within this thesis, consists in the attainment of explicit solutions for the eigenvalues involved in the calculation of the transfer matrix [74, 75]. These expressions provide the exact treatment of light propagation in multilayered systems with constituents that are magneto-optically active or possess dielectric birefringence (or a combination of both). The main equations for the matrices in Eq. I.4 are reproduced below in order to depict the idea behind the transfer matrix procedure. For the set of explicit solutions for the eigenvalues that facilitate the exact calculation of partial matrices, the interested reader is referred to the original articles [74, 75].

### ***General Transfer Matrix calculation***

The General Transfer Matrix in Eq. I.4 is obtained from the multiplication of the (i) product of partial transfer matrices, (ii) the incident matrix and (iii) the exit matrix.

---

<sup>66</sup> Here, only three (complex) matrix elements of the  $2 \times 2$  Fresnel reflectivity matrix are relevant, hence the given quantities being normalized with respect to  $r_{ss}$ .

The partial transfer matrix of a given layer within the considered stack depends on the layer thickness  $d$  and the electromagnetic response function of the layer material (the dielectric tensor). The light angular frequency  $\omega$  and the in-plane component of the incident wavevector  $k_x = N_a \sin \theta_a$  must be considered as well. Schubert and coworkers start the calculation from the set of differential equations derived by Berreman [271] for the in-plane components of the electric and magnetic fields

$$\partial_z \Psi(z) = ik_0 \Delta(z) \Psi(z), \quad (\text{I.6})$$

where  $k_0 = \omega/c$ , with  $c$  being the speed of light. The vector  $\Psi(z) = (E_x, E_y, H_x, H_y)^T$  represents the  $z$ -dependent field components of monochromatic light. The matrix  $\Delta$  is represented on the basis of the symmetric and asymmetric parts of the dielectric tensor, these being  $s_{ij} = \frac{\epsilon_{ij} + \epsilon_{ji}}{2}$  and  $a_{ij} = \frac{\epsilon_{ij} - \epsilon_{ji}}{2}$ , respectively. The matrix  $\Delta$  then reads as

$$\Delta = \begin{pmatrix} -k_x \frac{s_{13} - a_{13}}{s_{33}} & -k_x \frac{s_{23} - a_{23}}{s_{33}} & 0 & 1 - \frac{k_x^2}{s_{33}} \\ 0 & 0 & -1 & 0 \\ \frac{(s_{23} + a_{23})(s_{13} - a_{13}) - (s_{12} - a_{12})}{s_{33}} & k_x^2 - s_{22} + \frac{(s_{23} - a_{23})(s_{23} + a_{23})}{s_{33}} & 0 & k_x \frac{s_{23} + a_{23}}{s_{33}} \\ s_{11} - \frac{(s_{13} + a_{13})(s_{13} - a_{13})}{s_{33}} & (s_{12} + a_{12}) - \frac{(s_{23} - a_{23})(s_{13} + a_{13})}{s_{33}} & 0 & -k_x \frac{s_{13} + a_{13}}{s_{33}} \end{pmatrix}. \quad (\text{I.7})$$

In the special case of an optically isotropic, magneto-optically active medium, the matrix  $\Delta$  has the following dependence on the Cartesian components of magnetization  $s$

$$\Delta = \begin{pmatrix} ik_x Q m_y & -ik_x Q m_x & 0 & 1 - \frac{k_x^2}{N^2} \\ 0 & 0 & -1 & 0 \\ N^2(iQ m_z - Q^2 m_x m_y) & k_x^2 - N^2(1 - Q^2 m_x^2) & 0 & -ik_x Q m_x \\ N^2(1 - Q^2 m_y^2) & N^2(iQ m_z + Q^2 m_x m_y) & 0 & -ik_x Q m_y \end{pmatrix}. \quad (\text{I.8})$$

Upon light being transmitted through the layer, the field vector  $\Psi(z)$  can be propagated as follows

$$\Psi(z + d) = \exp\left(i \frac{\omega}{c} \Delta d\right) \Psi(z) = \mathbf{T}_p \Psi(z), \quad (\text{I.9})$$

from where the definition  $\mathbf{T}_p = \exp(i \frac{\omega}{c} \Delta d)$  of the partial transfer matrix is obtained, which also accounts for all multiple reflections at interfaces during light propagation.

The exponential matrix function in Eq. I.9 can be evaluated by different methods. A common approach consists on expanding the exponential in a series, provided that the quantity  $\frac{\omega d}{c}$  is small (thin layer as compared to the light wavelength). The approach followed by Schubert and coworkers is instead using the Cayley-Hamilton theorem [74, 75] according to which one can expand the exponential in a finite series up to the  $n - 1$  power, where  $n$  is the rank of the matrix. The partial matrix thus reads as

$$\mathbf{T}_p = \exp\left(i \frac{\omega}{c} \Delta d\right) = \beta_0 \mathbf{I} + \beta_1 \Delta + \beta_2 \Delta^2 + \beta_3 \Delta^3, \quad (\text{I.10})$$

which is valid independent of whether the constituent layers are thin. Here,  $\mathbf{I}$  is the identity matrix and the scalars  $\{\beta_0, \dots, \beta_3\}$  must obey

$$\exp\left(i \frac{\omega}{c} q_k d\right) = \sum_{j=0}^3 \beta_j q_k^j \quad (\text{I.11})$$

where  $q_k$  represents the set of four eigenvalues belonging to the matrix  $\Delta$ . The eigenvalues correspond to the four plane waves that describe light propagation in the layer under consideration (two forward-traveling and two back-traveling). The analytical expressions for the eigenvalues can be found in Ref. [75].

Besides the partial transfer matrices, the incident and exit matrices need to be computed as well. The incident matrix connects the tangential parts of the incoming waves to the interface of the first layer, while the exit matrix does the equivalent operation from the last layer to the exit medium (substrate).

In fact, it is the inverse of the incident matrix what it is needed to obtain the transfer matrix in Eq. I.4. This reads as [74]

$$\mathbf{L}_a^{-1} = \frac{1}{2} \begin{pmatrix} 0 & 1 & -1/n_a \cos \theta_a & 0 \\ 0 & 1 & 1/n_a \cos \theta_a & 0 \\ 1/\cos \theta_a & 0 & 0 & 1/n_a \\ -1/\cos \theta_a & 0 & 0 & 1/n_a \end{pmatrix}, \quad (\text{I.12})$$

and hence  $\mathbf{L}_a^{-1}$  depends only on the incident light angle  $\theta_a$  and the (complex) refractive index of the incident medium. In this thesis,  $n_a = 1$  is always assumed for air.

Finally, the exit matrix  $\mathbf{L}_f$  upon assuming an optically isotropic substrate is

$$\mathbf{L}_f = \begin{pmatrix} 0 & 0 & \cos \theta_f & 0 \\ 1 & 0 & 0 & 0 \\ -n_f \cos \theta_f & 0 & 0 & n_f \\ 0 & 0 & 0 & 0 \end{pmatrix}, \quad (\text{I.13})$$

where  $n_f$  is the refractive index of the substrate or exit medium and the cosine of the exit angle  $\theta_f$  can be obtained from Snell's law as  $\cos \theta_f = \sqrt{1 - [(n_a/n_f) \sin \theta_f]^2}$ .

In the present thesis an optically isotropic substrate was always considered. For the case of an optically anisotropic substrate, the reader is referred to the original work by Schubert [74].

## Appendix II

# Derivation of the $\delta I/I$ expression for the GME technique

### A. The $\delta I/I$ formula

The starting point for deriving the  $\delta I/I(\varphi_1, \varphi_2)$  expression for GME lies on the reflection matrix of the magnetized medium, which within linear magneto-optical Kerr effects reads as [58, 69, 71]

$$R = \begin{pmatrix} r_{ss} & r_{sp} \\ r_{ps} & r_{pp} \end{pmatrix} = \begin{pmatrix} r_s & \alpha + \gamma \\ -\alpha + \gamma & r_p + \beta \end{pmatrix} = r_p \begin{pmatrix} \tilde{r}_s & \tilde{\alpha} + \tilde{\gamma} \\ -\tilde{\alpha} + \tilde{\gamma} & 1 + \tilde{\beta} \end{pmatrix} = r_p \tilde{R}. \quad (\text{II.1})$$

Here, the element  $\tilde{r}_s$  is related to the purely optical reflectivity coefficient, while  $\tilde{\alpha}$ ,  $\tilde{\beta}$  and  $\tilde{\gamma}$  are the magnetically induced matrix elements associated to the longitudinal, transverse and polar Kerr effects, respectively. The magneto-optical matrix elements  $\tilde{\alpha}$ ,  $\tilde{\beta}$  and  $\tilde{\gamma}$  change the sign upon magnetization inversion and are typically two to four orders of magnitude smaller than  $\tilde{r}_s$  (or even smaller).

The simplified version of the GME setup consists of a laser-source, a rotatable linear polarizer (P1), the sample (R), a second rotatable polarizer (P2) and a photodetector. The electric field of the light arriving to the photodetector is obtained by multiplying the corresponding matrix of the optical elements in the setup

$$E_D = P2 \cdot R \cdot P1 \cdot E_I, \quad (\text{II.2})$$

where the most general polarization state for the incident light is assumed,  $E_I = \begin{pmatrix} a \\ b \end{pmatrix}$ , with  $a, b$  being complex numbers fulfilling the normalization condition  $a^*a + b^*b = 1$ . The matrix multiplication in Eq. II.2 is then written as

$$E_D = r_p \begin{pmatrix} \cos^2 \varphi_2 & \sin \varphi_2 \cos \varphi_2 \\ \sin \varphi_2 \cos \varphi_2 & \sin^2 \varphi_2 \end{pmatrix} \begin{pmatrix} \tilde{r}_s & \tilde{\alpha} + \tilde{\gamma} \\ -\tilde{\alpha} + \tilde{\gamma} & 1 + \tilde{\beta} \end{pmatrix} \begin{pmatrix} \cos^2 \varphi_1 & \sin \varphi_1 \cos \varphi_1 \\ \sin \varphi_1 \cos \varphi_1 & \sin^2 \varphi_1 \end{pmatrix} \begin{pmatrix} a \\ b \end{pmatrix}. \quad (\text{II.3})$$

The intensity measured at the photodetector for an arbitrary magnetization state  $\mathbf{M}$  is then proportional to the square of the electric field vector, which is expanded as

$$\begin{aligned} I(\mathbf{M}) &= E_D^* \cdot E_D \\ &= f_{ab}(a, b, \varphi_1) \cdot |r_p|^2 \cdot \{ |\tilde{r}_s|^2 \cos^2 \varphi_1 \cos^2 \varphi_2 \\ &\quad + 2\text{Re}[\tilde{r}_s \cdot (\tilde{\gamma}^* - \tilde{\alpha}^*)] \cos^2 \varphi_1 \cos \varphi_2 \sin \varphi_2 \\ &\quad + [|\tilde{\alpha}|^2 + |\tilde{\gamma}|^2 - 2\text{Re}(\tilde{\alpha} \cdot \tilde{\gamma}^*)] \cos^2 \varphi_1 \sin^2 \varphi_2 \\ &\quad + 2\text{Re}[\tilde{r}_s \cdot (\tilde{\gamma}^* + \tilde{\alpha}^*)] \cos \varphi_1 \sin \varphi_1 \cos^2 \varphi_2 \\ &\quad + [2|\tilde{\gamma}|^2 - 2|\tilde{\alpha}|^2 + 2\text{Re}(\tilde{r}_s) + 2\text{Re}(\tilde{r}_s \cdot \tilde{\beta}^*)] \cos \varphi_1 \sin \varphi_1 \cos \varphi_2 \sin \varphi_2 \\ &\quad + [2\text{Re}(\tilde{\gamma} - \tilde{\alpha}) + 2\text{Re}(\tilde{\gamma} \cdot \tilde{\beta}^* - \tilde{\alpha} \cdot \tilde{\beta}^*)] \cos \varphi_1 \sin \varphi_1 \sin^2 \varphi_2 \\ &\quad + [|\tilde{\alpha}|^2 + |\tilde{\gamma}|^2 + 2\text{Re}(\tilde{\alpha} \cdot \tilde{\gamma}^*)] \sin^2 \varphi_1 \cos^2 \varphi_2 \\ &\quad + [2\text{Re}(\tilde{\gamma} + \tilde{\alpha}) + 2\text{Re}(\tilde{\gamma} \cdot \tilde{\beta}^* + \tilde{\alpha} \cdot \tilde{\beta}^*)] \sin^2 \varphi_1 \cos \varphi_2 \sin \varphi_2 \\ &\quad + [1 + 2\text{Re}(\tilde{\beta}) + |\tilde{\beta}|^2] \sin^2 \varphi_1 \sin^2 \varphi_2 \}. \end{aligned} \quad (\text{II.4})$$

In the expression above, the function  $f_{ab}$  multiplying the entire sum of terms reads as

$$f_{ab}(a, b, \varphi_1) = |a|^2 \cos^2 \varphi_1 + 2\text{Re}(ab^*) \cos \varphi_1 \sin \varphi_1 + |b|^2 \sin^2 \varphi_1, \quad (\text{II.5})$$

which is dependent on the polarization state of the incident light as well as on the polarizer angle  $\varphi_1$ . Following the results in Eq. II.5, one can proceed to calculate the intensity at the photodetector at the inverted magnetization state by using the symmetry of the upon this operation of the reflection matrix elements  $\tilde{r}_s, \tilde{\alpha}, \tilde{\beta}$  and  $\tilde{\gamma}$

$$I(\mathbf{M}) = I(\tilde{r}_s, \tilde{\alpha}, \tilde{\beta}, \tilde{\gamma}) \rightarrow I(-\mathbf{M}) = I(\tilde{r}_s, -\tilde{\alpha}, -\tilde{\beta}, -\tilde{\gamma}), \quad (\text{II.6})$$

in which the magnetically induced elements change the sign upon magnetization inversion. The above expressions thus give access to the fractional intensity change of the magneto-optical signal upon magnetization inversion

$$\frac{\delta I}{I}(\varphi_1, \varphi_2) = \frac{I(\mathbf{M}) - I(-\mathbf{M})}{[I(\mathbf{M}) + I(-\mathbf{M})]/2}, \quad (\text{II.7})$$

which is our quantity of interest. The numerator in Eq. II.7 reads as

$$\begin{aligned} I(\mathbf{M}) - I(-\mathbf{M}) &= 4f_{ab}(a, b, \varphi_1) \cdot \{ \text{Re}(\tilde{\alpha})(\sin^2 \varphi_1 \cos \varphi_2 \sin \varphi_2 - \cos \varphi_1 \sin \varphi_1 \sin^2 \varphi_2) \\ &\quad + \text{Re}(\tilde{r}_s \cdot \tilde{\alpha}^*)(\cos \varphi_1 \sin \varphi_1 \cos^2 \varphi_2 - \cos^2 \varphi_1 \cos \varphi_2 \sin \varphi_2) \\ &\quad + \text{Re}(\tilde{\beta}) \sin^2 \varphi_1 \sin^2 \varphi_2 \\ &\quad + \text{Re}(\tilde{r}_s \cdot \tilde{\beta}^*) \cos \varphi_1 \sin \varphi_1 \cos \varphi_2 \sin \varphi_2 \\ &\quad + \text{Re}(\tilde{\gamma})(\sin^2 \varphi_1 \cos \varphi_2 \sin \varphi_2 + \cos \varphi_1 \sin \varphi_1 \sin^2 \varphi_2) \\ &\quad + \text{Re}(\tilde{r}_s \cdot \tilde{\gamma}^*)(\cos \varphi_1 \sin \varphi_1 \cos^2 \varphi_2 - \cos^2 \varphi_1 \cos \varphi_2 \sin \varphi_2) \} \\ &= 4f_{ab}(a, b, \varphi_1) \cdot \{ B_1 f_1 + B_2 f_2 + B_3 f_3 + B_4 f_4 + B_5 f_5 + B_6 f_6 \}, \end{aligned} \quad (\text{II.8})$$

while the denominator takes the form

$$\begin{aligned} \frac{[I(\mathbf{M}) + I(-\mathbf{M})]}{2} &= f_{ab}(a, b, \varphi_1) \cdot \{ \sin^2 \varphi_1 \sin^2 \varphi_2 + |\tilde{r}_s|^2 \cos^2 \varphi_1 \cos^2 \varphi_2 \\ &\quad + \text{Re}(\tilde{r}_s) \cos \varphi_1 \sin \varphi_1 \cos \varphi_2 \sin \varphi_2 \} \\ &\quad + O\left(|\tilde{\alpha}|^2, |\tilde{\beta}|^2, |\tilde{\gamma}|^2, \text{Re}(\tilde{\alpha} \cdot \tilde{\beta}^*), \text{Re}(\tilde{\alpha} \cdot \tilde{\gamma}^*), \text{Re}(\tilde{\gamma} \cdot \tilde{\beta}^*)\right) \\ &= f_{ab}(a, b, \varphi_1) \cdot \{ f_3 + B_7 f_7 + 2B_8 f_4 \} + \text{higher order terms} \end{aligned} \quad (\text{II.9})$$

The expressions in Eqs. II.8 and II.9 have been summarized by introducing eight  $B_i$  real parameters associated to the four complex reflection matrix elements  $\tilde{r}_s$ ,  $\tilde{\alpha}$ ,  $\tilde{\beta}$  and  $\tilde{\gamma}$

$$\begin{aligned} B_1 &= \text{Re}(\tilde{\alpha}) & B_2 &= \text{Re}(\tilde{r}_s \cdot \tilde{\alpha}^*) \\ B_3 &= \text{Re}(\tilde{\beta}) & B_4 &= \text{Re}(\tilde{r}_s \cdot \tilde{\beta}^*) \\ B_5 &= \text{Re}(\tilde{\gamma}) & B_6 &= \text{Re}(\tilde{r}_s \cdot \tilde{\gamma}^*) \\ B_7 &= |\tilde{r}_s|^2 & B_8 &= \text{Re}(\tilde{r}_s), \end{aligned} \quad (\text{II.10})$$

as well as seven  $f_i$  functions that depend on the polarizer angles  $\varphi_1$  and  $\varphi_2$

$$\begin{aligned}
 f_1(\varphi_1, \varphi_2) &= \sin^2 \varphi_1 \sin \varphi_2 \cos \varphi_2 - \sin^2 \varphi_2 \sin \varphi_1 \cos \varphi_1 \\
 f_2(\varphi_1, \varphi_2) &= \cos^2 \varphi_2 \sin \varphi_1 \cos \varphi_1 - \cos^2 \varphi_1 \sin \varphi_2 \cos \varphi_2 \\
 f_3(\varphi_1, \varphi_2) &= \sin^2 \varphi_1 \sin^2 \varphi_2 \\
 f_4(\varphi_1, \varphi_2) &= \sin \varphi_1 \cos \varphi_1 \sin \varphi_2 \cos \varphi_2 \\
 f_5(\varphi_1, \varphi_2) &= \sin^2 \varphi_1 \sin \varphi_2 \cos \varphi_2 + \sin^2 \varphi_2 \sin \varphi_1 \cos \varphi_1 \\
 f_6(\varphi_1, \varphi_2) &= \cos^2 \varphi_2 \sin \varphi_1 \cos \varphi_1 + \cos^2 \varphi_1 \sin \varphi_2 \cos \varphi_2 \\
 f_7(\varphi_1, \varphi_2) &= \cos^2 \varphi_1 \cos^2 \varphi_2.
 \end{aligned}
 \tag{II.11}$$

Eventually, the  $\delta I/I$  quantity introduced in Eq. II.7 is written in the following compact form by utilizing the  $B_i$  parameters and the  $f_i$  functions

$$\frac{\delta I}{I}(\varphi_1, \varphi_2) = \frac{I(+\mathbf{M}) - I(-\mathbf{M})}{[I(+\mathbf{M}) + I(-\mathbf{M})]/2} = 4 \frac{B_1 f_1 + B_2 f_2 + B_3 f_3 + B_4 f_4 + B_5 f_5 + B_6 f_6}{f_3 + B_7 f_7 + 2B_8 f_4}
 \tag{II.12}$$

and hence does not depend on the  $f_{ab}(a, b, \varphi_1)$  function, which cancels out upon taking the division of Eqs. II.8 and II.9. Thus, in principle, the  $\delta I/I$  quantity is only influenced by the reflection matrix elements and the polarizer angles, while it does not depend on the particular polarization state of the incident light,  $E_I = \begin{pmatrix} a \\ b \end{pmatrix}$ . The quadratic-in-magnetization elements here only appear in the denominator part of the  $\delta I/I$  expression, as they vanish in the numerator part due to the difference building. These quadratic terms do not result from the presence of quadratic-in-magnetization contributions to the dielectric tensor, but rather from crossed multiplication terms arising from the assumed linear magneto-optical effects. Given the considerably smaller magnitude of  $\tilde{\alpha}$ ,  $\tilde{\beta}$  and  $\tilde{\gamma}$  as compared to  $\tilde{r}_s$ , these quadratic terms can be safely neglected from the denominator without substantially impacting the measurable  $\delta I/I$  quantity. The adopted strategy of using  $\delta I/I$  as the quantity of interest in GME naturally gets rid of the major quadratic magneto-optical effects, thus largely facilitating the data analysis.

## B. Impact of the background offset on the GME analysis

The denominator in the  $\delta I/I$  expression (Eq. II.12) takes its minimum value when the polarizers P1 and P2 are set in the  $s/p$  or  $p/s$  polarization configurations, that is, for the polarizer angle pairs  $(\varphi_1, \varphi_2) = (0^\circ, 90^\circ)$  and  $(90^\circ, 0^\circ)$ , defined as the crossed-polarizer

configurations. Specifically, the denominator in  $\delta I/I$  is zero for these particular symmetry points. There exist, however, a number of experimental limitations causing a residual background intensity that do not commonly allow measuring an exactly null intensity at the crossing point of the polarizers. Such factors include:

- i. The background intensity that may come from the ambient light and does not take part in the magneto-optical experiment.<sup>67</sup>
- ii. The non-ideal polarizing action of the Glan-Taylor polarizers, despite their extinction ratio being of the order of 100 000:1.
- iii. Weak depolarization effects of the laser light upon reflection from the sample or transmission through the optical elements of the setup.
- iv. The inherent dark current of the Si-diode photodetector, which can spontaneously produce electron-hole pairs and hence measure an effective current in the absence of any incident light<sup>68</sup>.

In order to account for such deviations (in contrast to the ideal situation illustrated by the previous equations) one can add a background offset parameter  $I_b$  to the intensity measured at the photodetector

$$I(\mathbf{M}) \rightarrow I(\mathbf{M}) + I_b \quad \text{and} \quad I(-\mathbf{M}) \rightarrow I(-\mathbf{M}) + I_b. \quad (\text{II.13})$$

From here, it is evident that the subtraction and the sum of the quantities  $I(\mathbf{M})$  and  $I(-\mathbf{M})$ , to be employed in the numerator and denominator in  $\delta I/I$  are not equally affected by the inclusion of the offset parameter, leading to

$$\begin{aligned} I(\mathbf{M}) - I(-\mathbf{M}) &\rightarrow [I(\mathbf{M}) + I_b] - [I(-\mathbf{M}) + I_b] = I(\mathbf{M}) - I(-\mathbf{M}) \\ I(\mathbf{M}) + I(-\mathbf{M}) &\rightarrow [I(\mathbf{M}) + I_b] + [I(-\mathbf{M}) + I_b] = I(\mathbf{M}) + I(-\mathbf{M}) + 2I_b, \end{aligned} \quad (\text{II.14})$$

upon which the offset term is cancelled out in the numerator but remains in the denominator. This in turn leads to a slightly modified expression of the  $\delta I/I$  expression

$$\frac{\delta I}{I}(\varphi_1, \varphi_2) = 4 \frac{B_1 f_1 + B_2 f_2 + B_3 f_3 + B_4 f_4 + B_5 f_5 + B_6 f_6}{f_3 + B_7 f_7 + 2B_8 f_4 + I_b/f_{ab}(a, b, \varphi_1)}, \quad (\text{II.15})$$

<sup>67</sup> It is usually difficult to get rid of this offset, despite we were using a wavelength specific bandpass filter at  $\lambda = 635 \pm 2$  nm placed just before the photodetector.

<sup>68</sup> This is the only non-optical effect we consider here, which is additionally dependent on the electrical amplification by the photodetector and controlled via its gain settings.

which now depends on the polarization state of the incident light through the function  $f_{ab}(a, b, \varphi_1)$  (see Eq. II 5). Assuming that the quantity  $I_b$  is constant throughout the entire experiment, Eq. II.15 implies the existence of an effective background offset amounting to  $I_b/f_{ab}(a, b, \varphi_1)$ , dependent on  $a, b$  but more significantly on  $\varphi_1$ . While the former are commonly fixed during the experiment, it is necessary to vary the angle  $\varphi_1$  in order to perform ellipsometry. This in turn means that for every different  $\varphi_1$  at which the  $\delta I/I$  is acquired, a different intensity offset will be recorded.

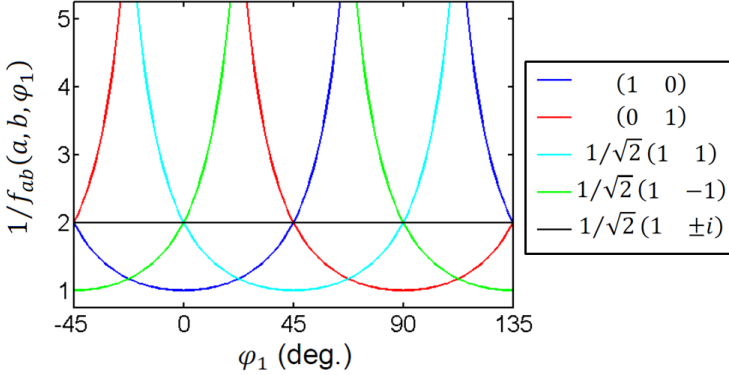


**Fig. II.1:** Dependence of the effective offset on the polarizer orientation  $\varphi_1$  for different  $(a, b)$  polarization states of the incident light.

This situation is illustrated in Fig. II.1, where the  $1/f_{ab}(a, b, \varphi_1)$  function is plotted against  $\varphi_1$  for different polarization states of the incoming light  $(a, b)$ . For linearly polarized light configurations, the  $1/f_{ab}$  intensity offset noticeably changes its value with  $\varphi_1$ , even diverging for  $\varphi_1$  values corresponding to an orthogonal orientation to the input polarization state. This result reflects the problematic of performing ellipsometry upon selecting a  $\varphi_1$  orientation perpendicular to a linearly polarized light input, as the intensity passing through the P1 polarizer is dramatically diminished and the intensity offset  $I_b$  being the only measurable quantity.

The situation changes if the input polarization state now consists of circularly polarized light,  $\begin{pmatrix} a \\ b \end{pmatrix} = \frac{1}{\sqrt{2}} \begin{pmatrix} 1 \\ \pm i \end{pmatrix}$ , as the  $f_{ab}(a, b, \varphi_1)$  function takes the constant value

$$f_{ab}(a, \pm ia, \varphi_1) = \left| \frac{1}{\sqrt{2}} \right|^2 \cdot |\cos \varphi_1 \pm i \sin \varphi_1|^2 = \frac{1}{2}. \quad (\text{II.16})$$

In such a way, the intensity of light passing through the P1 polarizer and incident onto the sample is the same regardless of the polarizer orientation  $\varphi_1$ .

In order to set this desired experimental condition, a  $\lambda/4$  retarder is placed right after the laser source, with its fast axis oriented at  $45^\circ$  away from the polarization plane of the laser light, upon which circularly polarized light is obtained.

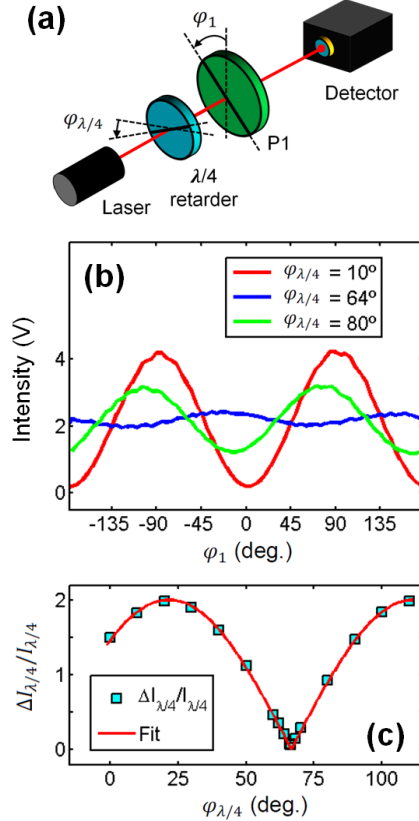


**Fig. II.2:** (a) Reduced setup to measure the intensity passing through the P1 polarizer upon placing a  $\lambda/4$  retarder right after the laser source. (b)  $\varphi_1$  dependence of the measured intensity for different  $\varphi_{\lambda/4}$  orientations of the retarder. (c) Fractional intensity variation vs  $\varphi_{\lambda/4}$ .

The appropriate retarder orientation is found by measuring the  $\varphi_1$  dependence of the light intensity passing through the P1 polarizer for different  $\varphi_{\lambda/4}$  retarder orientations[see Fig. II.2(a)]. Exemplary curves are shown in Fig. II.2(b) where the modulation of the curve varies substantially with  $\varphi_{\lambda/4}$  as the light impinging onto the polarizer P1 is closer or further from the circular polarized state. In particular, the largest modulation is expected when the fast axis is aligned with the polarization plane of the laser light, while no modulation is expected when the angle between the two is  $45^\circ$ . One can track the  $\varphi_{\lambda/4}$  dependence of the modulation amplitude, defined as

$$\frac{\Delta I_{\lambda/4}}{I_{\lambda/4}} = \frac{I_{max} - I_{min}}{(I_{max} + I_{min})/2} \quad (\text{II.17})$$

and that has been plotted in the Fig. II.2(c) vs  $\varphi_{\lambda/4}$ . The modulation reaches a maximum value close to 2 (for  $I_{min} \approx 0$ ) and a minimum value of nearly zero (for  $I_{max} \approx I_{min}$ ). Fitting the modulation amplitude dependence on  $\varphi_{\lambda/4}$  using the absolute value of a sine function with  $2\varphi_{\lambda/4}$  periodicity leads to the retarder angle  $\varphi_{\lambda/4,0} = 66.4^\circ$  as the condition at which the fast axis is oriented at  $45^\circ$  from the polarization plane of the laser light.

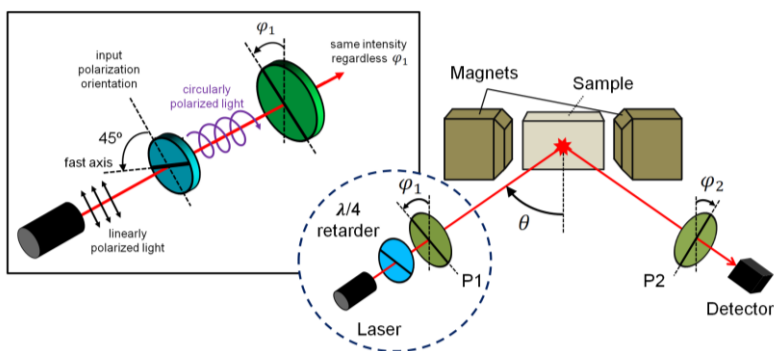


**Fig. II.3:** Schematic of the optimized GME setup. The implementation of an appropriately oriented quarter waveplate in the setup allows having the same intensity incident onto the sample independent of  $\varphi_1$ .

Thus, implementing a  $\lambda/4$  retarder right after the laser source in the GME setup (Fig. II.3) allows recovering the  $\delta I/I(\varphi_1, \varphi_2)$  expression utilized throughout this thesis with a constant offset term of  $I_0 = 2I_b$

$$\frac{\delta I}{I}(\varphi_1, \varphi_2) = 4 \frac{B_1 f_1 + B_2 f_2 + B_3 f_3 + B_4 f_4 + B_5 f_5 + B_6 f_6}{f_3 + B_7 f_7 + 2B_8 f_4 + I_0}, \quad (\text{II.18})$$

as well as provides stable operation and signal-to-noise ratio conditions for ellipsometric measurements<sup>69</sup>.

<sup>69</sup> While it cannot be completely excluded that the background intensity offset  $I_b$  is dependent on the incident polarization state ( $a, b$ ) or the polarizer angle  $\varphi_1$ , our results (for example, in Fig. II.2) show that this contribution, if existing, can be safely neglected.

## Appendix III

# Magneto-optical anisotropy effects in systems with uniaxial symmetry

### A. Magneto-optical anisotropy and crystal symmetry

The macroscopic description of electromagnetic interactions in crystals is expressed by appropriate materials tensors, the form of which is the same for a given crystal class<sup>70</sup>. Under the assumption of small magnetization induced magneto-optical Kerr effects, the most general form of the dielectric tensor can be expanded as [272]

$$\epsilon_{ij} = \epsilon_{ij}^{(0)} + \left[ \frac{\partial \epsilon_{ij}}{\partial M_k} \right]_{\mathbf{M}=0} M_k + \frac{1}{2} \left[ \frac{\partial^2 \epsilon_{ij}}{\partial M_k \partial M_l} \right]_{\mathbf{M}=0} M_k M_l = \epsilon_{ij}^{(0)} + K_{ijk} M_k + G_{ijkl} M_k M_l, \quad (\text{III.1})$$

where  $\epsilon_{ij}^{(0)} = \epsilon_{ji}^{(0)}$  denote the permittivity tensor components for  $\mathbf{M} = 0$  (for simplicity,  $\epsilon_{11}^{(0)} = \epsilon_{22}^{(0)} = \epsilon_{33}^{(0)}$  will be assumed, implying optical anisotropy)<sup>71,72</sup>.  $K_{ijk}$  and  $G_{ijkl}$  are termed as the linear and quadratic magneto-optical tensors, respectively. The resulting dielectric tensor is required to obey the Onsager reciprocity relation

---

<sup>70</sup> This is true for the bulk case, as it does not account for the presence of surfaces, interfaces, etc.

<sup>71</sup> The indices  $i, j, k, l$  denote the Cartesian axes  $x_1, x_2, x_3 \rightarrow x, y, z$ . The sum convention is understood.

<sup>72</sup> Here we use the ‘capital  $\mathbf{M}$ ’ for magnetization, in order avoid confusions with the indices.

$$\epsilon_{ij}(\mathbf{M}) = \epsilon_{ji}(-\mathbf{M}), \quad (\text{III.2})$$

which implies the following condition for the elements linear in  $M_k$

$$\epsilon_{ij}^{(1)} = K_{ijk}M_k = -K_{jik}M_k = -\epsilon_{ji}^{(1)}, \quad (\text{III.3})$$

and hence resulting into  $K_{iik} = 0$  and  $K_{ijk} = -K_{jik}$ . On the other hand, Eq. III.2 imposes for quadratic-in-magnetization components that

$$\epsilon_{ij}^{(2)} = G_{ijkl}M_kM_l = G_{ijkl}(-M_k)(-M_l) = \epsilon_{ji}^{(2)}, \quad (\text{III.4})$$

such that  $G_{ijkl} = G_{jikl} = G_{ijlk} = G_{jilk}$  is concluded.

In the following, only first order magneto-optical effects shall be considered for studying the magneto-optical anisotropy properties of uniaxial crystals. The axial tensor<sup>73</sup>  $K_{ijk}$  has in principle  $3^3 = 27$  independent elements. However, upon imposing  $K_{iik} = 0$  (9 out of 27 are zero) and  $K_{ijk} = -K_{jik}$  (from the non zero ones, only the half of them are independent), we are left with 9 independent tensor elements for the most general crystallographic class, such that the dielectric tensor takes the form

$$\begin{pmatrix} \epsilon_{23} \\ \epsilon_{31} \\ \epsilon_{12} \\ \epsilon_{32} \\ \epsilon_{13} \\ \epsilon_{21} \end{pmatrix} = \begin{pmatrix} K_{231} & K_{232} & K_{233} \\ K_{311} & K_{312} & K_{313} \\ K_{121} & K_{122} & K_{123} \\ -K_{231} & -K_{232} & -K_{233} \\ -K_{311} & -K_{312} & -K_{313} \\ -K_{121} & -K_{122} & -K_{123} \end{pmatrix} \begin{pmatrix} M_1 \\ M_2 \\ M_3 \end{pmatrix}. \quad (\text{III.5})$$

Besides the Onsager reciprocity relation, the crystal symmetry of the material imposes additional constraints, further reducing the number of independent tensor components. This is known as the Neumann's principle, stating that "*the symmetry elements of any physical property of a crystal must include all the symmetry elements of the point group of the crystal*". The tensor components transform according to [273]

$$\epsilon'_{ij} = a_{im}a_{jn}\epsilon_{mn} \quad \text{and} \quad K'_{ijk} = a_{im}a_{jn}a_{ko}K_{mno}, \quad (\text{III.6})$$

---

<sup>73</sup> The components of an axial tensor change their sign under spatial inversion.

where the tensor  $a_{ij}$  represents the associated transformation. The constraints on the tensor components can be derived from the fact that the symmetry operations of the crystal point group leave the permittivity tensor unchanged. An often studied material in this thesis, hcp Co, belongs to the point group  $6/mmm = D_{6h}$  of the hexagonal system (space group No. 194, ). In such a case, and after the pertinent operations, the linear magneto-optical tensor reads as

$$\begin{pmatrix} \varepsilon_{23} \\ \varepsilon_{31} \\ \varepsilon_{12} \\ \varepsilon_{32} \\ \varepsilon_{13} \\ \varepsilon_{21} \end{pmatrix} = \begin{pmatrix} K_{231} & 0 & 0 \\ 0 & K_{312} & 0 \\ 0 & 0 & K_{312} \\ -K_{231} & 0 & 0 \\ 0 & -K_{312} & 0 \\ 0 & 0 & -K_{312} \end{pmatrix} \begin{pmatrix} M_1 \\ M_2 \\ M_3 \end{pmatrix}, \quad (\text{III.7})$$

for the case in which the principal axis (or  $c$  axis) is oriented along the  $x_1 = x$  axis<sup>74</sup>. Thus linear magneto-optical effects for hcp Co can be described by means of the two tensor elements we are left with, which are

$$K_{231} = i\varepsilon^{(0)}Q_{\parallel} \quad \text{and} \quad K_{312} = i\varepsilon^{(0)}Q_{\perp} \quad (\text{III.8})$$

The complex factors  $Q_{\parallel}$  and  $Q_{\perp}$  correspond to the magneto-optical coupling strength when the magnetization is pointing along and perpendicular to the uniaxial  $c$  axis. Here,  $\varepsilon^{(0)} = N^2$ , with  $N = n + i\kappa$  being the refractive index of the material. Thus for the aforementioned configuration ( $c$  axis  $\parallel$   $x$ -axis), the dielectric tensor reads as<sup>75</sup>

$$\vec{\varepsilon} = N^2 \begin{pmatrix} 1 & iQ_{\perp}M_z & -iQ_{\perp}M_y \\ -iQ_{\perp}M_z & 1 & iQ_{\parallel}M_x \\ iQ_{\perp}M_y & -iQ_{\parallel}M_x & 1 \end{pmatrix}. \quad (\text{III.9})$$

The difference between the magneto-optical coupling strengths in hcp Co when the magnetization is oriented along or perpendicular to the  $c$ -axis has been experimentally verified by earlier works [157, 164] as well as in the present thesis, where for a photon energy of 1.95 eV ( $\lambda = 635$  nm), the absolute value of  $Q_{\perp}$  is a 10-15% higher than that of  $Q_{\parallel}$ , while this largely depends on strain for thin films.

<sup>74</sup> This is in contrast to the common description in the literature, where the symmetry axis is usually set along the  $x_3 = z$  axis [272].

<sup>75</sup> With  $\varepsilon_{11}^{(0)} = \varepsilon_{33}^{(0)} = N^2$  for the  $6/mmm$  crystal class, under assuming optical isotropy.

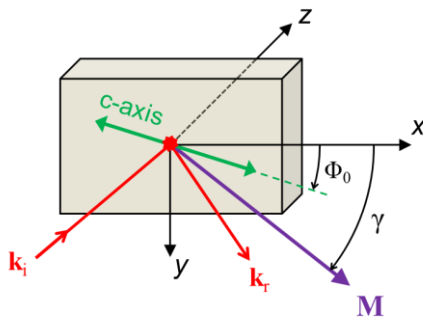


**Fig. III.1:** Schematic of the MOKE experiment, indicating the Cartesian coordinates, the incident and reflected beams ( $\mathbf{k}_i$  and  $\mathbf{k}_r$ ), the in-plane magnetization vector ( $\mathbf{M}$ ) and the  $c$  axis, as well as their respective angles  $\gamma$  and  $\Phi_0$ .

In order to study a more general case of an arbitrary orientation of the  $c$  axis within the  $xy$  sample surface plane, we consider a clock-wise rotation of the sample within the air/material interface by an angle  $\Phi_0$  about the  $z$ -axis (see Fig. III.1). The matrix representing this operation is

$$\mathcal{R}(\Phi_0) = (\mathcal{R}_{ij}) = \begin{pmatrix} \cos \Phi_0 & -\sin \Phi_0 & 0 \\ \sin \Phi_0 & \cos \Phi_0 & 0 \\ 0 & 0 & 1 \end{pmatrix}, \quad (\text{III.10})$$

by which we transform the tensor in Eq. III.9 following  $\vec{\epsilon}'(\Phi_0) = \mathcal{R}(\Phi_0) \cdot \vec{\epsilon} \cdot \mathcal{R}^T(\Phi_0)$ . After performing this rotation operation, it turns out that the only dielectric tensor elements that are modified with respect to Eq. III.9 are

$$\begin{aligned} \epsilon'_{13} &= -\epsilon'_{31} = -iN^2Q_{\parallel}[(1 + \tau \cos^2 \Phi_0)M_y - \tau \cos \Phi_0 \sin \Phi_0 M_x] \\ \epsilon'_{23} &= -\epsilon'_{32} = iN^2Q_{\parallel}[(1 + \tau \sin^2 \Phi_0)M_x - \tau \cos \Phi_0 \sin \Phi_0 M_y], \end{aligned} \quad (\text{III.11})$$

where we have defined the magneto-optical anisotropy coefficient  $\tau = (Q_{\perp} - Q_{\parallel})/Q_{\parallel}$ . Eq. III.11 implies that these particular off-diagonal tensor elements most generally depend on both in-plane magnetization components ( $M_x$ ,  $M_y$ ) instead of only one each.

With the purpose of relating the newly calculated dielectric tensor elements to the measurable MOKE polarization effects, we employ the formulas for the Fresnel coefficients for a semi-infinite magnetized medium. By assuming that the material is

magnetized in the  $xy$  plane, such that  $M_z = 0$  (without considering polar Kerr effects), the Fresnel equations read now as

$$\begin{aligned}
 r_{ss} &= \frac{\cos \theta - N \cos \theta'}{\cos \theta + N \cos \theta'} \\
 r_{pp} &= r_p - \frac{2 \cos \theta \sin \theta'}{N(N \cos \theta + \cos \theta')} \varepsilon_{13} = \frac{N \cos \theta - \cos \theta'}{N \cos \theta + \cos \theta'} - \frac{2 \cos \theta \sin \theta'}{N(N \cos \theta + \cos \theta')} \varepsilon'_{13} \\
 r_{sp} &= -r_{ps} = -\frac{\cos \theta \tan \theta'}{N(N \cos \theta + \cos \theta')(\cos \theta + N \cos \theta')} \varepsilon'_{23},
 \end{aligned}
 \tag{III.12}$$

from which the polarization effect commonly classified as the longitudinal Kerr effect now can be read, in terms of the complex Kerr angle as

$$\theta_K + i\varepsilon_K = \frac{r_{sp}}{r_p} = \tilde{\alpha}' [(1 + \tau \sin^2 \Phi_0) M_x - \tau \cos \Phi_0 \sin \Phi_0 M_y],
 \tag{III.13}$$

with  $\tilde{\alpha}' = -iNQ_{\parallel} \cos \theta \tan \theta' / [(N \cos \theta - \cos \theta')(\cos \theta + N \cos \theta')]$ . In addition, the reflectivity effect typically associated with the transverse Kerr effect reads as

$$\frac{r_{pp} - r_p}{r_p} = \tilde{\beta}' [(1 + \tau \cos^2 \Phi_0) M_y - \tau \cos \Phi_0 \sin \Phi_0 M_x],
 \tag{III.14}$$

with  $\tilde{\beta}' = 2iNQ_{\parallel} \cos \theta \sin \theta' / [N \cos \theta - \cos \theta']$ .

According to these results, the magnetization component  $M_x$  brings not only the conventional contribution to  $r_{sp}$  giving rise to a Kerr rotation and ellipticity, but also leads to a change in the reflectivity term  $r_{pp}$  (Eq. III.14) if magneto-optical anisotropy is present. Correspondingly, the transverse magnetization  $M_y$  now generates an additional polarization change effect in  $r_{sp}$  besides the common magnetic contribution to the  $p$ -polarization reflectivity term  $r_{pp}$  (see Eq. III.13 and a schematic of the phenomenon in Fig. III.2). For cases in which  $Q_{\parallel} = Q_{\perp}$  (i.e.  $\tau = 0$ ), the usual individual dependence of  $r_{sp}$  and  $r_{pp}$  on  $M_x$  and  $M_y$ , respectively, is restored. The individual dependence is also recovered for  $\Phi_0$  value that align the  $c$  axis with either the  $x$ - or  $y$ -axis, that is, for  $\Phi_0 = 0^\circ, \pm 90^\circ, \pm 180^\circ$ .

Thus the existence of an anomalous magnetization dependence of the first-order magneto-optical Fresnel coefficients is uncovered here under the presence of magneto-optical anisotropy. The mixed dependence of  $r_{sp}$  and  $r_{pp}$  on the in-plane magnetization components must be carefully considered when performing MOKE magnetometry, as neglecting magneto-optical anisotropy effects could lead to incorrect data interpretation upon the specificity of the different Kerr geometries on individual magnetization components does not generally hold. Particular attention should be put on systems potentially featuring magneto-optical anisotropy, such as strained epitaxial films, patterned arrays, and thin films with ultrathin metallic overcoats [274].

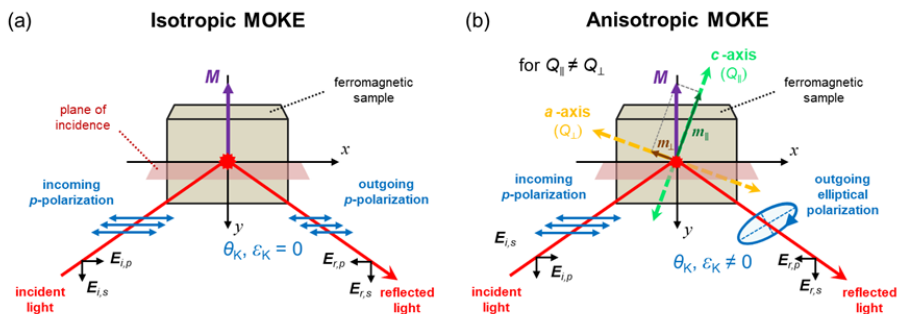


**Fig. III.2:** Schematic of a MOKE experiment for isotropic vs anisotropic first-order magneto-optics in the case of a  $p$ -polarized incident light and a transverse magnetization. The plane of incidence is the  $xz$  plane. (a) For isotropic magneto-optics, the outgoing polarization state is purely  $p$ -polarized, from which null Kerr rotation and ellipticity follow. (b) Under uniaxial magneto-optical anisotropy, the reflected light is an elliptically polarized wave, resulting into non-zero Kerr rotation and ellipticity.

With the purpose of addressing the question of how magneto-optical Kerr effects should be classified, we propose to redefine the longitudinal Kerr effect as the entirety of reflection matrix terms that are caused by the presence of a longitudinal component of magnetization  $M_x$ , i.e. the magnetization component that is defined by the  $x$ -axis, in which the sample plane and the plane of incidence intersect. Correspondingly, the transverse MOKE effect describes the entirety of the reflection matrix terms caused by a transverse magnetization  $M_y$ . Analogously, while not considered here, equivalent variations of the MOKE effects originated by a polar magnetization component  $M_z$  can be anticipated.

# List of publications

## *In this thesis*

- J. A. Arregi, J. B. González-Díaz, E. Bergaretxe, O. Idigoras, T. Unsal, and A. Berger  
“Study of generalized magneto-optical ellipsometry reliability”  
*J. Appl. Phys.* **111**, 103912 (2012)  
- Chapter 3 -
- J. B. González-Díaz, J. A. Arregi, E. Bergaretxe, M. J. Fertin, O. Idigoras, and A. Berger  
“Anomalous magneto-optical behavior of uniaxial Co/CoO bilayer films”  
*J. Magn. Magn. Mater.* **325**, 147 (2013)  
- Chapter 3 -
- J. A. Arregi, J. B. González-Díaz, N. Soriano, B. Mora, and A. Berger  
“Surface-topography induced optical and magneto-optical anisotropy of permalloy gratings”  
*J. Phys. D.: Appl. Phys.* **48**, 305002 (2015)  
- Chapter 5 -
- J. A. Arregi, J. B. González-Díaz, O. Idigoras, and A. Berger  
“Strain-induced magneto-optical anisotropy in epitaxial hcp Co-films”  
*Phys. Rev. B* **92**, 184405 (2015)  
- Chapter 4 -
- J. A. Arregi, P. Riego, and A. Berger  
“What is the longitudinal magneto-optical Kerr effect?”  
*J. Phys. D.: Appl. Phys.* **50**, 03LT01 (2017)  
- Appendix III -
- J. A. Arregi, P. Riego, E. Y. Vedmedenko, and A. Berger  
“Oscillatory Dzyaloshinskii-Moriya type magnetic interlayer exchange coupling”  
*in preparation*  
- Chapter 6 -

### ***Other publications***

- J. A. Arregi, O. Idigoras, P. Vavassori, and A. Berger  
“Field orientation dependent decorrelation of magnetization reversal in uniaxial Co-films”  
*Appl. Phys. Lett.* **100**, 262403 (2012)
- J. B. González-Díaz, J. A. Arregi, A. Martínez-de-Guerenu, F. Arizti, and A. Berger  
“Quantitative magneto-optical characterization of diffusive reflected light from rough steel samples”  
*J. Appl. Phys.* **113**, 153904 (2013)
- C. González-Fuentes, J.B. González-Díaz, L. Fallarino, J. A. Arregi, and A. Berger  
“Influence of the light incidence angle on the precision of generalized magneto-optical ellipsometry”  
*J. Magn. Magn. Mater.* **386**, 150 (2015)
- V. Uhlř, J. A. Arregi, and E. E. Fullerton  
“Colossal magnetic phase transition asymmetry in mesoscale FeRh stripes”  
*Nat. Commun.* **7**, 13113 (2016)
- P. Riego, S. Vélez, J. M. Gómez-Pérez, J. A. Arregi, L. E. Hueso, F. Casanova, and A. Berger  
“Absence of detectable current-induced magneto-optical Kerr effects in Pt, Ta and W”  
*Appl. Phys. Lett.* **109**, 172402 (2016)
- E. Vedmedenko, P. Riego, J. A. Arregi, and A. Berger  
“Interlayer Dzyaloshinskii-Moriya interactions”  
*Phys. Rev. Lett.* **122**, 257202 (2019)

# Acknowledgments

*[Dr. Frankenstein and Igor are digging up a body in the cemetery.]*

*–What a filthy job!*

*–It could be worse.*

*–How?*

*–It could be raining.*

*[Thunder. Lightning. And rain.]*

in ‘Young Frankenstein’ (Mel Brooks, 1974)

I want to thank my advisor Andreas Berger for giving me the opportunity to work with him, for every piece of knowledge, advice and values he shared with me, for everything I could learn from him (despite me not being able to take full advantage of it). I am grateful for his kindness, for his understanding during the difficult times and for his continuous efforts to help me.

I am also grateful to Paolo Vavassori for his positive spirit, for his clear explanations and for being always ready to help out, and for introducing me to my first ever MOKE setup in the lab.

My warmest gratitude goes to Olatz Idigoras, who was mentoring me in the lab upon my arrival to the Nanomagnetism group and who taught me so many things in the beginning. For the nice shared discussions and jokes, and even when we needed to deal with some level of frustration. I am also very happy to have worked with Juan B. González-Díaz, who gave me very valuable insights into magneto-optics and with whom I enjoyed very much working together. It has equally been a pleasure to work with Lorenzo Fallarino and Patricia Riego, with whom I learned a lot and will be always grateful for. They enormously contributed to making the daily work in Nanogune very pleasant. I feel very lucky to have found such extraordinary people in my way. I am also very grateful to all the assistance César Rufo gave me during my years in the group, for his kindness and readiness. I also want to thank Marie Fertin for her valuable help with the spectroscopic ellipsometer, even if the ellipsometer itself did not always agree to collaborate with us in the same way.

I am also grateful to all the assistance and kindness from the administration and technical team at Nanogune, who I really have appreciated over the years, in particular Maria, Itziar, Yurdana, Miryam, Eider and Julene, as well as Ralph, Gorka Pazos, Gorka Arregui and Carlos. A big thank you to the cleaning staff at Nanogune for their kindness and cheerfulness.

I am very grateful to Eric Fullerton and Vojtěch Uhlíř for giving me the great opportunity to work with them during the 3-month research stay at University of California San Diego, as well as to all the kind colleagues I met during my time there.

I thank Prof. Evangelos Papaioannou and Prof. Tomáš Šikola for reading my manuscript and for writing a recommendation for the international PhD mention.

I would also like to thank to Txema Pitarke for giving me the excellent opportunity to conduct my PhD at CIC Nanogune.

I gratefully acknowledge the fellowship from the Spanish Ministry of Economy and Competitiveness during my PhD studies.

Life in Nanogune (and Donosti) would have not been the same without all the nice colleagues I had the luck to meet: Ania, Marcin, Ondrej, Marco Gobbi, Marco Donolato, Matteo, Txema, Raúl, Jon Zubeltzu, Martin, Wiwat, Thales, Luca, Mano, Mikel, Nicolò, Amilcar, Marta, María, Miren, Oihana, Libe, Carmen, Eva, Roger, Marie, Fede, Saul and the Graphenea people (Ilargi, Amaia, Mainer, Alba, Amaia), among others made this journey more beautiful and funnier.

Eskerrik asko nere onduan hainbeste urte pasau dozuen Paulo ta Estitxuri. Zuek Donostin eukittia familiartian egotia moduan izan da. Berdin zurekin, Jokin, biba zu ta alkarrekin pasautako abenturak! Donostin lagun zahar zein berrixekin topo iñ ahal izan dot. Mila esker Haizea, Berta eta Kristina (gora armosu taldea!), Mar, Carmen eta Bea. Mila esker Ido zure goxotasun ta barre infinitoagatik. Antzerki taldeko lagunei, bereziki Nereari, ni hain ondo zaindu izanagatik, eta Perniri, zapatak fundamentuz zela garbiketean dian erakutsi nostazulako.

Leioako lagun zaharrei, Pello, Ivan, Gorka... zein nere lagun “torontoarrei”, bereziki Iban, Marta, Ekiñe, eta Paulari, beti erakutsitako estimuagatik zein nigan sinistu izanagatik.

I will always be grateful to Vojtěch Uhlíř for giving me an opportunity to continue in research and to resume a life project, for his support and trust even when I was not doing so great. For his positive approach to problem solving and his dedication. I also thank from the bottom of my heart the people I have met in my české dobrodružství (Flajš, 3x Michal, Lucie, Jirka, Lukáš, Marek, Igor, Libor, Ondra...), for their friendliness and help. Moltes gràcies també a Xavi!

Mila esker bihotz-bihotzez Itzi, zure maittasun danagatik, pasautako momentu polit eta ederengatik, emundako laguntza danagatik, mila esker gaur egun be hor egotiatatik.

Bihotz-bihotzez eskerrak nere Oñatiko lagunei, Joseba, Ando ta Juleni, hainbestegatik, askotan gauza zailak errez ittiagatik. Tiagori, bihar dana baino lehen hegan alde iñ doskuen arren, hirekin hainbeste disfratau gixualako. Eskerrik asko jada gu bezain txantxikua dan Ainhoari, zure irribarre ta presentzia ederra guri erregalaittiagatik. Muxuak ta besarkadak Oihana, Bea, Nere, ta Kizkiri. Eskerrik asko Arani ta Aneri, edozein lekutan ta modutan etxian sentiarazten naizuelako. Eskerrik asko urte hauetan entzun ta lagundu nauzuenei.

Eskerrik asko nere gurasuei, anai-arrebei, Mateo, Lidia ta Carmeni, zuen babes, maittasun ta laguntza danagatik, oso zorteduna sentitten naiz zuekin. Azkenik, eskerrik asko zuri, Zilda, nere onduan egotiatatik, zure babes ta maittasunagatik, ta emuten dostazun zorion danagatik.

# References

- [1] S. Blundell, "Magnetism in condensed matter", Oxford University Press, Oxford (2001)
- [2] N. Spaldin, "Magnetic Materials: Fundamentals and Applications", Cambridge University Press, Cambridge (2010)
- [3] A. Moser, K. Takano, D.T. Margulies, M. Albrecht, Y. Sonobe, Y. Ikeda, S.H. Sun, and E. E. Fullerton, "Magnetic recording: advancing into the future", *J. Phys. D: Appl. Phys.* **35**, R157 (2002)
- [4] G. Srajer, L. H. Lewis, S. D. Bader, A. J. Epstein, C. S. Fadley, E. E. Fullerton A. Hoffmann J. B. Kortright, K. M. Krishnan, S. A. Majetich, T. S. Rahman, C. A. Ross, M. B. Salamon, I. K. Schuller, T. C. Schulthess, and J. Z. Sun, "Advances in nanomagnetism via X-ray techniques", *J. Magn. Magn. Mater.* **307**, 1 (2006)
- [5] R. Allenspach, "Thin-Film Magnetism" in *Surface and Interface Science (Vol 4)*, K. Wandelt (Ed.), Wiley-VCH Verlag (2014)
- [6] L. M. Falicov, D. T. Pierce, S. D. Bader, R. Gronsky, K. B. Hathaway, H. J. Hopster, D. N. Lambeth, S. S. P. Parkin, G. Prinz, M. Salamon, and I. K. Schuller, "Surface, interface, and thin-film magnetism", *J. Mater. Research* **5**, 1299 (1990)
- [7] C. Chappert, A. Fert, and F. N. Van Dau, "The emergence of spin electronics in data storage", *Nat. Mater.* **6**, 813 (2007).
- [8] P. Grünberg, R. Schreiber, Y. Pang, M. B. Brodsky, and H. Sowers, "Layered Magnetic Structures: Evidence for Antiferromagnetic Coupling of Fe Layers across Cr Interlayers", *Phys. Rev. Lett.* **57**, 2442 (1986)
- [9] M. N. Baibich, J. M. Broto, A. Fert, F. Nguyen Van Dau, F. Petroff, P. Eitenne, G. Creuzet, A. Friederich, and J. Chazelas, "Giant Magnetoresistance of (001) Fe/(001) Cr Magnetic Superlattices", *Phys. Rev. Lett.* **61**, 2472 (1988)
- [10] G. Binasch, P. Grünberg, F. Saurenbach, and W. Zinn, "Enhanced magnetoresistance in layered magnetic structures with antiferromagnetic interlayer exchange", *Phys. Rev. B* **39**, 4828 (1989)
- [11] S. S. P. Parkin, C. Kaiser, A. Panchula, P. M. Rice, B. Hughes, M. Samant, and S.-H. Yang, "Giant tunnelling magnetoresistance at room temperature with MgO (100) tunnel barriers". *Nat. Mater.* **3**, 862 (2004)
- [12] S. Yuasa, T. Nagahama, A. Fukushima, Y. Suzuki, and K. Ando, "Giant room-temperature magnetoresistance in single-crystal Fe/MgO/Fe magnetic tunnel junctions", *Nat. Mater.* **3**, 868 (2004)
- [13] L. Floridi, "Information: A Very Short Introduction", Oxford University Press, Oxford (2010)
- [14] D. Weller, and A. Moser, "Thermal effect limits in ultrahigh-density magnetic recording", *IEEE. Trans. Magn.* **35**, 4423 (1999)

- [15] H. W. Schumacher, C. Chappert, P. Crozat, R. C. Sousa, P. P. Freitas, J. Miltat, J. Fassbender, and B. Hillebrands, “Phase Coherent Precessional Magnetization Reversal in Microscopic Spin Valve Elements”, *Phys. Rev. Lett.* **90**, 017201 (2003)
- [16] M. H. Kryder, E. C. Gage, T. W. McDaniel, W. A. Challener, R. E. Rottmayer, G. Ju, Y. T. Hsia, and M.F. Erden, “Heat assisted magnetic recording”, *Proc. IEEE* **96**, 1810 (2008)
- [17] D. Sander, S. O. Valenzuela, D. Makarov, C. H. Marrows, E. E. Fullerton, P. Fischer, J. McCord, P. Vavassori, S. Mangin, P. Pirro, B. Hillebrands, A. D. Kent, T. Jungwirth, O. Gutfleisch, C. G. Kim, and A Berger, “The 2017 Magnetism Roadmap”, *J. Phys. D: Appl. Phys.* **50**, 363001 (2017)
- [18] F. Hellman, A. Hoffmann, Y. Tserkovnyak, G. S. Beach, E. E. Fullerton, C. Leighton, A. H. MacDonald, D. C. Ralph, D. A. Arena, H. A. Dürr, P. Fischer, J. Grollier, J. P. Heremans, T. Jungwirth, A. V. Kimel, B. Koopmans, I. N. Krivorotov, S. J. May, A. K. Petford-Long, J. M. Rondinelli, I. K. Schuller, A. N. Slavin, M. D. Stiles, O. Tchernishyov, A. Thiaville, and B. L. Zink, “Interface-induced phenomena in magnetism”, *Rev. Mod. Phys.* **89**, 025006 (2017)
- [19] J. A. Katine, F. J. Albert, R. A. Buhrman, E. B. Myers, and D. C. Ralph, “Current-Driven Magnetization Reversal and Spin-Wave Excitations in Co /Cu /Co Pillars”, *Phys. Rev. Lett.* **84**, 3149 (2000)
- [20] A. Brataas, A. D. Kent, and H. Ohno, “Current-induced torques in magnetic materials”, *Nat. Mater.* **11**, 372 (2012)
- [21] B. Dieny and M. Chshiev, “Perpendicular magnetic anisotropy at transition metal/oxide interfaces and applications”, *Rev. Mod. Phys.* **89**, 025008 (2017)
- [22] A. Manchon, J. Železný, I. M. Miron, T. Jungwirth, J. Sinova, A. Thiaville, K. Garello, and P. Gambardella, “Current-induced spin-orbit torques in ferromagnetic and antiferromagnetic systems”, *Rev. Mod. Phys.* **91**, 035004 (2019)
- [23] D. A. Allwood, G. Xiong, C.C. Faulkner, D. Atkinson, D. Petit, and R. P. Cowburn, “Magnetic domain-wall logic”, *Science* **309**, 1688 (2005).
- [24] S. S. Parkin, M. Hayashi, and L. Thomas, “Magnetic domain-wall racetrack memory”, *Science* **320**, 190 (2008)
- [25] A. Fert, V. Cros, and J. Sampaio, “Skyrmions on the track”, *Nat. Nanotechnol.* **8**, 152 (2013)
- [26] V. V. Kruglyak, S. O. Demokritov, and D. Grundler, “Magnonics”, *J. Phys. D: Appl. Phys.* **43**, 260301 (2010)
- [27] A. Kirilyuk, A. V. Kimel, and T. Rasing, “Ultrafast optical manipulation of magnetic order”, *Rev. Mod. Phys.* **82**, 2731 (2010)
- [28] T. Jungwirth, X. Marti, P. Wadley, and J. Wunderlich, “Antiferromagnetic spintronics”, *Nat. Nanotechnol.* **11**, 231 (2016)
- [29] O. Gutfleisch, M. A. Willard, E. Brück, C.H Chen, S. G. Sankar, and J. P. Liu, “Magnetic materials and devices for the 21st century: stronger, lighter, and more energy efficient”, *Adv. Mater.* **23**, 821 (2011)
- [30] Q. A. Pankhurst, J. Connolly, S. K. Jones, and J. Dobson, “Applications of magnetic nanoparticles in biomedicine”, *J. Phys. D: Appl. Phys.* **36**, R167 (2003)
- [31] E. A. Périgo, G. Hemery, O. Sandre, D. Ortega, E. Garaio, F. Plazaola, and F. J. Teran, “Fundamentals and advances in magnetic hyperthermia”, *Appl. Phys. Rev.* **2**, 041302 (2015)

- [32] M. Goiriena-Goikoetxea, D. Muñoz, I. Orue, M. L. Fernández-Gubieda, J. Bokor, A. Muela, and A. García-Arribas, "Disk-shaped magnetic particles for cancer therapy", *Appl. Phys. Rev.* **7**, 011306 (2020)
- [33] J. M. D. Coey, "Magnetism and Magnetic Materials", Cambridge University Press, Cambridge (2010)
- [34] G. Bertotti, "Hysteresis in magnetism: for physicists, materials scientists, and engineers", Academic Press (1998)
- [35] A. Aharoni, "Introduction to the Theory of Ferromagnetism", Clarendon Press, New York (2000)
- [36] D. Sander, "The correlation between mechanical stress and magnetic anisotropy in ultrathin films", *Rep. Prog. Phys.* **62**, 809 (1999)
- [37] I. Dzyaloshinskii, "A thermodynamic theory of 'weak' ferromagnetism of antiferromagnetics", *J. Phys. Chem. Solids* **4**, 241–255 (1958)
- [38] T. Moriya, "Anisotropic superexchange interaction and weak ferromagnetism", *Phys. Rev.* **120**, 91 (1960)
- [39] A. Fert, and P. M. Levy, "Role of Anisotropic Exchange Interactions in Determining the Properties of Spin-Glasses", *Phys. Rev. Lett.* **44**, 1538 (1980)
- [40] S. Mühlbauer, B. Binz, F. Jonietz, C. Pfleiderer, A. Rosch, A. Neubauer, R. Georgii, and P. Böni, "Skyrmion lattice in a chiral magnet", *Science* **323**, 915 (2009)
- [41] A. Fert, "Magnetic and Transport Properties of Metallic Multilayers", in *Metallic Multilayers* (Eds. A. Chamberod and J. Hillairet), *Mat. Sci. Forum* **59-60**, 439 (1990)
- [42] S. Heinze, K. von Bergmann, M. Menzel, J. Brede, A. Kubetzka, R. Wiesendanger, G. Bihlmayer, and S. Blügel, "Spontaneous atomic-scale magnetic skyrmion lattice in two dimensions", *Nat. Phys.* **7**, 713 (2011)
- [43] G. Chen, J. Zhu, A. Quesada, J. Li, A. T. N'Diaye, Y. Huo, T. P. Ma, Y. Chen, H. Y. Kwon, C. Won, Z. Q. Qiu, A. K. Schmid, and Y. Z. Wu, "Novel Chiral Magnetic Domain Wall Structure in Fe/Ni/Cu(001) Films", *Phys. Rev. Lett.* **110**, 177204 (2013)
- [44] G. Chen, T. Ma, A. T. N'Diaye, H. Kwon, C. Won, Y. Wu, and A. K. Schmid, "Tailoring the chirality of magnetic domain walls by interface engineering", *Nat. Commun.* **4**, 2671 (2013)
- [45] C. Moreau-Luchaire, C. Moutafis, N. Reyren, J. Sampaio, C. A. F. Vaz, N. Van Horne, K. Bouzehouane, K. Garcia, C. Deranlot, P. Warnicke, P. Wohlhüter, J.-M. George, M. Weigand, J. Raabe, V. Cros, and A. Fert, "Additive interfacial chiral interaction in multilayers for stabilization of small individual skyrmions at room temperature", *Nat. Nanotechnol.* **11**, 444 (2016)
- [46] S. Woo, K. Litzius, B. Krüger, M.-Y. Im, L. Caretta, K. Richter, M. Mann, A. Krone, R. M. Reeve, M. Weigand, P. Agrawal, I. Lemesch, M.-A. Mawass, P. Fischer, M. Kläui, and G. S. D. Beach, "Observation of room-temperature magnetic skyrmions and their current-driven dynamics in ultrathin metallic ferromagnets," *Nat. Mater.* **15**, 501 (2016)
- [47] S. S. P. Parkin, N. More, and K. P. Roche, "Oscillations in Exchange Coupling and Magnetoresistance in Metallic Superlattice Structures: Co/Ru, Co/Cr, and Fe/Cr", *Phys. Rev. Lett.* **64**, 2304 (1990)
- [48] S. S. P. Parkin, "Systematic Variation of the Strength and Oscillation Period of Indirect Magnetic Exchange Coupling through the 3d, 4d, and 5d Transition Metals" *Phys. Rev. Lett.* **67**, 3598 (1991)

- [49] P. Bruno, and C. Chappert, “Ruderman-Kittel theory of oscillatory interlayer exchange coupling”, *Phys. Rev. B* **46**, 261 (1992)
- [50] M. Rühlig, R. Schäfer, A. Hubert, R. Mosler, J. A. Wolf, S. Demokritov, and P. Grünberg, “Domain Observations on Fe-Cr-Fe Layered Structures. Evidence for a Biquadratic Coupling Effect”, *Phys. Stat. Sol. (a)* **125**, 635 (1991)
- [51] S. O. Demokritov, “Biquadratic interlayer coupling in layered magnetic systems”, *J. Phys. D: Appl. Phys.* **31**, 925 (1998)
- [52] A. Vansteenkiste, J. Leliaert, M. Dvornik, M. Helsen, F. Garcia-Sanchez, and B. Van Waeyenberge, “The design and verification of MuMax3”, *AIP Adv.* **4**, 107133 (2014)
- [53] E. C. Stoner, and E. P. Wohlfarth, “A mechanism of magnetic hysteresis in heterogeneous alloys”, *Phil. Trans. R. Soc. London A* **240**, 599 (1948); reprinted in *IEEE Trans. Magn.* **27**, 3475 (1991)
- [54] C. Tannous and J. Gieraltowski, “The Stoner-Wohlfarth model of Ferromagnetism”, *Eur. J. Phys.* **29**, 475 (2008)
- [55] C. R. Chang, and D. R. Fredkin, “The mechanism of nucleation in uniaxial ferromagnets”, *J. Appl. Phys.* **63**, 3425 (1988)
- [56] Q. Peng, and H. J. Richter, “Analysis of thermal effects in thin-film media”, *J. Appl. Phys.* **93**, 7399 (2003)
- [57] M. J. Freiser, “A Survey of Magneto-Optic Effects”, *IEEE Trans. Magn.* **4**, 152 (1968)
- [58] Z. Q. Qiu, and S. D. Bader, “Surface magneto-optic Kerr effect (SMOKE)”, *J. Magn. Mater.* **200**, 664 (1999)
- [59] Z. Q. Qiu, and S. D. Bader, “Surface magneto-optic Kerr effect”, *Rev. Sci. Instr.* **71**, 1243 (2000)
- [60] W. Kuch, R. Schäfer, P. Fischer, and F. U. Hillebrecht, “Magnetic microscopy of layered structures”, Springer Berlin Heidelberg (2015)
- [61] J. Kerr, “On rotation of the plane of polarization by reflection from the pole of a magnet”, *Philos. Mag.* **3**, 321 (1877)
- [62] J. Kerr, “On reflection of polarized light from the equatorial surface of a magnet”, *Philos. Mag.* **5**, 161 (1878)
- [63] M. Nývlt, “Optical interactions in ultrathin magnetic film structures”, Ph.D. Thesis, Charles University Prague (1996)
- [64] H. R. Hulme “The Faraday effect in ferromagnetics”, *Proc. R. Soc. London, Ser. A* **135**, 237 (1932)
- [65] C. Kittel, “Optical rotation by ferromagnetic substances”, *Phys. Rev.* **83**, 208(A) (1951)
- [66] P. N. Argyres, “Theory of Faraday and Kerr Effects in Ferromagnetics”, *Phys. Rev.* **97**, 334 (1955)
- [67] G. R. Fowles, “Introduction to Modern Optics”, Dover, New York, (1989)
- [68] P. S. Pershan, “Magneto-optical effects,” *J. Appl. Phys.* **38**, 1482 (1967)
- [69] G. Metzger, P. Pluvinage, and R. Torguet, “Termes linéaires et quadratiques dans l’effet magnéto-optique de Kerr”, *Ann. Phys.* **10**, 5 (1965)
- [70] R. P. Hunt, “Magneto-Optic Scattering from Thin Solid Films”, *J. Appl. Phys.* **38**, 1652 (1967)

- [71] C.-Y. You, S.-C. Shin, “Generalized analytic formulae for magneto-optical Kerr effects”, *J. Appl. Phys.* **84**, 541 (1998)
- [72] Š. Višňovský, “Magneto-optical ellipsometry”, *Czech. J. Phys. B* **36**, 625 (1986)
- [73] J. Zak, E. R. Moog, C. Liu, and S. D. Bader, “Magneto-optics of multilayers with arbitrary magnetization directions”, *Phys. Rev. B* **43**, 6423 (1991)
- [74] M. Schubert, “Polarization-dependent optical parameters of arbitrarily anisotropic homogeneous layered systems”, *Phys. Rev. B* **53**, 4265 (1996)
- [75] M. Schubert, T. E. Tiwald, and J. A. Woollam, “Explicit solutions for the optical properties of arbitrary magneto-optic materials in generalized ellipsometry”, *Appl. Opt.* **38**, 177 (1999)
- [76] P. Bruno, Y. Suzuki, and C. Chappert, “Magneto-optical Kerr effect in a paramagnetic overlayer on a ferromagnetic substrate: A spin-polarized quantum size effect”, *Phys. Rev. B* **53**, 9214 (1996)
- [77] J. Hamrle. “Magneto-optical determination of the in-depth magnetization profile in magnetic multilayers”, Ph.D. thesis, University Paris XI, Orsay and Charles University, Prague (2003)
- [78] M. Mansuripur, “The Physical Principles of Magneto-Optical Recording”, Cambridge, Cambridge University Press (1995)
- [79] E. R. Moog, S. D. Bader, “Smoke signals from ferromagnetic monolayers: p(1×1) Fe/Au(100)”, *Superlattices Microstruct.* **1**, 543 (1985)
- [80] C. Liu, and S. D. Bader, “Two-Dimensional Phase Transition of Ultrathin Iron Films on Pd(100)”, *J. Appl. Phys.* **67**, 5758 (1990)
- [81] Z. Q. Qiu, J. Pearson, A. Berger, and S. D. Bader, “Short-period oscillations in the interlayer magnetic coupling of wedged Fe(100)/Mo(100)/Fe(100) grown on Mo(100) by molecular-beam epitaxy”, *Phys. Rev. Lett.* **68**, 1398 (1992)
- [82] Z. Q. Qiu, J. Pearson, and S. D. Bader, “Asymmetry of the spin reorientation transition in ultrathin Fe films and wedges grown on Ag (100)”, *Phys. Rev. Lett.* **70**, 1006 (1993)
- [83] C. Daboo, J. A. C. Bland, R. J. Hicken, A. J. R. Ives, M. J. Baird, and M. J. Walker, “Vectorial magnetometry with the magneto-optic Kerr effect applied to Co/Cu/Co trilayer structures”, *Phys. Rev. B* **47**, 11852 (1993)
- [84] A. Berger, and M. R. Pufall, “Generalized magneto-optical ellipsometry”, *Appl. Phys. Lett.* **71**, 965 (1997)
- [85] P. Vavassori, “Polarization modulation technique for magneto-optical quantitative vector magnetometry”, *Appl. Phys. Lett.* **77**, 1605 (2000)
- [86] J. Hamrle, J. Ferré, M. Nývlt, and Š. Višňovský, “In-depth resolution of the magneto-optical Kerr effect in ferromagnetic multilayers”, *Phys. Rev. B* **66**, 224423 (2002)
- [87] R. Morales, Z.-P. Li, O. Petracic, X. Batlle, I. K. Schuller, J. Olamit, and K. Liu, “Magnetization depth dependence in exchange biased thin films”, *Appl. Phys. Lett.* **89**, 072504 (2006)
- [88] A. Hubert and R. Schäfer, “Magnetic Domains: The Analysis of Magnetic Microstructures”, Springer-Verlag, Berlin (1998)
- [89] J. McCord, “Progress in magnetic domain observation by advanced magneto-optical microscopy”, *J. Phys. D: Appl. Phys.* **48**, 333001 (2015)

- [90] W. Jiang, P. Upadhyaya, W. Zhang, G. Yu, M. B. Jungfleisch, F. Y. Fradin, J. E. Pearson, Y. Tserkovnyak, K. L. Wang, O. Heinonen, S. G. E. te Velthuis, and A. Hoffmann, “Blowing magnetic skyrmion bubbles”, *Science* **349**, 283 (2015)
- [91] E. Nikulina, O. Idigoras, P. Vavassori, A. Chuvilin, and A. Berger, “Magneto-optical magnetometry of individual 30 nm cobalt nanowires grown by electron beam induced deposition”, *Appl. Phys. Lett.* **100**, 142401 (2012)
- [92] D. A. Allwood, G. Xiong, M. D. Cooke, and R. P. Cowburn, “Magneto-optical Kerr effect analysis of magnetic nanostructures”, *J. Phys. D: Appl. Phys.* **36**, 2175 (2003)
- [93] M. Grimsditch, and P. Vavassori, “The diffracted magneto-optic Kerr effect: what does it tell you?”, *J. Phys.: Condens. Matter* **16**, R275 (2004)
- [94] E. Beaurepaire, J.-C. Merle, A. Daunois, and J.-Y. Bigot, “Ultrafast Spin Dynamics in Ferromagnetic Nickel”. *Phys. Rev. Lett.* **76**, 4250 (1996)
- [95] C. D. Stanciu, F. Hansteen, A. V. Kimel, A. Kirilyuk, A. Tsukamoto, A. Itoh, and Th. Rasing, “All-Optical Magnetic Recording with Circularly Polarized Light”, *Phys. Rev. Lett.* **99**, 047601 (2007)
- [96] S. Mangin, M. Gottwald, C.-H. Lambert, D. Steil, V. Uhlíř, L. Pang, M. Hehn, S. Alebrand, M. Cinchetti, G. Malinowski, Y. Fainman, M. Aeschlimann, and E. E. Fullerton, “Engineered materials for all-optical helicity-dependent magnetic switching”, *Nat. Mater.* **13**, 286 (2014)
- [97] C.-H. Lambert, S. Mangin, B. S. D. Ch. S. Varaprasad, Y. K. Takahashi, M. Hehn, M. Cinchetti, G. Malinowski, K. Hono, Y. Fainman, M. Aeschlimann, and E. E. Fullerton, “All-optical control of ferromagnetic thin films and nanostructures”, *Science* **345**, 1337 (2014)
- [98] J. Gorchon, C. H. Lambert, Y. Yang, A. Pattabi, R. B. Wilson, S. Salahuddin, and J. Bokor, “Single shot ultrafast all optical magnetization switching of ferromagnetic Co/Pt multilayers”, *Appl. Phys. Lett.* **111**, 042401 (2017)
- [99] T. Higo, H. Man, D. B. Gopman, L. Wu, T. Koretsune, O. M. J. van ’t Erve, Y. P. Kabanov, D. Rees, Y. Li, M.-T. Suzuki, S. Patankar, M. Ikhlas, C. L. Chien, R. Arita, R. D. Shull, J. Orenstein, and S. Nakatsuji., “Large magneto-optical Kerr effect and imaging of magnetic octupole domains in an antiferromagnetic metal”, *Nat. Photon.* **12**, 73 (2018)
- [100] V. Saidl, P. Němec, P. Wadley, V. Hills, R. P. Campion, V. Novák, K. W. Edmonds, F. Maccherozzi, S. S. Dhesi, B. L. Gallagher, F. Trojánek, J. Kuneš, J. Železný, P. Malý, and T. Jungwirth, “Optical determination of the Néel vector in a CuMnAs thin-film antiferromagnet”, *Nat. Photon.* **11**, 91 (2017)
- [101] Z. Zheng, J. Y. Shi, Q. Li, T. Gu, H. Xia, L. Q. Shen, F. Jin, H. C. Yuan, Y. Z. Wu, L. Y. Chen, and H. B. Zhao, “Magneto-optical probe of ultrafast spin dynamics in antiferromagnetic CoO thin films”, *Phys. Rev. B* **98**, 134409 (2018)
- [102] J. Xu, C. Zhou, M. Jia, D. Shi, C. Liu, H. Chen, G. Chen, G. Zhang, Y. Liang, J. Li, W. Zhang, and Y. Wu, “Imaging antiferromagnetic domains in nickel oxide thin films by optical birefringence effect”, *Phys. Rev. B* **100**, 134413 (2019)
- [103] Y. K. Kato, R. C. Myers, A. C. Gossard, D. D. Awschalom, “Observation of the Spin Hall Effect in Semiconductors”, *Science* **306**, 1910 (2004)
- [104] C. Stamm, C. Murer, M. Berritta, J. Feng, M. Gabureac, P. M. Oppeneer, and P. Gambardella, “Magneto-Optical Detection of the Spin Hall Effect in Pt and W Thin Films”, *Phys. Rev. Lett.* **119**, 087203 (2017)
- [105] V. V. Temnov, G. Armelles, U. Woggon, D. Guzatov, A. Cebollada, A. Garcia-Martin, J. M. Garcia-Martin, T. Thomay, A. Leitenstorfer, and R. Bratschitsch, “Active magneto-plasmonics in hybrid metal–ferromagnet structures”, *Nat. Photon.* **4**, 107 (2010)

- [106] G. Armelles, A. Cebollada, A. García-Martín, and M. U. González, “Magnetoplasmonics: Combining Magnetic and Plasmonic Functionalities”, *Adv. Opt. Mater.* **1**, 10 (2013)
- [107] S. D. Pappas, P. Lang, T. Eul, M. Hartelt, A. García-Martín, B. Hillebrands, M. Aeschlimann, E. Th. Papaioannou, “Near-field mechanism of the enhanced broadband magneto-optical activity of hybrid Au loaded Bi: YIG”, *Nanoscale* **12**, 7309 (2020)
- [108] D. L. Smith, “Thin-Film Deposition: Principles and Practice”, McGraw-Hill Inc., New York (1995)
- [109] R. V. Stuart, “Vacuum Technology, Thin Films, and Sputtering. An Introduction”, Academic Press, New York (2012)
- [110] P. J. Kelly, and R. D. Arnell, “Magnetron sputtering: a review of recent developments and applications”, *Vacuum* **56**, 159 (2000)
- [111] <http://www.ajaint.com/whatis.htm>
- [112] O. Idigoras, “Magnetization reversal behavior of ferromagnetic thin films and nano-structures”, Ph.D. Thesis, University of the Basque Country (2013)
- [113] B. C. Schwartz, R. D. Silkensen, and G. Steving, “RF bias sputtering method for producing insulating films free of surface irregularities”, *US Patent No.* 4036723 (1977)
- [114] G. A. Prinz, “Stabilization of bcc Co via Epitaxial Growth on GaAs”, *Phys. Rev. Lett.* **54**, 1051 (1985)
- [115] J. A. Nielsen, D. McMorrow, “Elements of Modern X-ray Physics”, Wiley (2001)
- [116] M. Birkholz, “Thin film analysis by x-ray scattering”, Wiley-VCH, Weinheim (2006)
- [117] M. Björck, and G. Andersson, “GenX: an extensible X-ray reflectivity refinement program utilizing differential evolution”, *J. Appl. Cryst.* **40**, 1174 (2007)
- [118] C. D. Graham, “High-Sensitivity Magnetization Measurements”, *J. Mater. Sci. Technol.* **16**, 97 (2000)
- [119] R. M. A. Azzam and N. M. Bashara, “Ellipsometry and Polarized Light”, North Holland, Amsterdam, (1977)
- [120] T. Hofmann, C. M. Herzinger, A. Boosalis, T. E. Tiwald, J. A. Woollam, and M. Schubert, “Variable-wavelength frequency-domain terahertz ellipsometry”, *Rev. Sci. Instr.* **81**, 023101 (2010)
- [121] P. B. Johnson, and R. W. Christy, “Optical Constants of the Noble Metals”, *Phys. Rev. B* **6**, 4370 (1972)
- [122] H.G. Tompkins, and E.A. Irene (Eds.), “Handbook of Ellipsometry”, Springer, Berlin (2005)
- [123] W. J. M. A. Geerts, J. C. Lodder, and Th. J. A. Popma, “A combined optical and magneto-optical measurement system”, *Rev. Sci. Instrum.* **63**, 1805 (1992)
- [124] Z. Celinski, and Z. Yan, “Dielectric tensor characterization of  $\text{Mn}_{0.53}\text{Bi}_{0.47}$  and  $\text{Mn}_{0.52}\text{Bi}_{0.44}\text{Sb}_{0.04}$  films”, *J. Appl. Phys.* **79**, 6200 (1996)
- [125] P. Q. J. Nederpel, and J. W. D. Martens, “Magneto-optical ellipsometer”, *Rev. Sci. Instrum.* **56** 687 (1985)
- [126] W. A. McGahan, L.-Y. Chen, and J. A. Woollam, “Variable angle of incidence analysis of magneto-optic multilayers”, *J. Appl. Phys.* **67** (1990)

- [127] X. Gao, D. W. Glenn, S. Heckens, D. W. Thompson, and J. A. Woollam, “Spectroscopic ellipsometry and magneto-optic Kerr effects in Co/Pt multilayers”, *J. Appl. Phys.* **82**, 4525 (1997)
- [128] A. Berger, and M. R. Pufall, “Quantitative vector magnetometry using generalized magneto-optical ellipsometry”, *J. Appl. Phys.* **85**, 4583 (1999)
- [129] P. Yeh, “Optics of anisotropic layered media: a new 4 x 4 matrix algebra”, *Surf. Sci.* **96**, 41 (1980)
- [130] M. R. Pufall, and A. Berger, “Studying the reversal mode of the magnetization vector versus applied field angle using generalized magneto-optical ellipsometry”, *J. Appl. Phys.* **87**, 5834 (2000)
- [131] G. Neuber, R. Rauer, J. Kunze, T. Korn, C. Pels, G. Meier, U. Merkt, J. Bäckström, and M. Rübhausen, “Temperature-dependent spectral generalized magneto-optical ellipsometry”, *Appl. Phys. Lett.* **83**, 4509 (2003)
- [132] M. Bastjan, S. G. Singer, G. Neuber, S. Eller, N. Aliouane, D. N. Argyriou, S. L. Cooper, and M. Rübhausen, “Magneto-optical study of the spin-polarized electronic states in multiferroic TbMnO<sub>3</sub>”, *Phys. Rev. B* **77**, 193105 (2008)
- [133] K. Mok, G. J. Kovács, J. McCord, L. Li, M. Helm, and H. Schmidt, “Magneto-optical coupling in ferromagnetic thin films investigated by vector-magneto-optical generalized ellipsometry”, *Phys. Rev. B* **84**, 094413 (2011)
- [134] D. Schmidt, T. Hofmann, C. M. Herzinger, E. Schubert, and M. Schubert, “Magneto-optical properties of cobalt slanted columnar thin films”, *Appl. Phys. Lett.* **96**, 091906 (2010)
- [135] D. Schmidt, C. Briley, E. Schubert, and M. Schubert, “Vector magneto-optical generalized ellipsometry for sculptured thin-fims”, *Appl. Phys. Lett.* **102**, 123109 (2013)
- [136] C. Briley, D. Schmidt, T. Hofmann, E. Schubert, and M. Schubert, “Anisotropic magneto-optical hysteresis of permalloy slanted columnar thin films determined by vector magneto-optical generalized ellipsometry”, *Appl. Phys. Lett.* **106**, 133104 (2015)
- [137] J. M. Florczak, and E. Dan Dahlberg, “Magnetization reversal in (100) Fe thin films”, *Phys. Rev. B* **44**, 9338 (1991)
- [138] Z. J. Yang, and M. R. Scheinfein, “Combined three-axis surface magneto-optical Kerr effects in the study of surface and ultrathin-film magnetism”, *J. Appl. Phys.* **74**, 6810 (1993)
- [139] H. F. Ding, S. Pütter, H. P. Oepen, and J. Kirschner, “Experimental method for separating longitudinal and polar Kerr signals”, *J. Magn. Magn. Mater.* **212**, 5 (2000)
- [140] J.-W. Lee, J. Kim, S.-K. Kim, J.-R. Jeong, and S.-C. Shin, “Full vectorial spin-reorientation transition and magnetization reversal study in ultrathin ferromagnetic films using magneto-optical Kerr effects”, *Phys. Rev. B* **65**, 144437 (2002)
- [141] S.-C. Shin, J.-W. Lee, S.-K. Kim, and J. Kim, “In situ vectorial magnetization reversal study of ultrathin Co films on Pd (111) using magneto-optical Kerr effects”, *Appl. Phys. Lett.* **81**, 91 (2002)
- [142] J. M. Teixeira, R. Lusche, J. Ventura, R. Fermento, F. Carpinteiro, J. P. Araujo, J. B. Sousa, S. Cardoso, and P. P. Freitas, “Versatile, high sensitivity, and automatized angular dependent vectorial Kerr magnetometer for the analysis of nanostructured materials”, *Rev. Sci. Instrum.* **82**, 043902 (2012)

- [143] E. Jiménez, N. Mikuszeit, J. L. F. Cuñado, P. Perna, J. Pedrosa, D. Maccariello, C. Rodrigo, M. A. Niño, A. Bollero, J. Camarero, and R. Miranda, “Vectorial Kerr magnetometer for simultaneous and quantitative measurements of the in-plane magnetization components”, *Rev. Sci. Instrum.* **85**, 053904 (2014)
- [144] G. Traeger, L. Wenzel, and A. Hubert, “Magneto-optical Effects in Non-Uniformly Magnetized Media”, *IEEE Trans. Magn.* **29**, 3408 (1993)
- [145] T. Verduci, C. Rufo, A. Berger, V. Metlushko, B. Ilic, and P. Vavassori, *Appl. Phys. Lett.* **99**, 092501 (2011)
- [146] J. A. Arregi, J. B. González-Díaz, E. Bergaretxe, O. Idigoras, T. Unsal, and A. Berger, “Study of generalized magneto-optical ellipsometry reliability”, *J. Appl. Phys.* **111**, 103912 (2012)
- [147] P. R. Bevington, and D. K. Robinson “Data Reduction and Error Analysis for the Physical Sciences” (3rd Ed.), McGraw-Hill (2002)
- [148] W. Yang, D. N. Lambeth, and D. E. Laughlin, “Unicrystal Co-alloy media on Si (110)”, *J. Appl. Phys.* **85**, 4723 (1999)
- [149] O. Idigoras, P. Vavassori, J.M. Porro, and A. Berger, “Kerr microscopy study of magnetization reversal in uniaxial Co-films”, *J. Magn. Magn. Mater.* **322**, L57 (2010)
- [150] O. Idigoras, A. K. Suszka, P. Vavassori, P. Landeros, J. M. Porro, and A. Berger, “Collapse of hard-axis behavior in uniaxial Co films”, *Phys. Rev. B* **84**, 132403 (2011)
- [151] P. B. Johnson, and R. W. Christy, “Optical constants of transition metals: Ti, V, Cr, Mn, Fe, Co, Ni, and Pd”, *Phys. Rev. B* **9**, 5056 (1974)
- [152] A. K. Suszka, O. Idigoras, E. Nikulina, A. Chuvilin, and A. Berger, “Crystallography-Driven Positive Exchange Bias in Co/CoO Bilayers”, *Phys. Rev. Lett.* **109**, 177205 (2012)
- [153] J. B. González-Díaz, J. A. Arregi, E. Bergaretxe, M. J. Fertin, O. Idigoras, and A. Berger, “Anomalous magneto-optical behavior of uniaxial Co/CoO bilayer films”, *J. Magn. Magn. Mater.* **325**, 147 (2013)
- [154] L. Néel, “Anisotropie magnétique superficielle et surstructures d'orientation”, *J. Phys. Radium* **15**, 225 (1954)
- [155] R. Wu, and A. J. Freeman, “Spin-orbit induced magnetic phenomena in bulk metals and their surfaces and interfaces”, *J. Magn. Magn. Mater.* **200**, 498 (1999)
- [156] E. A. Ganshina, G. S. Krinchik, L. S. Mironova, and A. S. Tablin, “Anisotropy of the magneto-optical properties of cobalt single crystals”, *Sov. Phys. JETP* **51**, 329 (1980)
- [157] D. Weller, G. R. Harp, R. F. C. Farrow, A. Cebollada, and J. Sticht, “Orientation dependence of the polar Kerr effect in fcc and hcp Co”, *Phys. Rev. Lett.* **72**, 2097 (1994)
- [158] Th. Hermann, K. Lüdge, W. Richter, K. G. Georgarakis, P. Pouloupoulos, R. Nünthel, J. Lindner, M. Wahl, and N. Esser, “Optical anisotropy and magneto-optical properties of Ni on preoxidized Cu(110)”, *Phys. Rev. B* **73**, 134408 (2006)
- [159] G. S. Krinchik, E. A. Ganshina, and V. S. Gushchin, “Orientation magneto-optic effect in nickel and ferrosilicon monocrystals”, *Sov. Phys. JETP* **33**, 115 (1971)
- [160] G. S. Krinchik, E. A. Ganshina, and V. S. Gushchin, “Anisotropy of magneto-optical orientation effect in single crystal of nickel”, *J. Physique* **32**, C1-1061 (1971)
- [161] Yu. A. Uspenskii, E. T. Kulatov, and S. V. Halilov, “Effect of anisotropy on magneto-optical properties of uniaxial crystals: Application to CrO<sub>2</sub>”, *Phys. Rev. B* **54**, 474 (1996)

- [162] L. Uba, S. Uba, V. N. Antonov, A. N. Yaresko, T. Ślęzak, and J. Korecki, “Magneto-optical anisotropy study of Fe<sub>n</sub>/Au<sub>n</sub> superlattices”, *Phys. Rev. B* **62**, 13731 (2000)
- [163] J. Ğrondilova, M. Rickart, J. Mistrík, K. Postava, Š. Višňovský, T. Yamaguchi, R. Lopušnik, S. O. Demokritov, and B. Hillebrands, “Anisotropy of magneto-optical spectra in ultrathin Fe/au/Fe bilayers”, *J. Appl. Phys.* **91**, 8246 (2002)
- [164] R. M. Osgood III, K. T. Riggs, A. E. Johnson, J. E. Mattson, C. H. Sowers, and S. D. Bader, “Magneto-optic constants of hcp and fcc Co films”, *Phys. Rev. B* **56**, 2627 (1997)
- [165] H. Rathgen, M. I. Katsnelson, O. Eriksson, and G. Zwicknagl, “Polar magneto-optical Kerr effect for low-symmetric ferromagnets”, *Phys. Rev. B* **72**, 014451 (2005)
- [166] J. B. Kortright and S.-K. Kim, “Resonant magneto-optical properties of Fe near its 2p levels: Measurement and applications”, *Phys. Rev. B* **62**, 12216 (2000)
- [167] M. Vomir, L. H. F. Andrade, L. Guidoni, E. Beaurepaire, and J.-Y. Bigot, “Real space trajectory of the ultrafast magnetization dynamics in ferromagnetic metals”, *Phys. Rev. Lett.* **94**, 237601 (2005)
- [168] <http://refractiveindex.info> via (1) D. T. Pierce and W. E. Spicer, “Electronic structure of amorphous Si from photoemission and optical studies”, *Phys. Rev. B* **5**, 3017 (1972) & (2) “Handbook of Optical Constants of Solids” (Ed. E. D. Palik), Academic Press, Boston (1985)
- [169] J. W. Matthews, and J. L. Crawford, “Accommodation of misfit between single-crystal films of nickel and copper”, *Thin Solid Films* **5**, 187 (1970)
- [170] D. Sander, S. Ouazi, A. Enders, Th. Gutjahr-Löser, V. S. Stepanyuk, D. I. Bazhanov and J. Kirschner, “Stress, strain and magnetostriction in epitaxial films”, *J. Phys.: Condens. Matter* **14**, 4165 (2002)
- [171] T. Pan, G. W. D. Spratt, L. Tang, and D. E. Laughlin, “Magnetic properties of evaporated Co oxide tape media”, *J. Magn. Magn. Mater.*, **155**, 309 (1996)
- [172] C. Chappert, and P. Bruno, “Magnetic anisotropy in metallic ultrathin films and related experiments on cobalt films”, *J. Appl. Phys.* **64**, 5736 (1988)
- [173] D. Sander, “The magnetic anisotropy and spin reorientation of nanostructures and nanoscale films”, *J. Phys. Condens. Matter* **16**, R603 (2004)
- [174] M. R. Parker, “Magneto-optical anisotropy in nickel”, *Phys. Stat. Sol. (b)* **49**, 299 (1972)
- [175] K. Postava, D. Hrabovský, J. Pištora, A. R. Fert, Š. Višňovský, and T. Yamaguchi, “Anisotropy of quadratic magneto-optic effects in reflection”, *J. Appl. Phys.* **91**, 7293 (2002)
- [176] A. V. Pethukov, Th. Rasing, T. Katayama, N. Nakajima, and Y. Suzuki, “Anisotropic third-order magneto-optical Kerr effect”, *J. Appl. Phys.* **83** (1998)
- [177] R. M. Osgood III, B. M. Clemens, and R. L. White, “Asymmetric magneto-optic response in anisotropic thin films”, *Phys. Rev. B* **55**, 8990 (1997)
- [178] G. Y. Guo, and H. Ebert, “Theoretical investigation of the orientation dependence of the magneto-optical Kerr effect in Co”, *Phys. Rev. B* **50**, 10377 (1994)
- [179] P. M. Oppeneer, T. Kraft, and H. Eschrig, “Anisotropic magneto-optical Kerr effect of hcp and fcc Co from first principles”, *Phys. Rev. B* **52**, 3577 (1995)
- [180] W. Yang, D. N. Lambeth, and D. E. Laughlin, “Dependence of Co anisotropy constants on temperature, processing, and underlayer”, *J. Appl. Phys.* **87**, 6884 (2000)
- [181] V. Sokalski, D. E. Laughlin, and J.-G. Zhu, “Magnetic anisotropy and stacking faults in Co and Co<sub>84</sub>Pt<sub>16</sub> epitaxially grown thin films”, *J. Appl. Phys.* **110**, (2011)

- [182] N. Kikuchi, O. Kitakami, S. Okamoto, Y. Shimada, A. Sakuma, Y. Otani, and K. Fukamichi, "Influence of 5d transition elements on the magnetocrystalline anisotropy of hcp-Co", *J. Phys.: Condens. Matter* **11**, L485 (1999)
- [183] T. Shimatsu, Y. Okazaki, H. Sato, H. Muraoka, H. Aoi, T. Sakurai, S. Okamoto, O. Kitakami, S. Tanii, and A. Sakuma, "Uniaxial magnetic anisotropy in Co and Co-Pt based perpendicular films in relation to lattice deformation", *J. Appl. Phys.* **103**, 07F524 (2008)
- [184] J.-J. Wang, T. Sakurai, K. Ishida, N. Kikuchi, S. Okamoto, H. Sato, T. Shimatsu, and O. Kitakami, "Magnetic anisotropy of epitaxially grown Co and its alloy thin films", *J. Phys.: Condens. Matter* **21**, 185008 (2009)
- [185] G. H. O. Daalderop, P. J. Kelly, and M. F. H. Schuurmans, "First-principles calculation of the magnetocrystalline anisotropy energy density of iron, cobalt and nickel", *Phys. Rev. B* **41**, 11919 (1990)
- [186] A. Sakuma, "First Principle Calculation of the Magnetocrystalline Anisotropy Energy of FePt and CoPt Ordered Alloys", *J. Phys. Soc. Jap.* **63**, 3053 (1994)
- [187] P. Krams, B. Hillebrands, G. Güntherodt, and H. P. Oepen, "Magnetic anisotropies of ultrathin Co films on Cu(1 1 13) substrates", *Phys. Rev. B* **49**, 3633 (1994)
- [188] H. Fritzsche, J. Kohlhepp, and U. Gradmann, "Epitaxial strain and magnetic anisotropy in ultrathin Co films on W(110)", *Phys. Rev. B* **51**, 15933 (1995)
- [189] W. Weber, A. Bischof, R. Allenspach, C. H. Back, J. Fassbender, U. May, B. Schirmer, R. M. Jungblut, G. Güntherodt, and B. Hillebrands, "Structural relaxation and magnetic anisotropy in Co/Cu(001) films", *Phys. Rev. B* **54**, 4075 (1996)
- [190] O. Idigoras, A. K. Suszka, P. Vavassori, B. Obry, B. Hillebrands, P. Landeros, and A. Berger, "Magnetization reversal of in-plane uniaxial Co films and its dependence on epitaxial alignment", *J. Appl. Phys.* **115**, 083912 (2014)
- [191] R. N. Tait, T. Smy, and M. J. Brett, "Structural anisotropy in oblique incidence thin metal films", *J. Vac. Sci. Technol. A* **10**, 1518 (1992)
- [192] L. Abelman, and C. Lodder, "Oblique evaporation and surface diffusion", *Thin Solid Films* **305**, 1 (1997)
- [193] J. A. Arregi, J. B. González-Díaz, O. Idigoras, and A. Berger, "Strain-induced magneto-optical anisotropy in epitaxial hcp Co- films", *Phys. Rev. B* **92**, 184405(2015)
- [194] M. Krawczyk, and D. Grundler, "Review and prospects of magnonic crystals and devices with reprogrammable band structure", *J. Phys.: Condens. Matter* **26**, 123202 (2014)
- [195] L. J. Heyderman, and R. L. Stamps, "Artificial ferroic systems: novel functionality from structure, interactions and dynamics", *J. Phys.: Condens. Matter* **25**, 363201 (2013)
- [196] S. A. Nikitov, Ph. Tailhades, and C. S. Tsai, "Spin waves in periodic magnetic structures – magnonic crystals", *J. Magn. Magn. Mater.* **236**, 320 (2001)
- [197] I. L. Lyubchanskii, N. N. Dadoenkova, M. I. Lyubchanskii, E. A. Shapobalov, and Th. Rasing, *Magneto-photonic crystals*, *J. Phys. D: Appl. Phys.* **36**, R277 (2002)
- [198] G. Gubbiotti, S. Tacchi, G. Carlotti, N. Singh, S. Goolaup, A. O. Adeyeye, and M. Kostylev, "Collective spin modes in monodimensional magnonic crystals consisting of dipolarly coupled nanowires", *Appl. Phys. Lett.* **90**, 092503 (2007)
- [199] M. P. Kostylev, G. Gubbiotti, J.-G. Hu, G. Carlotti, T. Ono, and R. L. Stamps, "Dipole-exchange propagating spin-wave modes in metallic ferromagnetic stripes", *Phys. Rev. B* **76**, 054422 (2007)

- [200] J. Topp, D. Heitmann, M. P. Kostylev, and D. Grundler, “Making a Reconfigurable Artificial Crystal by Ordering Bistable Magnetic Nanowires”, *Phys. Rev. Lett.* **104**, 207205 (2010)
- [201] A. V. Chumak, T. Neumann, A. A. Serga, B. Hillebrands, and M. P. Kostylev, “A current-controlled, dynamic magnonic crystal”, *J. Phys. D.: Appl. Phys.* **42**, 205005 (2009)
- [202] N. Kostylev, I. S. Maksymov, A. O. Adeyeye, S. Samarin, M. Kostylev, and J. F. Williams, “Plasmon-assisted high reflectivity and strong magneto-optical Kerr effect in permalloy gratings”, *Appl. Phys. Lett.* **102**, 121907 (2013)
- [203] S. Mathias, C. La-O-Vorakiat, P. Grychtol, P. Granitzka, E. Turgut, J. M. Shaw, R. Adam, H. T. Nembach, M. E. Siemens, S. Eich, C. M. Schneider, T. J. Silva, M. Aeschlimann, M. M. Murnane, and H. C. Kapteyn, “Probing the timescale of the exchange interaction in a ferromagnetic alloy”, *Proc. Natl. Acad. Sci. U.S.A.* **109**, 4792 (2012)
- [204] J. B. González-Díaz, J. A. Arregi, A. Martínez-de-Guerenu, F. Arizti, and A. Berger, “Quantitative magneto-optical characterization of diffusive reflected light from rough steel samples”, *J. Appl. Phys.* **113**, 153904 (2013)
- [205] D. Atkinson, D. A. Allwood, G. Xiong, M. D. Cooke, C. C. Faulkner, and R. P. Cowburn, “Magnetic domain-wall dynamics in a submicrometre ferromagnetic structure”, *Nat. Mater.* **2**, 85 (2003)
- [206] A. Westphalen, M.-S. Lee, A. Remhof, and H. Zabel, “Vector and Bragg Magneto-optical Kerr effect for the analysis of nanostructured magnetic arrays”, *Rev. Sci. Instrum.* **78**, 121301 (2007)
- [207] A. Yariv, and P. Yeh, “Electromagnetic propagation in periodic stratified media. II. Birefringence, phase matching, and x-ray lasers”, *J. Opt. Soc. Am.* **67**, 438 (1977)
- [208] D. C. Flanders, “Submicrometer periodicity gratings as artificial anisotropic dielectrics”, *Appl. Phys. Lett.* **42**, 492 (1983)
- [209] C. Yang, and P. Yeh, “Artificial uniaxial and biaxial dielectrics with the use of photoinduced gratings”, *J. Appl. Phys.* **81**, 23 (1997)
- [210] M. Born and E. Wolf, “Principles of Optics” (7<sup>th</sup> edition), p. 837, Cambridge University Press, New York (1999)
- [211] I. Richter, P.-C. Sun, F. Xu, and Y. Fainman, “Design considerations of form birefringent microstructures”, *Appl. Opt.* **34**, 2421 (1995)
- [212] F. Xu, R.-C. Tyan, P.-C. Sun, Y. Fainman, C.-C. Chen, and A. Scherer, “Fabrication, modeling, and characterization of form birefringent nanostructures”, *Opt. Lett.* **20**, 2457 (1995)
- [213] Y. M. Strelniker, and D. J. Bergman, “Strong angular magneto-induced anisotropy of Voigt effect in metal-dielectric metamaterials with periodic nanostructures”, *Phys. Rev. B* **89** 125312 (2014)
- [214] D. W. Thompson, M. J. DeVries, T. E. Tiwald, and J. A. Woollam, “Determination of optical anisotropy in calcite from ultraviolet to mid-infrared by generalized ellipsometry”, *Thin Solid Films* **313-314**, 341 (1998)
- [215] G. E. Jellison Jr., L. A. Boatner, J. D. Budai, B.-S. Jeong, and D. P. Norton, “Spectroscopic ellipsometry of thin film and bulk anatase (TiO<sub>2</sub>)”, *J. Appl. Phys.* **93**, 9537 (2003)
- [216] J. Kranz, and Ch. Schrödter, “Measuring the Magneto-optic Kerr Effect by Diffraction”, *Appl. Phys. A* **31**, 59 (1983)

- [217] O. Geoffroy, D. Givord, Y. Otani, B. Pannetier, A. D. Santos, and M. Schlenker, *J. Magn. Magn. Mater.* **121**, 516 (1993)
- [218] P. Vavassori, V. Metlushko, R. M. Osgood III, M. Grimsditch, U. Welp, G. Crabtree, W. Fan, S. R. J. Bueck, B. Ilic, and P. Hesketh, "Magnetic information in the light diffracted by a negative dot array of Fe", *Phys. Rev. B* **59**, 6337 (1999)
- [219] P. Vavassori, M. Grimsditch, V. Novosad, V. Metlushko, and B. Ilic, "Metastable states during magnetization reversal in square permalloy rings", *Phys. Rev. B* **67**, 134429 (2003)
- [220] P. Vavassori, N. Zaluzec, V. Metlushko, V. Novosad, B. Ilic, and M. Grimsditch, "Magnetization reversal via single and double vortex states in submicron Permalloy ellipses", *Phys. Rev. B* **69**, 214404 (2004)
- [221] R.A. Azzam, and N. M. Bashara, "Polarization Characteristics of Scattered Radiation from a Diffraction Grating by Ellipsometry with Application to Surface Roughness", *Phys. Rev. B* **5** 4721 (1972)
- [222] Q. Xie, M.H. Hong, H.L. Tan, G.X. Chen, L.P. Shi, and T.C. Chong, "Fabrication of nanostructures with laser interference lithography", *J. Alloys Compd.* **449**, 261 (2006)
- [223] C. Redondo, S. Moralejo, F. Castaño, W. Lee, K. Nielsch, C. A. Ross, and F. J. Castaño, "Additive patterning of ion-beam-sputtered non-conformal Ni<sub>80</sub>Fe<sub>20</sub> and Co<sub>70</sub>Fe<sub>30</sub> magnetic films", *Nanotechnology* **17**, 2040 (2006)
- [224] V. Novosad, Y. Souche, V. Pishko, T. Crozes, Y. Otani, and K. Fukamichi, "Magneto-optical Kerr effect in conical diffraction geometry of micron-sized Fe<sub>3</sub>Si wire array", *IEEE Trans. Mag.* **35**, 3145 (1999)
- [225] R. Antos, J. Mistrik, T. Yamaguchi, Š. Višňovský, S. O. Demokritov, and B. Hillebrands, "Evidence of native oxides on the capping and substrate of Permalloy gratings by magneto-optical spectroscopy in the zeroth- and first-diffraction orders", *Appl. Phys. Lett.* **86**, 231101 (2005)
- [226] R. Antos, J. Mistrik, T. Yamaguchi, S. Visnovsky, S.O. Demokritov, and B. Hillebrands, "Evaluation of the quality of Permalloy gratings by diffracted magneto-optical spectroscopy," *Opt. Express* **13**, 4651 (2005)
- [227] R. Antos, J. Mistrik, T. Yamaguchi, M. Veis, E. Liskova, S. Visnovsky, J. Pistora, B. Hillebrands, S. O. Demokritov, T. Kimura, and Y. Otani, "Magneto-optical spectroscopic scatterometry for analyzing patterned magnetic nanostructures," *J. Magn. Soc. Jpn.* **30**, 630 (2006)
- [228] Y. Suzuki, C. Chappert, P. Bruno, and P. Veillet, "Simple model for the magneto-optical Kerr diffraction of a regular array of magnetic dots", *J. Magn. Magn. Mater.* **165**, 516 (1997)
- [229] D. E. Aspnes, "Approximate solution of ellipsometric equations for optically biaxial crystals", *J. Opt. Soc. Am.* **70**, 1275 (1980)
- [230] G. E. Jellison Jr., and J. S. Baba, "Pseudodielectric functions of uniaxial materials in certain symmetry directions", *J. Opt. Soc. Am. A* **23**, 468 (2006)
- [231] T. Schmitte, T. Schemberg, K. Westerholt, H. Zabel, K. Schindler, and U. Kunze, "Magneto-optical Kerr effects of ferromagnetic Ni-gratings", *J. Appl. Phys.* **87**, 5630 (2000)
- [232] J. B. Kim, Y. H. Lu, M. H. Cho, G. J. Lee, Y. P. Lee, J. Y. Rhee, and C.S. Yoon, "Diffracted magneto-optical Kerr effect in one-dimensional magnetic gratings", *Appl. Phys. Lett.* **94**, 151110 (2009)

- [233] T. Schmitte, K. Theis-Bröhl, V. Leiner, H. Zabel, S. Kirsch, and A. Carl, “Magneto-optical study of the magnetization reversal process of Fe nanowires”, *J. Phys.: Condens. Matter* **14**, 7525 (2002)
- [234] K. Theis-Bröhl, K. T. Schmitte, V. Leiner, H. Zabel, K. Rott, H. Brückl, and J. McCord, CoFe stripes: “Magnetization reversal study by polarized neutron scattering and magneto-optical Kerr effect”, *Phys. Rev. B* **67**, 184415 (2003)
- [235] J. A. Arregi, J. B. González-Díaz, N. Soriano, B. Mora, and A. Berger, “Surface-topography induced optical and magneto-optical anisotropy of permalloy gratings”, *J. Phys. D: Appl. Phys.* **48**, 305002 (2015)
- [236] P. Grünberg, “Layered magnetic structures: History, highlights, applications”, *Physics Today* **54**, 31 (2001)
- [237] F. J. Himpsel, J.E. Ortega, G.J. Mankey, and R.F. Willis, “Magnetic Nanostructures”, *Advances in Physics* **47**, 511 (1997)
- [238] P. Bruno, and C. Chappert, “Oscillatory Coupling between Ferromagnetic Layers Separated by a Nonmagnetic Metal Spacer”, *Phys. Rev. Lett.* **67**, 1602 (1991)
- [239] Z. Q. Qiu, J. Pearson, and S. D. Bader, “Oscillatory interlayer magnetic coupling of wedged Co/Cu/Co sandwiches grown on Cu(100) by molecular beam epitaxy”, *Phys. Rev. B* **46**, 8659(R) (1992)
- [240] J. E. Ortega, F. J. Himpsel, “Quantum well states as mediators of magnetic coupling in superlattices”, *Phys. Rev. Lett.* **69**, 844 (1992)
- [241] J. E. Ortega, F. J. Himpsel, G. J. Mankey, R. F. Willis, “Quantum-well states and magnetic coupling between ferromagnetic through a noble metal layer”, *Phys. Rev. B* **47**, 1540 (1993)
- [242] P. Bruno, “Interlayer exchange coupling: a unified physical picture”, *J. Magn. Magn. Mater.* **121**, 248 (1993)
- [243] F. J. Himpsel, “Magnetic Quantum Wells” *J. Phys.: Condens. Matter* **11**, 9483 (1999)
- [244] S.D. Bader, Dongqi Li, “Magneto-optical and photoemission studies of ultrathin wedges”, *J. Magn. Magn. Mater.* **156**, 153 (1996)
- [245] W. R. Bennett, W. Schwarzacher, and W. F. Egelhoff, Jr., “Concurrent Enhancement of Kerr Rotation and Antiferromagnetic Coupling in Epitaxial Fe/Cu/Fe Structures”, *Phys. Rev. Lett.* **65**, 3169 (1990)
- [246] W. Geerts, Y. Suzuki, T. Katayama, K. Tanaka, K. Ando, and S. Yoshida, “Thickness-dependent oscillation of the magneto-optical properties of Au-sandwiched (001) Fe films”, *Phys. Rev. B* **50**, 12581 (1994)
- [247] Y. Suzuki, T. Katayama, S. Yoshida, K. Tanaka, and K. Sato, “New Magneto-Optical Transition in Ultrathin Fe(100) films”, *Phys. Rev. Lett.* **68**, 3355 (1992)
- [248] A. Carl and D. Weller, “Short period oscillations in the Kerr effect of 4d- and 5d-transition metal wedges on Co films”, *J. Appl. Phys.* **76**, 6116 (1994)
- [249] D. Weller and A. Carl, “Oscillatory Paramagnetic Magneto-Optical Kerr Effect in Ru Wedges on Co”, *Phys. Rev. Lett.* **75**, 190 (1995)
- [250] Y. Suzuki, T. Katayama, P. Bruno, S. Yuasa, and E. Tamura, “Oscillatory Magneto-Optical Effect in a Au (001) Film Deposited on Fe: Experimental Confirmation of a Spin-Polarized Quantum Size Effect”, *Phys. Rev. Lett.* **80**, 5200 (1998)

- [251] B. N. Engel, M. H. Wiedmann, R. A. Van Leeuwen, and C. M. Falco, “Anomalous magnetic anisotropy in ultrathin transition metals”, *Phys. Rev. B* **48**, 9894(R) (1993)
- [252] C. H. Back, W. Weber, Ch. Würsch, A. Bischof, D. Pescia, R. Allenspach, “Magnetic anisotropy oscillations”, *J. Appl. Phys.* **81**, 5054 (1997)
- [253] G. Traeger, L. Wenzel, and A. Hubert, “Computer Experiments on the Information Depth and Figure of Merit in Magneto-optics”, *phys. stat. sol. (a)* **131**, 201 (1992)
- [254] A. Hrabec, N. A. Porter, A. Wells, M. J. Benitez, G. Burnell, S. McVitie, D. McGrouther, T. A. Moore, and C. H. Marrows, “Measuring and tailoring the Dzyaloshinskii-Moriya interaction in perpendicularly magnetized thin films”, *Phys. Rev. B* **90**, 020402(R) (2014)
- [255] E. Y. Vedmedenko, P. Riego, J. A. Arregi, and A. Berger, “Interlayer Dzyaloshinskii-Moriya interactions”, *Phys. Rev. Lett.* **122**, 257202 (2019)
- [256] A. A. Khajetoorians, M. Steinbrecher, M. Ternes, M. Bouhassoune, M. dos Santos Dias, S. Lounis, J. Wiebe, and R. Wiesendanger, “Tailoring the chiral magnetic interaction between two individual atoms”, *Nat. Commun.* **7**, 10620 (2016)
- [257] A. Fernández-Pacheco, E. Vedmedenko, F. Ummelen, R. Mansell, D. Petit and R. P. Cowburn, “Symmetry-breaking interlayer Dzyaloshinskii-Moriya interactions in synthetic antiferromagnets”, *Nat. Mater.* **18**, 679 (2019)
- [258] D.-S. Han, K. Lee, J.-P. Hanke, Y. Mokrousov, K.-W. Kim, W. Yoo, Y. L. W. van Hees, T.-W. Kim, R. Lavrijsen, C.-Y. You, H. J. M. Swagten, M.-H. Jung, and M. Kläui, “Long-range chiral exchange interaction in synthetic antiferromagnets”, *Nat. Mater.* **18**, 703 (2019)
- [259] P. Riego, S. Tomita, K. Murakami, T. Kodama, N. Hosoito, H. Yanagi, and A. Berger, “Enhanced magneto-optical effects in Py/Ag/Bi trilayers”, *J. Phys. D: Appl. Phys.* **50**, 19LT01 (2017)
- [260] S. Tomita, T. Suwa, P. Riego, A. Berger, N. Hosoito, and H. Yanagi, “Enhanced Magneto-Optical Activities of Modulated Fe-Pt Multilayer Metamaterials”, *Phys. Rev. Appl.* **11**, 064010 (2019)
- [261] Yu. Tsema, M. Savoini, A. Tsukamoto, A. V. Kimel, A. Kirilyuk, and Th. Rasing, “Layer-sensitive magneto-optical spectroscopic study of magnetization dynamics in multilayered RE-TM structures”, *Appl. Phys. Lett.* **109**, 172403 (2016)
- [262] E. E Fullerton, J.S Jiang, and S.D Bader, “Hard/soft magnetic heterostructures: model exchange-spring magnets”, *J. Magn. Magn. Mater.* **200**, 392 (1999)
- [263] L. Fallarino, B. J. Kirby, M. Pancaldi, P. Riego, A. L. Balk, C. W. Miller, P. Vavassori, and A. Berger, “Magnetic properties of epitaxial CoCr films with depth-dependent exchange-coupling profiles”, *Phys. Rev. B* **95**, 134445 (2017)
- [264] A. R. Khorsand, M. Savoini, A. Kirilyuk, A. V. Kimel, A. Tsukamoto, A. Itoh, and Th. Rasing, “Element-Specific Probing of Ultrafast Spin Dynamics in Multisublattice Magnets with Visible Light”, *Phys. Rev. Lett.* **110**, 107205 (2013)
- [265] E. Roman, Y. Mokrousov, and I. Souza, “Orientation Dependence of the Intrinsic Anomalous Hall Effect in hcp Cobalt”, *Phys. Rev. Lett.* **103**, 097203 (2009)
- [266] M. G. Moharam, and T. K. Gaylord, “Rigorous coupled-wave analysis of planar-grating diffraction”, *J. Opt. Soc. Am.* **71**, 811 (1981)

- [267] E. Y. Vedmedenko, R. K. Kawakami, D. D. Sheka, P. Gambardella, A. Kirilyuk, A. Hirohata, C. Binck, O. Chubykalo-Fesenko, S. Sanvito, B. J. Kirby, J. Grollier, K. Everschor-Sitte, T. Kampfrath, C.-Y. You, and A. Berger, "The 2020 magnetism roadmap", *J. Phys. D: Appl. Phys.* **53**, 453001 (2020)
- [268] A. D. Kent, "Spintronics: Perpendicular all the way", *Nat. Mater.* **9**, 699 (2010)
- [269] P. Riego, S. Vélez, J. M. Gómez-Pérez, J. A. Arregi, L. E. Hueso, F. Casanova, and A. Berger, "Absence of detectable current-induced magneto-optical Kerr effects in Pt, Ta and W", *Appl. Phys. Lett.* **109**, 172402 (2016)
- [270] R. Atkinson, and P. H. Lissberger, "Sign conventions in magneto-optical calculations and measurements," *Appl. Opt.* **31**, 6076 (1992)
- [271] D. W. Berreman, "Optics in Stratified and Anisotropic Media: 4×4-Matrix Formulation", *J. Opt. Soc. Am.* **62**, 502 (1972)
- [272] Š. Višňovský, "Magneto-optical permittivity tensor in crystals", *Czech. J. Phys. B* **36**, 1484 (1986)
- [273] J. F. Nye, "Physical Properties of Crystals", Clarendon Press, Oxford (1964)
- [274] J. A. Arregi, P. Riego, and A. Berger, "What is the longitudinal magneto-optical Kerr effect?", *J. Phys. D: Appl. Phys.* **50**, 03LT01 (2017)